UNIVERSITÀ DEGLI STUDI DI MILANO

SCUOLA DI DOTTORATO
FISICA, ASTROFISICA E FISICA APPLICATA

DIPARTIMENTO
FISICA

CORSO DI DOTTORATO DI RICERCA IN
FISICA, ASTROFISICA E FISICA APPLICATA
CICLO XXIII

Observation of the $W \to \tau\nu$ process in the ATLAS Experiment

Settore scientifico disciplinare FIS/04

Tesi di Dottorato di:
Lidia Dell'Asta

Supervisore: Prof. Francesco Ragusa
Coordinatore: Prof. Marco Bersanelli

A.A. 2009-2010

Contents

Introduction

The ATLAS Experiment (A Toroidal LHC ApparatuS) [1] is a multi-purpose detector, operating at the LHC (Large Hadron Collider) [2].

In this thesis I present the first observation of $W \to \tau\nu_\tau$ decays in ATLAS with pp collisions at 7 TeV centre-of-mass energy. The amount of data used corresponds to an integrated luminosity of 2.46 ± 0.27 pb^{-1}. The $W \to \tau\nu_\tau$ decays are searched in the channel in which the tau decays into a ν_τ and a hadronic system. These events are characterized by the presence of a hadronic jet (τ-jet) and missing energy, due to the undetected neutrinos from W and tau decays. The $W \to \tau\nu_\tau$ channel, with a cross section 10 times greater than the $Z \to \tau\tau$, is the most abundant source of taus in first data and therefore provides the first opportunity to see real hadronically decaying taus. These decays are difficult to identify in hadronic collisions, where QCD jets are produced with a much higher cross section. A tau-jet can be distinguished from QCD jets by exploiting its characteristics, such as its narrowness and the low number of associated tracks. The main backgrounds to $W \to \tau_{\rm h}\nu_\tau$ decays are leptonic decays of W and Z bosons (EW background) and QCD jets. As the uncertainties connected with the QCD jets production (both on the shape and on the cross section of the process) are big, this background has been estimated directly from data, without relying on the simulation.

As the main aspects of the analysis concern the identification of hadronically decaying taus, the measurement of the missing energy and the trigger, they are separately discussed in three chapters. Chapter 2 describes how the identification of hadronically decaying taus is performed in ATLAS. My contribution concerns the study of the performance of $\tau_{\rm h}$ identification for events characterised by the presence of a hadronic tau candidate and missing energy, which is the signature of $W \to \tau_{\rm h}\nu_\tau$ decays. Chapter 3 explains how the amount of the missing energy is measured. The performance on its reconstruction are shown and the possible sources of fake missing energy explained. As missing energy and related quantities play a fundamental role in the $W \to \tau_{\rm h}\nu_\tau$ analysis, these quantities have been carefully checked. In Chapter 4 the triggering aspects are described. In particular, I evaluated the efficiency of the trigger chosen for the analysis on the selected events. Finally, in Chapter 5 the analysis that brought to the observation of $W \to \tau_{\rm h}\nu_\tau$ decays and first hadronically decaying taus in ATLAS is explained.

My motivation to work on tau leptons arises from the expertise I accumulated during the first two years of my PhD on the ATLAS Pixel Detector and tracking, which can provide a useful contribution to tau identification. As taus have a relatively long lifetime, $\tau_\tau = (290.6 \pm 1.0) \times 10^{-15}$ s, tracks associated to it are characterised by a measurable impact parameter, which is of the order of $c\tau_\tau = 87.11$ μm. This fact can be used to exploit tracking information to distinguish tau jets from other jets. To use such information, a good resolution on the impact parameter is needed. The error on the impact parameter is dominated by detector misalignments. So, a good alignment, close to the nominal value, is necessary. Since an alignment of suitable quality was reached just after the last data

reprocessing, started at the end of October, the performance of the tracking system at the time of the analysis of data for first $W \to \tau\nu_\tau$ decays observation were not at the level needed to be used to improve $\tau_{\rm h}$ identification. But there is room in the future to work in this direction. Anyway, the performance reached by the tracking system were already adequate to help in the identification of particles containing a b quark, that usually have much larger impact parameters respect to the one of taus, of the order of $c\tau \sim 450$ μm.

To provide a homogeneous presentation of the results of this thesis, I decided not to report on the activity I carried out during the first two years of my PhD thesis, before the start of the LHC collisions, when I worked actively in ATLAS Pixel Detector community. My main contributions concerned both the simulation and the analysis of the first cosmic data. Concerning the simulation, I revised both the detector geometry and the material description in the simulation. This work brought to a new and more detailed description of the detector in the simulation and to a more precise and realistic determination of the radiation length of the package. I also developed a tool to validate the digitisation and clusterisation processes. This tool has been useful to determine the intrinsic resolution of the Pixel Detector and to study in detail the energy loss in the silicon. During cosmic ray data taking, I got involved in the Pixel Detector operations and I gave my contribution to data analysis. In particular, I investigated the collection of charge in the pixels. I studied the charge sharing phenomenon at Monte Carlo level and I worked on the determination of the charge calibration. The results have been published in three ATLAS Internal Notes [3, 4, 5]. The work has recently been included in a paper on the commissioning of the Inner Detector that has been accepted for publication by the European Physical Journal [6].

Chapter 1

Tau physics in the ATLAS Experiment

The tau lepton is the third generation lepton of the Standard Model whose properties have been studied in detail in the past decades. Because of its high mass, it is an interesting probe for many processes beyond the Standard Model that couples preferentially to heavy objects. In this chapter the main properties of the tau lepton and its role in the ATLAS physics program will be presented.

In Sections 1.1 and 1.2 the main aspects of tau decays are outlined, along with the description of the interesting channels with taus in the final state. In Section 1.3 the decay of vector bosons Z and W is described. Particular attention is paid to the decay with taus in the final state.

In Section 1.4 a brief description of the LHC and the performance it reached in the first year of high energy pp collisions is reported. Finally, in Section 1.5 the ATLAS Experiment is described in detail.

1.1 Tau lepton

The tau lepton belongs to the third family of fermions of the Standard Model, which is characterized by the large mass of its components.

The tau lepton was discovered by Martin Perl and his collaborators in 1975 [7]. The experiment that brought to the discovery was done at SLAC, with SPEAR, a e^+e^- collider ring, using a magnetic detector from LBL. With a coverage of the polar angle of $50° \leq \theta \leq 130°$ and a fully coverage of the azimuthal angle, they could detect and identify electrons, muons, photons and hadrons. Using collision at $\sqrt{s} > 4$ GeV, they found 64 anomalous events of the type:

$$e^+ + e^- \rightarrow e^\pm + \mu^\mp + \geq 2 \text{ undetected paricles} \tag{1.1}$$

without any other particle being detected. The conclusion was that for those events there was no conventional explaination. By studies of energy conservation they defined that the undetected particles were at least two. Further studies established the full compatibility between data and the production of a pair of oppositely charged heavy leptons, each of which decays into an electron or a muon and relative neutrinos [8]:

$$e^+ + e^- \rightarrow \tau^+ + \tau^- \rightarrow e^\pm + \mu^\mp + 4\nu \tag{1.2}$$

The tau properties are summarised in Table 1.1. Because of its mass the tau is the only lepton allowed to decay both in leptonic, i.e. into an electron or a muon and two

neutrinos, and hadronic channels, i.e. into a neutrino and hadrons, predominantly $\pi^{\pm}$ and π^0. At high-energy colliders the taus are often produced with a large Lorentz boost and the decay products form a τ-jet. The τ-jet is usually a narrow jet, with few associated charged particles (i.e. few associated tracks).

Since purely leptonic τ decays (τ_ℓ in the following) cannot be easily distinguished from electrons and muons from $W \to e\nu_e$ or $W \to \mu\nu_\mu$ decays, the analysis presented in this thesis uses only hadronically decaying τ leptons (τ_{h} in the following). The BR for hadronic decay is $64.79 \pm 0.07\%$ [9].

Concerning the hadronic tau lepton decays, 77% contain one charged particle (and are called 1-prong) and the rest contain mainly three charged particles (3-prong).

Properties	
Spin	1/2
Mass	1776.82 ± 0.16 MeV
Mean life	$(290.6 \pm 1.0) \times 10^{-15}$ s
Decay modes and branching ratios	
$\tau \to e\nu_e\nu_\tau$	$(17.85 \pm 0.05)\%$
$\tau \to \mu\nu_\mu\nu_\tau$	$(17.36 \pm 0.05)\%$
$\tau \to h^{\pm}\mathrm{neutr.}\nu_\tau$	$(64.79 \pm 0.07)\%$

Table 1.1: Tau lepton properties. [9]

One important characteristic of the tau lepton is that it has a measurable mean life $\tau_\tau = (290.6 \pm 1.0) \times 10^{-15}$ s. This lifetime was accurately measured at LEP with $e^+e^- \to \tau^+\tau^-$ events using the fact that charged particles from tau dacays are characterised by a measurable impact parameter with respect to the interaction point, which is of order $c\tau_\tau = 87.11$ μm. As an example of a measurement which exploits both the properties of 1-prong and 3-prong decays see [10].

The impact parameter measurement requires high precision tracking detector. Previous experiments mainly relied on silicon microstrip devices, while at the LHC silicon pixels are essential to get a low occupancy rate.

1.2 Tau lepton in dicovery physics

One of the main goal of the experiments at the CERN Large Hadron Collider (LHC) is the discovery of the Higgs boson, which is the only particle in the Standard Model that has not been observed so far.

The search strategies for Higgs boson depend on its mass. If the Higgs boson has a low mass, in the range m_H<120 GeV, one of the most interesting channel is the $H \to \tau\tau$, with a ∼10% branching ratio (see Figure 1.1): this channel has a good yield while being easier to identify than the main decay channel $H \to b\bar{b}$.

In two Higgs doublets extensions of the Standard Model (including Supersymmetry) a charged Higgs boson is also predicted, whose branching ratio into $\tau\nu$ depends on the ratio between the vacuum expectation values of the two doublets $\tan\beta$. It is anyway dominant for m_{H^+}<180 GeV (Figure. 1.2). Direct searches for charged Higgs bosons in the decay modes $H^{\pm} \to \tau\nu$ and $H^{\pm} \to$ cs have been carried out at LEP, yielding a lower bound of 78.6 GeV on $m_{H^{\pm}}$ [12]. At the Tevatron, the CDF and D0 experiments have performed direct and indirect searches for the charged Higgs boson through the process $p\bar{p} \to t\bar{t}$ with

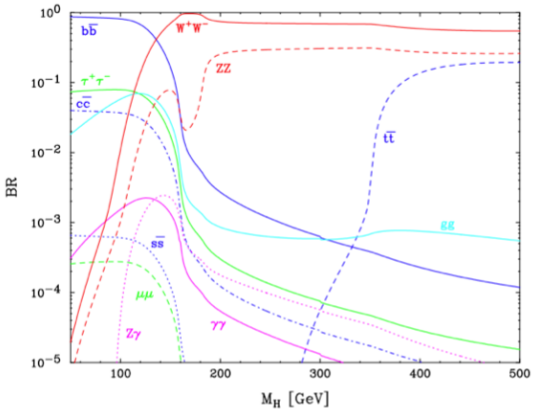

Figure 1.1: Main Standard Model Higgs boson branching ratios as a function of mass, M_H, as calculated by the HDECAY code. [11]

at least one top quark decaying via $t \to H^{\pm}b$. These searches have excluded the small and large $\tan\beta$ regions for $H^{\pm}$ masses up to ∼160 GeV [13, 14].

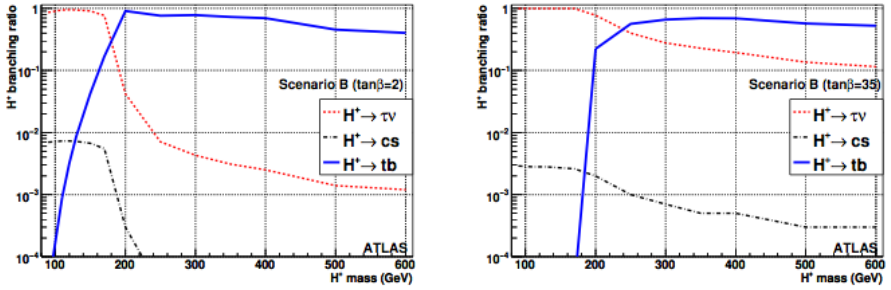

Figure 1.2: Charged Higgs boson branching ratios as a function of m_{H^+} for $\tan\beta = 2$ and $\tan\beta = 35$ and three selected decay modes. [15]

1.3 Z and W bosons decaying into taus

Given these two interesting channels in which to look for the Higgs boson, it is therefore important to know well the two Standard Model processes which are a background to them, namely $Z \to \tau\tau$ and $W \to \tau\nu_\tau$. Moreover, given their large cross section, they offer the first opportunity to study tau hadronic decays in detail.

At hadronic machines, such as the Tevatron and the LHC, vector bosons are produced through the Drell-Yan process; the relevant diagrams (up to next-to-leading order) are displayed in Figure 1.3. The main production process comes from $q\bar{q}$ annihilation, but the production can happen accompanied by a strongly interacting parton in the final state, that is, by the production of jets of hadrons.

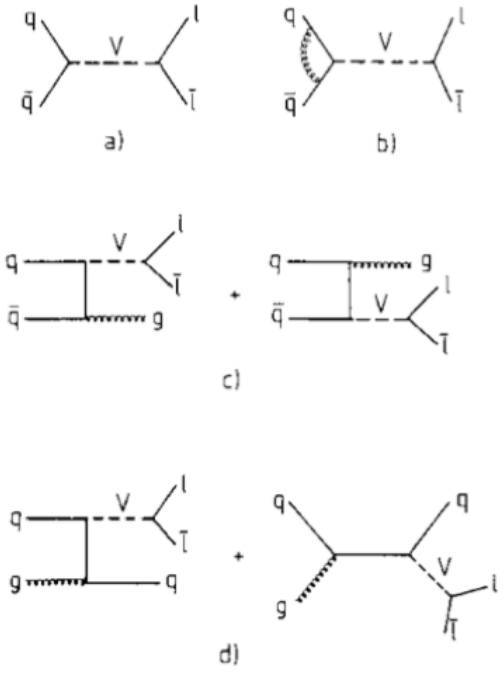

Figure 1.3: Feynman diagrams for the hadronic production of vector bosons V in QCD at leading and next-to-leading order. (a) Drell Yan (0^{th} order), (b) QCD virtual correction, (c) QCD annhilation with gluon radiation, (d) QCD Compton process [16].

The production cross sections for Z and W bosons at hadron colliders are shown in Figure 1.4, together with those of other relevant processes.

The Z boson can decay into a pair of quarks or into a pair of leptons. As at hadronic machines the Z hadronic decay is very difficult to be distinguished from the overwhelming QCD background, usually the Z is studied in its leptonic decay channels. The $Z \to ee$ and $Z \to \mu\mu$ decays have already been studied by the ATLAS Experiment at the LHC, with the measurement of their cross sections in pp 7 TeV collisions [18]. The measurement was found to be in agreement with the NNLO predictions, which foresee a cross section of 0.99 nb.

The W boson can decay into a pair of quarks or into a charged lepton and a neutrino. The ATLAS Experiment has already measured the cross sections of $W \to e\nu_e$ and $W \to \mu\nu_\mu$ decays [19] with 7 TeV collision data. It was found to be in agreement with NNLO predictions of 10.46 nb. The limiting factor of the measurements is still the systematic

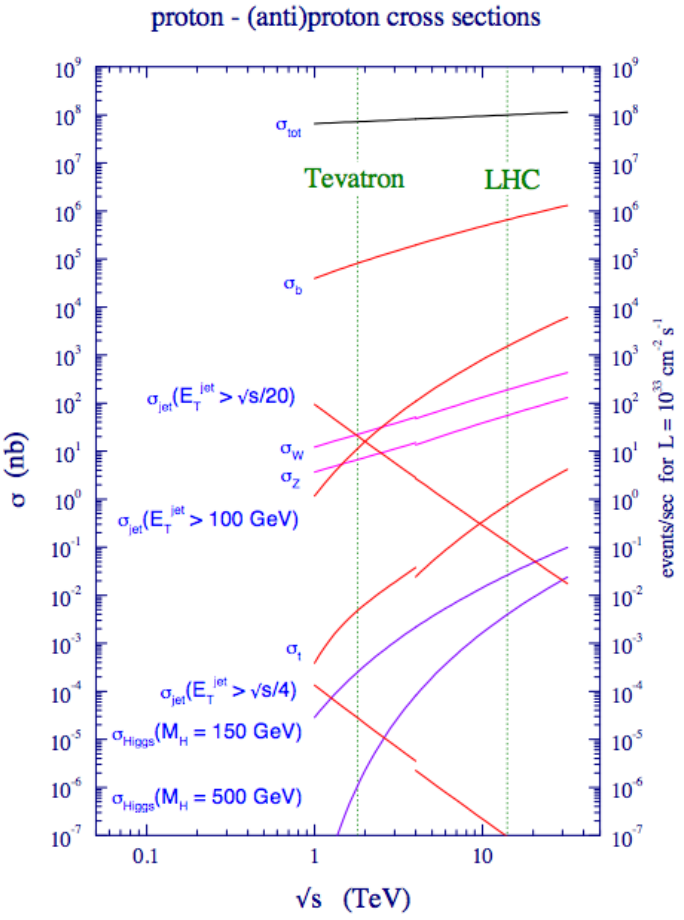

Figure 1.4: Standard Model cross sections at the Tevatron and LHC colliders. [17]

uncertainty from the jet energy scale determination and from the luminosity.

The measurement of the charge asymmetry provides important information about parton distribution functions. Inclusive measurements have been performed at the Tevatron [20, 21, 22, 23], for both $W \to e\nu_e$ and $W \to \mu\nu_\mu$ events and the data have been included in global fits of parton distributions [24, 25]. The lepton asymmetry is defined as:

$$A = \frac{\sigma^{\ell^+} - \sigma^{\ell^-}}{\sigma^{\ell^+} + \sigma^{\ell^-}} \tag{1.3}$$

In contrast to proton-antiproton collisions, the cross sections for W^+ and W^- production measured with proton-proton collisions are asymmetric due to the absence of valence antiquarks in the proton: the overall asymmetry is predicted to be significantly different from zero. The asymmetry varies as a function of lepton pseudorapidity since it is highly correlated with the kinematic phase space of the incoming partons and hence each η-bin probes partons with different average values of the momentum fraction. The charge asymmetry for $W \to e\nu_e$ and $W \to \mu\nu_\mu$ channels has already been measured by the ATLAS Experiment with 7 TeV collision data [19]. The measurement is in agreement with the predictions and it is shown in Figure 1.5.

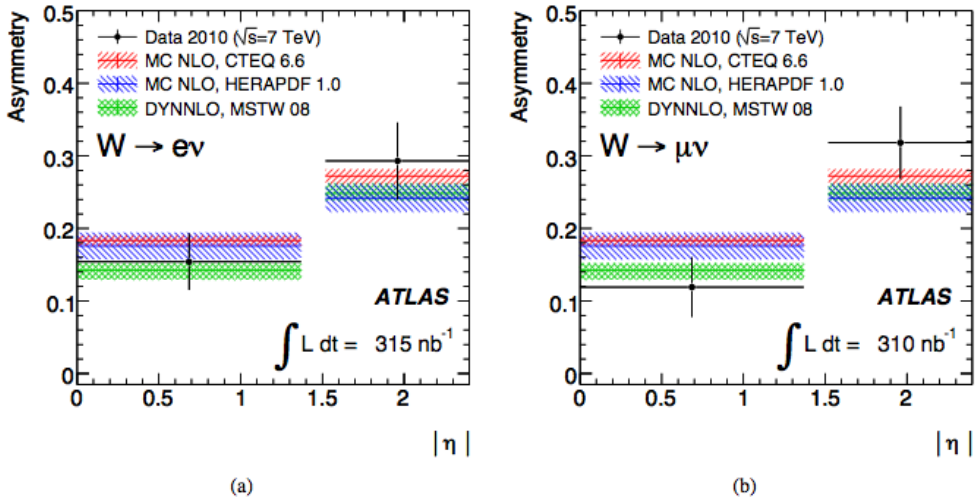

Figure 1.5: Lepton charge asymmetries for the electron (a) and muon (b) channels. Superimposed are several theoretical predictions. [19]

1.3.1 $Z \to \tau\tau$ decays

For the $Z \to \tau\tau$ channel the branching ratio is $(3.367 \pm 0.008)\%$ [9]. The $Z \to \tau\tau$ decay can be studied both in the case in which one tau decays leptonically into an electron or a muon and two neutrinos, while the other tau decays into hadrons and a neutrino, and in the case in which both taus decay hadronically, giving two back-to-back tau jets and neutrinos. The selection of the first channel is easier and less contaminated by QCD jets, as the presence of an isolated lepton helps in rejecting such a background.

The status of the art of the measurements of $Z \to \tau\tau$ decays is the cross section measurement accomplished by the CDF and D0 experiments at the Tevatron collider.

The measurment of the $Z \to \tau\tau$ cross section provides a test of universality, when compared to the $Z \to ee$ and $Z \to \mu\mu$ counterparts. Moreover the production mechanism at hadron colliders (see Figure 1.3) makes this cross section sensitive to higher order QCD corrections, both to the partonic cross sections and to the PDFs.

The CDF collaboration studied the $Z \to \tau\tau$ process in the $Z \to \tau\tau \to e\tau_{\mathrm{h}}$ channel [26]: one tau decays to an electron and two neutrinos and the other decays into a hadronic system and a neutrino. The measurement is based on an integrated luminosity of 350 pb^{-1} of data taken at $\sqrt{s} = 1.96$ TeV. The derived cross section is $\sigma(\mathrm{p\bar{p}} \to Z) \times BR(Z \to \tau\tau) = 264 \pm 23(\mathrm{stat.}) \pm 14(\mathrm{syst.}) \pm 15(\mathrm{lumi.})$ pb, which is in agreement with the next-to-next-to-leading order QCD prediction.

The D0 collaboration instead presented results on the $Z \to \tau\tau \to \mu\tau_{\mathrm{h}}$ channel and the $Z \to \tau\tau \to \mu e$ together [27]. Using 1 fb^{-1} of data, the cross section was measured to be $\sigma(\mathrm{p\bar{p}} \to Z) \times BR(Z \to \tau\tau) = 249 \pm 8(\mathrm{stat.}) \pm 12(\mathrm{syst.}) \pm 15(\mathrm{lumi.})$ pb.

The two measurements done at Tevatron agree with each other within uncertainties and are consistent with the Standard Model prediction.

At the LHC it is planned to study the $Z \to \tau\tau$ channel first of all as a control channel to test the detector performance. Especially when studied in the mode where a tau decays leptonically and the other hadronically, the $Z \to \tau\tau$ events contain many different reconstructed objects (leptons, taus, missing transverse energy), and is therefore useful to calibrate the absolute energy scales of these objects and to evaluate trigger, reconstruction and identification efficiencies. Then the $Z \to \tau\tau$ cross section will be measured as well.

Preliminary signal has been recently presented by the CMS collaboration [28].

1.3.2 $W \to \tau\nu_\tau$ decays

For the W boson, the branching ratio into $\tau\nu_\tau$ is (11.25 ± 0.20) %. The $W \to \tau_{\rm h}\nu_\tau$ channel is more complicated to select than the $Z \to \tau\tau$ channel, because the signature is just a tau jet accompanied by missing energy. Therefore the QCD contamination is higher, even though the amount of missing energy can be used to reduce this background.

Measurements concerning the $W \to \tau_{\rm h}\nu_\tau$ channel at hadron colliders have been already performed with Run I and Run II data at Tevatron experiments. The measurement of the W boson production cross section times branching ratio to tau lepton and neutrino can be used with the corresponding result from the electron channel to test one of the fundamental concepts in the Standard Model: the universality of the leptonic couplings to the weak charged current.

The CDF Collaboration measured the cross section for $\sigma(\mathrm{p\bar{p}} \to W) \times BR(W \to \tau\nu_\tau)$ and the ratio BR($W \to \tau\nu_\tau$)/BR($W \to e\nu_e$) in $\mathrm{p\bar{p}}$ collisions at $\sqrt{s} = 1.8$ TeV (Run I) [29]. The amount of data analysed was 4.5 pb^{-1}. They found $\sigma(W \to \tau\nu_\tau) = 2.05 \pm 0.27$nb, were the error takes into account both the statistical and the systematic error. The ratio BR($W \to \tau\nu_\tau$)/BR($W \to e\nu_e$) was found to be 0.97 ± 0.07, in agreement with lepton universality.

More recently, the D0 Collaboration [30] did the same measurement at the same centre-of-mass energy but using 18 pb^{-1}. The cross section was measured to be 2.22 ± 0.09 (stat.) ± 0.10 (syst.) ± 0.10 (lumi.) nb. This value is in agreement with the previous CDF result. It is interesting to notice that the limiting factor of the measurement comes from the systematic uncertainty on the energy scale. In fact, the number that is quoted as systematic uncertainty comes from the uncertainty on the acceptance, which is dominated by the uncertainty on the determination of the energy scale. The systematic uncertainty from the luminosity measurement is of the same order of magnitude. An uncertainty of 4.5% from luminosity is quoted. The value which is quoted now for the experiments at the LHC is around 11%, but it is foreseen that it will be soon reduced. It is therefore clear that, to have a good cross section measurement at the LHC, it will be fundamental to keep the systematic on the luminosity and the energy scale under the 5%.

Along with the cross section, D0 measured also the branching ratio BR($W \to \tau\nu_\tau$)/BR($W \to e\nu_e$), with the same amount of data. It was found to be 0.980 ± 0.031.

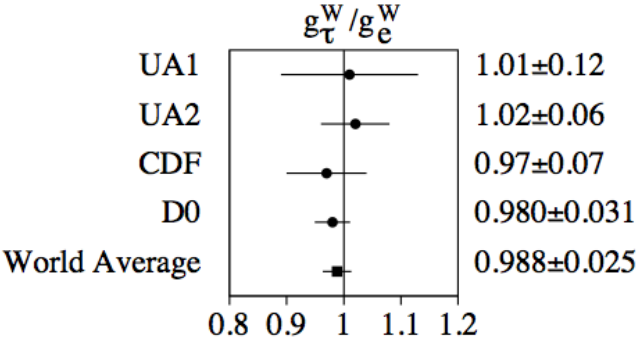

Figure 1.6: BR($W \to \tau\nu_\tau$)/BR($W \to e\nu_e$) from UA1 [31], UA2 [32], CDF [29], and D0 [30].

The last interesting measurement done at Tevatron concerning the $W \to \tau_{\rm h}\nu_\tau$ channel

are the measurements done by CDF with $p\bar{p}$ collisions at $\sqrt{s} = 1.96$ TeV (Run II) [33]. Using 72 pb^{-1} the cross section of $W \to \tau\nu_\tau$ decays was measure to be 2.62 $\pm$ 0.07 (stat.) $\pm$ 0.21 (syst.) $\pm$ 0.16 (lumi.) nb and the branching ratio BR($W \to \tau\nu_\tau$)/BR($W \to e\nu_e$) 0.99 $\pm$ 0.04 (stat.) $\pm$ 0.07 (syst.).

In Figure 1.6 it is reported a summary of the measurements of BR($W \to \tau\nu_\tau$)/BR($W \to e\nu_e$), taken from [30], done with different centre-of-mass-energy and both at $p\bar{p}$ and e^+e^- colliders.

At the LHC, those measurements will be repeated with the first data at low instantaneous luminosity, however in more difficult conditions than at the Tevatron, since the expected signal-to-background ratio will be 10 times smaller. The period of data taking with an instantaneous luminosity of 10^{31} cm^{-2}s^{-1} provides a unique possibility for observing this channel since even at a luminosity of 10^{32} cm^{-2}s^{-1}, the thresholds needed to limit trigger rates to the available bandwidth will be too high to efficiently collect signal events.

In this thesis, the first observation of such decays at the ATLAS Experiment will be described (Chapter 5). Already with an integrated luminosity of only 2.46 ± 0.27 pb^{-1} it was possible to see the charge asymmetry described before.

In order to illustrate the kind of events to be studied and how they manifest themselves in the ATLAS detector, in Figure 1.7 the event display of one of the first $W \to \tau_h\nu_\tau$ candidate recorded by the ATLAS Experiment is shown. The typical signature of such decays is clear: the event is characterised by one jet reconstructed as a tau jet and missing energy.

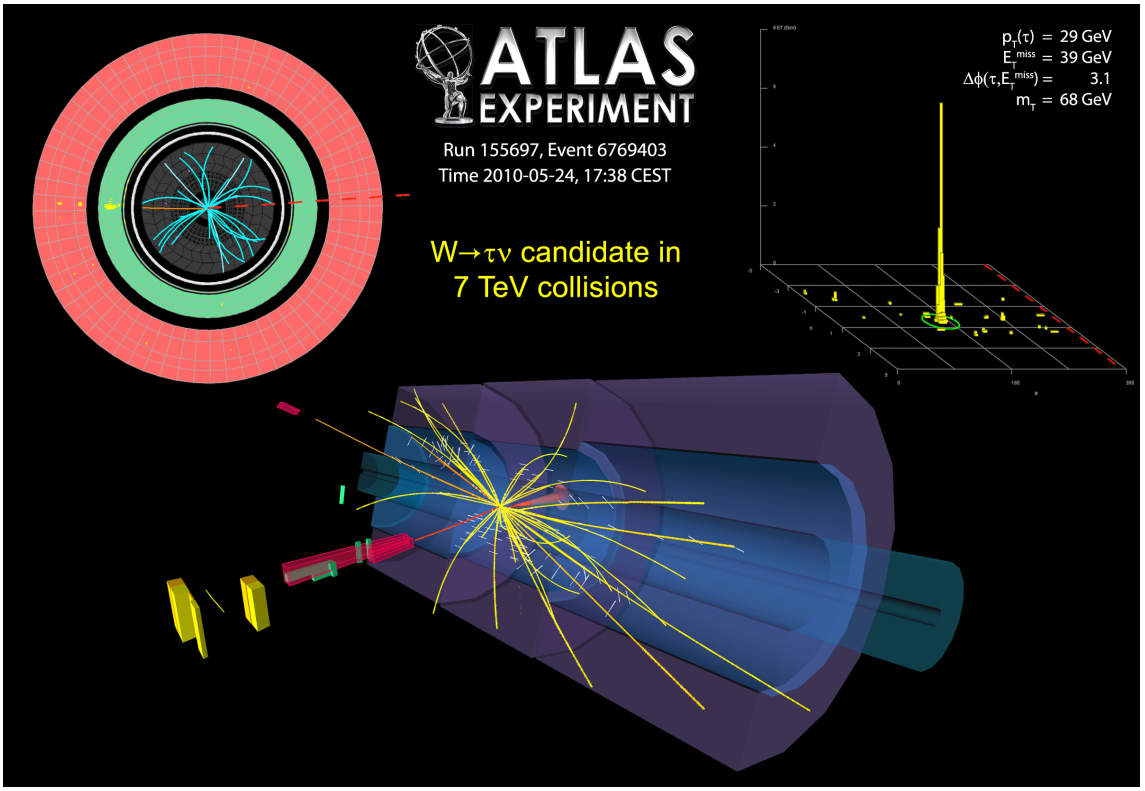

Figure 1.7: Event display of one of the first $W \to \tau_h\nu_\tau$ decay candidate, collected on 24 May 2010. Event properties: p_T = 29 GeV, E_T^{miss} = 39 GeV, $\Delta\phi(\tau_h, E_T^{miss})$ = 3.1 and m_T = 68 GeV. No additional object (electron, photon, muon or jet) was found in the event.

This event was collected on 24 May, 2010. The event passes the event selection described

in Section 5.4. The τ_{h} candidate has a transverse momentum p_{T} of 29 GeV and it is reconstructed as a 1 prong decay. The $E_{\mathrm{T}}^{\mathrm{miss}}$ amounts to 39 GeV. The separation in the ϕ direction between the τ_{h} candidate and the $E_{\mathrm{T}}^{\mathrm{miss}}$ is 3.1. The reconstructed tau is the only high-momentum object in the event: no other jets, muons, electrons or photons were found.

The top left view of the event display shows a projection in the $x - y$ plane. The track, associated to the τ_{h}, is well isolated and is depicted as a red-orange line. The energy deposits in the electromagnetic (green ring) and in the hadronic (pink ring) calorimeters are shown in yellow. The $E_{\mathrm{T}}^{\mathrm{miss}}$ direction is shown as a red dotted line.

In the 3D view, the energy deposits in the calorimeters are combined in clusters (purple boxes) forming a narrow shower typical of a hadronic tau decay.

1.4 The LHC

The LHC (Large Hadron Collider) [2] is actually the largest and highest-energy particle accelerator in the world.

It has been built at CERN, in the same circular tunnel formerly used by LEP (Large Electron Positron Collider). It is a 27 km long tunnel, dug at a depth varying between 50 and 175 meters below the ground.

The LHC had been designed to provide both proton-proton (pp) and heavy ion (HI) collisions. For pp collisions, the design luminosity is 10^{34} cm^{-2}s^{-1} and the foreseen centre-of-mass energy for the collision is 14 TeV. In the first year of operation at high energy, the maximum instantaneous luminosity that has been reached is slightly higher than 2 10^{32} cm^{-2}s^{-1}, while collisions up to 7 TeV have been provided. For HI collisions, the project foresaw to use lead ions with an energy of 2.8 TeV per nucleon, reaching a peak luminosity of 10^{27} cm^{-2}s^{-1}. In the first month of HI running (November 2010) collision at 2.76 TeV per nucleon took place, reaching a peak instantaneous luminosity of 28.8 10^{24} cm^{-2}s^{-1}.

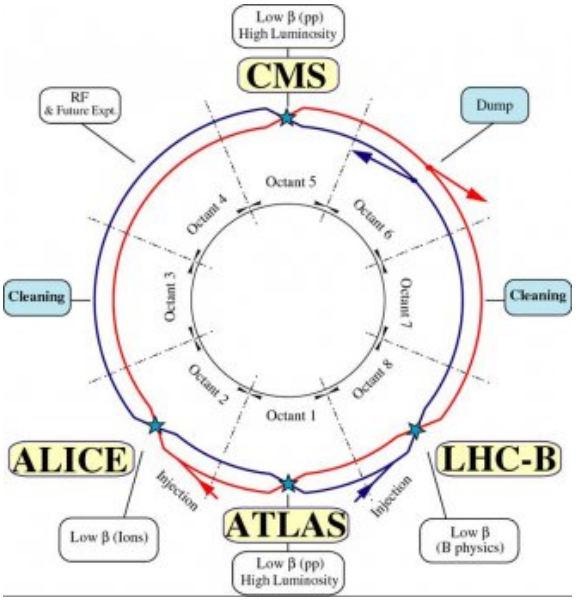

Figure 1.8: A schematic view of the LHC, its two beams and the four interaction regions.

The LHC is mainly composed by superconducting magnets. They operate at a temperature of 1.9 K, which is provided by a cryogenic system based on liquid helium. The LHC is equipped with a 400 MHz superconducting cavity system. Different types of magnets compose the LHC, according to different operations to be performed on the beams. Dipole magnets (for a total of 1232 magnets) keep the beams on their circular trajectory, while quadrupole magnets (for a total of 392) are used to keep the beams focused, in order to maximize the chances of interaction between the particles in the four intersection points, where the two beams cross. Close to these four intersection points, the LHC has straight sections, in which the two beam pipes, in which particles circulate, become one and the particles are then made collide. At the collision points, four big experiments have been built: ATLAS [1], CMS [34], LHCb [35] and ALICE [36]. The first two are multi-purpose experiments, designed to study high transverse momentum events for the search of the Higgs boson and other phenomena beyond the Standard Model. LHCb has instead been designed especially to study b-physics, while ALICE was built to work with heavy ion collisions, to study the formation of a quark-gluon plasma. A schematic view of the LHC,

the two beams and the four interaction regions is shown in Figure 1.8. Colliding particles in the LHC are bunched together, into 2808 bunches, so that interactions happen every 25 ns. During the commissioning phase, the number of bunches circulating is lower.

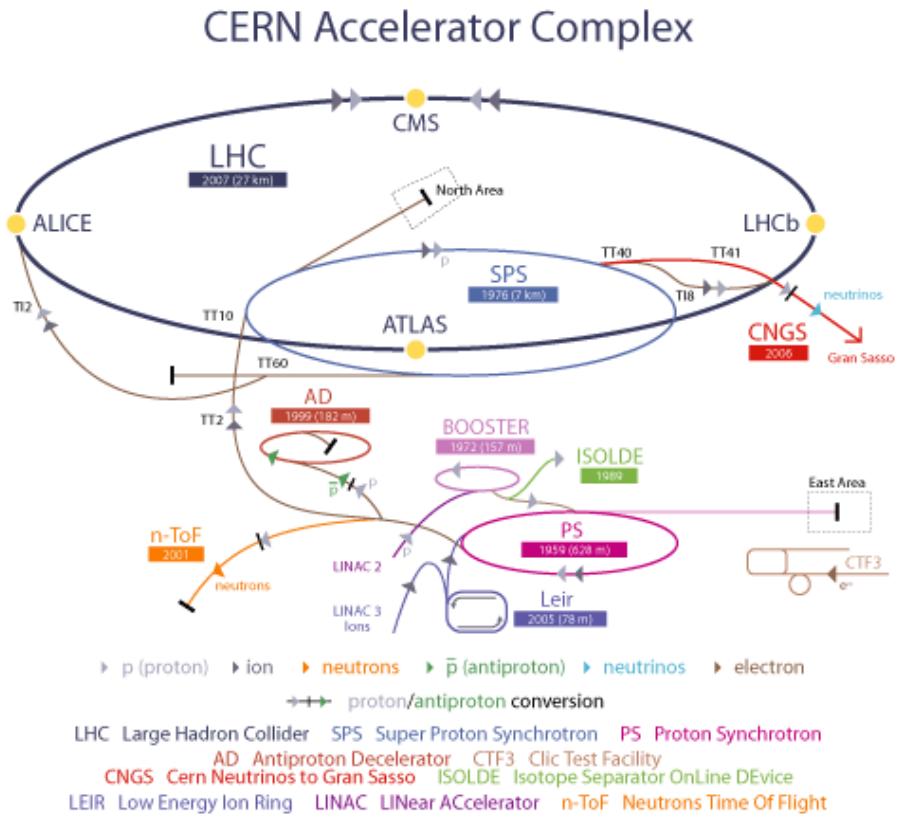

Figure 1.9: A schematic view of the acceleration chain at CERN.

Before being injected into the LHC, particles are accelerated step by step up to the injection energy of 450 GeV, by a series of accelerators. For protons, the first system is the linear accelerator LINAC2, which generates them at an energy of 50 MeV. Protons then go through the Proton Synchrotron Booster (PSB) and are accelerated to 1.4 GeV. Then they are injected into the Proton Synchrotron (PS), where they are accelerated to 26 GeV. Finally, the Super Proton Synchrotron (SPS) is used to further increase their energy to 450 GeV. For lead ions the production is different. They are first accelerated by the linear accelerator LINAC 3. Then the Low-Energy Ion Ring (LEIR) is used as an ion storage and cooler unit. The ions are then further accelerated by the PS and SPS before being injected into the LHC ring. The different accelerators are shown in Figure 1.9.

The LHC started its operations on 10 September 2008, with the first beams circulating into the rings, in both directions, without collisions. After a commissioning phase, first collisions were expected few days later. Unfortunately, on 19 September of the same year a major accident happened, due to defective electrical connection between two magnets. In the accident 53 magnets were damaged. This caused a long stop of the machine, to repair the damaged magnets, to check the electrical connections and to improve the safety systems.

During Autumn 2009, after more than one year stop, the operations started again, with the first collisions at a centre-of-mass energy of 900 GeV recorded by the four experiments on 23 November 2009. After a 900 GeV collisions data taking, the centre-of-mass energy

was further increased to 2.36 TeV, beating the Tevatron's previous record of 0.98 TeV per beam and giving therefore collisions at the highest energy ever reached before.

After some months, the first collisions at 7 TeV were registered, on 30 March 2010, starting a new running period that went on until the beginning of November, when the LHC provided the first heavy ion collisions.

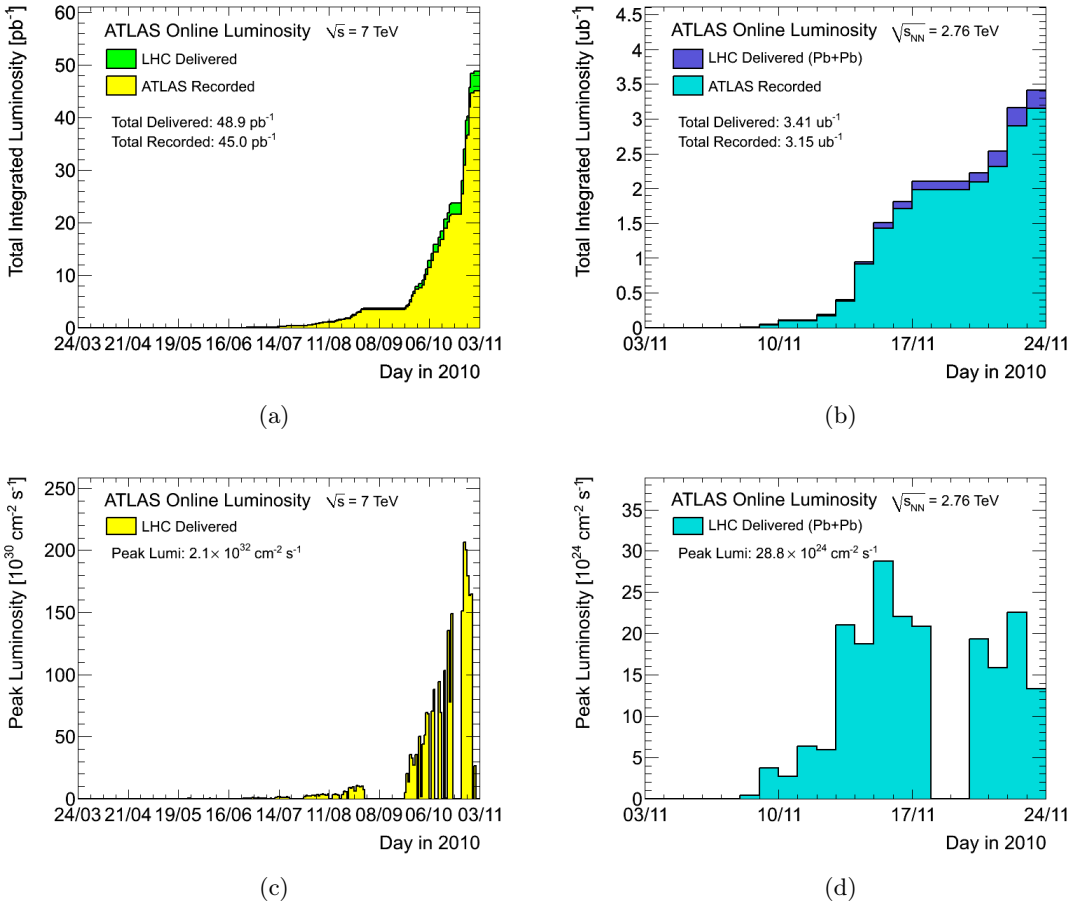

Figure 1.10: Cumulative luminosity versus day delivered (green) to, and recorded (yellow) by ATLAS during stable beams (a) for 7 TeV centre-of-mass energy pp collisions and (b) 2.76 TeV per nucleon lead-lead collisions. The maximum instantaneous luminosity versus day delivered to ATLAS (c) in pp collisions and (d) in lead-lead collisions. Given is the luminosity as determined from counting rates measured by the luminosity detectors.

During the 7 TeV running, the machine underwent an intense commissioning phase. At the beginning of the operations, the luminosity was very low, of the order of 10^{27} $\mathrm{cm}^{-2}\mathrm{s}^{-1}$, and there was just one bunch circulating in each beam. The higher luminosity was achieved both by increasing the intensity and the number of the bunches, and by squeezing the beams. At the end of the pp collision program, the highest instantaneous luminosity reached by the LHC was 2.1 10^{32} $\mathrm{cm}^{-2}\mathrm{s}^{-1}$, as shown in Figure 1.10.

1.5 The ATLAS Experiment

The ATLAS (A Toroidal LHC ApparatuS) Experiment is one of the four detectors built at the CERN LHC. It is positioned at Point1, in a cavern at a depth of 100 m.

With its height of 25 m and its length of 44 m, the ATLAS Experiment is one of the biggest detectors ever built. It weights about 7000 tons. After the cavern was completed, the construction started in 2003 and it went on until July 2007, with the insertion of the innermost detector and the lowering of the last end-cap toroidal magnet. A scheme of the detector and of its components is shown in Figure 1.11.

In the following, after a brief introduction on the physics motivation of the ATLAS Experiment, the various systems composing the detector will be described in detail.

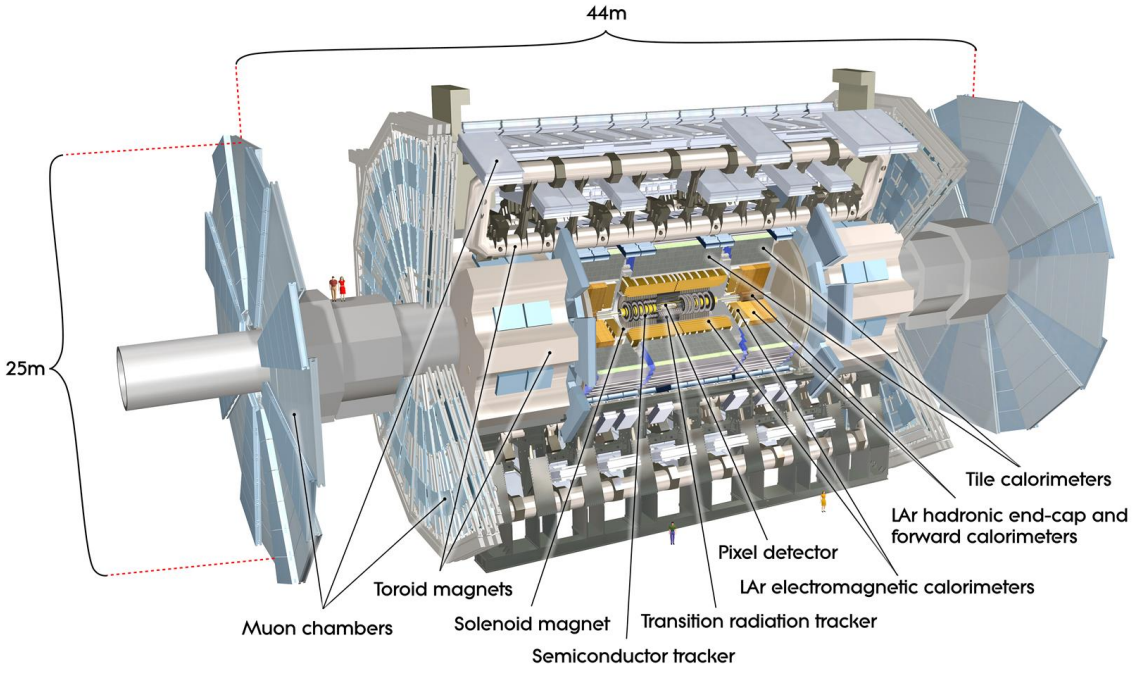

Figure 1.11: A schematic view of the ATLAS Experiment.

1.5.1 Physics motivation

LHC will provide a rich physics potential, ranging from more precise measurements of Standard Model parameters to the search for new physics phenomena [37]. In this section, an overview of the experimental program is given.

Higgs boson While the Standard Model of electroweak and strong interactions is in excellent agreement with the numerous experimental measurements, the dynamics responsible for electroweak symmetry breaking is still unknown. Within the Standard Model, the Higgs mechanism is invoked to break the electroweak symmetry. A doublet of complex scalar fields is introduced, of which a single neutral scalar physical particle, the Higgs boson, remains after symmetry breaking.

Within the Standard Model, the Higgs boson is the only particle that has not been discovered so far. The direct search at the e^+e^- collider LEP has led to a lower

bound on its mass of 114.4 GeV [38]. Recently, the experiments at Tevatron have excluded at 95%C.L. a SM Higgs with a mass in the mass range $160 < m_H < 170$ GeV [39].

The search strategies for Higgs boson depend on its mass. If the Higgs boson has a low mass, in the range $m_H < 120$ GeV, one of the most interesting channel is the $H \to \tau\tau$, with a $\sim$10% branching ratio. In two Higgs doublets extentions of the Standard Model (including Supersymmetry) a charged Higgs boson is also predicted, whose branching ratio into $\tau\nu$ depends on the ratio between the vacuum expectation values of the two doublets $\tan\beta$.

Standard Model Figure 1.4 shows the cross-section for the production of many Standard Model particles during collisions, as a function of the energy in the centre of mass ($\sqrt{s}$). The high luminosity and increased cross-sections available at the LHC, with respect to the Tevatron experiments, enable many high-precision tests of QCD, electroweak interactions, and flavour physics.

Supersymmetry Supersymmetry (SUSY) is one of the theoretically favoured candidates for physics beyond the Standard Model. Models of supersymmetry involve new, highly massive particles. These usually decay into high-energy quarks and stable heavy particles that are very unlikely to interact with ordinary matter. Supersymmetric events are expected to be characterised by several high-momentum jets and missing transverse energy [40].

Heavy ion physics The data taking with Pb-Pb collisions will give the possibility to discover new phenomena, even though the ATLAS Experiment has not been thought for heavy ion collisions. In particular, thanks to the good performance of the calorimeter system, already with few μb^{-1} of data it has been possible to observe the "jet-quenching" [41], which is a new phenomena characterised by large dijet asymmetries, not observed in proton-proton collisions, which may point to an interpretation in terms of strong parton energy loss in a hot, dense medium.

1.5.2 Detector description

A complete description of the ATLAS detector can be found in [1]. The ATLAS detector has been built surrounding the interaction region. It is composed of a tracking system, calorimeters and muon spectrometers.

The general requirements for the LHC experiments translate into nominal detector performance goals for the ATLAS detector are reported in Table 1.2.

The global reference frame adopted by ATLAS is centred on the nominal interaction point, which is defined as the origin of the coordinate system. The beam direction defines the z-axis and the $x-y$ plane is transverse to the beams. The positive x-axis is defined as pointing from the interaction point to the centre of the LHC ring and the positive y-axis is defined as pointing upwards. The side-A of the detector is defined as that with positive z and side-C is that with negative z. Given the symmetry of the system, a cylindrical coordinate system is often used: the azimuthal angle ϕ is measured around the z-axis, and the polar angle θ is the angle from the beam axis. The pseudorapidity is defined as $\eta = -\ln(\tan\frac{\theta}{2})$. Transverse quantities, such as the transverse momentum p_{T} , the transverse energy E_{T} and the missing transverse energy $E_{\text{T}}^{\text{miss}}$ are defined in the $x-y$ plane. The distance R in the pseudorapidity-azimuthal space is defined as $R = \sqrt{\Delta\eta^2 + \Delta\phi^2}$.

Detector component	Required resolution	η coverage
Tracking	$\sigma_{p_T}/p_T = 0.05\% p_T \oplus 1\%$	$\pm$ 2.5 ($\pm$ 2.0 for the TRT)
EM calorimetry	$\sigma_E/E = 10\%/\sqrt{E} \oplus 0.7\%$	$\pm$ 3.2 ($\pm$ 2.5 for the trigger)
Hadronic calorimetry barrel and end-cap forward	 $\sigma_E/E = 50\%/\sqrt{E} \oplus 3\%$ $\sigma_E/E = 100\%/\sqrt{E} \oplus 10\%$	 $\pm$ 3.2 $3.1 < \lvert\eta\rvert < 4.9$
Muon spectrometer	$\sigma_{p_T}/p_T = 10\% p_T$ at p_T = 1 TeV	$\pm$ 2.7 ($\pm$ 2.4 for the trigger)

Table 1.2: Nominal detector performance goals and coverage for the ATLAS detector.[1]

The magnets

ATLAS has a system of four large superconducting magnets (Figure 1.12). This magnetic system is 22 m in diameter and 26 m in length, with a stored energy of 1.6 GJ. The four magnets provide the magnetic field over a volume of approximately 12 000 m^3 (defined as the region in which the field exceeds 50 mT). The structure of the ATLAS detector itself is determined by the layout of the magnetic system.

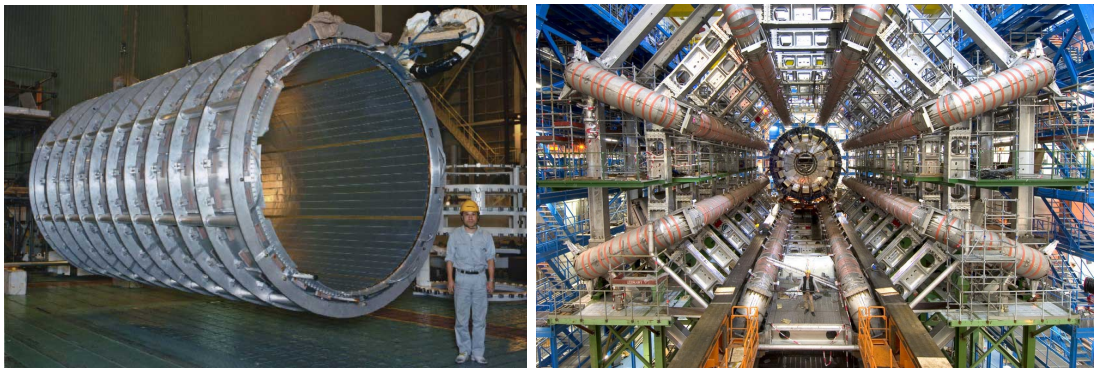

(a) (b)

Figure 1.12: Photos of the magnets of the ATLAS Experiment: (a) the solenoid and (b) the barrel toroid.

The central solenoid is designed to provide a 2 T axial field. To achieve the desired calorimeter performance, the layout is carefully optimised to keep the material thickness in front of the calorimeter as low as possible, resulting in the solenoid assembly contributing a total of ∼0.66 radiation lengths at normal incidence. The inner and outer diameters of the solenoid are 2.46 m and 2.56 m and its axial length is 5.8 m. The flux is returned by the steel of the ATLAS hadronic calorimeter and its girder structure.

The system that generates the magnetic field for the muon spectrometer is composed of three large air-core toroids: one barrel component and two end-caps. The field is centred on the beam axis, perpendicular to the solenoidal field that serves the Inner Detector. The two end-cap toroids (inner diameter 1.65 m, outed diameter 10.7 m, length 5.0 m) are inserted in the barrel toroid (inner diameter 9.4 m, outed diameter 20.1 m, length 25.3 m) at each end and line up with the central solenoid. Each of the three toroids consists of

eight coils assembled radially and symmetrically around the beam axis.

The performance of the toroids in terms of bending power is characterized by the field integral $\int \mathrm{Bdl}$, where B is the field component normal to the muon direction and the integral is computed along an infinite momentum muon trajectory, between the innermost and outermost muon-chamber planes.

The barrel toroid provides 1.5 to 5.5 Tm of bending power in the pseudorapidity range $0 < |\eta| < 1.4$, and the end-cap toroids approximately 1 to 7.5 Tm in the region $1.6 < |\eta| < 2.7$. The bending power is lower in the transition regions where the two magnets overlap ($1.4 < |\eta| < 1.6$).

The Inner Detector

The Inner Detector is the innermost system of the ATLAS detector. It is composed by three subdetectors: two silicon detectors, the Pixel Detector and the SemiConductor Tracker (SCT), and the Transition Radiation Tracker (TRT). A schematic view of the Inner Detector is shown in Figure 1.13. It is immersed in an axial magnetic field of 2 T, provided by a solenoid placed immediately behind the tracker. The overall dimensions of the tracking system are 2.1 m in diameter and 6.2 m in length.

The Inner Detector measures tracks from the passage of charged particles. Being immersed in a magnetic field, it also measures the p_{T} of tracks. Moreover, good performances on position determination are essential for secondary vertexes identification, which are the signature, for example, of b-quark originated jets and tau leptons. A good knowledge of charge release in the active elements of the Pixel Detector can also help in particle identification for particles with very low momenta. From the transition radiation of the TRT it is possible to discriminate electrons from heavier particles.

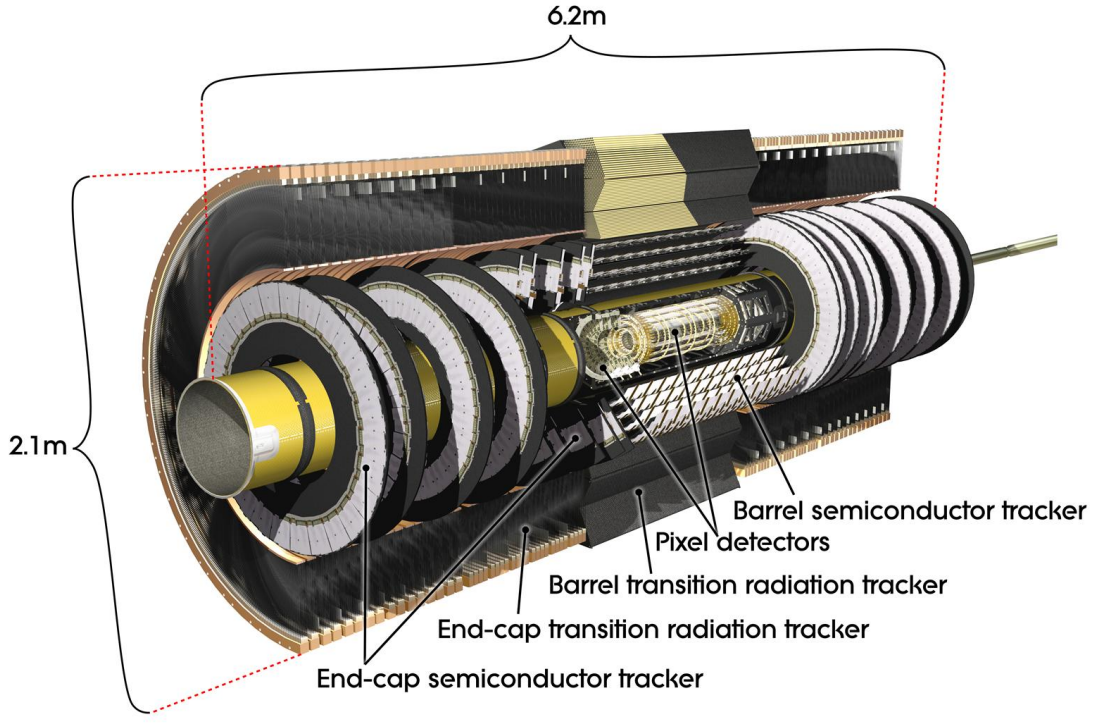

Figure 1.13: A schematic view of the Inner Detector of the ATLAS Experiment.

The Inner Detector was completely installed in June 2007, with the insertion of the Pixel Detector. After the commissioning of the cooling system (needed for Pixel and SCT), the commissioning of the full tracking system with cosmic ray data started [6]. Good performance have been reached by the three subdetectors.

The Pixel Detector The Pixel Detector is the nearest system to the collision point of the LHC beams. It is composed by three cylindrical layers in the barrel region (at radii 50.5 mm, 88.5 mm and 122.5 mm) and two end-caps, each consisting of three disks (located at 495 mm, 580 mm and 650 mm from the detector centre). The Pixel Detector provides three precision measurement points for tracks with pseudorapidity $|\eta| < 2.5$ and it has a full coverage in ϕ.

The detector structure is made of low-mass carbon fiber and integrates the cooling system, resulting in a total contribution to X_0 of about 3% per layer. Moreover, all the detector components are designed to sustain a radiation dose of ∼500 kGy, which is the dose expected during detector life time.

The basic elements of the Pixel Detector are the modules, that are identical for barrel and disks. In the barrel region, modules are arranged in overlapping staves of 13 modules each, while in the disks 6-modules form a sector, for a total of 1744 modules.

The sensor [42] is made of n^+-in-n silicon and is 256 ± 3 μm thick. Each module covers an active area of 16.4×60.8 mm^2 and contains 47 232 pixels, which corresponds to ∼80.4 million channels for the whole detector. The typical pixel size is 50×400 μm^2. The short side is oriented along the Rϕ direction, while the longer pitch is oriented approximately along the z direction in the barrel and along R in the endcaps.

A module is read out by 16 radiation-hard front-end chips [43] bump-bonded to the sensor. Each chip contains 18 columns × 160 rows of readout cells.

The pulse height measurement of the Pixel Detector is based on the Time-over-Threshold (ToT) of signals.

The design requirement was to achieve a resolution of 10 μm in the azimuthal direction and 115 μm along the beam direction. The alignment precision should be better than 7 μm in order not to worsen the detector resolution by more than 20%.

The SCT The SemiConductor Tracker (SCT) is the second element of the tracking system, going from the beam pipe outwards. It is composed by four cylinders in the barrel region, with radii between 299 mm and 514 mm and a full length of 1492 mm. Each of the two end-caps consists of 9 disks. It provides typically eight strip measurements (four space-points) for particles originating in the beam-interaction region.

The detector consists of 4088 modules. The strips in the barrel are approximately parallel to the solenoid field and beam axis, and have a constant pitch of 80 μm, while in the end-caps the strip direction is radial and of variable pitch. Most modules [44, 45] consist of four silicon-strip sensors [46]; two sensors on each side are daisy-chained together to give 768 strips of approximately 12 cm in length. A second pair of identical sensors is glued back-to-back with the first pair at a stereo angle of 40 mrad to provide space points.

The strips are read out by radiation-hard front-end readout chips [47], each chip reading out 128 channels; the total number of readout channels is ∼6.3 million.

The hit information is binary: a hit is registered if the pulse height in a channel exceeds a preset threshold, normally corresponding to a charge of 1 fC.

The intrinsic accuracies of the SCT are 17 μm in the azimuthal direction and 580 μm along the beam direction.

The TRT The Transition Radiation Tracker (TRT) is the outermost system of the Inner Detector and its sensitive volume covers radial distances from 563 mm to 1066 mm.

The detector consists of 298 304 proportional drift tubes (straws), 4 mm in diameter, read out by ∼351 000 electronic channels.

The straws in the barrel region are arranged in three cylindrical layers and 32 ϕ sectors; they have split anodes and are read out from each side [48]. The straws in the end-cap regions are radially oriented and arranged in 80 wheel-like modular structures [49]. The TRT straw layout is designed so that charged particles with transverse momentum $p_{\mathrm{T}} >$ 0.5 GeV and with pseudorapidity $|\eta| < 2.0$ cross typically more than 30 straws.

The TRT can also be used for particle identification. Its tubes are interleaved with layers of polypropylene fibres and foils: a charged particle that passes through the boundary region between materials with a different refraction index emits X-ray radiation whose intensity is proportional to the relativistic γ factor. The TRT works with two threshold levels (defined at the level of the discriminator in the radiation-hard front-end electronics [50]): the ratio of the high threshold hits versus all the hits can be used to identify electrons.

Cooling system The Pixel Detector and the SCT share a cooling system [51], which is a bi-phase evaporative system which is designed to deliver C_3F_8 fluid at -25 °C in the low-mass cooling structures on the detector. The target temperature for the silicon sensors after irradiation is 0 °C for the Pixel Detector and -7 °C for the SCT; these values were chosen to mitigate the effects of radiation damage.

In contrast to the silicon detectors, the TRT operates at room temperature. The electronics is cooled by a monophase-liquid cooling loop separate from the Pixel and SCT bi-phase system.

The calorimeters

The calorimeter system includes both electromagnetic (EM) and hadronic (Had) calorimeters. The first is dedicated to the measurement of electrons and photons, the latter to the measurement of hadrons. These calorimeters cover the range $|\eta| < 4.9$, using different techniques suited to the widely varying requirements of the physics processes of interest and of the radiation environment over this large η-range. A schematic view of the calorimeter system is shown in Figure 1.14.

The main purpose of the calorimeters is to measure the energy of the particles and their position. One of the most important requirements for calorimeters is to provide good containment for electromagnetic and hadronic showers, as well as limit punch-through into the muon system. Therefore, calorimeter depth is an important consideration. The total thickness of the EM calorimeter is more than 22 radiation lengths (X_0) in the barrel and more than 24 X_0 in the end-caps. The approximate 9.7 interaction lengths (λ) of active calorimeter in the barrel (10 λ in the end-caps) are adequate to provide good resolution for high-energy jets. The total thickness, including 1.3 λ from the outer support, is 11 λ at η = 0 and has been shown both by measurements and simulations to be sufficient to reduce punch-through well below the irreducible level of prompt or decay muons.

Both a good resolution in the determination of particle energy and a hermetic coverage are essential for the determination of missing energy (Chapter 3), which is the non detected energy due to particles, such as neutrinos, that escape detection.

The electromagnetic calorimeters The EM calorimeter is a lead liquid Argon (LAr) detector. To ensure the maximum azimuthal coverage the EM calorimeter was designed

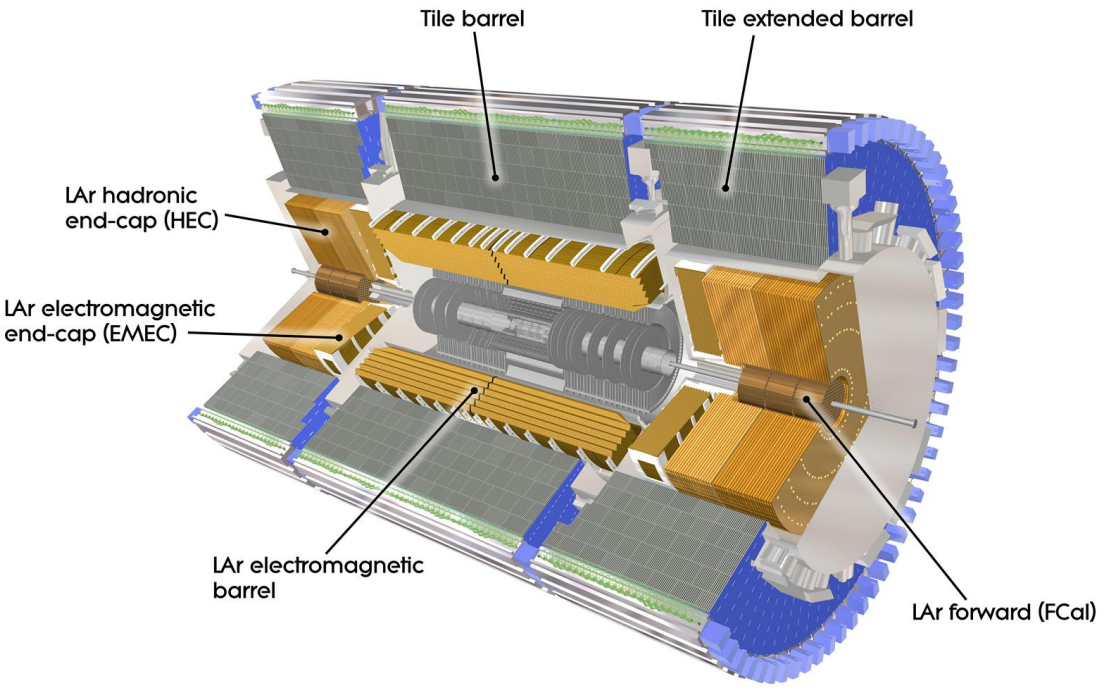

Figure 1.14: A schematic view of the calorimeter system of the ATLAS Experiment.

with an accordion geometry: the readout electrodes and the lead absorbers are laid out radially and folded so that particles can not cross the calorimeter without being detected [52]. It is divided into one barrel part ($|\eta| < 1.475$) and two end-caps ($1.375 < |\eta| < 3.2$), each one with its own cryostat. The position of the central solenoid in front of the EM calorimeter demands optimisation of the material in order to achieve the desired calorimeter performance. As a consequence, the central solenoid and the LAr calorimeter share a common vacuum vessel, thereby eliminating two vacuum walls. The barrel calorimeter consists of two identical half-barrels, separated by a small gap (4 mm) at z = 0. Each end-cap calorimeter is mechanically divided into two coaxial wheels: an outer wheel covering the region $1.375 < |\eta| < 2.5$, and an inner wheel covering the region $2.5 < |\eta| < 3.2$.

Over the region devoted to precision physics ($|\eta| < 2.5$), the EM calorimeter is segmented into three longitudinal sections: strips, middle and back. While most of the energy of electrons and photons is collected in the middle, the fine granularity of the strips is necessary to improve the $\gamma - \pi^0$ discrimination and the back measures the tails of highly energetic electromagnetic showers, and helps to distinguish electromagnetic and hadronic deposits. For the end-cap inner wheel, the calorimeter is segmented in two longitudinal sections and has a coarser lateral granularity than for the rest of the acceptance. The region $|\eta| < 1.8$ is equipped with a pre-sampler detector, which is used to correct for the energy lost by electrons and photons before entering the calorimeter. The pre-sampler consists of an active LAr layer of thickness 1.1 cm (0.5 cm) in the barrel (end-cap) region.

The transition region between the barrel and end-cap EM calorimeters, $1.37 < |\eta| < 1.52$, is expected to have poorer performance because of the higher amount of passive material in front of the calorimeter.

The hadronic calorimeters The hadronic calorimeter is realized with a variety of techniques depending on the region: central, end-cap and forward.

In the central region there is the Tile Calorimeter (Tile) [53], which is placed directly outside the EM calorimeter envelope. The Tile is a sampling calorimeter which uses steel as absorber and scintillating tiles as active material. It is divided into a barrel ($|\eta| < 1.0$) and two extended barrels ($0.8 < |\eta| < 1.7$). Radially, the Tile calorimeter goes from an inner radius of 2.28 m to an outer radius of 4.25 m. It is longitudinally segmented in three layers approximately 1.5, 4.1 and 1.8 interaction lengths thick for the barrel and 1.5, 2.6, and 3.3 interaction length for the extended barrel. The total detector thickness at the outer edge of the tile-instrumented region is 9.7 λ at $\eta = 0$.

The Hadronic End-cap Calorimeter (HEC) consists of two independent wheels per end-cap, located directly behind the end-cap EM calorimeter and sharing the same LAr cryostats. It covers the region $1.5 < |\eta| < 3.1$, overlapping both with the Tiles and the Forward Calorimeter. The HEC uses the LAr technology. Each wheel is divided into two longitudinal segments, for a total of four layers per end-cap. The wheels closest to the interaction point are built from 25 mm parallel copper plates, while those further away use 50 mm copper plates. The outer radius of the copper plates is 2.03 m, while the inner radius is 0.475 m (except in the overlap region with the forward calorimeter where this radius becomes 0.372 m). The copper plates are interleaved with 8.5 mm LAr gaps, providing the active medium for this sampling calorimeter.

The Forward Calorimeter (FCal) covers the $3.1 < |\eta| < 4.9$ region and is another LAr based detector. It is integrated into the end-cap cryostats, as this provides clear benefits in terms of uniformity of the calorimetric coverage as well as reduced radiation background levels in the muon spectrometer. The FCal is approximately 10 interaction lengths deep, and consists of three modules in each end-cap: the absorber of the first module is copper, which is optimised for electromagnetic measurements, while for other two is tungsten, which is used to measure predominantly the energy of hadronic interactions. The region where the FCal is set is very close to the beam pipe, so the expected radiation dose is very high. Therefore the electrode structure is different from the accordion geometry, consisting in a structure of concentric rods and tubes parallel to the beam axis. The LAr in the gap between the rod and the tube is the sensitive medium.

The muon system

The layout of the muon system [54] is shown in Figure 1.15. This system is used to measure muons, that are the only visible particles that can traverse the calorimeter system. It is based on the magnetic deflection of muon tracks. Such a large volume magnetic field, which is necessary to bend the particle trajectories, is provided by the large barrel toroid in the region $|\eta| < 1.4$, by two smaller end-cap magnets in the $1.6 < |\eta| < 2.7$ region and by a combination of the two in the transition region ($1.4 < |\eta| < 1.6$). This magnet configuration provides a field which is mostly orthogonal to the muon trajectories, while minimising the degradation of resolution due to multiple scattering.

The muon system has two different functions: it is needed for high precision tracking of muons and also for triggering on them.

Concerning the tracking measurement, this is performed over most of the η-range by the Monitored Drift Tubes (MDT). At large pseudorapidities and close to the interaction point, Cathode Strip Chambers (CSC) with higher granularity are used: they have been designed to withstand the demanding rate and background conditions. The stringent requirements on the relative alignment of the muon chamber layers are met by the combination of

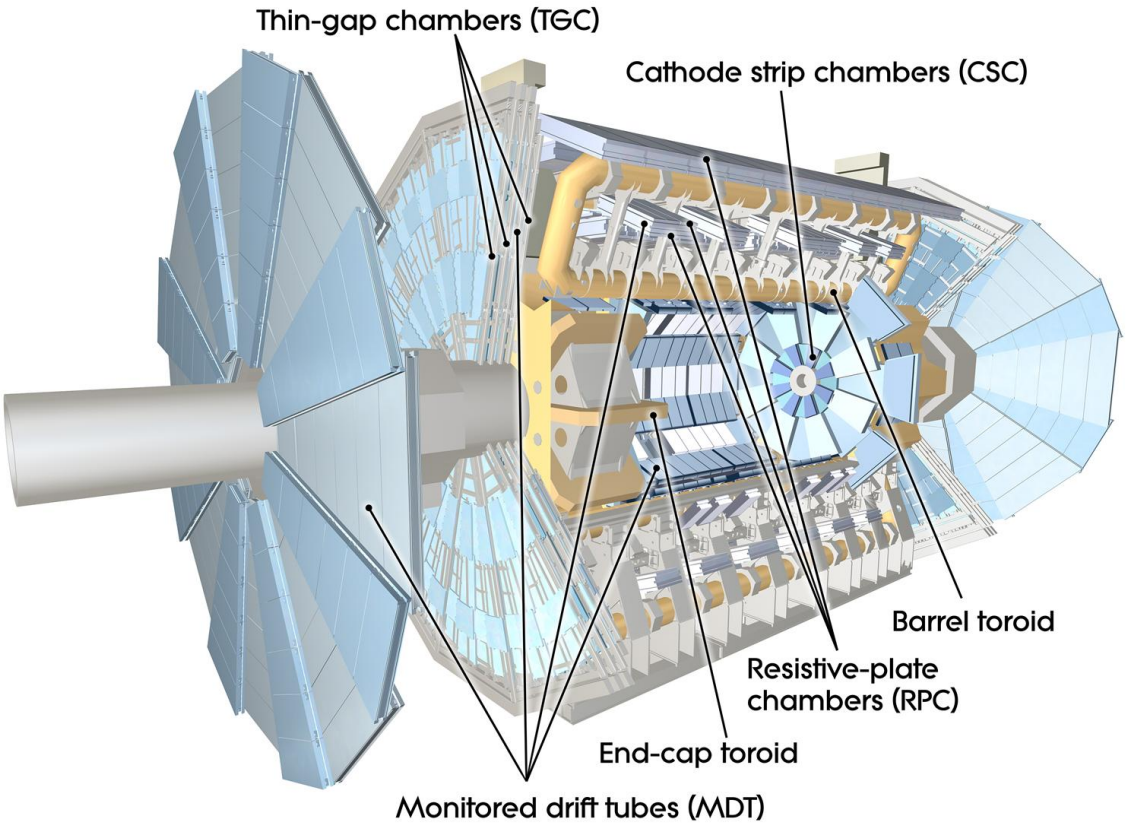

Figure 1.15: A schematic view of the muon spectrometer system of the ATLAS Experiment.

precision mechanical-assembly techniques and optical alignment systems both within and between muon chambers.

Concerning the triggering function of the muon system, it covers the pseudorapidity range $|\eta| < 2.4$. Resistive Plate Chambers (RPC) are used in the barrel and Thin Gap Chambers (TGC) in the end-cap regions. The trigger chambers for the muon spectrometer serve a three-fold purpose: to provide bunch-crossing identification, to provide well-defined transverse momentum thresholds and to measure the muon coordinate in the direction orthogonal to that determined by the precision-tracking chambers.

The barrel chambers are positioned on three cylinders concentric with the beam axis, at radii of about 5, 7.5, and 10 m. They cover the pseudorapidity range $|\eta| < 1$. The end-cap chambers cover the range $1 < |\eta| < 2.7$ and are arranged in four disks at distances of 7, 10, 14, and 21-23 m from the interaction point, concentric with the beam axis. In the barrel there are three triggering stations, provided by the RPC. They are located on both sides of the middle MDT station, and directly inside the outer MDT station. In the end-caps, the trigger is provided by three stations of TGCs located near the middle MDT station.

Forward detectors

One measurement which is very important for almost every physics analysis is the luminosity measurement [55]. As it is a fundamental quantity, three different detectors help in its determination. At ± 17 m from the interaction region there is the LUCID (LUminosity measurement using Čerenkov Integrating Detector) [56]. It detects inelastic pp scattering

in the forward direction and it is the main online relative-luminosity monitor for ATLAS. It is also used, before collisions are delivered by the LHC, to check the beam losses. For the beam monitoring, also another detector has been inserted: the BCM (Beam condition Monitor).

The other detector used for luminosity measurement is ALFA (Absolute Luminosity For ATLAS) [57]. It is located at ±240 m from the interaction point. It consists of scintillating fibre trackers located inside Roman pots which are designed to approach as close as 1 mm from the beam.

The last detector is ZDC (Zero-Degree Calorimeter) [57], which plays a key role in determining the centrality of heavy-ion collisions. It is located at ±140 m from the interaction point, just beyond the point where the common straight-section vacuum-pipe divides back into two independent beam-pipes. The ZDC modules consist of layers of alternating quartz rods and tungsten plates which measure neutral particles at pseudorapidities $|\eta| \geq 8.2$.

1.5.3 Physics analysis model

After the data taking campaigns at 900 GeV and the at 2.36 TeV, on 30 March 2010 ATLAS started the data taking with 7 TeV pp collisions. At the end of the pp running period, ATLAS accumulated 45 pb^{-1} of integrated luminosity, of the 48.9 pb^{-1} delivered by the LHC (Figure 1.10). After that the heavy ion collisions started and at the day of writing, 3.5 μb^{-1} were accumulated.

ATLAS data are available to collaboration members in a variety of formats to fulfil the requirements of several kind of analyses: development of reconstruction algorithms, detector calibration, debugging and, finally, physics analysis. Data for physics analysis need to be filtered according to detector conditions (Good Run List based on data quality assessment) and are accessed using the LHC Computing Grid [58]. In the following of this section, these aspects are detailed.

Data format

ATLAS data is centrally divided in different streams, which correspond to the trigger that have been fired by the event. For example, in the analysis presented in this thesis the so-called "L1Calo" stream has been considered, for which one trigger based on (hadronic or electromagnetic) calorimeter information has been fired.

There are different data formats produced when data is collected.

The first two data format that are not used for analysis: the Byte-stream Data, which is a persistent presentation of the event data flowing from the High Level Trigger (which is the last level of the trigger decision, Chapter 4) and the Raw Data Object Data (RDO) which is a C++ object representation of the byte-stream information. The latter can be sometimes used for detailed detector studies, when information about each single channel is needed.

Once the raw data has been collected and the program of offline calibrations has been performed, the reconstruction can start. The Event Summary Data (ESD) are the output of the reconstruction: these samples contain all the information about the detectors (e.g. energy released in each calorimeter cell) and about the reconstructed physics object (e.g. jets). ESDs contain enough information to do, for example, track refitting: this is therefore the format usually used for the rapid tuning of reconstruction algorithms and calibrations.

The following step is the production of Analysis Object Data (AOD) samples, which contain only a summary of the reconstruction (e.g. the information about calorimeter cells

is not copied into AODs).

From these data format, some derived samples (dESD, dAOD) can be extracted, in which just a subset of the events is retained, but the informations at event level remain the same.

Another available data format are flat ntuples[1] (Derived Physics Data, DPD), which are derived from ESDs or AODs. These were mainly thought to be used by performance working groups, but they are intensively used also in physics analyses. Each performance group produces its own DPD, with a subset of event information. These ntuples are therefore small and easy to handle. In the analysis presented in this thesis, the DPD produced by the ATLAS Tau Working Group have been used.

Moreover, to further decrease data dimensions, retaining only the events and informations that are interesting for the analysis, a preselection is applied to the events, before the DPD production. The reduction is done following three criteria:

Skimming : this implies the selection of the desired events from a larger dataset, e.g. selecting only events with a certain amount of missing energy;

Thinning : this implies the selection of only the required objects or containers of objects from the desired events, e.g. discarding photon containers if not needed;

Slimming : this implies the selection of just the desired properties of an object, e.g. not using all the informations about calorimeter cells associated to a jet.

The last data format that can be useful for analysis are TAG files. Every reconstructed or analysis file in the system has a corresponding TAG file, which summarizes some interesting information for the events, e.g. the number of reconstructed electrons or the p_{T} of the most energetic jet and so on. TAG files are non meant for analysis, but they are used for a quick selection of the events.

Data quality

After data has been taken, runs are assigned several data quality flags which define if the data are good enough to be used for physics analysis. Data quality flags are assigned for each sub-detector (separately for each component, i.e. barrel or end-cap) and for each reconstructed object (e.g. taus, electrons and photons, muons etc.) in each detector region (e.g. taus is the barrel region etc.). Moreover, the flags are assigned on a luminosity block[2] (LB) base, to maximize the amount of data useful for the analyses.

The flags are assigned by data quality shifters, looking at the status of the detector during a particular run and checking a set of histograms with interesting distributions, e.g. the distribution of timing for the pixel hits. A tool is implemented which automatically checks if the distribution under investigation is good or not, just comparing the distribution to a reference. But the data quality flag still needs to be assessed by a human being.

For each physics analysis, according to the reconstructed object involved in it, a list of good quality luminosity blocks is defined: this is the so-called Good Run List (GRL). This is obtained combining all the data quality flags and good LB from the interesting subsystems/objects.

[1] TTree objects based on the ROOT package [59].

[2] The real time length of a luminosity block depends on the machine luminosity. For $\mathcal{L} = 10^{31}$ cm^{-2}s^{-1} it is 60 seconds.

Data distribution

The ATLAS Computing Model [60] foresees that just limited operations are done in situ by the computing facility at CERN (Tier0). The rest of the operation is done at the other computing sites (Tier1 and Tier2), which are spread around the world.

The Tier0 is at CERN and performs monitoring, calibration and first-pass processing; it also hosts the first secure copy of the raw data and of the first pass output data formats.

The 10 Tier1 sites receive the raw data and the first pass processing, and host the second secure copy of the raw data. They provide scheduled access for physics and detector groups to the processed data, and perform the reprocessing when calibrations and algorithms improve. They also host copies of the conditions database.

The Tier2 sites are associated with a Tier1, and provide on-demand access to processed data for physics analysts. Derived datasets produced by the physics groups are copied to the Tier2 facilities for further analysis. The Tier2 facilities also provide the simulation capacity for the experiment, with the simulated data housed at Tier1s.

Chapter 2

Tau reconstruction and identification

In this chapter, the reconstruction and identification of hadronically decaying taus will be described. In Section 2.1 a brief introduction recalls the main feature of τ_{h} decays. In Section 2.2 it is described how τ_{h} are reconstructed at the ATLAS Experiment. As the reconstruction alone does not provide enough rejection factor against QCD jets, Section 2.3 shows how the identification is performed and which are the performance obtained on 7 TeV collision data. Finally in Section 2.4 it is explained how τ_{h} are discriminated from electrons.

2.1 Introduction

Tau leptons can decay both in channels with pure leptonic final states and states with hadrons and a tau neutrino. Leptons from the tau decay cannot be easily separated from prompt leptons and therefore the signature of the presence of tau decay are a hadronic system accompanied by missing energy. In the following, when referring to τ decays, the hadronic decay will be always meant and the symbol τ_{h} will be used to indicate hadronically decaying τ leptons.

Taus decay into final states with one or three charged particles and a variable number of neutral particles. Decays in five charged particles are also possible, but the probability is much lower. Moreover, in a environment such as the one at the LHC, with an overwhelming QCD background, such decays are difficult to be distinguished from the background. Decays with one (three) charged particle(s) are usually referred to as 1(3)-prong(s) decays.

The signature of a τ_{h} candidate is therefore a narrow jet with few tracks and calorimeter showers associated to them or to accompanying π^0 and K^0.

The Inner Detector provides information on the charged hadronic single or multi track system reconstructed in isolation from the rest of the event. Those tracks neither should match track segments in the muon spectrometer nor reveal features characteristic of an electron track. In the case of a three-track system, they should be well collimated in (η, ϕ) space. If more than one track is associated to the τ_{h}, the tau decay vertex can be reconstructed and the decay length can be measured. The charge of the decaying τ lepton can be directly determined from the charge(s) of its decay product(s).

Calorimetry provides information on the energy deposition from the visible decay products. As it will be discussed in Section 2.2, taus are well collimated leading to a relatively narrow shower in the electromagnetic calorimeter with, for 1-prong decays with one or few π^0, a significant pure electromagnetic component. Namely about 55% of the energy is carried by π^0 in the case of single prong decays on average.

Hadronically decaying τ leptons are distinguished from QCD jets on the basis of the low track multiplicity in the narrow cone, of the characteristics of the track system and of the shapes of the calorimetric showers. From this information, a set of identification variables is built, to which either a traditional cut selection or a multi-variate discrimination techniques are applied.

2.2 Tau Reconstruction

Hadronically decaying τ leptons are reconstructed using two different types of seeds. The seed can be either a track or a calorimeter seed.

Track-seeded τ_{h} The algorithm which reconstructs track-seeded candidate is called `tau1p3p`. This algorithm provides candidates with up to 10 tracks reconstructed in a core region, but for most of the analyses only 1, 3 track candidates should be used. The reason of allowing up to 10 tracks for the τ_{h} candidate is to help in controlling the normalisation of the QCD background.

The `tau1p3p` algorithm first identifies and qualifies a leading track, which becomes the seed to build the candidate. Then it creates the candidate with up to 10 tracks in a core region, defining also (η, ϕ) position and the energy of the candidate.

The leading track mast have $p_{\mathrm{T}} > 6$ GeV and has to satisfy particular quality criteria on:

- the number of associated hits in the silicon detectors (Pixel and SCT): $N_{Si} > 7$ hits,
- the impact parameter respect to the interaction vertex: $|d_0| < 2$ mm and $|z_0| \times \sin\theta < 10$ mm.

The nearby tracks are searched for in a cone of $\Delta\mathrm{R}$[1] $= 0.2$ around the seed. The (η, ϕ) of a candidate is defined by the direction at the perigee of the leading track (for the single-prong mode) or barycentre of the multi tracks system weighted with $p_{\mathrm{T\,track}}$.

Calorimeter-seeded τ_{h} The algorithm which reconstructs calorimeter seeded τ_{h} is called `tauRec`. The seed is a calorimeter jets reconstructed with the Anti-Kt algorithm [61] (using a distance parameter D = 0.4) from topological clusters (topoclusters) [62] with calibrated $E_{\mathrm{T}} > 10$ GeV from the global cell energy-density weighting calibration scheme [63] (explained in Section 3.1). The p_{T} of the τ_{h} candidate is further adjusted by applying correction factors extracted from Monte Carlo studies, as a function of E_{T} and η and the number of associated tracks.

Double-seeded τ_{h} If the seeding track and jet are within a distance $\Delta R < 0.2$, the τ_{h} candidate is considered to be double-seeded. In this case both-seeded candidates are built: the information about energy and calorimetric quantities are reconstructed by the `tauRec` algorithm, while information concerning position and tracks come from the `tau1p3p` algorithm.

The reconstruction of τ_{h} candidates provides very little rejection against QCD jet background. Rejection comes from a separate identification step and is usually based on several discriminating variables. Identification methods for τ_{h} candidates include selections based on simple cuts, boosted decision trees, and projective likelihood methods [64, 65].

[1] ΔR is defined as $\sqrt{\Delta\phi^2 + \Delta\eta^2}$.

2.3 Tau Identification

Since a hadronic τ_{h} decay is characterized by collimated energy deposits in the calorimeters and one or few collimated tracks, these properties are used to distinguish them from QCD jets. The variables that are used in the identification of τ_{h} leptons include:

Cluster mass : the invariant mass computed from associated topoclusters (m_{clusters}).

Track mass : the invariant mass of the track system (m_{tracks}).

Track radius : the p_{T} weighted track width:

$$\mathrm{R}_{\mathrm{track}} = \frac{\sum_i^{\Delta\mathrm{R}_i<0.2} p_{\mathrm{T},i}\Delta\mathrm{R}_i}{\sum_i^{\Delta\mathrm{R}_i<0.2} p_{\mathrm{T},i}} \tag{2.1}$$

where i runs over all tracks associated to the τ_{h} candidate, $\Delta\mathrm{R}_i$ is defined relative to the τ_{h} jet seed axis and $p_{T,i}$ is the track transverse momentum.

Leading track momentum fraction : defined as:

$$f_{\mathrm{trk},1} = \frac{p_{\mathrm{T},1}^{\mathrm{track}}}{p_{\mathrm{T}}^{\tau}} \tag{2.2}$$

where $p_{\mathrm{T},1}^{\mathrm{track}}$ is the transverse momentum of the leading track of the τ_{h} candidate and p_{T}^{τ} is the transverse momentum of the τ_{h} candidate.

Electromagnetic radius : the transverse energy weighted shower width in the electromagnetic (EM) calorimeter:

$$\mathrm{R}_{\mathrm{EM}} = \frac{\sum_i^{\Delta\mathrm{R}_i<0.4} E_{\mathrm{T},i}^{\mathrm{EM}}\Delta\mathrm{R}_i}{\sum_i^{\Delta\mathrm{R}_i<0.4} E_{\mathrm{T},i}^{\mathrm{EM}}} \tag{2.3}$$

where i runs over cells in the first three layers of the EM calorimeter associated to the τ_{h} candidate, $\Delta\mathrm{R}_i$ is defined relative to the τ_{h} jet seed axis and $E_{\mathrm{T},i}^{\mathrm{EM}}$ is the cell transverse energy.

Hadronic radius : the transverse energy weighted shower width in the hadronic (Had) calorimeter:

$$\mathrm{R}_{\mathrm{Had}} = \frac{\sum_i^{\Delta\mathrm{R}_i<0.4} E_{\mathrm{T},i}^{\mathrm{Had}}\Delta\mathrm{R}_i}{\sum_i^{\Delta\mathrm{R}_i<0.4} E_{\mathrm{T},i}^{\mathrm{Had}}} \tag{2.4}$$

where i runs over cells in the last electromagnetic calorimeter layer and in the hadronic calorimeter associated to the τ_{h} candidate, $\Delta\mathrm{R}_i$ is defined relative to the τ_{h} jet seed axis and $E_{\mathrm{T},i}^{\mathrm{Had}}$ is the cell transverse energy. This choice is made since many electrons or photons in the relevant energy range do not reach the last sampling layer in the electromagnetic calorimeter, while hadrons often deposit energy in this layer.

Core energy fraction : (also called *cetrality fraction*) the fraction of transverse energy in the core ($\Delta\mathrm{R} < 0.1$) of the τ_{h} candidate:

$$f_{\mathrm{core}} = \frac{\sum_i^{\Delta\mathrm{R}<0.1} E_{\mathrm{T},i}}{\sum_i^{\Delta\mathrm{R}<0.4} E_{\mathrm{T},i}} \tag{2.5}$$

where i runs over all cells associated to the τ_{h} candidate within $\Delta\mathrm{R}_i$ of the τ_{h} jet seed axis.

Isolation energy fraction : the fraction of transverse energy in a ring ($0.1 < \Delta R < 0.2$) of the τ_h candidate:

$$f_{\text{ring}} = \frac{\sum_i^{0.1<\Delta R<0.2} E_{T,i}}{\sum_i^{\Delta R<0.4} E_{T,i}} \tag{2.6}$$

where i runs over all cells associated to the τ_h candidate within ΔR_i of the τ_h jet seed axis.

Electromagnetic fraction : the fraction of GCW calibrated transverse energy of the τ_h candidate deposited in the EM calorimeter:

$$f_{\text{EM}} = \frac{\sum_i^{\Delta R_i<0.4} E_{T,i}^{\text{GCW}}}{\sum_j^{\Delta R_i<0.4} E_{T,j}^{\text{GCW}}} \tag{2.7}$$

where $E_{T,i}$ ($E_{T,j}$) is the GCW calibrated transverse energy deposited in cell i (j), and i runs over the cells in the three layers of the EM calorimeter, while j runs over the cells in all layers of the calorimeter.

The distributions for some of these identification variables are shown in Figure 2.1 for τ_h candidates in 7 TeV collision data and simulated QCD jets[2]. The background enriched data sample was selected (on an integrated luminosity of 244 nb^{-1}) using a tau trigger (L1_TAU5, described in Section 4.2) and by requiring two reconstructed τ_h jets, with opposite directions. This requirements aimed at selecting events with back-to-back jets, enriching the sample with fake τ_h candidates from QCD jet processes that form the primary background to signatures such as $Z \to \tau\tau$. The distributions for τ_h candidates matched to true τ_h leptons in a $Z \to \tau\tau$ Monte Carlo sample are also overlaid.

When comparing distribution such as the R_{EM}, it was found that the agreement between data and Monte Carlo expectations was not good [67]. Deep investigations of the discrepancies brought to attribute the source of the discrepancy was a bad description of the soft jet activity. Therefore data were compared to Monte Carlo samples with other underlying event descriptions, different from the default one, which is ATLAS MC09 [68]. From these studies [69], it has been shown that the DW tune [70] of Pythia, which uses virtuality-ordered showers and was derived to describe the CDF II underlying event and Drell-Yan data, models the forward activity of the underlying event better than the MC09 tune.

The distributions shown in Figure 2.1 are therefore plotted for Monte Carlo QCD jets with the DW tuning. In particular, with respect to previous results reported in [67], the distributions for R_{EM} and f_{core} are more consistent with the data for the DW Monte Carlo tuning. The agreement of the distributions for data and Monte Carlo samples is quite good for all identification variables.

Among these variables, only few of them were chosen to provide the identification of τ_h in first data [66]. The attempt was to keep the number of identification variables as low as possible to be able to provide very soon a reliable identification, keeping a good rejection factor respect to QCD jets. The chosen variables are: the track radius, the leading track momentum fraction and the electromagnetic radius. The reason of this choice is mainly related to the better agreement between data and Monte Carlo for them.

[2]The QCD jets background has been generated such that the allowed range of the transverse momentum of the outgoing partons in the rest frame of the hard interaction is restricted to be between 8 and 1120 GeV. The p_T ranges are: $p_T(J0) : 8 - 17$ GeV, $p_T(J1) : 17 - 35$ GeV and $p_T(JX) : 35(2^{X-2}) - 35(2^{X-1})$ GeV, up to J6.

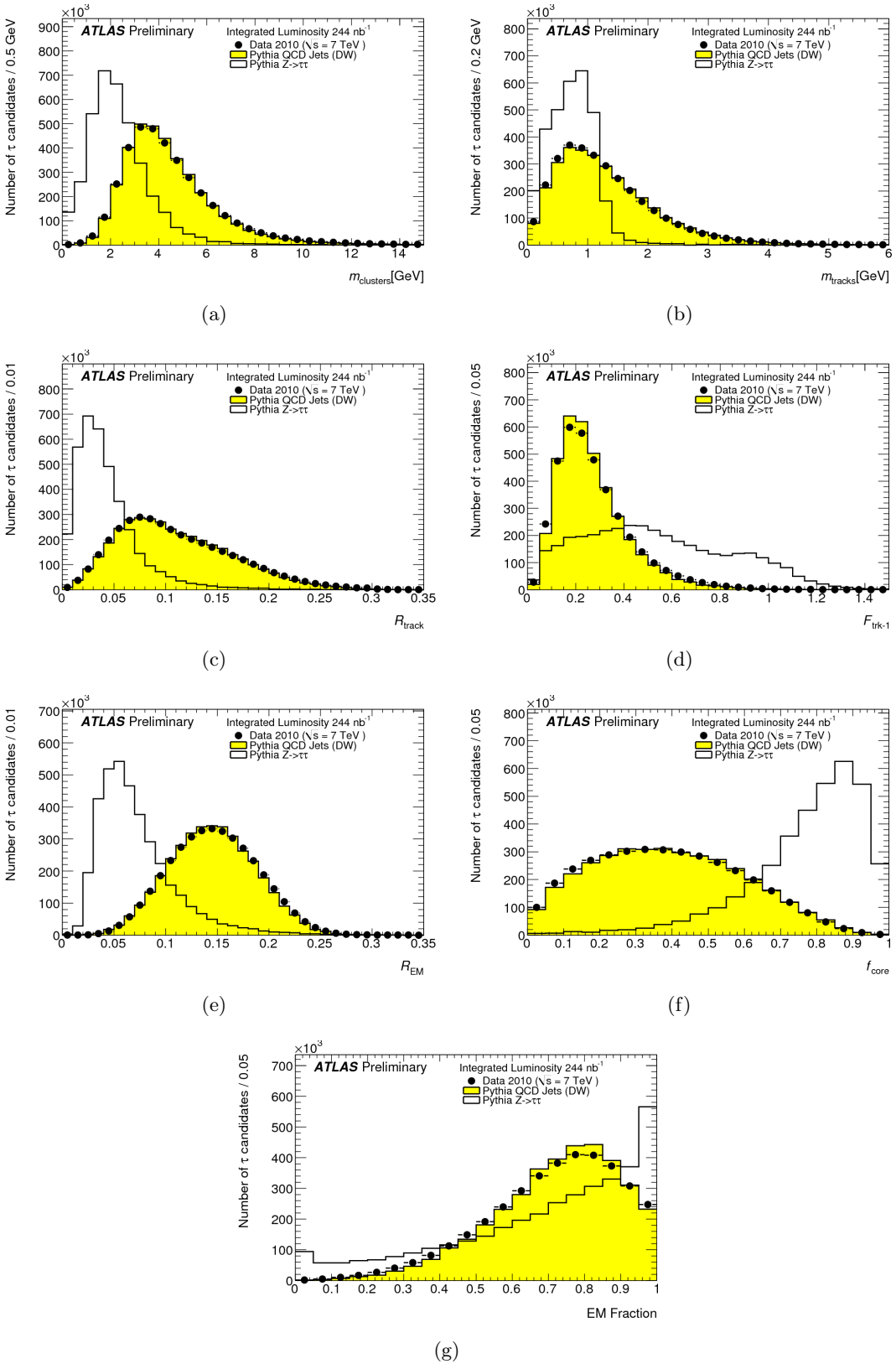

Figure 2.1: (a) Cluster mass, (b) track mass, (c) track radius, (d) leading track momentum fraction, (e) electromagnetic radius, (f) core energy fraction and (g) EM fraction of τ_{h} candidates. The number of τ_{h} candidates in Monte Carlo samples are normalized to the number of τ_{h} candidates selected in data. The statistical errors on the Monte Carlo are negligible.[66]

The identification is cut based: depending on the number of tracks associated to the τ_{h} candidate, three threshold cuts are defined for each variable. The values of the cuts are reported in Table 2.1. These thresholds are set to get a signal efficiency, tuned on $Z \to \tau\tau$ events, of 30% (*tight* identification level), 50% (*medium*) or 60% (*loose*). This choice is adequate for $W \to \tau_{\mathrm{h}}\nu_\tau$ decays since the p_{T} range of τ_{h} is similar.

$R_{EM} <$	$R_{track} <$	$f_{trk,1} >$	sig eff	bkg eff
1-prong				
0.08	0.09	0.06	0.599	0.137
0.07	0.08	0.12	0.497	0.0825
0.05	0.08	0.12	0.274	0.0262
multi-prong				
0.15	0.12	0.12	0.57	0.468
0.12	0.08	0.24	0.499	0.161
0.09	0.05	0.32	0.296	0.0282

Table 2.1: Values of the cuts used to identify τ_{h}. Three levels of identification are defined, with different efficiencies in the signal selection.

The signal efficiency is defined as:

$$\varepsilon_{\mathrm{sig}} = \frac{N^{\tau}_{\mathrm{pass,match}}}{N^{\tau}_{\mathrm{match}}} \tag{2.8}$$

where $N^{\tau}_{\mathrm{match}}$ is the number of reconstructed τ_{h} candidates that are matched within $\Delta R < 0.2$ of a true hadronically decaying τ lepton with visible transverse momentum $p_{\mathrm{T}}^{\mathrm{vis}} > 15$ GeV and visible pseudorapidity $|\eta^{\mathrm{vis}}| < 2.5$, reconstructed with the correct number of associated tracks; while $N^{\tau}_{\mathrm{pass,match}}$ is the number of these reconstructed candidates that pass the identification criteria.

The background efficiency is defined as:

$$\varepsilon_{\mathrm{bkg}} = \frac{N^{bkg}_{\mathrm{pass}}}{N^{bkg}_{\mathrm{total}}} \tag{2.9}$$

where N^{bkg}_{pass} is the number of the τ_{h} candidates that pass the identification criteria, and N^{bkg}_{total} is the number of τ_{h} candidates.

Figure 2.2 shows the background efficiencies obtained for data and Monte Carlo samples as a function of the reconstructed p^{τ}_{T} for loose, medium, and tight selections. Table 2.2 summarizes the average efficiency over the whole spectrum of background events measured in 7 TeV collision data, as well as the one obtained from Monte Carlo. The background efficiencies measured in data agree well with the Monte Carlo prediction, showing the good performance with data of the cut-based identification that was optimized with Monte Carlo samples.

For the future, multivariate identification algorithms will be used, based on boosted decision trees (BDT) and projective likelihood (LL). The BDT uses all the variables listed previously (make exception for R_{Had} and f_{ring}), while the LL uses the same variables as BDT except f_{core} (due to correlations with other variables), to provide discrimination of τ_{h} leptons against jets. The LL is trained using signal and background Monte Carlo samples split in five separate p_{T} bins, while the BDT does not split its training samples. The distributions for the BDT score and LL score are shown in Figure 2.3 for τ_{h} candidates

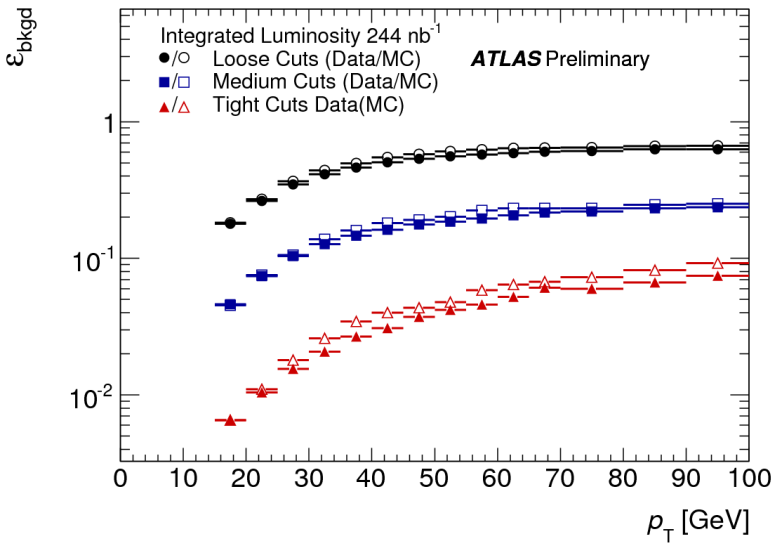

Figure 2.2: Background efficiencies obtained for data and Monte Carlo samples as a function of the reconstructed p_{T} of the τ_{h} candidate.[66]

Selection	$\varepsilon_{\mathrm{bkg}}$ (data)	$\varepsilon_{\mathrm{bkg}}$ (MC)
loose	$(3.2\pm0.2) \times 10^{-1}$	3.4×10^{-1}
medium	$(9.5\pm1.0) \times 10^{-2}$	9.9×10^{-2}
tight	$(1.6\pm0.3) \times 10^{-2}$	1.9×10^{-2}

Table 2.2: Background efficiencies for loose, medium, and tight selection cuts. The measured background efficiencies in data are compared to the Monte Carlo with DW tune prediction. Uncertainties for the background efficiencies in data are from transverse momentum calibration and pile-up effects.[66]

in data and in the Monte Carlo samples. The distributions for τ_{h} candidates matched to true τ_{h} leptons in a $Z \to \tau\tau$ Monte Carlo sample are also overlaid. The distributions agree reasonably well between data and the Monte Carlo samples, and demonstrate the strong separation power of these multivariate discriminants. The background efficiencies obtained for the BDT and LL are also compared to those obtained for the cut-based identification for medium and tight criteria in Figure 2.4. The signal efficiencies of the BDT and LL as a function of the p_{T} of the hadronic tau are also shown in comparison with the cut-based identification. The increased rejection power against fake τ_{h} candidates of the more sophisticated BDT and LL discriminants is evident, although not accurately described by the Monte Carlo prediction.

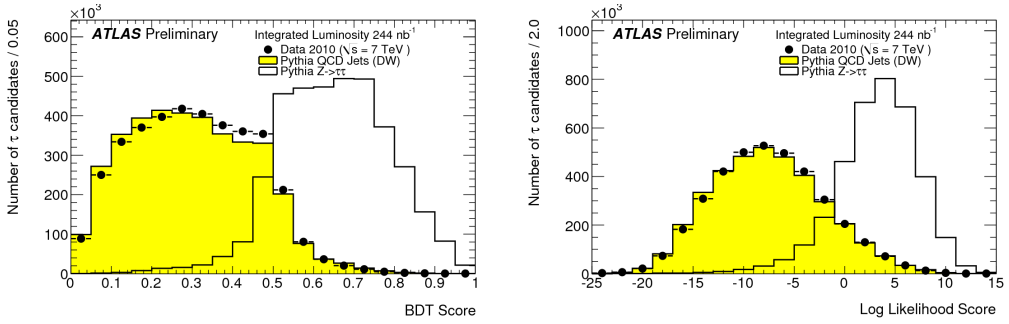

(a) (b)

Figure 2.3: The (a) BDT jet score and (b) LL score for τ_{h} candidates in data and Monte Carlo samples. The number of τ_{h} candidates in Monte Carlo samples is normalized to the number of τ_{h} candidates in the data.[66]

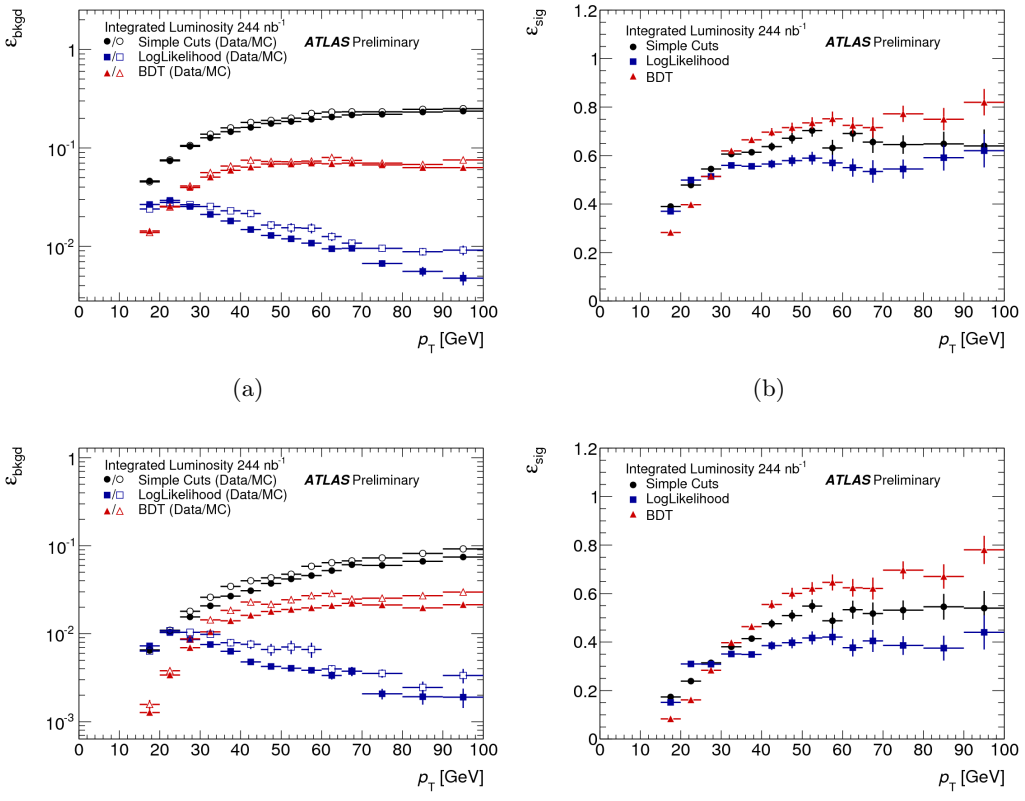

(a) (b)

(c) (d)

Figure 2.4: (a) Background efficiencies in data and Monte Carlo as a function of the p_{T} of the τ_{h} candidate with the medium selection for cut-based, BDT, and LL identification. (b) Signal efficiencies from Monte Carlo as a function of p_{T} of the τ_{h} candidate with the medium selection for cut-based, BDT, and LL identification. (c) Background efficiencies in data and Monte Carlo as a function of p_{T} of the τ_{h} candidate with the tight selection for cut-based, BDT, and LL identification. (d) Signal efficiencies from Monte Carlo as a function of p_{T} of the τ_{h} candidate with the tight selection for cut-based, BDT, and LL identification.[66]

2.3.1 Performance in $\tau_{\mathrm{h}} + E_{\mathrm{T}}^{\mathrm{miss}}$ events

In preparation for the observation of the $W \to \tau_{\mathrm{h}}\nu_{\tau}$ signal described in Chapter 5, characterised by the presence of a τ_{h} lepton and missing transverse energy in the final state, the performance of τ_{h} identification were checked on events with high $E_{\mathrm{T}}^{\mathrm{miss}}$, as it important to check that no distortion is introduced in the discriminating variables by the kinematic range selection.

Figure 2.5 shows the distributions of kinematic and identification variables for reconstructed τ_{h}. Data refers to 7 TeV collision data. Not to suffer from pile-up effects, only events with one well reconstructed vertex were taken into account. Plots are normalised to unity. The events pass the selection described in Section 5.4, up to the cut on the cleaning of bad jets. Basically, events are good collision events, passing a combined trigger of $\tau_{\mathrm{h}} + E_{\mathrm{T}}^{\mathrm{miss}}$ (Chapter 4) and a cut on $E_{\mathrm{T}}^{\mathrm{miss}} > 25$ GeV (Chapter 3). Data is overlaid with QCD jets simulated with DW tune (as explained before). As a cut on $E_{\mathrm{T}}^{\mathrm{miss}}$ would have reduced too much the amount of QCD simulated events, this cut was not applied for Monte Carlo. As data is preskimmed with a selection on $E_{\mathrm{T}}^{\mathrm{miss}}$, this cut was not avoidable on data. The difference for this cut is anyway to be considered negligible, as to pass the trigger the event must have enough reconstructed missing transverse energy.

The distributions shown in Figure 2.5 show a good agreement between data and simulation. In Figure 2.6 the comparison of the three identification variables is shown, at Monte Carlo level, between simulated sample with different underlying event tunings. It can be noticed that two identification variables (namely the electromagnetic radius and the track radius) are better described by the DW tuning of the Monte Carlo: in MC09 they are shifted to a lower value than in data, and this would therefore provide an overestimation of the selection efficiency. On the other hand for the leading track momentum fraction the MC09 tuning gives a better description: DW overestimates the low $f_{\mathrm{trk},1}$ peak at 0.2. Also in this case MC09 would give an efficiency estimation higher than DW, given the higher fraction at high $f_{\mathrm{trk},1}$.

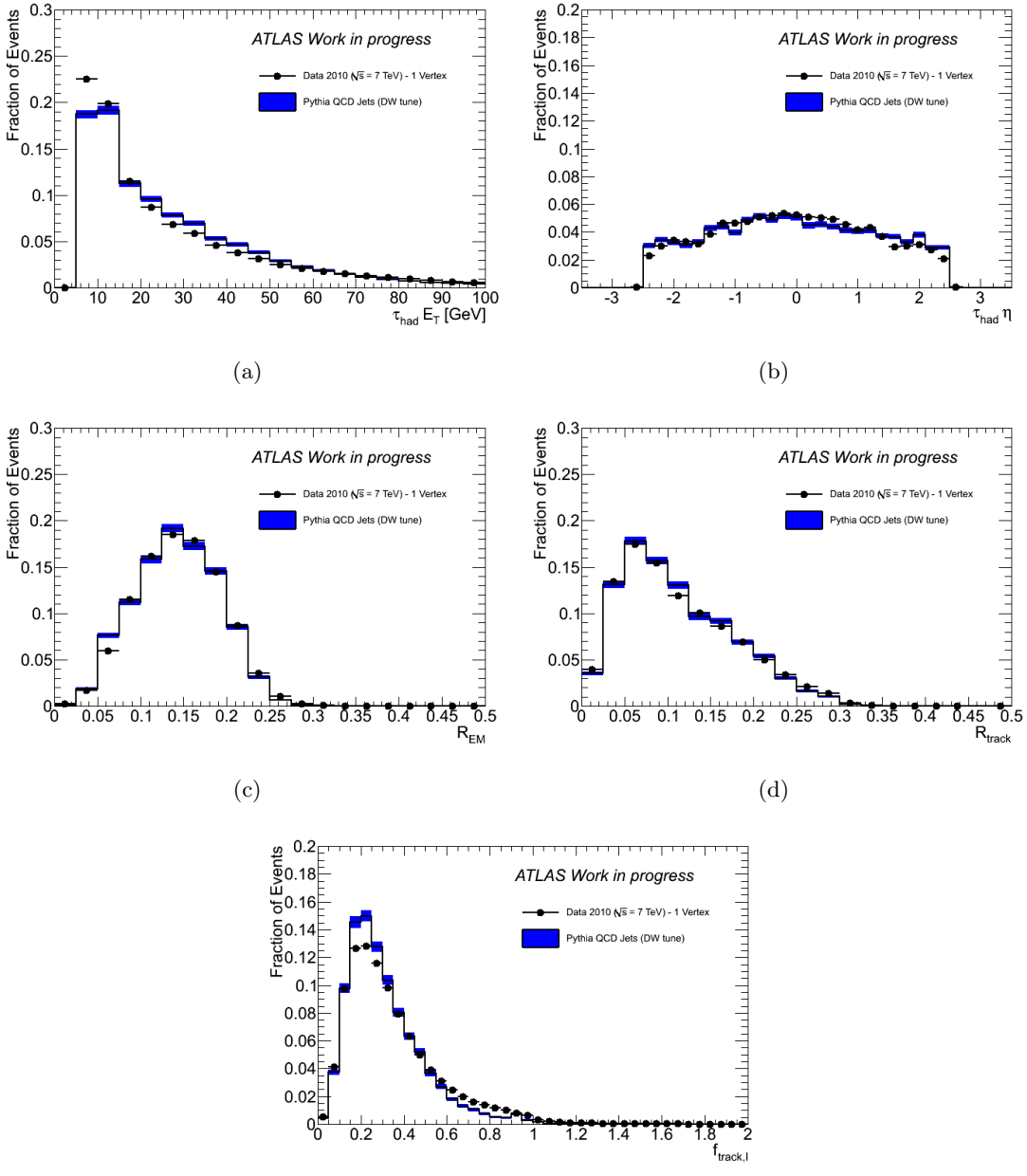

Figure 2.5: Distributions for reconstructed τ_{h} candidates which pass a combined trigger of τ_{h} + $E_{\mathrm{T}}^{\mathrm{miss}}$ trigger and the first two preselection criteria defined in Section 5.4.1 for data and simulated Monte Carlo QCD jets samples. Distributions show (a) p_{T} , (b) η, (c) electromagnetic radius, (d) track radius and (e) leading track momentum fraction of the τ_{h} candidate.

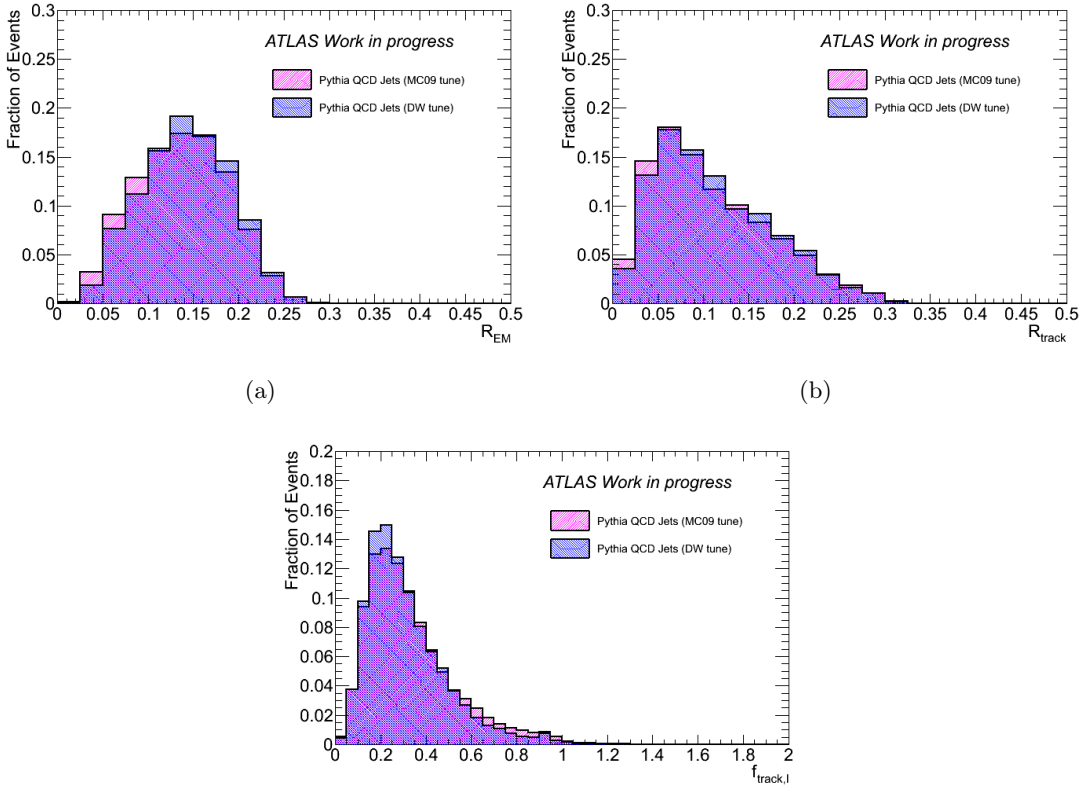

Figure 2.6: Distributions for reconstructed τ_{h} candidates which pass a combined trigger of τ_{h} + $E_{\mathrm{T}}^{\mathrm{miss}}$ trigger and the first two preselection criteria defined in Section 5.4.1 for simulated Monte Carlo QCD jets samples with different underlying event tunings (DW and MC09). Distributions show (a) electromagnetic radius, (b) track radius and (c) leading track momentum fraction of the τ_{h} candidate.

2.4 Electron veto

An efficient rejection of tracks originating from isolated electrons is important for rejecting backgrounds from $W \to e\nu_e$ and $Z \to ee$ events. Without the use of a dedicated veto algorithm, the majority of electrons would be identified as single-prong hadronic τ candidates, as both hadronically decaying τ leptons and electrons are characterised by narrow and isolated calorimeter showers and low track multiplicity. One possibility would be to reject tracks which have been identified as good electron candidates by the base-line ATLAS reconstruction algorithm (in ATLAS jargon that is referred to as the *isEM* flag). This procedure is found to reject 65.7% of electrons from $W \to e\nu_e$ events with a loss of efficiency for true hadronic tau decays with $p_T^{track} > 9$ GeV of less than 1%.

To achieve a more stringent selection, a dedicated algorithm for electron vetoing has been developed, aiming at a much higher rejection factor while, at the same time, retaining a small loss in efficiency.

The electron/hadron separation is based on four variables:

E^{Had}/p : the ratio between the uncalibrated energy deposited in the first layer of the hadronic calorimeter and the leading track momentum,

E^{EM}/p : the ratio between the uncalibrated energy deposited in the electromagnetic calorimeter and the momentum of the leading track,

E_{max}^{strip} : the largest (uncalibrated) energy deposit in the strip layer of the electromagnetic calorimeter not associated with the leading track,

N_{HT}/N_{LT} : the ratio of the number of high threshold to low threshold hits (including outliers) in the TRT for τ candidates with $|\eta| < 2.0$.

Studies performed on 14 TeV simulated samples showed that the algorithm gives a rejection factor 50 against electrons from $W \to e\nu_e$ at the expense of loosing 4% of signal from $W \to \tau_h\nu_\tau$. The algorithm efficiency[3] as a function of $|\eta|$ and p_T is shown in Figure 2.7. A detailed description of the algorithm can be found in [71].

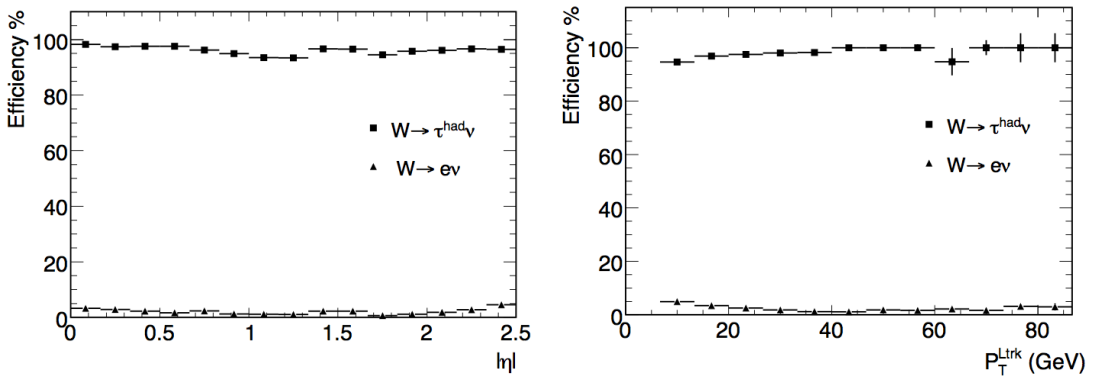

(a) (b)

Figure 2.7: τ_h-ID electron veto algorithm efficiency as a function of $|\eta|$ and p_T of the leading track. Simulations come from Monte Carlo at 14 TeV.[72]

[3]The efficiency for hadronic taus is defined with respect to reconstructed tau candidates and for electrons with respect to all electrons inside $|\eta| \leq 2.5$ with $p_T > 9$ GeV.

The performance of the electron veto algorithm has been studied with 900 GeV and 7 TeV collision data. In the following the results on 900 GeV data are presented. Events selected by a minimum bias trigger and with one reconstructed τ_{h} candidate were selected. Good agreement is observed within the statistical uncertainties. In Figure 2.8 the discriminating variables just listed are shown, for minimum bias events in 900 GeV collisions.

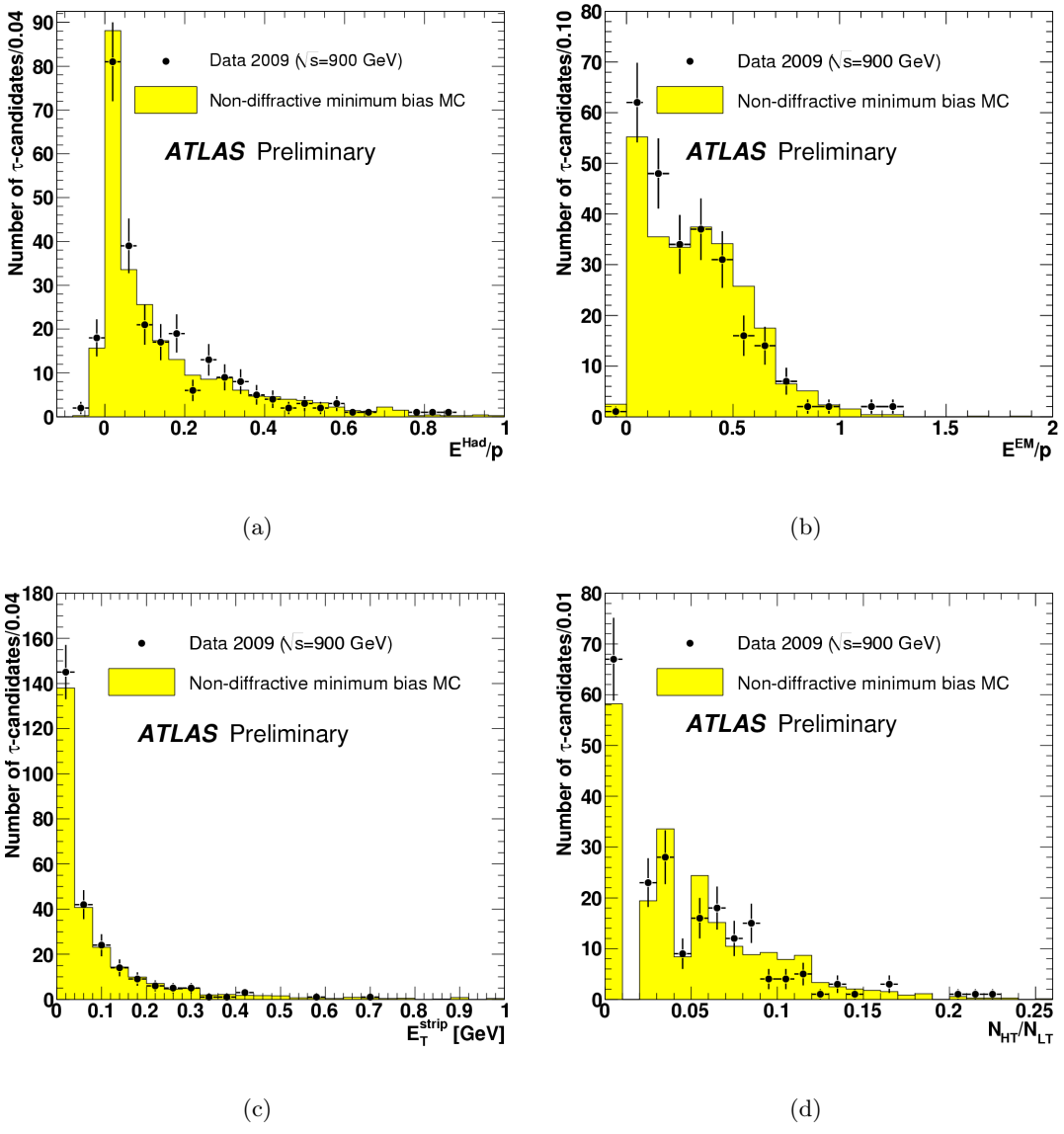

Figure 2.8: Variables used for electron rejection. (a) $\mathrm{E^{Had}/p}$, (b) $\mathrm{E^{EM}/p}$, (c) $\mathrm{E^{strip}_{max}}$ and (d) the ratio of high threshold to low threshold hits in the TRT. Data refers to minimum bias events in 900 GeV collisions.[73]

Chapter 3

Missing energy

Many physics measurements rely on the determination of the energy of particles which are not detected, such as neutrinos. This undetected energy is called *missing energy*. In hadron colliders such as the LHC, the initial momentum of the colliding partons along the beam axis is not known a priori, so the amount of total missing energy cannot be determined. However, the initial momentum transverse to the beam axis is zero, so the missing energy can be measured in its transverse direction. Missing transverse energy is usually indicated as $E_{\mathrm{T}}^{\mathrm{miss}}$.

The $W \to \tau_{\mathrm{h}}\nu_{\tau}$ decay observation presented in this thesis relies on $E_{\mathrm{T}}^{\mathrm{miss}}$ reconstruction: this quantity is indeed used to discriminate the signal from one of the most important background of the analysis, which is the background from QCD jets.

One crucial aspect of the measurement of missing energy is that *fake* missing energy may be caused by mismeasurements of the energy of detected particles or by detector effect, such as noise. For analysis relying on $E_{\mathrm{T}}^{\mathrm{miss}}$ measurement, it is essential to have good performances in $E_{\mathrm{T}}^{\mathrm{miss}}$ reconstruction.

In the following it will be described how $E_{\mathrm{T}}^{\mathrm{miss}}$ is reconstructed in ATLAS and it will be explained why it needs to be calibrated and how the calibration is performed. A procedure to reject events with fake $E_{\mathrm{T}}^{\mathrm{miss}}$ will be explained, as it will be used in the following for the analysis of $W \to \tau_{\mathrm{h}}\nu_{\tau}$ decays observation (Chapter 5). Furthermore, the performance of $E_{\mathrm{T}}^{\mathrm{miss}}$ reconstruction with 7 TeV collision data will be shown.

3.1 $E_{\mathrm{T}}^{\mathrm{miss}}$ reconstruction

The $E_{\mathrm{T}}^{\mathrm{miss}}$ reconstruction presently used in ATLAS for physics analysis includes contributions from transverse energy deposits in the calorimeters, corrections for energy loss in the cryostat, and measured muons. Its components along the coordinate axes in the $x - y$ plane therefore are:

$$E_{x(y)}^{\mathrm{miss}} = E_{x(y)}^{\mathrm{miss,calo}} + E_{x(y)}^{\mathrm{miss,cryo}} + E_{x(y)}^{\mathrm{miss},\mu} \tag{3.1}$$

The three terms will now be described in detail.

3.1.1 The $E_{\mathrm{T}}^{\mathrm{miss}}$ calorimeter term

The calorimeter term is defined as:

$$\begin{aligned} E_x^{\mathrm{miss,calo}} &= -\sum_{i=1}^{N_{\mathrm{cell}}} E_i \sin\theta_i \cos\phi_i \\ E_y^{\mathrm{miss,calo}} &= -\sum_{i=1}^{N_{\mathrm{cell}}} E_i \sin\theta_i \sin\phi_i \\ E_T^{\mathrm{miss,calo}} &= \sqrt{\left(E_x^{\mathrm{miss,calo}}\right)^2 + \left(E_y^{\mathrm{miss,calo}}\right)^2} \end{aligned} \tag{3.2}$$

where E_i, θ_i and ϕ_i are respectively the energy, the polar angle and the azimuthal angle of the calorimeter cells. The $E_{\mathrm{T}}^{\mathrm{miss}}$ is reconstructed over the range $|\eta| < 5$ using only calorimeter information.

Because of the high granularity of the calorimeter, it is crucial to suppress noise contributions, i.e. to limit the number of cells, N_{cell}, used in the $E_{\mathrm{T}}^{\mathrm{miss}}$ sum. This is done by using only cells belonging to three-dimensional topological clusters (topoclusters) [62]. These topoclusters are seeded by cells with deposited energy $|E_i| > 4\sigma_{noise}$[1], and are built by iteratively adding neighbouring cells with $|E_i| > 2\sigma_{noise}$ and, finally, by adding all neighbours of the accumulated cells.

$E_{\mathrm{T}}^{\mathrm{miss}}$ calibration The ATLAS calorimeters are "non-compensating", which means that the response to hadrons is lower than to electrons. In addition, energy is lost in the dead material in front of and between the calorimeters. Therefore, it is necessary to develop a dedicated calibration scheme for the hadronic energy deposits in calorimeters in which corrections for the different calorimeter response to hadrons and electrons/photons and for losses in inactive materials are applied [74]. This gives a better reconstruction of the mean of $E_{\mathrm{T}}^{\mathrm{miss}}$ and optimizes its resolution, as it will be shown in the following.

The first step in the commissioning of $E_{\mathrm{T}}^{\mathrm{miss}}$ reconstruction, is to calibrate all the topocluster cells with the same scheme, independently of the object they belong to. Two calibration schemes have been developed, both based on the cell energy density.

Global cell energy-density weighting calibration scheme. (Global calibration, GCW) This calibration scheme attempts to compensate for the different calorimeter response to hadronic and electromagnetic energy deposits by applying cell-level signal weights. These weights boost low density signals, which are more likely coming from hadronic activity. They are determined by minimizing the fluctuations between the reconstructed and particle jets in Monte Carlo simulation. The weights compensate also for energy losses in the dead material. These weights are applied to all calorimeter cells in the $E_{\mathrm{T}}^{\mathrm{miss}}$ calculation from Equation 3.3.

Local cluster weighting calibration scheme. (Local hadronic calibration, LCW) This calibration scheme uses properties of topoclusters to calibrate them individually. The scheme first classifies calorimeter topoclusters as electromagnetic or hadronic, according to the topocluster topology, and then weights all calorimeter cell signals in topoclusters according to the topocluster energy and the cell energy density. Additional corrections are applied to the topocluster energy for the energy deposited in the sensitive calorimeter volume but escaping the topocluster, and for the energy

[1] σ_{noise} is the Gaussian width of the cell energy distribution measured in randomly triggered events.

lost in the vicinity of the topocluster, in inactive material in front or in between calorimeter modules. These weights are determined from Monte Carlo simulations of charged and neutral pions and they are applied to all calorimeter cells in the $E_{\mathrm{T}}^{\mathrm{miss}}$ calculation from Equation 3.3.

Refinement of $E_{\mathrm{T}}^{\mathrm{miss}}$ calibration The final step is the refinement of the calibration of cells on the base of the reconstructed "physics" object they belong to (refined calibration or *RefFinal*). Calorimeter cells are associated with a parent reconstructed and identified high-p_{T} object, in a chosen order: electrons, photons, hadronically decaying τ-leptons, jets and muons. They are separately and independently calibrated, as are those belonging to topoclusters not associated with any such objects .

Once the cells are associated with categories of objects as described above and calibrated, $E_{\mathrm{T}}^{\mathrm{miss}}$ is calculated as follows:

$$E_{x(y)}^{\mathrm{miss,calib}} = E_{x(y)}^{\mathrm{miss,e}} + E_{x(y)}^{\mathrm{miss},\gamma} + E_{x(y)}^{\mathrm{miss},\tau} + E_{x(y)}^{\mathrm{miss,jets}} + E_{x(y)}^{\mathrm{miss,calo},\mu} + E_{x(y)}^{\mathrm{miss,CellOut}} \tag{3.3}$$

where each term is calculated from the negative sum of calibrated cell energies inside the corresponding objects. The $E_{x(y)}^{\mathrm{miss,calo},\mu}$ is the contribution to $E_{\mathrm{T}}^{\mathrm{miss}}$ from the energy lost by muons in the calorimeter. It contributes to the final $E_{\mathrm{T}}^{\mathrm{miss}}$ according to the muon type used for the calculation of the $E_{\mathrm{T}}^{\mathrm{miss}}$ muon term. The $E_{x(y)}^{\mathrm{miss,CellOut}}$ term is calculated from the cells in topoclusters which are not included in the reconstructed objects. This calibration improves the performance in terms of $E_{\mathrm{T}}^{\mathrm{miss}}$ mean and resolution for events containing electrons, photons, taus, and muons for which the GCW or the LCW are not appropriate.

The final $E_{x(y)}^{\mathrm{miss,calib}}$ is then calculated from equation 3.1 adding the $E_{x(y)}^{\mathrm{miss},\mu}$ and $E_{x(y)}^{\mathrm{miss,cryo}}$ terms (see also Figure 3.1).

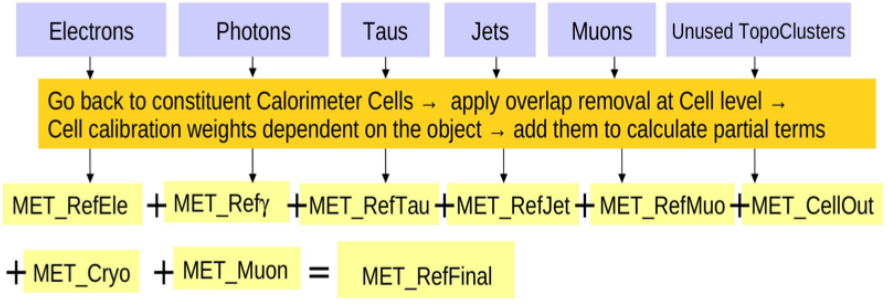

Figure 3.1: Sketch to illustrate how the reconstructed physics objects are used to reconstruct $E_{\mathrm{T}}^{\mathrm{miss}}$.[74]

3.1.2 The $E_{\mathrm{T}}^{\mathrm{miss}}$ muon term

The $E_{\mathrm{T}}^{\mathrm{miss}}$ muon term is calculated from the momenta of muons measured in a range of pseudorapidity:

$$E_{x(y)}^{\mathrm{miss},\mu} = -\sum_{selected\ muons} E_{x(y)}^{\mu} \tag{3.4}$$

In the region $|\eta| < 2.5$ only good-quality muons in the muon spectrometer with a matched track in the Inner Detector are considered. The matching requirement considerably reduces contributions from fake muons.

The muon term is calculated in a different way for isolated and non-isolated muons[2].

- The p_{T} of an isolated muon is determined from the combined measurement of the Inner Detector and muon spectrometer. In this case the energy lost by the muon in the calorimeters ($E_{x(y)}^{\mathrm{miss,calo},\mu}$) is not added to the calorimeter term.
- For a non-isolated muon, the energy lost in the calorimeter cannot be separated from the nearby jet energy. The muon spectrometer measurement of the muon momenta after energy loss in the calorimeter is therefore used unless there is a significant mismatch between the spectrometer and the combined measurement. In this case the combined measurement minus the parametrised energy loss in the calorimeter is used.

For higher values of the pseudorapidity outside the fiducial volume of the Inner Detector ($2.5 < |\eta| < 2.7$), there is no matched track requirement and the muon spectrometer is used alone.

Apart from the loss of muons outside the acceptance of the muon spectrometer ($|\eta| > 2.7$), muons are lost in other small regions not covered by the muon spectrometer. The muons reconstructed from the Inner Detector and calorimeter energy deposits can be used to recover these $E_{\mathrm{T}}^{\mathrm{miss}}$ contributions.

3.1.3 The $E_{\mathrm{T}}^{\mathrm{miss}}$ cryostat term

The correction for the energy lost in the cryostat between the LAr barrel electromagnetic calorimeter and the TileCal barrel hadronic calorimeter, which at a thickness of about half an interaction length can lead to significant energy losses in hadronic showers. When the calorimeter term is calibrated with the LCW scheme, a corresponding correction is already done at topocluster level, e.g. $E_{x(y)}^{\mathrm{miss,cryo}} = 0$.

The $E_{\mathrm{T}}^{\mathrm{miss}}$ reconstruction, when it is calibrated with GCW, recovers this loss of energy in the cryostat using the correlation of energies between the last layer of the LAr calorimeter and the first layer of the hadronic calorimeter. This correction is called the "cryostat term" when used for jet energy correction. It is defined as follows:

$$E_{x(y)}^{\mathrm{miss,cryo}} = -\sum_{jets} E_{x(y)}^{\mathrm{jet,cryo}} \tag{3.5}$$

where all reconstructed jets are summed in the event and:

$$\begin{aligned} E_{x}^{\mathrm{jet,cryo}} &= w^{\mathrm{cryo}} \sqrt{E_{EM3}^{\mathrm{jet}} \times E_{HAD1}^{\mathrm{jet}}} \frac{\cos\phi_{\mathrm{jet}}}{\cosh\eta_{\mathrm{jet}}} \\ E_{y}^{\mathrm{jet,cryo}} &= w^{\mathrm{cryo}} \sqrt{E_{EM3}^{\mathrm{jet}} \times E_{HAD1}^{\mathrm{jet}}} \frac{\sin\phi_{\mathrm{jet}}}{\cosh\eta_{\mathrm{jet}}} \end{aligned} \tag{3.6}$$

where w^{cryo} is a calibration factor, determined together with the cell signal calibration weights in the GCW fits. E_{EM3} and E_{HAD} are the energies in jets deposited on the third layer of the electromagnetic calorimeter and in the first layer of the hadronic calorimeter, respectively. The cryostat correction turns out to only be non-negligible for high-p_{T} jets.

[2]Non-isolated muons are those within the distance $\mathrm{R} = \sqrt{\Delta\eta^2 + \Delta\phi^2} < 0.3$ of a jet in the event

3.2 $E_{\mathrm{T}}^{\mathrm{miss}}$ and Jet cleaning

A misreconstruction of particles and of their energy can give fake $E_{\mathrm{T}}^{\mathrm{miss}}$. As the analysis presented in Chapter 5 relies on a $E_{\mathrm{T}}^{\mathrm{miss}}$ reconstructed only with the calorimeter term in 3.1, and calibrated with the LCW scheme, the main source of fake $E_{\mathrm{T}}^{\mathrm{miss}}$ is constituted by mismeasured jets. Is therefore essential for a good $E_{\mathrm{T}}^{\mathrm{miss}}$ reconstruction to reduce these contributions.

In collision data, misreconstructed jets arise from various sources, ranging from hardware problems, LHC beam conditions, and cosmic ray showers. Two types of misreconstructed jets have been taken into account: jets not associated to in-time energy depositions in the calorimeters, and jets coming from real energy depositions where the energy measurements are of limited confidence, as the energy depositions are in calorimeter regions which are noisy or not properly calibrated. The ATLAS group working on jet and $E_{\mathrm{T}}^{\mathrm{miss}}$ performance has developed some standard cleaning cuts meant to reject these types of misreconstruction [75]:

Single-cell jets in the HEC. Many misreconstructed jets are caused by sporadic noise bursts in the HEC, where most of the energy is in single calorimeter cells, with often some cross-talk in neighbouring cells. Jets reconstructed from these problematic channels are characterized by a large jet-energy fraction in the HEC, f_{HEC}, and a low number of cells containing most of the jet energy. These fake jets are tagged with the requirement: $f_{HEC} > 0.8$ and $\mathrm{n}_{90} \leq 5$, where n_{90} is the number of energy-ordered cells containing 90% of the jet energy.

Bad quality jets in the electromagnetic calorimeter. This category of misreconstructed jets is caused by the rare occurrence of noise bursts affecting the electromagnetic calorimeter, inducing coherent noise. These jets are characterized by cells with bad calorimeter reconstruction "quality" and with large reconstructed energy, causing large fractions of jet energy in only the electromagnetic calorimeter, f_{EM}. The calorimeter quality is a measure of the difference in the sampling of the measured pulse and the reference pulse shape that is used to reconstruct the cell energy [52]. In order to deal with jets that have a large portion of their energy accounted for by coherent noise, the variable $f_{quality}$ is defined, which is the fraction of jet energy from bad-quality calorimeter cells. Bad quality jets in the electromagnetic calorimeter are selected with: $|f_{quality}| > 0.8$ and $f_{EM} > 0.95$.

Out-of-time jets. Jets reconstructed from large out-of-time energy depositions in the calorimeter, for example those due to photons produced by cosmic ray muons, are eliminated. A loose cut on the jet time, t_{jet}, defined with respect to the event time, is applied. Jets are required to have an energy-squared-weighted cell time to be within two beam bunch crossings, i.e. out-of-time jets are selected with: $|t_{jet}| > 50$ ns.

Two sources of jets seeded by real energy depositions but located in problematic calorimeter regions are identified.

Jets extrapolated from masked cells. These jets have a large fraction of their energy from masked cells, whose energy is estimated by correction algorithms in the reconstruction software. In the reconstruction, typically the energy of these cells is extrapolated from the energy deposits in the neighbouring cells, rescaled by the volume of the cells. This correction needs to be fully validated in data for jets with a significant extrapolated energy. The variable f_{cor} is defined as the fraction of the

electromagnetic scale jet energy from cells within the jet which are included within in the list of problematic cells in the detector data-base, which are either dead or masked.

Large energy fraction in the Tile-Gap layers. These jets have a large energy deposit in scintillators located in the gap between the TileCal barrel and end-cap. The calibration of the scintillator response is not yet fully understood. These jets are characterized by a large value of f_{TG3}, where f_{TG3} is defined as the fraction of jet energy in the gap scintillators known as the TileGap3 layer.

The variables and cuts just described are used to define the "goodness" of jets: a flag (*good*, *bad* and *ugly*) is assigned to them and if a "bad" jet is present in the event, the event should be discarded.

The effect of the removal of misreconstructed jets is shown in Figure 3.2, where the $E_{\mathrm{T}}^{\mathrm{miss}}$ distribution at electromagnetic (EM) scale is shown, also in its components. The tails of the distributions, due to energy misreconstruction, are highly suppressed.

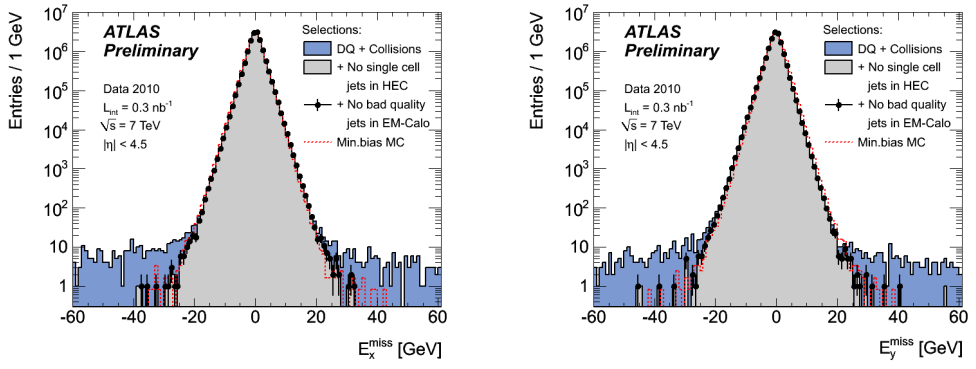

(a) (b)

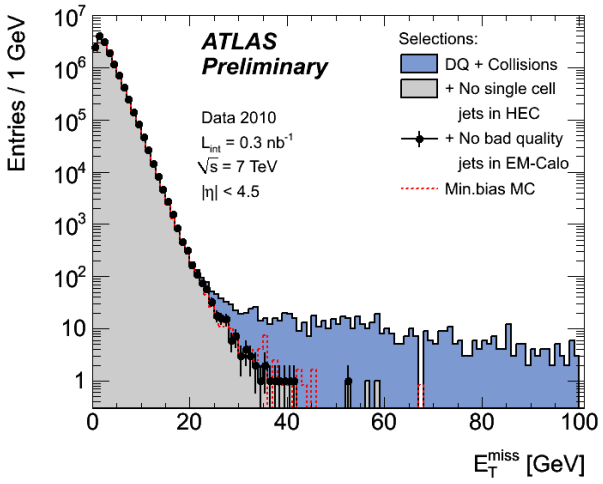

(c)

Figure 3.2: $E_{\mathrm{T}}^{\mathrm{miss}}$ distribution for 14.4 million collision events from 7 TeV data, after successive jet cleaning selections. Only topological clusters are used in the calculation, with energies calibrated at the electromagnetic scale. The corresponding distribution from the Monte Carlo simulation is overlaid and normalized to the number of events in data.[75]

3.3 Performance of $E_{\mathrm{T}}^{\mathrm{miss}}$ in proton-proton collisions

The performance of $E_{\mathrm{T}}^{\mathrm{miss}}$ reconstruction in proton-proton collisions have been evaluated on 900 GeV, 2.36 TeV and 7 TeV data. At the early stages of the data taking, just the calorimeter term in 3.1 is used for $E_{\mathrm{T}}^{\mathrm{miss}}$ computation, as in minimum bias events the contribution from muons is negligible. Moreover, topological cluster cells are calibrated at the EM scale. The performance of $E_{\mathrm{T}}^{\mathrm{miss}}$ at EM scale are presented in [76] for 900 GeV and 2.36 TeV collisions and in [77] for 7 TeV collisions.

The performance of calibrated $E_{\mathrm{T}}^{\mathrm{miss}}$ in 7 TeV collision data are presented in [74], with already some results concerning the refined calibration of $E_{\mathrm{T}}^{\mathrm{miss}}$. As the analysis for the observation of $W \to \tau_{\mathrm{h}}\nu_{\tau}$ decays presented in Chapter 5 relies only on the calorimeter term in 3.1 calibrated with a Local Hadron calibration scheme, in the following only the performance of this component with LCW calibration will be shown.

$E_{\mathrm{T}}^{\mathrm{miss}}$ calculated from calorimeters only The distributions of E_x^{miss} and E_y^{miss} obtained applying the Local Hadron calibration are shown in Figure 3.3. The distributions from Monte Carlo simulation are superimposed and normalized to the number of events in data. The small shift of the average E_y^{miss} in the data with respect to the simulation, observed in [77] and clearly visible also in Figure 3.2(b), is now corrected by an improved detector description in data reconstruction and simulation.

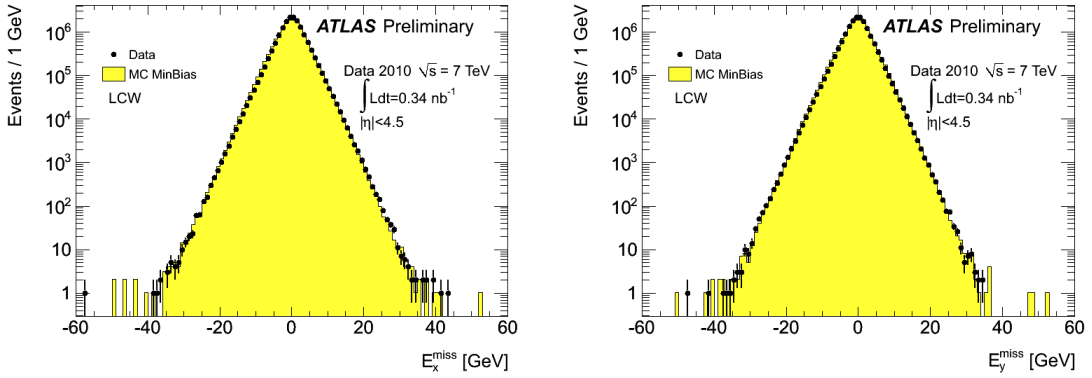

(a) (b)

Figure 3.3: Distributions of E_x^{miss} (left) and E_y^{miss} (right), as measured in a data sample of 15.2 million selected minimum bias events (dots) at 7 TeV centre-of-mass energy, recorded in April 2010. In the calculation only topocluster cells are used, with energies calibrated with the LCW calibration scheme. The expectations from Monte Carlo simulation are superimposed (histograms) and normalized to the number of events in the data.[74]

The $E_{\mathrm{T}}^{\mathrm{miss}}$ distribution is shown in Figure 3.4. No additional tails are created by the calibration, as it can be seen comparing Figure 3.4 with the $E_{\mathrm{T}}^{\mathrm{miss}}$ distribution at EM scale shown in [77].

Figure 3.5 shows the $E_{\mathrm{T}}^{\mathrm{miss}}$ distribution with significantly more data and where events with a high-p_{T} jet are selected. Outlier events are visible both in data and in Monte Carlo simulation. All of the events with large $E_{\mathrm{T}}^{\mathrm{miss}}$ contain high-p_{T} jets, with the $E_{\mathrm{T}}^{\mathrm{miss}}$ aligned or anti-aligned in ϕ with a high-p_{T} jet. This suggests jet energy mismeasurement as the source of this fake $E_{\mathrm{T}}^{\mathrm{miss}}$. Similar events are found in Monte Carlo simulation. Most of the mismeasured jets in these events enter the transition regions between the calorimeters,

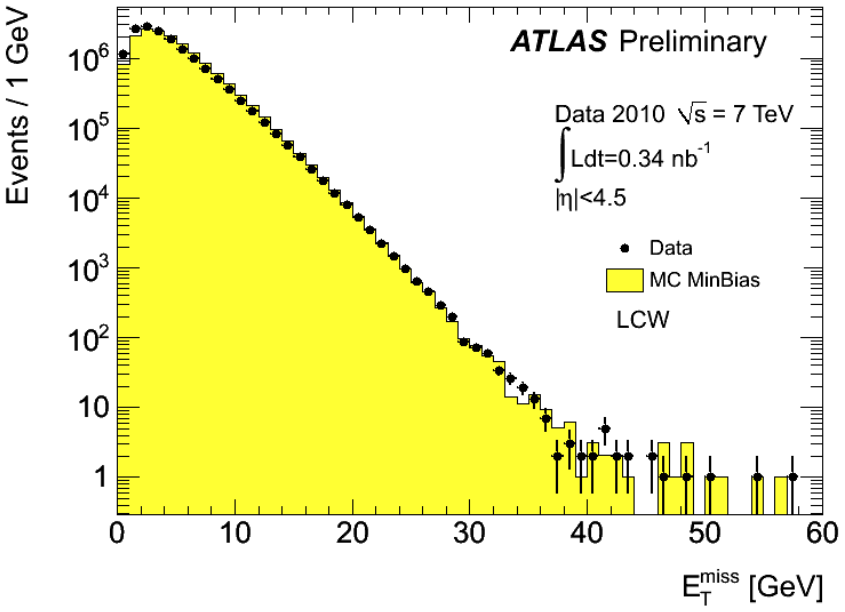

Figure 3.4: Distribution of $E_{\mathrm{T}}^{\mathrm{miss}}$ as measured in a data sample of 15.2 million selected minimum bias events (dots) at 7 TeV centre-of-mass energy, recorded in April 2010. In the calculation only topocluster cells are used, with energies calibrated with the LCW calibration scheme. The expectation from Monte Carlo simulation is superimposed (histogram) and normalized to the number of events in data.[74]

where the jet energy resolution is worse. These events can be rejected at the analysis level with a cut based on $\Delta\phi$(jet,$E_{\mathrm{T}}^{\mathrm{miss}}$). This is indeed done in the $W \to \tau_{\mathrm{h}}\nu_{\tau}$ decay analysis (Chapter 5). In Figure 3.6 the $\Delta\phi$(jet,$E_{\mathrm{T}}^{\mathrm{miss}}$) distribution for $W \to \tau_{\mathrm{h}}\nu_{\tau}$ events (multiplied by 200) and data, for events passing the cleaning cuts described in Section 5.4, is shown. At that stage of the event selection, data are dominated by QCD jets events.

$E_{\mathrm{T}}^{\mathrm{miss}}$ resolution A more quantitative evaluation of the $E_{\mathrm{T}}^{\mathrm{miss}}$ performance can be obtained from a study of the (E_x^{miss},E_y^{miss}) resolutions as function of the total transverse energy $\sum E_{\mathrm{T}}$, which is reconstructed from the calorimeters as:

$$\sum E_{\mathrm{T}} = \sum_{i=1}^{N_{\mathrm{cell}}} E_i \sin\theta_i \tag{3.7}$$

Here E_i and θ_i are the cell energy and the polar angle, respectively. The sum only includes cells belonging to topoclusters.

The $E_{\mathrm{T}}^{\mathrm{miss}}$ resolution, expressed as $\sigma(E_{x(y)}^{\mathrm{miss}})$, scales in good approximation as $\sigma(E_{x(y)}^{\mathrm{miss}}) = a \times \sqrt{\sum E_{\mathrm{T}}}$, with scaling factors a depending both on detector and reconstruction performances. A reasonable agreement between data and simulations is obtained, as it can be seen in Figure 3.7. The observed differences in the scale factors are less than 5% and are probably due to imperfections of the modelling of soft particle activity.

The performance of calibrated $E_{\mathrm{T}}^{\mathrm{miss}}$ in Figure 3.8, where the resolution of $E_{\mathrm{T}}^{\mathrm{miss}}$ calibrated with LCW is shown for data, superimposed with the fit to the Monte Carlo simulated resolution on the LCW calibrated scale. The resolution was found to be $0.49\sqrt{\sum E_{\mathrm{T}}}$ in data and $0.51\sqrt{\sum E_{\mathrm{T}}}$ in Monte Carlo.

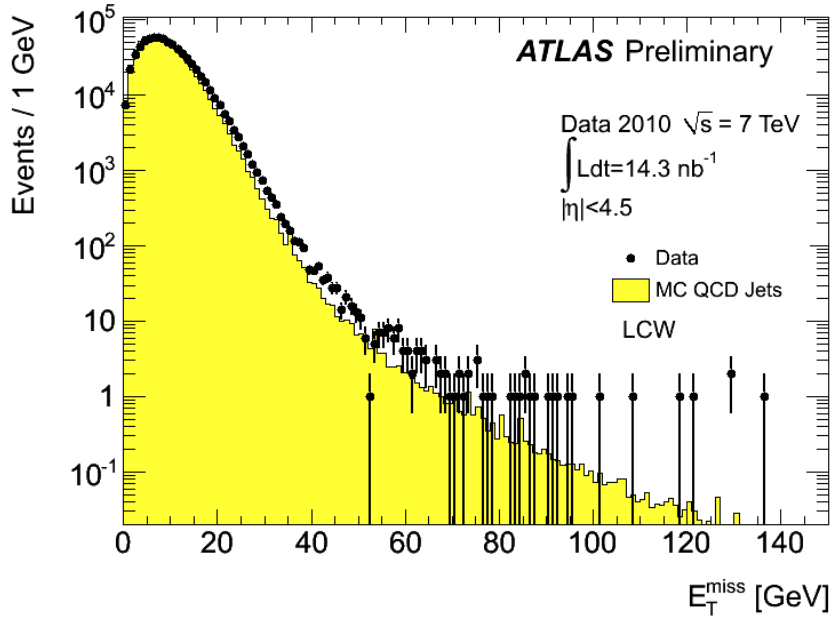

Figure 3.5: Distribution of $E_{\mathrm{T}}^{\mathrm{miss}}$ as measured in a data sample of about 700 thousand selected events with at least one jet, reconstructed with the anti-kt with R = 0.4 algorithm, with $p_{\mathrm{T}} > 20$ GeV at EM scale at 7 TeV centre-of-mass energy, recorded in April and May 2010 (dots). In the calculation only topocluster cells are used, with energies calibrated with the LCW. The expectation from Monte Carlo simulation is superimposed (histogram) and normalized to the number of events in data.[74]

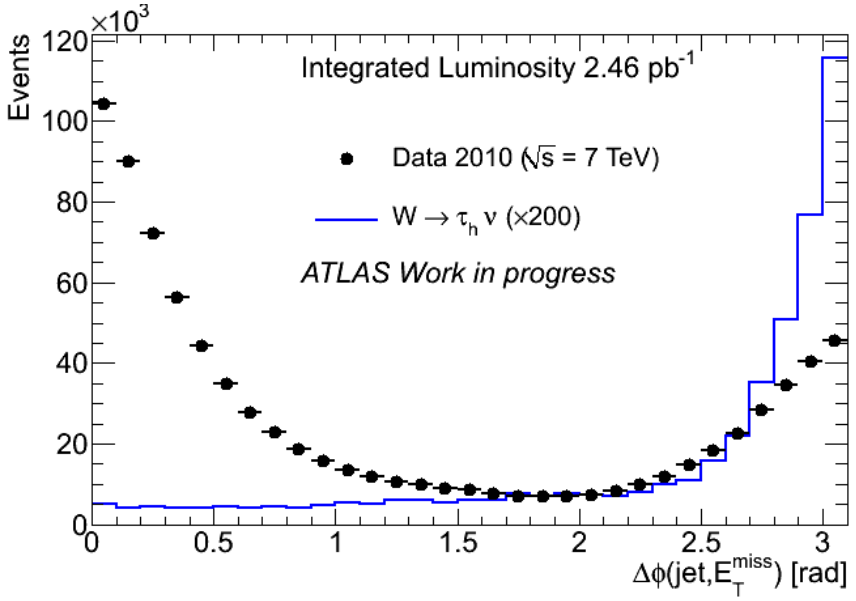

Figure 3.6: $\min(\Delta\phi(\mathrm{jet}, E_{\mathrm{T}}^{\mathrm{miss}}))$ distribution for Monte Carlo signal events and data. $W \to \tau_{\mathrm{h}}\nu_{\tau}$ events have been multiplied per 200 to make them visible.

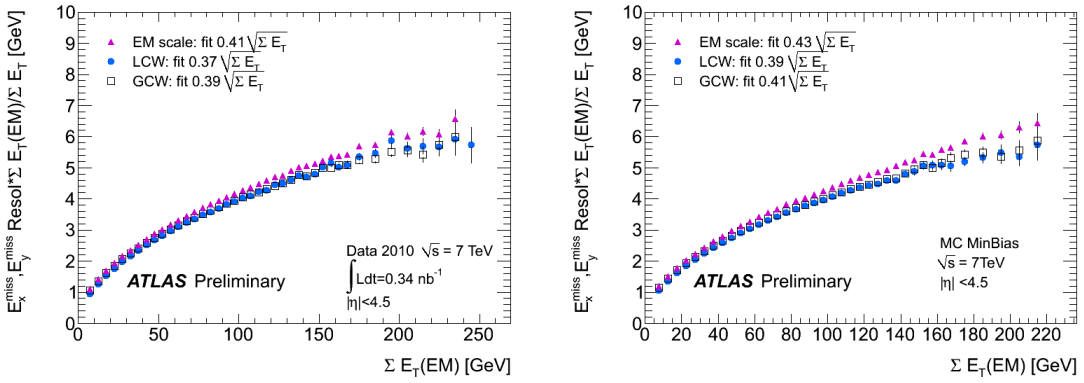

(a) (b)

Figure 3.7: E_x^{miss} and E_y^{miss} resolution scaled by the ratio of $\sum E_{\text{T}}$ at electromagnetic scale and calibrated as a function of the total transverse energy for minimum bias events for data taken at $\sqrt{s} = 7$ TeV (left) and Monte Carlo (right). E_x^{miss} and E_y^{miss} are computed with topocluster cells at the electromagnetic scale and calibrated with GCW and with LCW. The $\sum E_{\text{T}}$ on the x-axis is taken at the electromagnetic scale.[74]

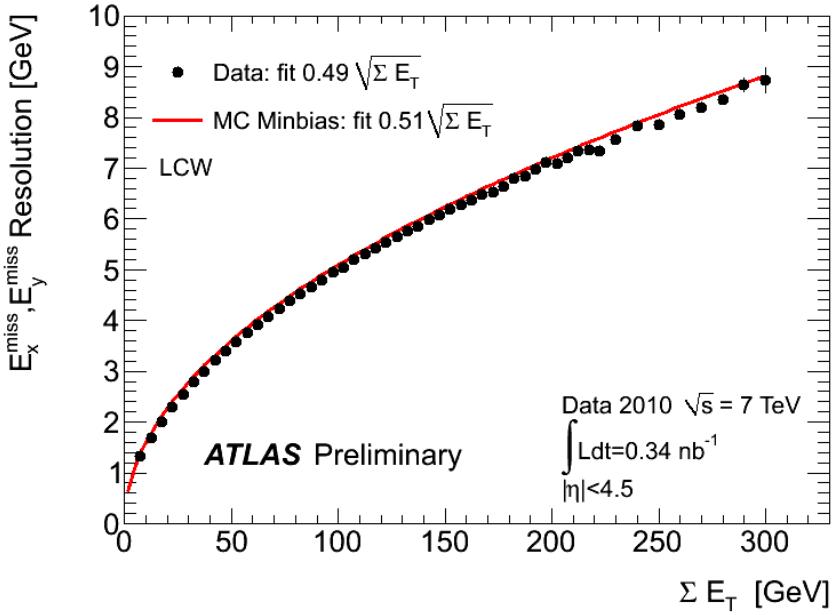

Figure 3.8: E_x^{miss} and E_y^{miss} resolution as a function of the total transverse energy for minimum bias events. The line represents a fit to the resolution obtained in the Monte Carlo simulation and the full dots represent the results from data taken at $\sqrt{s} = 7$ TeV. E_x^{miss}, E_y^{miss}, $\sum E_{\text{T}}$ are computed with topological cluster cells calibrated with LCW.[74]

Chapter 4

Trigger

In the following, the ATLAS Trigger system will be described. Section 4.1 contains a brief introduction about the ATLAS trigger architecture and requirements. As the analysis for the $W \to \tau_{\mathrm{h}}\nu_\tau$ decay observation presented in Chapter 5 relies on a combined trigger of tau and missing transverse energy, Section 4.2 describes in detail how the ATLAS tau trigger works. The performance of the tau trigger on 7 TeV collision data will be shown. Section 4.3 describes the ATLAS $E_{\mathrm{T}}^{\mathrm{miss}}$ trigger and finally in Section 4.4 the combined triggers are presented.

4.1 The ATLAS trigger system

At the LHC, the foreseen collision rate is of 40 MHz, with bunches colliding every 25 ns. The physical processes we are interested in happen at a much lower rate. For example, at a luminosity of 10^{32} cm^{-2}s^{-1}, $W \to \tau_{\mathrm{h}}\nu_\tau$ events (with a NNLO production cross section of 10.46 ± 0.52 nb) have a production rate of about 1 Hz. New physics, Higgs boson production and SUSY events will be produced even at a lower rate.

The ATLAS trigger system [78] is designed to record events at a rate of about 200 Hz, with a reduction of more than 5 orders of magnitude respect to the collision rate. This decision is driven mainly by two facts. First of all, interesting physics occurs mostly at rates of 10, 1 or < 0.1 Hz, so we are actually interested in a tiny fraction of the events produced. The second is resource limitation. One proton-proton collision event takes $\approx$1.5 MB of space for the raw event, and about the same amount for derived data (considering reconstructed event and data distribution). This ends up in approximately 6000 TB of data per year (considering 10^7 seconds of data taking per year). Moreover, the typical processing time per event is about 10 s, which means that 2000 CPUs are needed to sustain the processing rate.

To reduce the rate from 40 MHz to 200 Hz, the ATLAS Experiment relies on a three level trigger system, each step providing a refinement of the decision by more sophisticated algorithms and lower rates. It is important to say that, beside reducing the rate, having more trigger levels allows to use complex detector informations to make the trigger decision, such as full online track reconstruction.

The first level (Level1 or L1) is hardware-based and makes an initial decision based on timing from an electrostatic beam pick-up (BPTX), coarse detector information from muon trigger chambers and towers of calorimeter cells, together with multiplicity information from the Minimum Bias Trigger Scintillators (MBTS) and very forward detectors. The signatures considered by the L1 are high p_{T} electrons and photons, jets, hadronic tau decays (as explained in Section 4.2), high values of missing transverse energy. The L1

nominal output rate is 100 kHz. The L1 provides regions of interest (RoIs) to the following level.

The High Level trigger, which is composed by the second level trigger (Level2 or L2) and the Event Filter (EF), runs on a dedicated processor farm. The L2 examines the RoIs using more detector information than L1 (such as track informations): in this way, just part of the information of the full detector needs to be copied and sent to the trigger farms. The L2 works in parallel on more RoIs and subdetectors with more complete algorithms. The nominal output rate of L2 is about 1 kHz. The EF then has access to the complete event and uses reconstruction algorithms similar to the ones that are used offline. The output rate is then reduced to approximately 200 Hz.

For the different LHC running conditions, different trigger menus have been composed. A trigger menu is constituted by the various working trigger chains that make a decision on whether to record an event or not. Depending on the instantaneous luminosity some trigger can be prescaled or removed from the trigger menu. When a trigger is prescaled, only a certain fraction of the events that fire this trigger is actually recorded.

At the beginning of the data taking, when the instantaneous luminosity was low, only L1 trigger were activated. With the increase of the luminosity, also the HLT was inserted, first in pass through more (i.e. the trigger decision was made but was not used to reject the event), then in rejection mode. These steps in the turning on of the full trigger chain allowed to commission the trigger system step by step.

4.2 Tau trigger

In the following, the ATLAS tau trigger will be described. First, it will be explained which are the purposes and the physics analysis relying on such a trigger. Then it will be described how the tau trigger works and which are the variables used for the trigger decision. The performance of the tau trigger on 7 TeV collision data will be shown. Finally the acceptance of these triggers on $W \to \tau_{\mathrm{h}}\nu_\tau$ events will be shown.

4.2.1 Introduction

Tau triggers are meant to select hadronic tau lepton decays, which are characterised by the presence of one or three charged hadrons accompanied by a neutrino and possibly neutral pions.

At the initial luminosity of 10^{31} cm^{-2}s^{-1}, tau triggers [79, 80] are important to collect samples that are useful to understand the detector and the tau reconstruction software. Moreover, a combined trigger of tau and missing transverse energy is essential to provide data samples enriched in $W \to \tau_{\mathrm{h}}\nu_\tau$ events, which then will provide a unique sample of real τ_{h} needed to refine tau identification algorithms. Additionally, single tau triggers with large prescale factors will provide samples for rate studies of jets with tau-like signatures.

At high luminosity, tau triggers are essential to enable the collection of data samples for searches based on single tau lepton final states, like Minimal Supersymmetric Standard Model (MSSM) $H \to \tau_{\mathrm{h}}\nu_\tau$ decays. They will also be used for final states with more than one tau lepton, like SM Higgs boson, MSSM neutral Higgs boson, or Z boson decays.

The standard tau trigger is described in the next section. This trigger is designed to work both at low and high luminosity, obviously with different thresholds for the selecting variables. In the following section, a different tau trigger will be described. This trigger has been designed only for very first data, up to a luminosity of 10^{31} cm^{-2}s^{-1}. It is a

much simpler trigger, easy to commission and highly efficient, designed in view of the first τ_{h} observation.

4.2.2 Overview of the standard tau trigger

The L1 tau trigger selection is fully documented in [81]. It is a hardware trigger based on electromagnetic (EM) and hadronic (HAD) calorimeter information. It uses trigger towers with approximate size of $\Delta\eta \times \Delta\phi = 0.1 \times 0.1$, with a coverage up to $|\eta| < 2.5$ (determined by the high-granularity EM calorimetry and the Inner Detector coverage). In the selection of the L1 candidates, a RoI of 2×2 towers (0.2×0.2 in $\eta \times \phi$) is used. The L1 E_{T} is calculated from the energy defined by the two most energetic neighbouring central towers in the EM calorimeter plus the central 2×2 towers of the HAD calorimeter. In addition to the L1 E_{T} , two isolation quantities are also constructed from the isolation ring in the EM and HAD calorimeters (energy between 0.2×0.2 and 0.4×0.4 in the EM and HAD calorimeters). Different thresholds to these quantities define the various L1 tau triggers and the seed position is defined by the centre of the RoI. As an example, the trigger called L1_TAU5 requires $E_{\mathrm{T}} > 5$ GeV. Other typical triggers are L1_TAU6 and L1_TAU20, where the number in the name always defined the threshold on the τ_{h} E_{T} .

The selection at the HLT makes use of the tracking and full granularity calorimeter information. While fast and specialised algorithms are used at the L2, more sophisticated and precise determinations can be performed at the EF.

The L2 calorimeter algorithm first refines the L1 position using the second layer of the EM calorimeter. It then selects narrow jets in the detector by means of a calorimeter shape variable, the EM radius $\mathrm{R_{EM}}$, whic is an energy-weighted squared radius in a region of 0.6×0.6, i.e.:

$$\mathrm{R_{EM,L2}} = \frac{\sum_{\mathrm{cell}} E_{\mathrm{cell}} \Delta \mathrm{R}^2_{\mathrm{cell}}}{\sum_{\mathrm{cell}} E_{\mathrm{cell}}} \tag{4.1}$$

where $\Delta\mathrm{R} = \sqrt{(\Delta\eta)^2 + (\Delta\phi)^2}$ and the sum is only determined from the second layer of the EM calorimeter. Finally the total energy of all the layers of the EM and HAD calorimeters is computed. The EM radius together with the total energy are the basis of the L2 calorimeter selection.

The L2 track algorithm uses the standard L2 track reconstruction. To keep the L2 execution time within budget, only SCT and Pixel detectors are used. Tracks with $p_{\mathrm{T}} > 1.5$ GeV are reconstructed in a rectangular RoI of size $\eta \times \phi = 0.6 \times 0.6$ centered on the L2 calorimeter position. The highest p_{T} track is determined and three regions are defined: two cones around this track with radius $\Delta\mathrm{R}$ equal to 0.15 and equal to 0.3, respectively, and an isolation ring with $\Delta\mathrm{R}$ between 0.15 and 0.3. Two complementary selection variables with looser requirements are the total charge and the number of tracks in the 0.3 cone. A tight constraint on these two last quantities would be problematic because the number of fake tracks at L2 is higher than what the more sophisticated offline reconstruction finds. In addition, the offline reconstruction of single tau lepton final states (e.g. from $W \to \tau_{\mathrm{h}}\nu_{\tau}$) might rely in the future on an unbiased track distribution to estimate backgrounds and extract the number of signal events, so it is good to have the lightest possible requirements on the number of tracks of the τ_{h} candidate.

At the EF level, the selection follows the offline reconstruction procedure as closely as possible except that only data in the RoI defined by L2 is used. The EF track reconstruction is described in [82]. Tracking is performed in a rectangular RoI of size $\eta \times \phi = 0.6 \times 0.6$ centered around the L2 tau trigger candidate.

To create an EF tau trigger candidate, the EF single tau triggers executes the calorimeter and track-based identification in the following way. Cells in a rectangular region of size $\eta \times \phi = 0.8 \times 0.8$ centered around the L2 tau trigger candidate are collected and used to form a topological jet and reconstruct the direction of the EF tau trigger candidate. Additionally, some quality criteria are applied to tracks reconstructed in the RoI, and if more than one track is found a secondary vertex reconstruction is attempted. The transverse energy and the calorimeter shower shape variables are built from cells from all calorimeter layers collected in the RoI and using the newly reconstructed direction. Finally, an overall hadronic calibration [63] is applied to all cells, and a tau-specific jet calibration is applied to the tau trigger candidate. Some relevant quantities in the EF selection are the calibrated E_{T} , calculated for all EM and HAD cells found in a cone of $\Delta\mathrm{R} = 0.4$ and the EM radius. This quantity has a slightly different definition than at L2, i.e.:

$$\mathrm{R_{EM,EF}} = \frac{\sum_{\mathrm{cell}} E_{\mathrm{T,cell}} \Delta\mathrm{R_{cell}}}{\sum_{\mathrm{cell}} E_{\mathrm{T,cell}}} \tag{4.2}$$

as at EF level the transverse cell energies and the unsquared ΔR are used. Another important variable is the number of tracks which are associated to the reconstructed tau. The EF selection also uses the p_{T} of the leading track and the invariant mass from the tracks. Different selections for one and multi tracks reconstructed taus are applied.

An example of a standard tau trigger is tau12_loose. This trigger starts from selecting narrow clusters of trigger towers with a p_{T} threshold of 5 GeV at L1 (through L1_TAU5), which are the seed for the HLT. Subsequently, several τ_{h} identification requirements are imposed both at L2 and at EF. These requirements are summarised in Table 4.1.

Requirement	Level	tau12_loose	tauNoCut_hasTrk6
Tau E_{T}	L1	5 GeV	5 GeV
Tau E_{T}	L2	7.55 GeV	-
Leading track p_{T}	L2	1.5 GeV	6 GeV
# min tracks	L2	1	1
# max tracks	L2	10	-
Sum p_{T} isolation ratio	L2	0.1	-
EM Radius (diff from EF)	L2	0.0163	-
Min simple E_{T} flow	L2	15 GeV	-
# min tracks	EF	1	-
# max tracks	EF	10	-
Tau E_{T}	EF	12 GeV	-
EM Radius (1 prong)	EF	0.105	-
EM Radius (multi prong)	EF	0.125	-
Leading track p_{T} (1 prong)	EF	2.5 GeV	-
Leading track p_{T} (multi prong)	EF	2.5 GeV	-

Table 4.1: Requirements for simple tau triggers tau12_loose and tauNoCut_hasTrk6 at the three different trigger levels.

4.2.3 Overview of the tau trigger for first data

As already mentioned, a new and simpler trigger was designed for very first data taking. The idea was to have the simplest τ_{h} selection possible, to avoid for example any bias on

the track multiplicity spectrum of τ_{h} candidates.

This trigger starts from the same selection of the standard trigger at L1, i.e. a selection on τ_{h} E_{T} . Then at the L2 the only requirement is to have a track with quite high p_{T} . No other requirement is applied at EF.

An example of this trigger is tauNoCut_hasTrk6, which starts from the same selection at L1 as tau12_loose, but the only requirement it imposes at the HLT is the presence of a track at L2 with momentum greater than 6 GeV. This trigger turned out to be fundamental for the $W \to \tau_{\mathrm{h}}\nu_{\tau}$ decay observation and it has been chosen for the analysis described in Chapter 5.

4.2.4 Performance of the tau trigger with 7 TeV collision data

The performance of the tau trigger have been studied both on 900 GeV and on 7 TeV collision data. The results are reported in [83, 84]. Here a summary of the performance on 7 TeV data is reported: it will be shown the good agreement between data and simulation in the desctription of the quantities used by the trigger to take the decision.

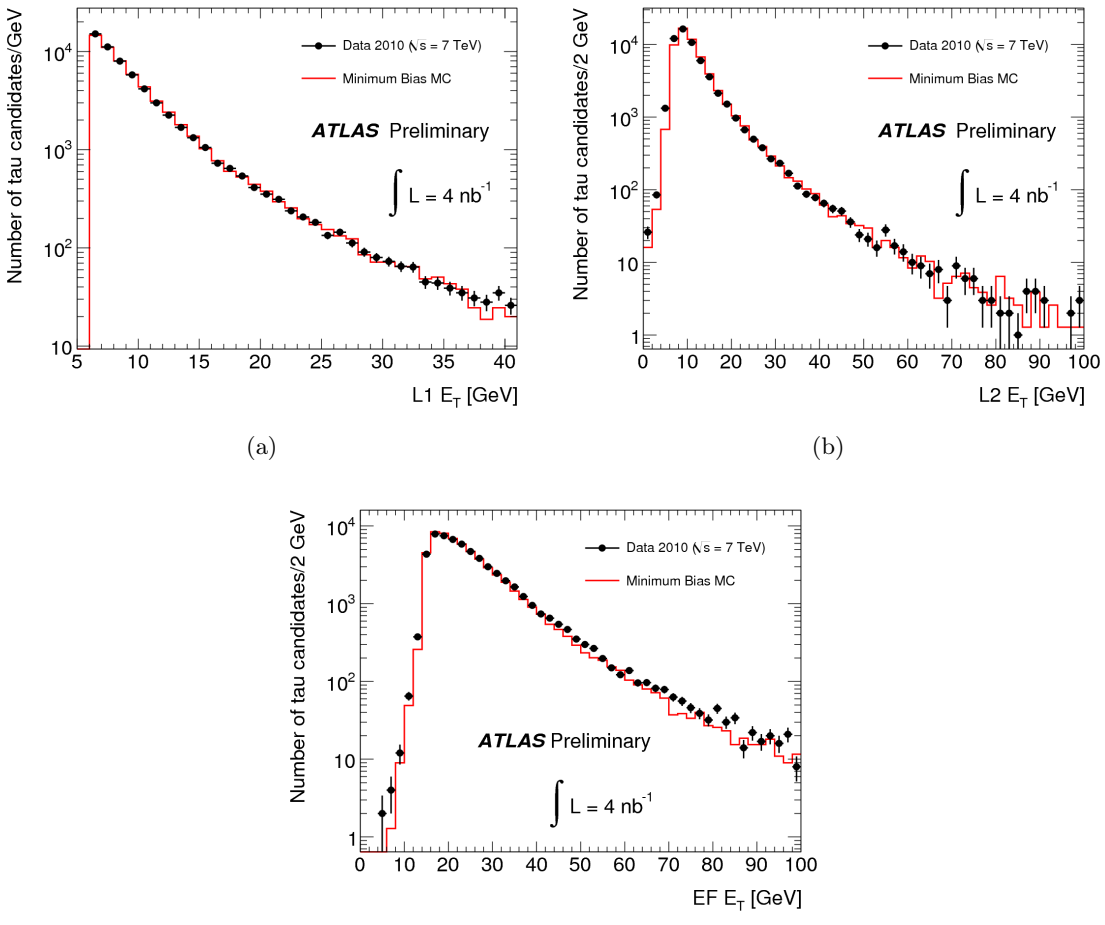

Figure 4.1: Comparison of the (a) L1, (b) L2, (c) EF tau candidate E_{T} distributions for 7 TeV data and Minimum Bias Monte Carlo.[84]

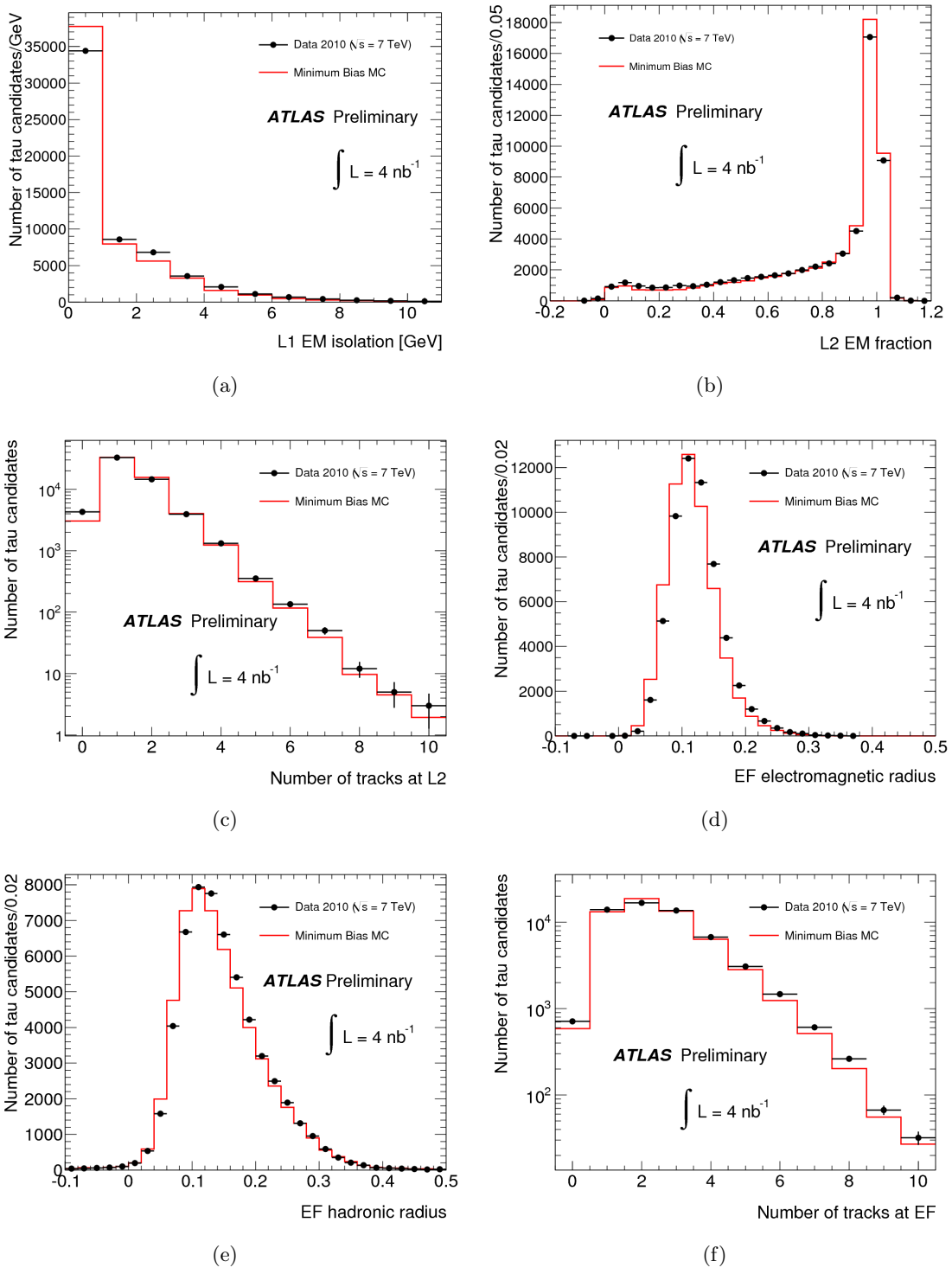

Figure 4.2: (a) Comparison of the L1 tau candidate EM isolation distribution for 7 TeV data and Minimum Bias Monte Carlo. (b) Comparison of the tau candidate EM fraction distribution at L2 for 7 TeV data and Minimum Bias Monte Carlo. The values below zero and above one appear because the EM and HAD energies can be negative after pedestal subtraction due to noise fluctuations. (c) Comparison of the tau candidate number of tracks distribution at L2 for 7 TeV data and Minimum Bias Monte Carlo. Comparison of the tau candidate (d) EM radius, (e) hadronic radius, (f) number of associated tracks distributions at EF for 7 TeV data and Minimum Bias Monte Carlo.[84]

Figure 4.1(a) shows the L1 transverse energy (E_{T}) distribution, along with the L2 and EF E_{T} distributions. As it was explained previously, the τ_{h} E_{T} at the three different levels is calculated using more refined information at each following step. The agreement between data and Monte Carlo is very good at all the levels.

As the E_{T} is reconstructed in a much narrower region at L2 than at EF, possible issues of current Monte Carlo simulations in reproducing energy distributions in the core and outer regions of jets would be much more evident in the L2 plot. This effect is clearly visible in the figures. Another common observation, at both levels, is the softer spectrum below the threshold for objects observed in data with respect to Monte Carlo. This has been observed also in other tau and jet offline analyses, and is correlated with the observation of the similar level of disagreement in the lateral shape distributions for jets in offline and at trigger level.

Figure 4.2(a) shows the L1 EM isolation energy described before. The tau triggers inserted in the trigger menu at the moment do not apply isolation requirements at L1, since at the current luminosities the rejection is sufficient without it. When luminosity increases, the isolation requirement will possibly be applied at L1 to reject more background. The spectrum observed in data is harder than the one expected from Monte Carlo simulation. However, the overall predicted rate after requiring EM isolation to be less than 6 GeV is similar to that observed in data.

An interesting variable, though currently not used in tau identification (Section 2.3), is the L2 electromagnetic fraction, displayed in Figure 4.2(b). The values below zero and above one appear because the EM and HAD energies can be negative after pedestal subtraction due to noise fluctuations. The peak observed at one is due to the collision events which have large energy deposits in the EM calorimeter. A fraction of those entries will come from photons (e.g. from π^0 decays) and electrons. Charged mesons will have a contribution to lower values as well. For non-collision related activity (like beam halo or cosmics) one expects a distribution with more entries around zero as this is simply caused by the larger volume of the hadronic calorimeters and the fact that cosmic muons meet this part of the calorimeter first (or even exclusively).

The number of tracks associated with the tau trigger candidate is another important variable for identification. In Figure 4.2(c) it is shown the number of tracks obtained with the L2 tracking algorithm with $p_{\mathrm{T}} > 1.5$ GeV in a cone of $\Delta\mathrm{R} < 0.1$ around the L2 position.

In Figure 4.2(d) and 4.2(e) the EM and HAD radiuses (decribed in Section 2.3) reconstructed at EF are shown. In general, the shape is well described but a slight shift in data with respect to Monte Carlo can be observed. A similar behaviour has been observed for offline reconstructed tau candidates.

Figure 4.2(f) shows the number of tracks with $p_{\mathrm{T}} > 1$ GeV found at the EF using the offline tau reconstruction algorithm, in a region of $\Delta\mathrm{R} < 0.3$ around the position of the tau candidate as calculated from calorimeter clusters. The distributions for this variable at L2 and EF is not identical due to the difference in the track requirements. At EF only 1% of tau trigger candidates have zero tracks.

An important part in understanding the tau trigger performance is the investigation of its efficiency in finding tau candidates reconstructed by the offline reconstruction algorithms. The data have been selected with the MBTS trigger in order to obtain an unbiased sample for estimating the L1 tau trigger efficiency. Figure 4.3 shows the fraction of the offline tau candidates which match geometrically to a L1 trigger object with $E_{\mathrm{T}} > 5$ GeV. The fraction is shown as a function of the uncalibrated E_{T} of the offline tau candidate.

The region of high transverse energy shows an excellent agreement between real and simulated collision data. In the lower E_{T} region, the efficiency in Monte Carlo is slightly

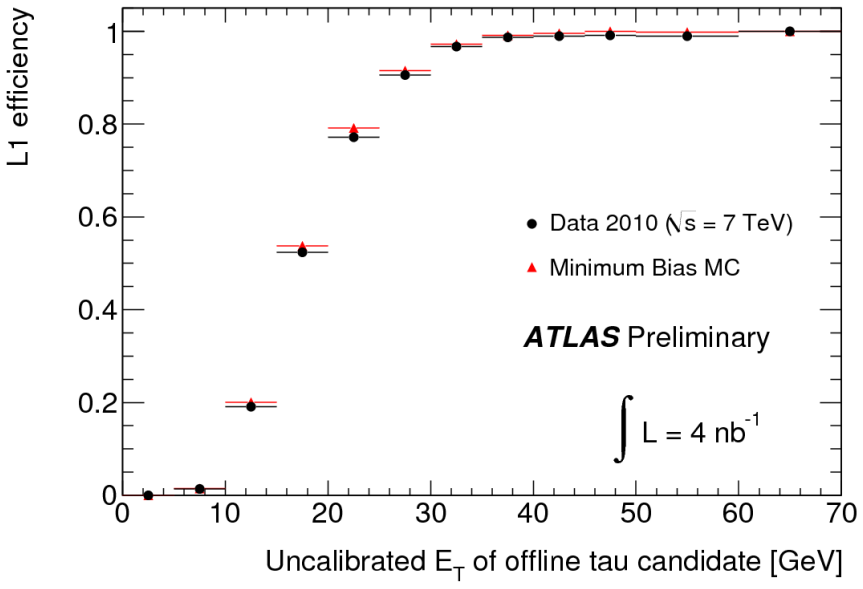

Figure 4.3: Fraction of the offline tau candidates matched to a L1 trigger object with E_{T} > 5 GeV as a function of the E_{T} of the offline tau candidate.[84]

higher than in real data. Further studies in different regions of pseudo-rapidity η indicate that the most significant contributions to the observed discrepancy come from the detector region with $|\eta| > 1.2$, especially the end-caps. In the barrel region of the detector, the discrepancies are negligible. Possible explanation could be that Monte Carlo simulation has an insufficient modelling of the noise seen in HEC in real data.

4.2.5 Tau triggers for $W \to \tau_{\mathrm{h}}\nu_{\tau}$ analysis

As it will be shown in the following, for the $W \to \tau_{\mathrm{h}}\nu_{\tau}$ decay observation, two simple tau triggers were taken into account: tau12_loose and tauNoCut_hasTrk6.

In Figure 4.4 the trigger efficiencies as a function of the τ_{h} E_{T} (turn-on curves) for the two simple τ_{h} triggers at the three trigger levels are shown. The efficiency is calculated respect to the $W \to \tau_{\mathrm{h}}\nu_{\tau}$ Monte Carlo events that pass the offline selection described in Section 5.4. The requirement on τ_{h} p_{T} is dropped, to show the full turn-on curve.

As already shown, the two triggers considered start from the same τ_{h} trigger signature at L1 (L1_TAU5). Then, at L2, they differentiate, with tauNoCut_hasTrk6 having a higher efficiency than L2_tau12_loose. This latter trigger is not fully efficient in the τ_{h} E_{T} range that will be considered in the following for the $W \to \tau_{\mathrm{h}}\nu_{\tau}$ decay observation. At EF, tauNoCut_hasTrk6 has no other requirement concerning τ_{h} and the efficiency remains the same as the one at L2, while EF_tau12_loose has further requirements, giving slightly lower efficiency at EF.

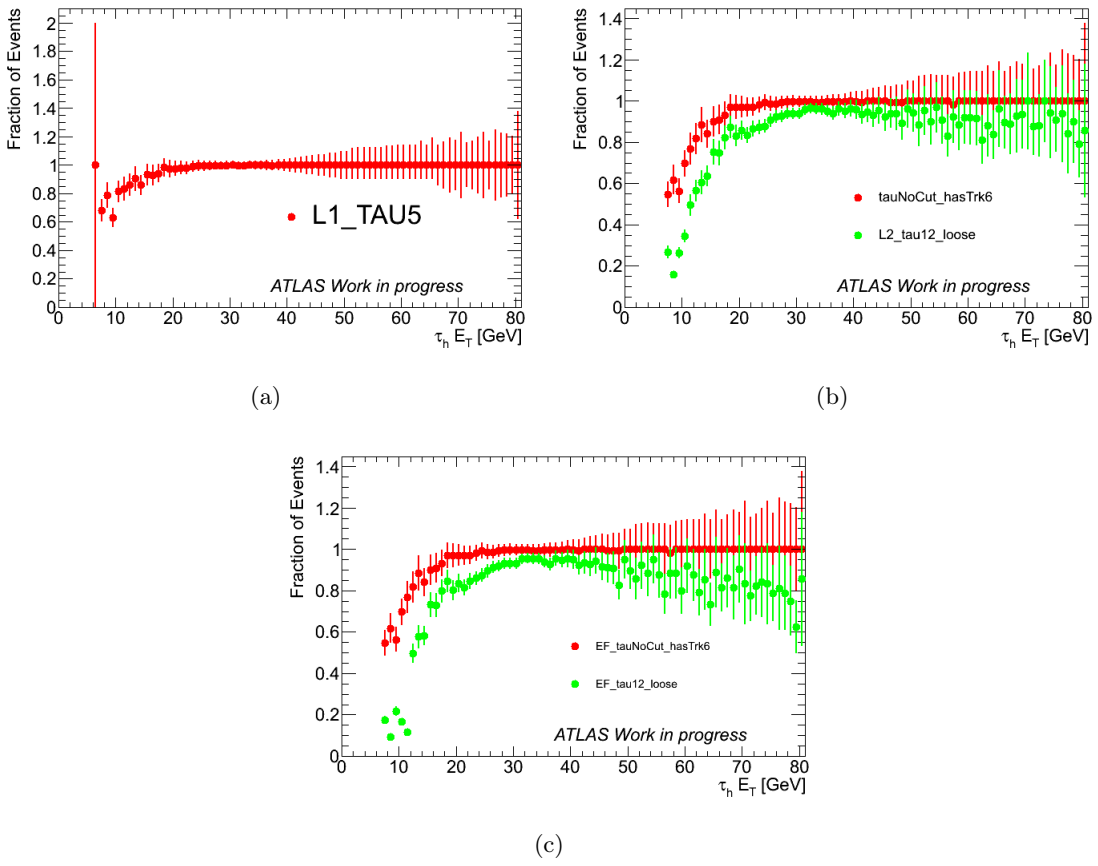

Figure 4.4: Turn-on for the simple τ_{h} triggers as a function of τ_{h} E_{T} reconstructed offline, for the three different trigger levels. The efficiency is computed for $W \to \tau_{\mathrm{h}}\nu_{\tau}$ Monte Carlo events which satisfy the offline selection reported in Section 5.4, except the cut on τ_{h} E_{T} itself.

4.3 $E_{\mathrm{T}}^{\mathrm{miss}}$ trigger

In the following, a brief description of the $E_{\mathrm{T}}^{\mathrm{miss}}$ trigger is reported. The basic features of the trigger will be explained and the acceptance of these triggers on $W \to \tau_{\mathrm{h}}\nu_{\tau}$ events will be shown.

4.3.1 Introduction

The ATLAS trigger system can also trigger on $E_{\mathrm{T}}^{\mathrm{miss}}$ [85]. This type of trigger will be very important in the future, for example in the search of SUSY events, as they are expected to be characterised by large amounts of $E_{\mathrm{T}}^{\mathrm{miss}}$. In addition to discovery perspectives, the $E_{\mathrm{T}}^{\mathrm{miss}}$ trigger can also be used in combination with other triggers to control the rate of signatures involving low energy objects. Finally, the negligible statistical correlation with lepton triggers make it ideal to estimate the performance of those lepton triggers (and vice versa).

The $E_{\mathrm{T}}^{\mathrm{miss}}$ trigger [86] requires that the magnitude of the vector sum of all transverse energies exceeds some thresholds. At L1, only calorimeter information from "trigger towers" is used. The decision is made on the analogue sums of all calorimeter cells in a (η, ϕ) range of 0.1×0.1 aligned along a given direction, formed by dedicated hardware. Next, the L1 pre-processor digitises and applies noise subtraction to the formed trigger towers, and then produces jet elements. Using all the jet elements in the event, the jet/energy processor then computes the calorimeter energy sums along the x-axis (E_x) and y-axis (E_y). Instead of computing $E_{\mathrm{T}}^{\mathrm{miss}}$ from the quadratic sum of E_x and E_y, a look-up-table is used to accept or reject the events based on the (x, y) components of the measured energies. The scalar sum of the energy deposited in the calorimeter ($\sum E_{\mathrm{T}}$) is obtained similarly, without the need for a look-up table to determine which thresholds the energy measurement satisfies.

The HLT consists of a set of software-based algorithms which either perform the $E_{\mathrm{T}}^{\mathrm{miss}}$ and $\sum E_{\mathrm{T}}$ reconstruction from detector input (Feature Extraction or FEX algorithms) or specify the selections which define the various $E_{\mathrm{T}}^{\mathrm{miss}}$ or $\sum E_{\mathrm{T}}$ trigger chains included in the trigger menu (hypothesis algorithms). Because $E_{\mathrm{T}}^{\mathrm{miss}}$ and $\sum E_{\mathrm{T}}$ are global quantities, they only need to be computed once per event. This makes it possible to design many different hypothesis testing algorithms, for very specific physics needs, without noticeably increasing the execution time which is one of the major constraints at trigger level.

At L2, the FEX algorithm simply retrieves the L1 result and refines it by applying a correction taking into account the muons reconstructed at L2. At EF, contributions from both calorimeters and muon spectrometers are recomputed using the full granularity of the detectors. The 3D missing momentum vector is computed, although only its transverse projection is used to select events. In order to reduce the electronic noise contribution and therefore improve the resolution of the $E_{\mathrm{T}}^{\mathrm{miss}}$ measurement, only positive energy calorimeter cells above $3\sigma_{noise}$ are considered in the $E_{\mathrm{T}}^{\mathrm{miss}}$ and $\sum E_{\mathrm{T}}$ reconstruction. This one-sided noise cut causes a shift in the $\sum E_{\mathrm{T}}$ measurement which can be somewhat accounted for by a similar shift in the $\sum E_{\mathrm{T}}$ thresholds defining the trigger chains. This resolution can be further improved by the application of a simple cell-based calibration, optimised to reproduce the offline calibrated MET and $\sum E_{\mathrm{T}}$ measurements.

4.3.2 Performance of the $E_{\mathrm{T}}^{\mathrm{miss}}$ trigger with 7 TeV collision data

The performance of the $E_{\mathrm{T}}^{\mathrm{miss}}$ trigger has been evaluated both on 900 GeV collision data [87] and on 7 TeV data [86].

Figure 4.5(a) shows the correlation between L1 and offline $E_{\mathrm{T}}^{\mathrm{miss}}$. The L1 to offline correlation is not linear. This is because L1 is still using conservative commissioning-phase values, and future modifications of these settings are expected to improve L1 $E_{\mathrm{T}}^{\mathrm{miss}}$. For this reason, all current trigger chains based on $E_{\mathrm{T}}^{\mathrm{miss}}$ or $\sum E_{\mathrm{T}}$ start with a rather low L1 threshold compared to the EF threshold.

Figure 4.5(b) compares EF and offline $E_{\mathrm{T}}^{\mathrm{miss}}$. A clear linear relationship can be seen between trigger level and reconstructed offline quantities. This indicates that the selections operated by the EF $E_{\mathrm{T}}^{\mathrm{miss}}$ and $\sum E_{\mathrm{T}}$ algorithms don't significantly bias offline $E_{\mathrm{T}}^{\mathrm{miss}}$ and $\sum E_{\mathrm{T}}$ measurements and that such triggers will be highly efficient.

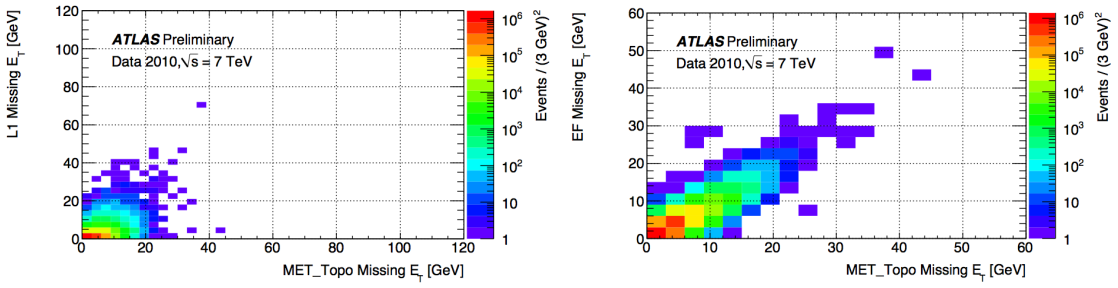

(a) (b)

Figure 4.5: (a) Correlation between $E_{\mathrm{T}}^{\mathrm{miss}}$ measured by the L1 trigger level and by the offline reconstruction, using topological clusters for collision candidates. (a) Correlation between $E_{\mathrm{T}}^{\mathrm{miss}}$ measured by the EF trigger level and by the offline reconstruction, using topological clusters for collision candidates.[86]

4.3.3 $E_{\mathrm{T}}^{\mathrm{miss}}$ triggers for $W \to \tau_{\mathrm{h}}\nu_{\tau}$ analysis

As it will be shown in the following, for the $W \to \tau_{\mathrm{h}}\nu_{\tau}$ decay observation, three simple $E_{\mathrm{T}}^{\mathrm{miss}}$ triggers were taken into account: xe15_noMu, EFxe15_noMu and EFxe12_noMu.

The notation *xe* followed by a number indicates the $E_{\mathrm{T}}^{\mathrm{miss}}$ trigger threshold. If an *EF* prefix is used, the $E_{\mathrm{T}}^{\mathrm{miss}}$ trigger has a very low threshold at L1 and a tight cut is only applied at the EF, with a resolution comparable to the offline reconstruction. If the prefix *EF* is missing, different $E_{\mathrm{T}}^{\mathrm{miss}}$ requirements are applied at all the three levels of the trigger. Finally, the *_noMu* suffix indicates that there were no muon corrections applied at the HLT for the $E_{\mathrm{T}}^{\mathrm{miss}}$ calculation. In this situation $E_{\mathrm{T}}^{\mathrm{miss}}$ is computed only using its calorimeter term. The absence of muon corrections at the trigger level has no effect on the analysis presented in Chapter 5, as the event selection foresees an explicit veto of events with reconstructed muons.

In Figure 4.6 the turn-on curves for the three simple $E_{\mathrm{T}}^{\mathrm{miss}}$ triggers at the three trigger levels are shown. The turn-on curves are plotted as a function of $E_{\mathrm{T}}^{\mathrm{miss}}$. The efficiency is calculated respect to the $W \to \tau_{\mathrm{h}}\nu_{\tau}$ Monte Carlo events that pass the offline selection described in Section 5.4, only the requirement on $E_{\mathrm{T}}^{\mathrm{miss}}$ is dropped, to show the full turn-on curve.

The trigger xe15_noMu requires 10 GeV of $E_{\mathrm{T}}^{\mathrm{miss}}$ at L1, 12 GeV L2 and 15 GeV at EF, as shown in the trigger chain summary presented in Table 4.2. The turn-on curve for such a trigger is very slow and the trigger reaches the efficiency plateau at $E_{\mathrm{T}}^{\mathrm{miss}} > 35$ GeV. This is due to the limited resolution on $E_{\mathrm{T}}^{\mathrm{miss}}$ at L1. The other two triggers do not have requirements at L1. At L2 the requirement on $E_{\mathrm{T}}^{\mathrm{miss}}$ both for EFxe15_noMu

and EFxe12_noMu is very low (5 GeV) and does not affect very much efficiency, while for xe15_noMu the request of having $E_{\mathrm{T}}^{\mathrm{miss}} > 12$ GeV again reduces the efficiency of this trigger. Finally, at EF EFxe12_noMu shows the higher efficiency, as it has the lower threshold. Nevertheless EFxe15_noMu is also fully efficient for the range of $E_{\mathrm{T}}^{\mathrm{miss}} > 30$ GeV that will be considered in $W \to \tau_{\mathrm{h}}\nu_{\tau}$ decay analysis.

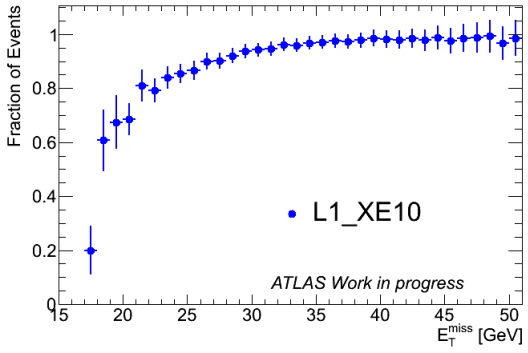

(a)

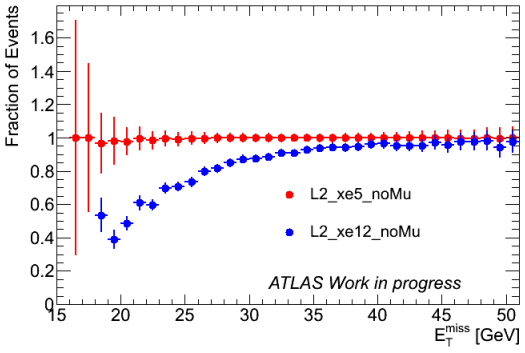

(b)

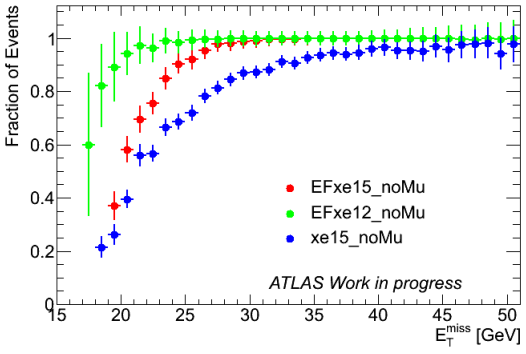

(c)

Figure 4.6: Turn-on for the simple $E_{\mathrm{T}}^{\mathrm{miss}}$ triggers as a function of $E_{\mathrm{T}}^{\mathrm{miss}}$ reconstructed offline, for the three different trigger levels. The efficiency is computed for $W \to \tau_{\mathrm{h}}\nu_{\tau}$ Monte Carlo events which satisfy the offline selection reported in Section 5.4, except the cut on $E_{\mathrm{T}}^{\mathrm{miss}}$ itself.

4.4 Combined tau triggers

Since τ triggers are basically trigger on jets, their rate is too high but for the lowest luminosity. They are therefore usually combined with other signatures. The following triggers are currently implemented in the ATLAS trigger menu, in addition to the single tau triggers already introduced:

tau+missing E_{T} This type of trigger covers a wide spectrum of physics channels. At low luminosity, when low thresholds can be maintained, this trigger is used for the selection of $W \to \tau_{\mathrm{h}}\nu_\tau$ events. Also $t\bar{t}$ events with tau leptons in the final state are selected by this trigger. The tau+$E_{\mathrm{T}}^{\mathrm{miss}}$ triggers at design luminosity are intended for SM or SUSY Higgs (neutral or charged) searches as well as for searches of new exotic particles like Z'. In the following some more details about this trigger will be given.

tau+ℓ, $\ell = e, \mu$ This type of trigger aims at selecting events with two tau leptons in the final state, like in the decays of Z boson, neutral SM or SUSY Higgs in tau pairs. In such a situation the leptonic decay of one τ and the hadronic decay of the other provide a good compromise between efficiency and background rejection. In addition, the tau+ℓ combination selects events with multiple leptons like $t\bar{t}$ or lepton flavour violating processes.

tau+tau This type of trigger records events where both tau leptons decay hadronically. While the rejection rate is less favourable than the tau+ℓ case, the sample collected is complementary to the above and both increases statistics and allows the reduction of systematic uncertainties due to lepton identification. This trigger is highly relevant for searches of Higgs boson or new exotic particles like Z'.

4.4.1 τ_{h} +$E_{\mathrm{T}}^{\mathrm{miss}}$ trigger signatures for $W \to \tau_{\mathrm{h}}\nu_\tau$ analysis

As already mentioned in the introduction, the trigger that has been selected for the $W \to \tau_{\mathrm{h}}\nu_\tau$ decay observation is a combined trigger of τ_{h} and $E_{\mathrm{T}}^{\mathrm{miss}}$. The available combined triggers are:

- EF_tauNoCut_hasTrk6_EFxe15_noMu
- EF_tau12_loose_EFxe12_noMu
- EF_tau12_loose_xe15_noMu

In the trigger definition, the first three symbols represent the τ_{h} signature described above, while the second part of the name refers to the $E_{\mathrm{T}}^{\mathrm{miss}}$ trigger.

In Table 4.2 the full trigger chain for these combined triggers is reported. As it can be seen, the three triggers have the same requirement for τ_{h} at L1, while they differ for the selection at HLT.

Figure 4.7 shows the fraction of events passing the three triggers taken into account. The turn-on curves are shown as a function of the offline reconstructed $E_{\mathrm{T}}^{\mathrm{miss}}$ and τ_{h} E_{T} . The efficiency is computed on simulated $W \to \tau_{\mathrm{h}}\nu_\tau$ event passing the selection that will be described in Section 5.4, except the selection on $E_{\mathrm{T}}^{\mathrm{miss}}$ for Figure 4.7(a) or the selection on the τ_{h} E_{T} for Figure 4.7(b). The chosen trigger reaches the plateau efficiency at $E_{\mathrm{T}}^{\mathrm{miss}} > 30$ GeV and $E_{\mathrm{T}}(\tau_{\mathrm{h}}) > 20$ GeV, being basically fully efficient on the events selected by the analysis.

		EF_tauNoCut_hasTrk6 _EFxe15_noMu	EF_tau12_loose _EFxe12_noMu	EF_tau12_loose _xe15_noMu
Tau requirement	L1	L1_TAU5	L1_TAU5	L1_TAU5
	L2	tauNoCut_hasTrk6	L2_tau12_loose	L2_tau12_loose
	EF	-	EF_tau12_loose	EF_tau12_loose
$E_{\mathrm{T}}^{\mathrm{miss}}$ requirement	L1	-	-	L1_XE10
	L2	L2_xe5	L2_xe5	L2_xe12
	EF	EF_xe15	EF_xe12	EF_xe15

Table 4.2: Full trigger chain description for some combined τ_{h} +$E_{\mathrm{T}}^{\mathrm{miss}}$ triggers.

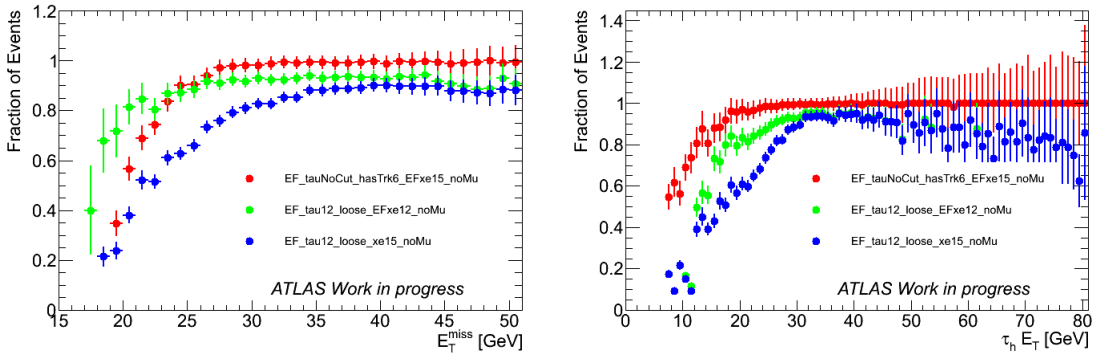

(a) (b)

Figure 4.7: Fraction of events passing the EF trigger as a function of (a) $E_{\mathrm{T}}^{\mathrm{miss}}$ and (b) τ_{h} E_{T} , for the three trigger presented in Section 5.3. Only events satisfying the offline selection described in Section 5.4 are considered. To show the turn-on curve full shape, the selection on $E_{\mathrm{T}}^{\mathrm{miss}}$ in (a) and the selection on τ_{h} p_{T} in (b) has not been applied.

Chapter 5

$W \to \tau_{\mathrm{h}}\nu_\tau$ observation

In this chapter, the first observation at the ATLAS Experiment of hadronically decaying taus from $W \to \tau_{\mathrm{h}}\nu_\tau$ decays is described.

In Section 5.1 the signature of the $W \to \tau_{\mathrm{h}}\nu_\tau$ decay is explained and the main issues of the analysis are outlined. The samples used in this analysis, both data and Monte Carlo, are described in Section 5.2. Section 5.3 is devoted to the trigger and its efficiency. In Section 5.4 the event selection is described in detail. As in the data sample considered in the following the presence of pile-up is important, Section 5.5 shows the effects of pile-up on the selection and how it was treated. The background from QCD jets have been evaluated directly from data: the method is described in Section 5.6, along with all the cross checks performed. Finally, the studies about the systematic uncertainties are reported in Section 5.7.

In the following $W^+ \to \tau_{\mathrm{h}}^+\nu_\tau$ decay (and charge conjugated $W^- \to \tau_{\mathrm{h}}^-\bar{\nu}_\tau$) will be indicated simply as $W \to \tau_{\mathrm{h}}\nu_\tau$, as well as $W \to e\nu_e$, $W \to \mu\nu_\mu$. $Z \to e^+e^-$, $Z \to \mu^+\mu^-$ and $Z \to \tau^+\tau^-$ will be indicated as $Z \to ee$, $Z \to \mu\mu$ and $Z \to \tau\tau$.

5.1 Introduction

For pp collisions at a centre-of-mass energy of 7 TeV, the $W \to \tau\nu_\tau$ signal is predicted to be produced with a cross section times branching ratio of $\sigma \times \mathrm{BR} = 10.46 \pm 0.52\,\mathrm{nb}$ at NNLO (with $\sigma^{\mathrm{NNLO}}_{\mathrm{W}^+\to\ell^+\nu} = 6.16 \pm 0.31\mathrm{nb}$, $\sigma^{\mathrm{NNLO}}_{\mathrm{W}^-\to\ell^-\nu} = 4.30 \pm 0.21\mathrm{nb}$). This predictions were calculated using the programs FEWZ [88] and ZWPROD [89, 90] with the MSTW 08 NNLO structure function parametrisation [24].This value is in good agreement with ATLAS measurement [19].

Since purely leptonic τ decays (τ_ℓ in the following) cannot be easily distinguished from electrons and muons from $W \to e\nu_e$ or $W \to \mu\nu_\mu$ decays, the analysis presented in this thesis uses only hadronically decaying τ leptons (τ_{h} in the following).

The signature of this process is the presence of a narrow hadronic jet (τ-jet) and missing transverse energy. $W \to \tau_{\mathrm{h}}\nu_\tau$ decays are dominated by events with relatively low-p_{T} W bosons producing τ leptons for which the typical visible transverse momentum of the final state is between 10 and 40 GeV (Figure 5.1(a)), where the visible transverse momentum is defined as the magnitude of the vectorial sum of the transverse momentum of the τ_{h} decay products except the neutrinos. In addition, the distribution of the missing transverse energy, associated with the neutrinos from the W and τ_{h} decays, has a maximum around 15 GeV and a significant tail up to about 80 GeV (Figure 5.1(b)).

The main backgrounds to this channel are QCD multi-jet production along with W and Z leptonic decays.

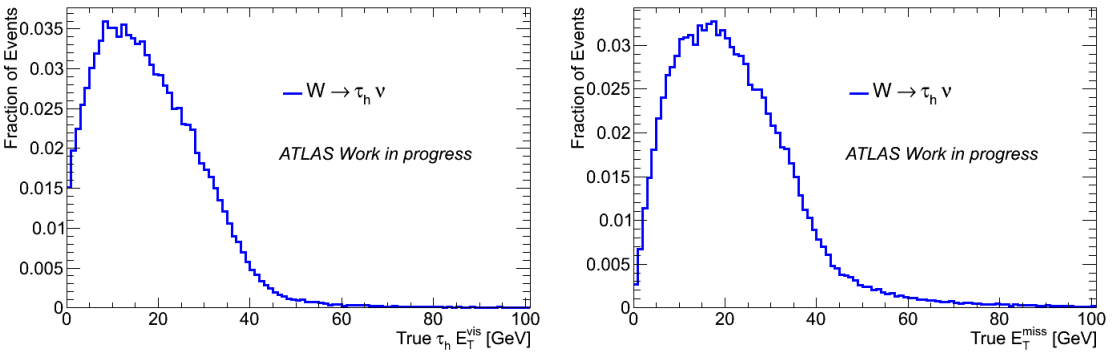

(a) (b)

Figure 5.1: Generator-level (a) visible transverse energy of hadronically decaying τ leptons and (b) missing transverse energy for $W \to \tau\nu_\tau$ events.

- QCD multi-jet events
  Misreconstructed QCD events where one jet is incorrectly identified as a hadronically decaying τ lepton and a significant amount of missing transverse energy is also misreconstructed constitute the dominant background source. Therefore, a good understanding and effective suppression of these processes is critical for the analysis. The cross section is several orders of magnitude larger than the signal cross section and it is affected by large uncertainties. Furthermore, the available simulated sample are not sufficienct to give a good estimate of this background. Therefore, a method to extract the amount of this background directly from data has been developed and it is discussed in Section 5.6.

- $W \to e\nu/\mu\nu$
  These processes contribute to the background if the lepton from the W boson decay is identified as a single-prong hadronically decaying τ lepton or if a fake τ_{h} candidate is reconstructed from a jet in the event. The first case is strongly suppressed by vetoing candidates tagged by an electron veto algorithm (see Section 2.4) and the second by requiring that no reconstructed electrons and muons are present in the event. The remaining small fraction of events for which the electron/muon is lost contributes with fake τ_{h} candidates from background jets.

  Figure 5.2 shown the ΔR separation between the τ_{h} candidate and the true and the reconstructed electron/muon. For $W \to \mu\nu_\mu$ events usually the tau is reconstructed from a jet in the event, while for $W \to e\nu_e$ events the fake τ_{h} comes from the electron.

- $W \to \tau\nu \to e\nu/\mu\nu$
  Leptonic decay modes of τ leptons are difficult to distinguish from primary electrons and muons. Therefore, this process contributes to the background and they are rjected similarly to $W \to e\nu_e$ and $W \to \mu\nu_\mu$.

- $Z \to ee/\mu\mu$
  Leptonic Z boson decays contribute if one of the decay electrons/muons is incorrectly reconstructed as a hadronically decaying τ lepton and the other one is lost, giving fake $E_{\mathrm{T}}^{\mathrm{miss}}$. As already discussed for the $W \to e\nu/\mu\nu$ processes, this background is strongly suppressed by explicitly vetoing single-prong electron-like τ_{h} candidates and

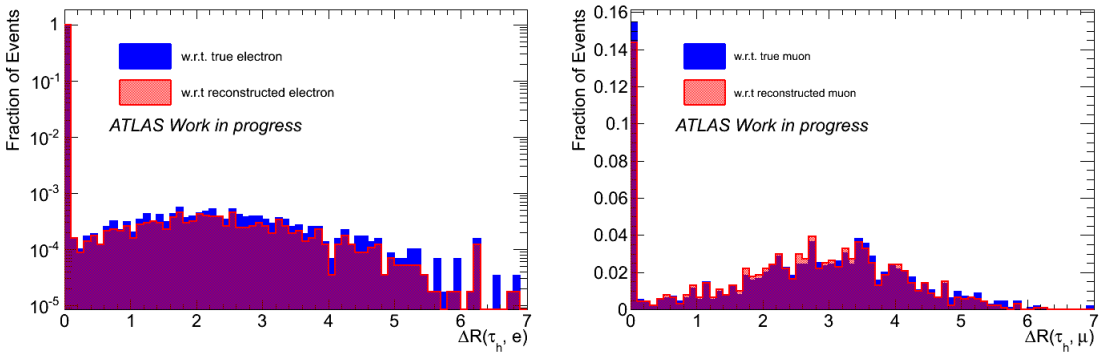

(a) (b)

Figure 5.2: ΔR separation between the τ_{h} candidate and the true or the reconstructed (a) electron in $W \to e\nu_e$ simulated events and (b) muon in $W \to \mu\nu_\mu$ simulated events. Monte Carlo generated without pile-up were used. Notice the different vertical scales.

by rejecting events with identified electrons and muons. As it will be shown in the following, these backgrounds are found to be negligible.

- $Z \to \tau\tau$
  The rate for this process is about ten times smaller than for the signal process. It contributes to the background if one of the τ leptons is identified as a hadronically decaying τ lepton.

- $t\bar{t}$
  Top quarks decay with 100% branching ratio in Wb. This process has a much smaller cross section than the signal process and contributes to the background if one of the Ws produces a τ lepton in its decay and the other one decays into a pair of quarks, an electron, or a muon which are not reconstructed. Fully hadronic decays can also contribute to the fake τ_{h} identification. As it will be shown in the following, also this background is found to be negligible.

In the following the background processes consisting of W and Z decays will be collectively named Electro-weak (EW) background.

5.1.1 Previous studies and real data analysis

The analysis presented in the following is based on the ones developed in previous studies on simulated data at different centre-of-mass energies, both at 14 TeV [91] and at 10 TeV [92]. When the LHC plans became clear and it was stated the energy of the collisions for the year 2010 would have been 7 TeV, the analysis was reoptimised for that centre-of-mass energy.

As data finally arrived, the analysis needed to be deeply revised as many of the assumptions on which it was based were not valid any more. Here the main aspects of the analysis are reported.

One of the main differences with respect to what had been foreseen is the LHC instantaneous luminosity. It was planned that the profile of the luminosity would have increased quite slowly, to allow the commissioning of the machine. In this schedule approximately 100 pb^{-1} would have been collected at a instantaneous luminosity of 10^{31} cm^{-2}s^{-1}. The

reality turned out to be quite different, as so far 45 pb^{-1} have been collected reaching a luminosity already higher than 10^{32} cm^{-2}s^{-1}. This fact has many effects on the analysis. First of all τ_{h} triggers, which are used in combination with $E_{\mathrm{T}}^{\mathrm{miss}}$ triggers to select the events, can be inserted in the trigger menu at high luminosity (already at 10^{32} cm^{-2}s^{-1}) just with very high thresholds and with big prescale factors. The trigger used in the analysis of this thesis has instead a very low threshold, to be fully efficient in the range of E_{T} considered (20–60 GeV). Such a trigger was already prescaled at a luminosity of 10^{31} cm^{-2}s^{-1} and the integrated luminosity it collected is about 2.5 pb^{-1}.

Another important aspect, still connected with luminosity, is the amount of pile-up events. The increase of luminosity was achieved also by increasing the number of protons in the bunches and by squeezing them. This increases the number of interactions per bunch crossing. In previous analysis pile-up effect were not taken deeply into consideration as, with a lower instantaneous luminosity, those effects were supposed to be negligible. But it turned out that the pile-up level in data is important: in particular, as explained in the following, some quantities used to select events are affected by pile-up and the selection efficiency therefore changes when instantaneous luminosity (and therefore pile-up level) increases.

The other main difference with respect to older analyses is that the τ_{h} identification that has been validated for first data analysis by the ATLAS Tau working group (described in Chapeter 2) is cut based and does not use multivariate techniques. The fake rate, even for a tight identification, is 1.6% (see Table 2.2). Therefore the τ_{h} identification alone is not enough to discriminate the signal from the QCD background. To reduce the background from those events, different approaches were tried. One consists in increasing the cut on $E_{\mathrm{T}}^{\mathrm{miss}}$: in this way the QCD background can be suppressed but the signal loss is also very important, as cutting at 30 GeV (as done in the analysis) already selects a tail of the distribution (Figure 5.1(b)). Another approach can be to select events with a high value of $\sum p_{\mathrm{T}}(\mathrm{jet})$: QCD events are peaked at lower values than the $W \to \tau_{\mathrm{h}}\nu_\tau$ signal. Also this cut was not enough effective to efficiently reduce the background. The requirement that turned out to be the best discriminator is a cut on the significance of $E_{\mathrm{T}}^{\mathrm{miss}}$, which is basically the ratio between $E_{\mathrm{T}}^{\mathrm{miss}}$ and its resolution.

All the details of the events selection for the analysis of 7 TeV data are described in Section 5.4. Even if the analysis needed to be revised and adjusted to match the new data situation, and although previous studies were counting on a higher statistics to claim for $W \to \tau_{\mathrm{h}}\nu_\tau$ decays observation, the measurement turned out to be feasible already with very few pb^{-1} of integrated luminosity.

5.2 Data sample

The analysis for the $W \to \tau_{\mathrm{h}}\nu_\tau$ observation has been performed on data collected between 30 March and 30 August 2010 by the ATLAS Experiment in proton-proton collisions at a centre-of-mass energy of 7 TeV.

Only data taken during periods with stable beams and with a good data quality for all the tracking and calorimeter sub-detectors are used. With these basic data quality criteria, described in detail in Section 5.2.1, the total integrated luminosity available for the analysis amounts to 2.46 ± 0.27 pb^{-1}.

Events are selected using all three ATLAS trigger levels (described in Chapter 4). The trigger requirements are based on the presence of a τ_{h} jet and $E_{\mathrm{T}}^{\mathrm{miss}}$ as main signatures of the $W \to \tau_{\mathrm{h}}\nu_\tau$ decay.

- The L1 trigger selects narrow clusters of trigger towers with a p_{T} threshold of 5 GeV.
- With the L2 trigger, tracks are reconstructed around the L1 candidate. The event is accepted if there is at least one track with $p_{\mathrm{T}} > 6$ GeV and $E_{\mathrm{T}}^{\mathrm{miss}}$ above 5 GeV.
- A full event reconstruction is performed at the EF level and the events are required to have $E_{\mathrm{T}}^{\mathrm{miss}} > 15$ GeV.

This trigger requirement has an efficiency of $99.2 \pm 0.1\%$, computed from Monte Carlo simulation, to select $W \to \tau_{\mathrm{h}}\nu_\tau$ events satisfying the selection criteria described in Section 5.4. A full description of the trigger and of its efficiency is reported in Chapter 4 and in Section 5.3.

The results from data presented here are compared to expectations based on Monte Carlo simulations. All references about Monte Carlo samples are collected in Section 5.2.2.

5.2.1 Data

Data samples

The data considered in this analysis is the data collected by the ATLAS Experiment during LHC collisions at a centre-of-mass energy of 7 TeV. The period of time considered goes from the end of March 2010, when the first collisions at 7 TeV were registered, to the end of August 2010. This data taking period was chosen to be able to use the same trigger during the whole period. In September the trigger used in this analysis was removed from the trigger menu.

In these first 6 months of collisions, the machine underwent an intense commissioning phase, so the running conditions changed significantly during this period. During the first run considered (run 152166, 30 March 2010) the peak luminosity that was reached was about 1.1 10^{27} $\mathrm{cm}^{-2}\mathrm{s}^{-1}$, with just one bunch circulating in the machine. The last run (run 162882, 30 August 2010) saw a peak luminosity of 9.9 10^{30} $\mathrm{cm}^{-2}\mathrm{s}^{-1}$ with 35 colliding bunches. So, during the considered data taking period, the instantaneous luminosity increased of approximately 4 order of magnitude.

The higher luminosity was achieved both by increasing the intensity and the number of the bunches, and by sqeezing the beams decreasing the $\beta^\star$ parameter (down to $\beta^\star = 2$ m). The increase in the number of protons in a bunch causes an increase of the number of interactions per bunch crossing, i.e. the number of in-time pile-up events. This fact has an important impact on the present analysis, as some reconstructed quantities used to discriminate the signal from the background are affected by pile-up. When comparing data to Monte Carlo simulations, pile-up effects have been taken into account and a description of the procedure is reported in Section 5.5.

Data streams and formats

The so-called "L1Calo" stream has been used (Section 1.5.3). This stream contains events which have fired at least one L1 calorimeter trigger, either electromagnetic or hadronic.

The data used data format is a flat ntuple (D3PDs, see Section 1.5.3) produced by the ATLAS Tau working group.

When the ntuple is produced, the events are preskimmed with the "OR" of different filters: the event must have $E_{\mathrm{T}}^{\mathrm{miss}} > 25$ GeV or at least one reconstructed τ_{h} with a minimum E_{T} of 25 GeV and satisfying different cuts on shape variables or they must have fired a tau trigger. The amount of events passing this preskimming is referred to as the

events in the first line of Table 5.4. This preskimming is not applied instead to Monte Carlo samples.

To simplify the selection, and to obtain a common starting point for data and simulated samples, the events considered are further skimmed (second line of Table 5.4) with a selection on $E_{\mathrm{T}}^{\mathrm{miss}} > 25$ GeV, considering $E_{\mathrm{T}}^{\mathrm{miss}}$ reconstructed only with the calorimeter contribution and calibrated with the Local Hadron calibration scheme (see Section 3).

Data quality requirements

Only data with good data quality is used for this analysis. The data quality selection is based on a combined Good Run List (GRL, see Section 1.5.3). These are the data quality requirements used in the analysis.

- The first main requirement is that events were collected while the LHC beams had been declared stable by the machine operators and ATLAS was ready to take data.
- The other main requirement is that data has been declared to be good from the point of view of τ_{h} reconstruction data quality.
- The last requirement is that also the data quality concerning the reconstruction of $E_{\mathrm{T}}^{\mathrm{miss}}$ is good. As in the analysis the muon contribution to $E_{\mathrm{T}}^{\mathrm{miss}}$ is not considered (see Section 3), for the data quality requirements only the calorimeter contributions are taken into account.

5.2.2 Monte Carlo

The Monte Carlo samples of signal and backgrounds (already described in Section 5.1) were generated at $\sqrt{s} = 7$ TeV with PYTHIA [93] and passed through a GEANT4 [94] simulation of the ATLAS detector [95]. The only exception is the $t\bar{t}$ background, which was generated using MC@NLO [96].

To take into account the presence of pile-up in data, the Monte Carlo samples were produced including effects of multiple interactions. The treatment of pile-up is explained later in Section 5.5.

When comparing distributions, such as $\sum E_{\mathrm{T}}$, it was found that the agreement between data and Monte Carlo expectations was not good. Deep investigations of the discrepancies brought to think that the source of the discrepancy was a bad description of the soft jet activity. Therefore data was compared to Monte Carlo samples with other underlying event descriptions, different from the default one, which is ATLAS MC09 [68]. From these studies [69], it has been shown that the DW tune [70] of Pythia, which uses virtuality-ordered showers and was derived to describe the CDF II underlying event and Drell-Yan data, models the forward activity of the underlying event better than the MC09 tune. Samples with DW tune were therefore used to assess some systematic uncertainties.

Table 5.1 shows the Monte Carlo datasets used in this analysis.

Monte Carlo dataset ID	Description	Generator	Tuning	Pile-up (average number of secondary vtx)	Simulation tag	Events	Cross Sec. (nb)	Note
107054	$W \to \tau\nu_\tau$	Pythia	MC09	$< 2 >$	e514_s765_s767_r1430_r1429	150 K	10.46	inclusive
106043	$W \to e\nu_e$	Pythia	MC09	$< 2 >$	e468_s765_s767_r1388_r1389	700 K	10.46	
106044	$W \to \mu\nu_\mu$	Pythia	MC09	$< 2 >$	e468_s765_s767_r1388_r1389	1 M	10.46	
106046	$Z \to ee$	Pythia	MC09	$< 2 >$	e468_s765_s767_r1388_r1389	1 M	0.99	
106047	$Z \to \mu\mu$	Pythia	MC09	$< 2 >$	e468_s765_s767_r1388_r1389	1 M	0.99	
106052	$Z \to \tau\tau$	Pythia	MC09	$< 2 >$	e468_s765_s767_r1430_r1429	100 K	0.99	
106023	$W \to \tau_{\mathrm{h}}\nu_\tau$	Pythia	MC09	no pile-up	e468_s765_s767_r1302	100 K	10.46	hadronic decay
106022	$W \to \tau_\ell\nu_\tau$	Pythia	MC09	no pile-up	e468_s765_s767_r1302	100 K	10.46	leptonic decay
106043	$W \to e\nu_e$	Pythia	MC09	no pile-up	e468_s765_s767_r1302	700 K	10.46	
106044	$W \to \mu\nu_\mu$	Pythia	MC09	no pile-up	e468_s765_s767_r1302	700 K	10.46	
106052	$Z \to \tau\tau$	Pythia	MC09	no pile-up	e468_s765_s767_r1302	200 K	0.99	
105200	$t\bar{t}$	MC@NLO	MC09	no pile-up	e510_s765_s767_r1302_r1306	1 M	0.144	semi-/leptonic decay
105204	$t\bar{t}$	MC@NLO	MC09	no pile-up	e540_s765_s767_r1302_r1306	150 K	0.144	hadronic decay
107414	$W \to \tau\nu_\tau$	Pythia	DW	no pile-up	e579_s766_s767_r1303_r1306	400 K	10.46	inclusive
107413	$Z \to \tau\tau$	Pythia	DW	no pile-up	e579_s766_s767_r1303_r1306	500 K	0.99	

Table 5.1: Monte Carlo samples used in the analysis.

5.3 Trigger

The main characteristics of $W \to \tau_{\mathrm{h}}\nu_\tau$ events are the hadronically decaying τ lepton and sizable $E_{\mathrm{T}}^{\mathrm{miss}}$. These signatures are used at the trigger level to select data samples enriched with signal events.

Different combined τ_{h} and $E_{\mathrm{T}}^{\mathrm{miss}}$ trigger items were actively selecting $W \to \tau_{\mathrm{h}}\nu_\tau$ events during the whole data-taking period (already illustrated in Chapter 4):

- EF_tauNoCut_hasTrk6_EFxe15_noMu
- EF_tau12_loose_EFxe12_noMu
- EF_tau12_loose_xe15_noMu

The EF_tauNoCut_hasTrk6_EFxe15_noMu trigger item has been chosen for the analysis presented here, as the best compromise between active time and trigger efficiency, which are summarised in Table 5.2.

Comparing the integrated luminosity collected by the three triggers (reported in Table 5.2, scaled for the prescale factors applied during the runs), EF_tau12_loose_EFxe12_noMu resulted to be the one which was more heavily prescaled.

The signal selection efficiency for EF_tauNoCut_hasTrk6_EFxe15_noMu is much higher than the one of EF_tau12_loose_xe15_noMu. So, for EF_tauNoCut_hasTrk6_EFxe15_noMu a higher prescale factor is compensated by higher selection efficiency. The lower selection efficiency of EF_tau12_loose_xe15_noMu is both due to the lower efficiency of the tau trigger part and to the slow turn-on curve of the $E_{\mathrm{T}}^{\mathrm{miss}}$ trigger (shown in Figure 4.6), connected with the low resolution of $E_{\mathrm{T}}^{\mathrm{miss}}$ trigger at the first two trigger levels. A determination of the efficiency of the three triggers is presented in the following of this section.

In the offline analysis, the EF_tauNoCut_hasTrk6_EFxe15_noMu requirements were also applied to early data, which were actually selected with the L1 trigger only, as the HLT was not active. The integrated luminosity relative to this period is negligible respect to the full sample, so any possible bias is small.

Trigger efficiency At this early stage of ATLAS's operation, a suitable event sample with τ_{h} and $E_{\mathrm{T}}^{\mathrm{miss}}$ selected by a trigger that is independent from the one used in this analysis is not yet available. The trigger selection has therefore been evaluated based on Monte Carlo simulations. The efficiencies of selecting the signal events using the three triggers are summarized in Table 5.2.

The turn-on curves for the three triggers as a function of $E_{\mathrm{T}}^{\mathrm{miss}}$ and τ_{h} E_{T} have been reported in Chapter 4 in Figure 4.7. From those distributions it can be seen that the chosen trigger reaches the plateau efficiency at $E_{\mathrm{T}}^{\mathrm{miss}} > 30$ GeV and $E_{\mathrm{T}}(\tau_{\mathrm{h}}) > 20$ GeV, being basically fully efficient on the events selected by the analysis.

Bias on the number of tacks spectrum Due to the very simple requirements of the tauNoCut_hasTrk6 trigger, it introduces less bias on the track multiplicity spectrum than the tau12_loose trigger (see Figure 5.3). In addition, it results in a smaller systematic uncertainty due to the fact that no selection based on the τ shower shape variables at the trigger level is performed. This makes the chosen trigger easier to understand and it reduces the releated systematic uncertainties.

	EF_tauNoCut_hasTrk6 _EFxe15_noMu	EF_tau12_loose _EFxe12_noMu	EF_tau12_loose _xe15_noMu
Efficiency			
L1	99.75±0.03	99.75±0.03	97.2±0.1
L2	99.59±0.04	93.7±0.2	91.0±0.2
EF	99.91±0.02	98.8±0.2	98.8±0.2
Overall	99.2±0.1	92.3±0.2	87.3±0.2
Integrated Luminosity			
PeriodA	0.4	0.4	0.4
PeriodB	8.2	8.2	8.2
PeriodC	8.5	8.5	8.5
PeriodD	291.2	291.2	291.2
PeriodE	1002.7	1002.7	1002.7
PeriodF	1148.1	689.5	1808.7
Total (nb^{-1})	2459.1	2000.5	3119.7

Table 5.2: Summary of trigger efficiency and collected luminosity. The L1 efficiency is computed with respect to all events satisfying the offline selection for $W \to \tau_{\mathrm{h}}\nu_\tau$ decays (see Section 5.4). The L2 and EF efficiencies are calculated with respect to events passing the preceding trigger level. The quoted uncertainties are statistical only. The integrated luminosity for each trigger is computed taking into account the prescaling factor.

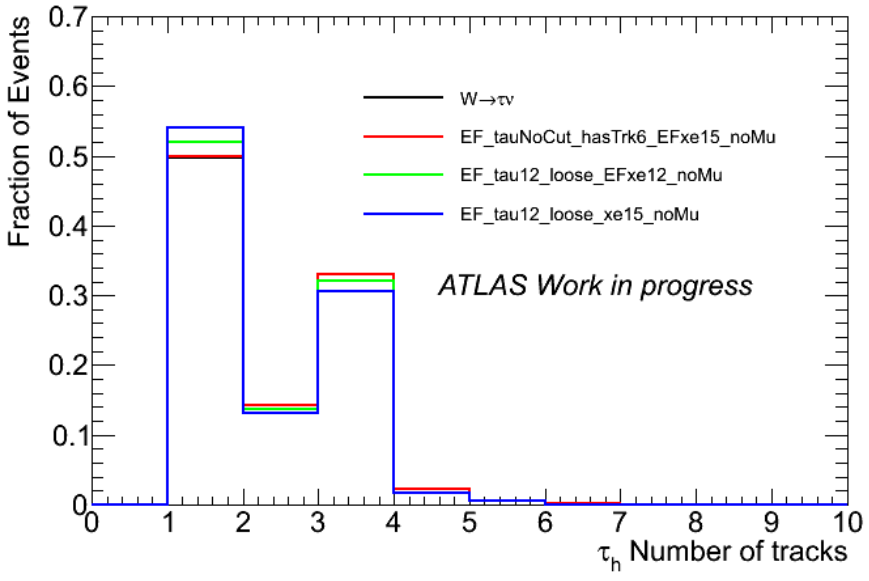

Figure 5.3: Distribution of the number of tracks for τ_{h} candidates satisfying the event selection explained in Section 5.4 for Monte Carlo signal events. The four distributions refer to events passing the selection without any requirement for the trigger and for events passing the event selection and three different trigger requirements.

Trigger matching In the analysis it is not required that the selected τ_{h} candidate is the object that actually fired the trigger.

The impact of trigger matching has been checked on the Monte Carlo simulated $W \to \tau_{\mathrm{h}}\nu_\tau$ sample without pile-up and it was found to reduce the signal selection efficiency by about 0.1%. The effect of trigger matching is therefore negligible for the determination of the trigger efficiency.

5.4 Event selection

In this section, the event selection that has been optimized to extract the signal from the background is described.

In addition to the selection of good data quality and the trigger requirements already outlined, further selection criteria are applied:

- events must pass an event cleaning which ensure that the reconstructed $E_{\mathrm{T}}^{\mathrm{miss}}$ comes from particles not detected and not from jet/$E_{\mathrm{T}}^{\mathrm{miss}}$ mismeasurements;
- the events are required to have the typical $W \to \tau_{\mathrm{h}}\nu_\tau$ signature;
- furthermore, events with electrons or muons are vetoed;
- finally, by means of a cut related to $E_{\mathrm{T}}^{\mathrm{miss}}$, the residual QCD background is rejected and the signal extracted.

These selections are described in detail below.

5.4.1 Jet/$E_{\mathrm{T}}^{\mathrm{miss}}$ mismeasurement cleaning

One of the most important variables to discriminate the signal from the background is the missing transverse energy. It is therefore important to reject events with misreconstructed or fake $E_{\mathrm{T}}^{\mathrm{miss}}$ (which is typical, for example, for QCD background events).

The rejection of events not coming from collisions and with misreconstructed $E_{\mathrm{T}}^{\mathrm{miss}}$ is based on four criteria.

Collision cleaning To ensure that at the event comes from a real collision, at least one primary vertex reconstructed with at least four tracks is required in the event. For events that pass the trigger, the impact of this cut is very small; anyhow it is an important sanity check.

Jet cleaning As it has been explained in the chapter concerning the reconstruction of $E_{\mathrm{T}}^{\mathrm{miss}}$ (Chapter 3), events with misreconstructed or "fake" jets produce tails in the distribution of missing transverse energy [75]. These jets arise from various sources, ranging from hardware problems, LHC beam conditions, and cosmic-ray showers and are flagged as bad quality during reconstruction.

In this analysis, if there is a jet affected by these problems, the whole event is rejected.

Jet in gap veto The ATLAS calorimeter has lower resolution in the transition region between the barrel and the end-cap calorimeters, at pseudorapidity $1.3 < |\eta| < 1.7$. If a jet is reconstructed in that region, the energy measurement is not reliable. This can reflect on a bad $E_{\mathrm{T}}^{\mathrm{miss}}$ reconstruction. For this reason events with a jet with $p_{\mathrm{T}} > 20$ GeV reconstructed in that pseudorapidity range are rejected.

QCD rejection In Figure 3.6 the minimum of the $\Delta\phi$ separation between jet and $E_{\mathrm{T}}^{\mathrm{miss}}$ is shown, both for Monte Carlo signal and for QCD background. For QCD jet events, usually there is one jet collinear with $E_{\mathrm{T}}^{\mathrm{miss}}$. This is due to a bad jet energy measurement, which determines fake $E_{\mathrm{T}}^{\mathrm{miss}}$ in the direction of the misreconstructed jet. To reject these events a cut on the minimum of $\Delta\phi$(jet,$E_{\mathrm{T}}^{\mathrm{miss}}$) < 0.5 rad, for jets with $p_{\mathrm{T}} > 20$ GeV is applied.

5.4.2 Eveng signature selection

After these event cleaning, the events are further required to have the typical $W \to \tau_{\mathrm{h}}\nu_\tau$ signature, i.e. missing energy due to the neutrinos that are not detected accompanied by a τ_{h} jet.

Missing transverse energy A missing transverse energy of $E_{\mathrm{T}}^{\mathrm{miss}} > 30$ GeV is required. Only the calorimetric $E_{\mathrm{T}}^{\mathrm{miss}}$ term is considered (Section 3.1). Moreover, $E_{\mathrm{T}}^{\mathrm{miss}}$ is calibrated with the local hadron calibration scheme LCW.

This requirement cuts on the tail of the $E_{\mathrm{T}}^{\mathrm{miss}}$ distribution (see Figure 5.1(b)). Since a $E_{\mathrm{T}}^{\mathrm{miss}}$ cut is already applied at the skimming and at the trigger level, the efficiency of this cut on Monte Carlo signal is about 72% respect events passing the previous cut. Its importance comes from the high rejection on QCD background events. In fact, at this stage of the cut-flow, events in data are dominated by QCD background jets and the efficiency of this cut on data is about 31%.

τ_{h} selection Candidates reconstructed by both τ_{h} reconstruction algorithms, the track-seeded and the calorimeter-seeded (Section 2.2), and identified as tight τ_{h} candidates (Section 2.3) are considered. The highest-p_{T} candidate of these is required to have a visible transverse momentum between 20 and 60 GeV. The event is rejected if the selected τ_{h} candidate is reconstructed in the pseudorapidity range $1.3 < |\eta| < 1.7$ which corresponds to the transition region in the calorimeter systems.

5.4.3 Lepton veto

As already mentioned in the introduction of the chapter, besides the QCD background, the other background sources to this analysis are $W \to e\nu_e$, $W \to \mu\nu_\mu$, $W \to \tau_\ell\nu_\tau$, $Z \to ee$, $Z \to \mu\mu$ and $Z \to \tau\tau$, referred to as electroweak (EW) background. The τ_{h} reconstructed is usually a fake, either coming from a misidentified electron or muon, either coming from a jet produced together with the W and Z.

To suppress EW background, different electron and muon vetoes are applied.

Electron vetoes First of all, an electron veto provided by the τ_{h}-ID algorithm (Section 2.4) is applied. This veto, based on shape variables, efficiently rejects events where an electron has faked a τ_{h}. This veto rejects 99% of the $W \to e\nu_e$ events which have survived the previous cuts and more than 99% of the $Z \to ee$ background.

To suppress events where the τ_{h} was reconstructed from a jet produced together with the W/Z bosons and the electron was correctly reconstructed, events with loose identified electrons [97], reconstructed by the Inner Detector and with $p_{\mathrm{T}} > 5$ GeV are rejected. This selection further suppresses $W \to e\nu_e$ background of 60%.

The events for which the τ_{h} is reconstructed from a jet in the event and the electron was lost, giving fake $E_{\mathrm{T}}^{\mathrm{miss}}$, remain as a background.

Muon veto For muon rejection, there is no explicit τ_{h}-ID veto, since they are already suppressed by the E_{T} selection, based on the calorimeter deposit. Therefore the rejection of EW background is based only on the rejection of events with combined muons [98] with $p_{\mathrm{T}} > 5$ GeV. The background from $W \to \mu\nu_\mu$ events is reduced of about 76% respect to the events passing the previous selection and the one from $Z \to \mu\mu$ of about 94%.

5.4.4 QCD background rejection

The current τ_{h}-ID has not enough rejection power against QCD events. Therefore a further selection is needed to achieve a good S/B ratio. In previous analysis based on Monte Carlo studies at 14 TeV [91] and 10 TeV [92] it was achieved by means of a tighter $E_{\mathrm{T}}^{\mathrm{miss}}$ cut and a selection on $\Delta\phi(\tau_{\mathrm{h}},E_{\mathrm{T}}^{\mathrm{miss}})$, but these criteria were not performant enough on early data. Therefore a rejection based on the significance of missing transverse energy has been introduced.

The significance of the missing transverse energy is defined as:

$$S_{E_{\mathrm{T}}^{\mathrm{miss}}} = \frac{E_{\mathrm{T}}^{\mathrm{miss}}[\mathrm{GeV}]}{0.5[\mathrm{GeV}^{1/2}]\sqrt{\sum E_T[\mathrm{GeV}]}}. \tag{5.1}$$

Events are rejected if $S_{E_{\mathrm{T}}^{\mathrm{miss}}} < 6$. This requirement effectively rejects QCD background, for which lower $S_{E_{\mathrm{T}}^{\mathrm{miss}}}$ values are expected than for $W \to \tau_{\mathrm{h}}\nu_\tau$ events. Figure 5.4 shows the two-dimensional distribution of $E_{\mathrm{T}}^{\mathrm{miss}}$ and $\sqrt{\sum E_{\mathrm{T}}}$ for signal and QCD background, together with the $S_{E_{\mathrm{T}}^{\mathrm{miss}}}$ requirement. The discriminating power of $S_{E_{\mathrm{T}}^{\mathrm{miss}}}$ is clearly visible.

In Figure 5.5 the rejection power of the cut on $S_{E_{\mathrm{T}}^{\mathrm{miss}}}$ is shown, separately for QCD events with different range of the transverse momentum of the outgoing partons in the rest frame of the hard interaction. From these figures, it is clear that the $S_{E_{\mathrm{T}}^{\mathrm{miss}}}$ cut is needed to reject QCD jet with low p_{T} , which are the most abundant. The $S_{E_{\mathrm{T}}^{\mathrm{miss}}}$ cut is also more effective than a simple $E_{\mathrm{T}}^{\mathrm{miss}}$ cut on high p_{T} QCD jets.

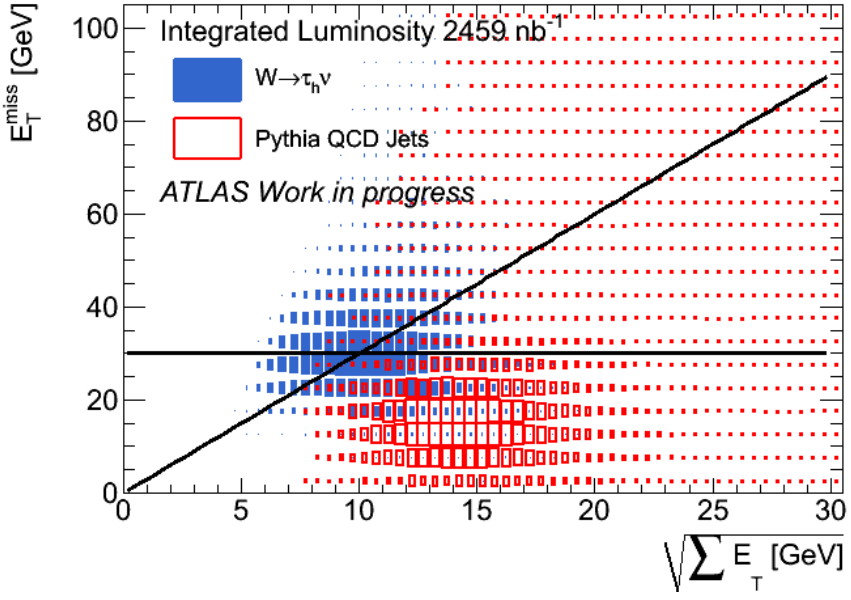

Figure 5.4: Distribution of events in the $E_{\mathrm{T}}^{\mathrm{miss}}$–$\sqrt{\sum E_{\mathrm{T}}}$ plane after the trigger requirement for simulated signal events and QCD background. The applied $E_{\mathrm{T}}^{\mathrm{miss}}$ and $S_{E_{\mathrm{T}}^{\mathrm{miss}}}$ criteria are indicated as solid lines.

5.4.5 Results

The selection just described has an efficiency of 1.24% on the signal and of 0.07% on the EW backgrounds.

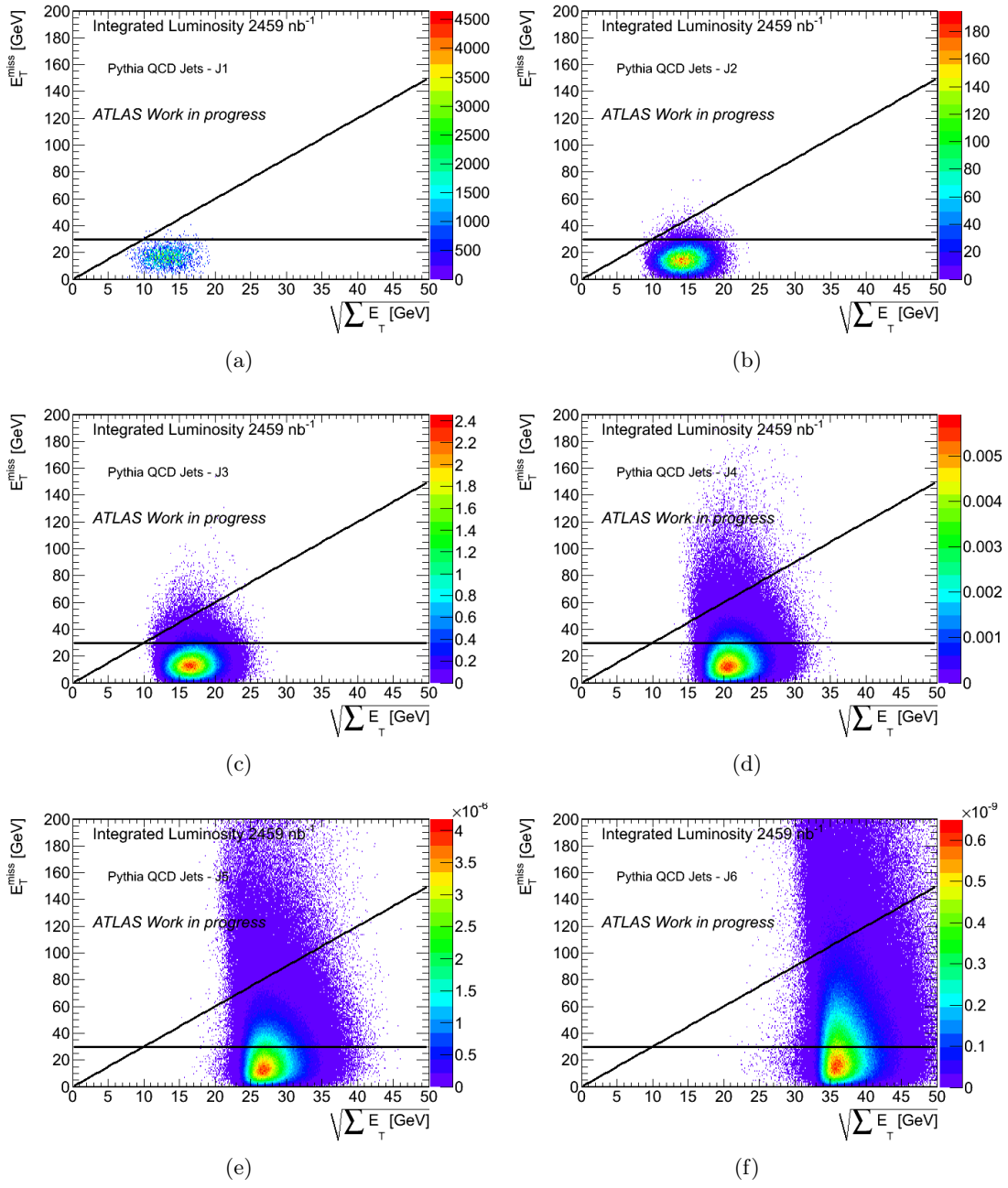

Figure 5.5: Distribution of events in the $E_{\mathrm{T}}^{\mathrm{miss}}$–$\sqrt{\sum E_{\mathrm{T}}}$ plane after the trigger requirement for the different QCD background samples. Each sample is scaled for its cross section multiplied by the collected luminosity. The applied $E_{\mathrm{T}}^{\mathrm{miss}}$ and $S_{E_{\mathrm{T}}^{\mathrm{miss}}}$ criteria are indicated as solid lines.

The selection results in 297 events in data for an integrated luminosity of 2.46 ± 0.27 pb^{-1}. For Monte Carlo simulation, the estimated number of signal events that pass the selection is 207.2 ± 6.0 events. The background from W and Z decays is 46.9 ± 1.6 events.

The QCD di-jet background must be estimated from data and the method is described in Section 5.6. In fact, the simulated samples are too small and the uncertainties on the shape and on the cross section too big to be able to rely on Monte Carlo for a good estimate

of this background.

As no Monte Carlo $t\bar{t}$ sample with pile-up is available, the $t\bar{t}$ contribution is determined from simulated samples without pile-up. In Table 5.5 the cut-flow for $t\bar{t}$ events, both for the leptonic/semi-leptonic and hadronic samples is reported. Considering that pile-up has the effect of reducing the number of expected events, the final expected events are much lower than the ones in the table. Therefore this background can be neglected.

An overview of the full event selection, for data and simulated electroweak background, is given in Table 5.4.

Concerning the $W \to e\nu_e$ background, which is the main component of the background at the end of the selection, it is rejected mainly by the $\tau_{\rm h}$-ID electron veto. Comparing the number of $W \to e\nu_e$ events in Table 5.4 with the number of events selected in data, it can be seen that after the selection of the $p_{\rm T}$ of the $\tau_{\rm h}$ candidate, $W \to e\nu_e$ is the main component of the data sample, with ∼6600 events out of the ∼11000 events selected in data. The $W \to e\nu_e$ background is reduced from ∼6600 events to ∼30 events by the two different electron vetoes.

The $W \to \mu\nu_\mu$ background is mainly suppressed by the cut on $E_{\rm T}^{\rm miss}$ and then by the $\tau_{\rm h}$ identification, as the identified tau jet usually come from a fake jet in the event. Finally the muon veto reduces this background to an amount of events slightly smaller than the $W \to e\nu_e$ background.

The $W \to \tau_\ell\nu_\tau$ background, being a mixture of the two backgrounds just described, is mainly reduced by means of cut on $E_{\rm T}^{\rm miss}$, $\tau_{\rm h}$ identification and lepton vetoes.

Concerning the background from $Z \to ee$, the stronger suppression comes from the skimming, which is actually a cut on the amount of $E_{\rm T}^{\rm miss}$ in the event. Further suppression, that makes this background negligible with less than 0.03 events expected, comes from the $\tau_{\rm h}$-ID electron veto. For the other Z backgrounds the rejection comes from the requirements of having a $\tau_{\rm h}$ in the event, both at the trigger level and then with the explicit selection of having a $\tau_{\rm h}$ reconstructed in the event.

The QCD background is the most important background, as it is produced with a cross section six times bigger than the $W \to \tau_{\rm h}\nu_\tau$ cross section. The main reduction of this background comes from the cut on $E_{\rm T}^{\rm miss}$. In fact, at the skimming level, the events selected in data, which are strongly dominated by QCD, are reduced from 30 M events to 4.5 M events. The QCD background dominates the composition of data down to the $\tau_{\rm h}$ candidate identification and the following cut on its $p_{\rm T}$. After the lepton vetoes the QCD background becomes again the main component of the data sample and it is only the cut on $S_{E_{\rm T}^{\rm miss}}$ that allows to efficiently extract the signal. In fact, just before the cut on $S_{E_{\rm T}^{\rm miss}}$, ∼3300 events are selected in data, where only ∼400 are expected to come from $W \to \tau_{\rm h}\nu_\tau$ decays. The other backgrounds are already reduced considerably. The $S_{E_{\rm T}^{\rm miss}}$ cut, with a reduction of a factor about 2 on the signal and on the EW backgrounds, has instead a reduction of more than an order of magnitude on data. Without the cut on $S_{E_{\rm T}^{\rm miss}}$ it would have been very hard to be able to extract the signal, because even a tighter cut simply on $E_{\rm T}^{\rm miss}$ does not allow to have a S/B ratio of about 2.3, as obtained with the selection explained in this section.

Period	Period A	Period B	Period C	Period D	Period E	Period F
Integrated Luminosity (nb^{-1})	0.4	8.2	8.5	291.2	1002.7	1148.1
Events	107467	2133767	1808345	13378415	4810759	7904627
Skimming	1915	24466	22157	566833	1428973	2517906
Trigger	109	2406	2460	132033	486922	605998
Collision cleaning	109	2406	2460	132028	486916	605991
Jet cleaning	96	2225	2291	123779	456043	565689
Jet in gap veto	69	1662	1701	94324	348404	432745
$min(\Delta\Phi(jet, E_{\mathrm{T}}^{\mathrm{miss}})) > 0.5$	34	848	884	54323	201222	254509
$E_{\mathrm{T}}^{\mathrm{miss}} > 30$ GeV	10	268	245	16619	60997	79057
τ_{h} identification	3	50	43	1727	5908	6924
$20 < p_{\mathrm{T}}(\tau_{\mathrm{h}}) < 60$ GeV	2	34	39	1309	4383	5093
τ_{h} in gap veto	2	33	38	1298	4350	5056
τ_{h}-ID electron veto	1	9	12	416	1624	1965
Electron veto	1	9	12	393	1517	1824
Muon veto	1	9	11	350	1359	1627
$S_{E_{\mathrm{T}}^{\mathrm{miss}}} > 6$	0	1	1	42	110	143
Events/nb^{-1}	0	0.12	0.12	0.14	0.11	0.12

Table 5.3: Number of events passing the selection criteria for data, divided on running periods.

	Data	$W \to \tau_{\mathrm{h}}\nu_\tau$	$W \to e\nu_e$	$W \to \mu\nu_\mu$	$W \to \tau_\ell\nu_\tau$	$Z \to ee$	$Z \to \mu\mu$	$Z \to \tau\tau$
Events	30143380	16664.7	25721.1	25721.1	9056.4	2434.4	2434.4	2434.4
Skimming	4562250	6033.5±25.8	17724.0±14.7	4781.0±10.0	2055.7±16.4	62.3±0.4	492.3±1.0	570.1±3.3
Trigger	1229928	3473.6±21.8	13264.3±15.8	2074.0±7.0	1111.9±12.8	44.7±0.3	197.0±0.7	299.8±2.5
Collision cleaning	1229910	3445.1±21.8	13177.1±15.8	2061.7±7.0	1105.2±12.8	44.0±0.3	195.9±0.7	297.2±2.5
Jet cleaning	1150123	3390.6±21.6	12988.1±15.8	2016.0±6.9	1083.5±12.7	42.8±0.3	190.9±0.7	291.7±2.5
Jet in gap veto	878905	2717.2±19.9	10392.0±15.5	1632.4±6.3	874.8±11.5	28.4±0.3	153.3±0.6	221.4±2.2
$min(\Delta\Phi(jet, E_{\mathrm{T}}^{\mathrm{miss}})) > 0.5$	511820	2577.6±19.4	10076.7±15.5	1568.6±6.2	826.5±11.2	13.5±0.2	145.2±0.6	179.1±2.0
$E_{\mathrm{T}}^{\mathrm{miss}} > 30$ GeV	157196	1857.3±16.9	8195.6±14.8	1340.4±5.7	608.2±9.8	6.4±0.1	124.9±0.5	128.1±1.7
τ_{h} identification	14655	582.0±9.9	6936.4±14.1	183.6±2.2	251.8±6.4	5.0±0.1	18.7±0.2	53.3±1.1
$20 < p_{\mathrm{T}}(\tau_{\mathrm{h}}) < 60$ GeV	10860	512.7±9.3	6613.6±13.8	110.5±1.7	174.1±5.4	3.4±0.1	10.6±0.2	42.6±1.0
τ_{h} in gap veto	10777	507.4±9.2	6570.0±13.8	109.5±1.7	172.6±5.3	3.3±0.1	10.5±0.2	42.0±1.0
τ_{h}-ID electron veto	4027	436.9±8.6	73.7±1.7	90.9±1.5	27.2±2.1	<0.05	8.4±0.1	30.6±0.9
Electron veto	3756	408.3±8.3	29.4±1.1	86.0±1.5	21.2±1.9	<0.03	7.8±0.1	26.1±0.8
Muon veto	3357	406.5±8.3	29.2±1.1	20.7±0.7	11.2±1.4	<0.03	0.48±0.03	18.3±0.7
$S_{E_{\mathrm{T}}^{\mathrm{miss}}} > 6$	297	207.2±6.0	16.3±0.8	14.4±0.6	8.2±1.2		0.34±0.03	7.6±0.4

Table 5.4: Number of events passing the selection criteria for data and expected values for Monte Carlo signal and EW background, normalized to the integrated luminosity of 2.46 ± 0.27 pb^{-1}.

	$t\bar{t}$ Semi-/Lep	$t\bar{t}$ Had
Events	196.88	157.22
Skimming	173.14±0.07	41.50±0.20
Trigger	163.54±0.08	32.32±0.19
Collision cleaning	163.54±0.08	32.32±0.19
Jet cleaning	160.65±0.09	31.64±0.19
Jet in gap veto	87.50±0.11	14.56±0.13
$min(\Delta\Phi(jet, E_{\mathrm{T}}^{\mathrm{miss}})) > 0.5$	53.51±0.10	1.97±0.05
$E_{\mathrm{T}}^{\mathrm{miss}} > 30$ GeV	51.44±0.10	1.13±0.04
τ_{h} identification	23.11±0.07	0.41±0.02
$20 < p_{\mathrm{T}}(\tau_{\mathrm{h}}) < 60$ GeV	11.91±0.05	0.15±0.01
τ_{h} in gap veto	11.84±0.05	0.15±0.01
τ_{h}-ID electron veto	4.02±0.03	0.14±0.01
Electron veto	2.72±0.03	0.11±0.01
Muon veto	1.13±0.02	0.07±0.01
$S_{E_{\mathrm{T}}^{\mathrm{miss}}} > 6$	0.75±0.01	<0.003

Table 5.5: Number of events passing the selection criteria for Monte Carlo $t\bar{t}$ events, normalized to the integrated luminosity of 2.46 ± 0.27 pb^{-1}.

5.5 Pile-up

As already mentioned in Section 5.2.1, the LHC luminosity conditions changed very much during the data taking period considered in this analysis. The increase in the instantaneous luminosity was also achieved by increasing the number of protons in the bunches and by squeezing the beams. These bring an increase in the number of pile-up events.

The amount of pile-up in data is estimated by counting the number of primary vertexes reconstructed in each event. The position of the primary vertexes is constrained by the size of the interaction region (*beam spot*) in the $x-y$ plane, but they are usually well separated along z where the beam spot size (~ 28 mm) is much larger than the resolution [99].

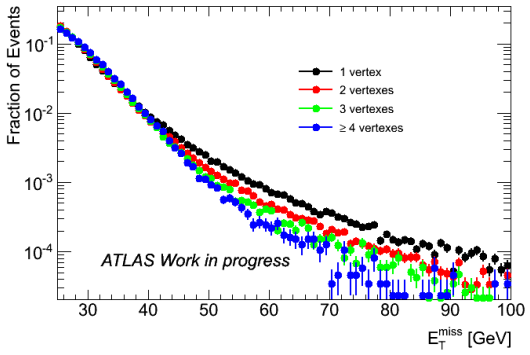

(a) $E_{\mathrm{T}}^{\mathrm{miss}}$

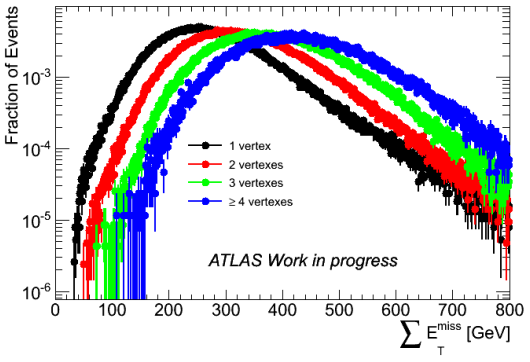

(b) $\sum E_{\mathrm{T}}$

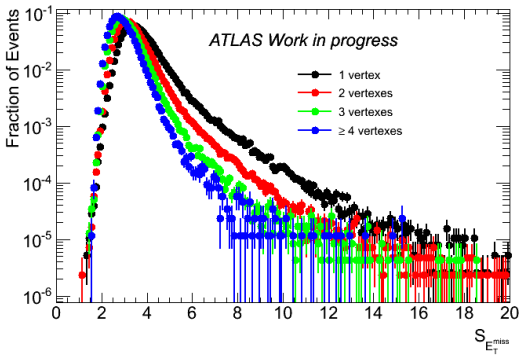

(c) $S_{E_{\mathrm{T}}^{\mathrm{miss}}}$

Figure 5.6: Distributions of $E_{\mathrm{T}}^{\mathrm{miss}}$, $\sum E_{\mathrm{T}}$ and $S_{E_{\mathrm{T}}^{\mathrm{miss}}}$ for data events with different numbers of well reconstructed vertexes. Events passing the selection cuts up to the jet cleaning were considered.

It has been found that requiring at least four tracks associated to a primary vertex provides a negligible amount of fakes. The classification of events according to the number of well reconstructed primary vertexes, after the jet cleaning cut, is shown in Table 5.6. Even if it is obtained by the superimposition of different run conditions, the distribution of the number of additional pile-up events ($\mathrm{N_{vtx-1}}$) is reasonably well described by a poissonian distribution with a mean value of 1.098.

Quantities related to missing transverse energy are heavily affected by pile-up. In Figure 5.6 $E_{\mathrm{T}}^{\mathrm{miss}}$, $\sum E_{\mathrm{T}}$ and $S_{E_{\mathrm{T}}^{\mathrm{miss}}}$ distributions for events with one, two, etc. well reconstructed vertexes are shown. It can be seen that the higher pile-up is, the wider is the acceptance of the cut on $E_{\mathrm{T}}^{\mathrm{miss}}$, whereas the selection related to $S_{E_{\mathrm{T}}^{\mathrm{miss}}}$ becomes less efficient, due to the

worse resolution coming from $\sqrt{\sum E_{\rm T}}$. On $W \to \tau_{\rm h}\nu_\tau$ signal, the efficiency of the cut flow is 2.1% for events with no pile-up and the selection efficiency is reduced to 1.2% if taking into account pile-up (for events with a mean of ∼2 additional vertexes). The reduction of the selection efficiency due to pile-up on the QCD background is even more important.

As the variables used to discriminate the signal from the background, namely $E_{\rm T}^{\rm miss}$ and $S_{E_{\rm T}^{\rm miss}}$, heavily depends on the pile-up level, it is important that these effects are simulated in Monte Carlo.

	N. of Events
1 vertex	381360
2 vertexes	418803
3 vertexes	234501
4 vertexes	86270
$\geq$ 5 vertexes	29189
Total	1150123

Table 5.6: Number of well reconstructed vertexes, with at least four associated tracks, in data. Events passing the event selection up to the jet cleaning cut were considered

Simulated samples with pile-up are available, but the mean number of well reconstructed vertexes does not match exactly the one in data. Therefore the Monte Carlo samples with pile-up were reweighted to reflect the vertex multiplicity found in data.

5.6 QCD background estimation from data

As it was mentioned in the introduction, the amount of QCD background affecting the analysis is estimated directly from data, without relying on Monte Carlo simulations. This choice was driven by several reasons. First of all the integrated luminosity corresponding to low p_{T} QCD samples is several order of magnitude smaller than the one needed in this analysis. On the other hand, the rejection power of the event selection is high. Therefore the number of simulated events surviving the cut-flow is not enough and no events survive the cuts in the lowest p_{T} jets samples. Moreover, the cross section of QCD jets production is very high, so these few simulated events passing the cuts have to be multiplied by huge scaling factors, ending up in an estimate affected by big uncertainties. Furthermore, the cross section of QCD jets production and the distribution of kinematic variables in the tail of the phase space overlapping with τ signal are not well known, resulting in additional uncertainty in the evaluation of the QCD background.

The a data-driven method used to estimate the normalisation and shape of kinematic and τ_{h}-ID variable distributions for the QCD background has been already used in other ATLAS analyses, such as the observation of prompt photons [100], and it is based on a two-dimensional side-bins background subtraction technique.

The method selects four independent data samples, three QCD background-dominated regions (control regions) and one signal-dominated region (signal region). The samples are selected with criteria on $S_{E_{\mathrm{T}}^{\mathrm{miss}}}$ and on τ_{h}-ID, which are assumed to be uncorrelated, after applying the event selection described in Section 5.4. In fact, $S_{E_{\mathrm{T}}^{\mathrm{miss}}}$ depends on global event properties and the τ_{h} candidate contributes to its value only through its total p_{T} , while the τ_{h}-ID is based on shower shapes and tracks of the τ_{h} candidate. An indirect correlation may arise anyhow due to the dependence of the τ_{h}-ID rejection on the p_{T} of the τ_{h} candidate, as it has been shown in Section 2.3. This effect is estimated in Section 5.7.6. The following four regions are used in this analysis:

- Region A: events with $S_{E_{\mathrm{T}}^{\mathrm{miss}}} > 6$ and τ_{h} candidates satisfying the tight τ_{h}-ID;
- Region B: events with $S_{E_{\mathrm{T}}^{\mathrm{miss}}} < 6$ and τ_{h} candidates satisfying the tight τ_{h}-ID;
- Region C: events with $S_{E_{\mathrm{T}}^{\mathrm{miss}}} > 6$ and τ_{h} candidates satisfying the loose τ_{h}-ID but failing the tight τ_{h}-ID;
- Region D: events with $S_{E_{\mathrm{T}}^{\mathrm{miss}}} < 6$ and τ_{h} candidates satisfying the loose τ_{h}-ID but failing the tight τ_{h}-ID.

Region A is referred to as the signal region and regions B, C and D as control regions. Figure 5.7 illustrates the four regions.

Assuming that the signal contribution in the three control regions is negligible, the observed numbers of candidates in them are due only to the background contribution. Assuming also that for the background the $S_{E_{\mathrm{T}}^{\mathrm{miss}}}$ distribution is independent on the τ_{h}-ID level, the background rejection of the $S_{E_{\mathrm{T}}^{\mathrm{miss}}}$ requirement can be measured in the background control sample of candidates failing the tight τ_{h}-ID criteria from the ratio $\mathrm{N^C/N^D}$, and then applied to the background yield in the region with tight τ_{h}-ID and low $S_{E_{\mathrm{T}}^{\mathrm{miss}}}$ ($\mathrm{N^B}$) to obtain a data-driven estimate for the background yield in the signal region.

Basically this prediction is based on two assumptions:

- the shape of the $S_{E_{\mathrm{T}}^{\mathrm{miss}}}$ distribution for QCD background is independent on the τ_{h}-ID requirement,

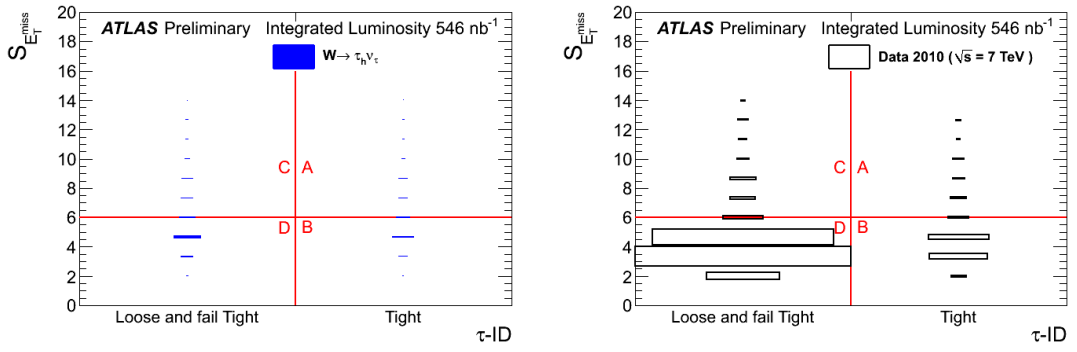

(a) (b)

Figure 5.7: $S_{E_{\mathrm{T}}^{\mathrm{miss}}}$ distribution for events in which the selected τ_{h} candidate passes the loose but fails the tight τ_{h}-ID and for events in which the selected τ_{h} candidate passes the tight τ_{h}-ID. Distributions are shown for (a) data and (b) $W \to \tau_{\mathrm{h}}\nu_\tau$ simulated events after applying the event selection described in Section 5.4, except for the last requirement on $S_{E_{\mathrm{T}}^{\mathrm{miss}}}$ and the loosening of τ_{h}-ID requirement. The area of the boxes are proportional to the event yield.[101]

- the signal and electroweak background contribution in the three control regions is negligible.

5.6.1 Evaluation of QCD background

Provided that the two assumptions are satisfied, the method does not rely on any other input and the estimate for QCD background in the signal region A is then obtained by:

$$\mathrm{N}^{\mathrm{A}}_{\mathrm{QCD}} = \mathrm{N}^{\mathrm{B}}\mathrm{N}^{\mathrm{C}}/\mathrm{N}^{\mathrm{D}} \tag{5.2}$$

where N^i represents the number of observed events in region i.

The assumption that the shape of the $S_{E_{\mathrm{T}}^{\mathrm{miss}}}$ distribution for QCD background in regions AB and CD is the same has been verified with a data control sample, as described in Section 5.6.3.

The second assumption, requiring the signal and EW background contamination in the control regions to be small, is not fully satisfied (as it can be seen for the signal in Figure 5.7(b)) and corrections to account for this contamination have to be applied. The contamination is checked using $W \to \tau_{\mathrm{h}}\nu_\tau$ and EW Monte Carlo samples. Table 5.7 shows the number of data events and the expected signal and EW background events (in the following $\mathrm{N}^i_{\mathrm{sig}}$ and $\mathrm{N}^i_{\mathrm{EW}}$, respectively) in regions A, B, C and D. The ratios of simulated signal and EW background events in the control regions and the signal region are denoted by the coefficients:

$$\mathrm{c}_i = \frac{\mathrm{N}^i_{\mathrm{sig}} + \mathrm{N}^i_{\mathrm{EW}}}{\mathrm{N}^{\mathrm{A}}_{\mathrm{sig}} + \mathrm{N}^{\mathrm{A}}_{\mathrm{EW}}}, \qquad i = \mathrm{B}, \mathrm{C}, \mathrm{D} \tag{5.3}$$

which are also summarized in Table 5.7.

To take into account the signal and EW background contamination in the control regions, the number of observed events in the control regions is therefore corrected as following:

$$\mathrm{N}^i \to \mathrm{N}^i_{\mathrm{corr}} = \mathrm{N}^i - \mathrm{c}_i(\mathrm{N}^{\mathrm{A}} - \mathrm{N}^{\mathrm{A}}_{\mathrm{QCD}}) \qquad i = \mathrm{B}, \mathrm{C}, \mathrm{D} \tag{5.4}$$

	A	B	C	D
Data	297	3060	1125	38456
$W \to \tau_h \nu_\tau$	207.2±6.0	199.3±5.8	295.9±7.1	310.7±7.3
EW	46.9±1.6	33.1±1.2	196.1±3.5	127.1±2.7
c_i		0.91±0.04	1.94±0.03	1.72±0.03

Table 5.7: Number of observed events in the four regions for the data-driven estimation of QCD background. Monte Carlo estimates of the number of $W \to \tau_h \nu_\tau$ signal and EW background events and the correction coefficients c_i are also shown.

Therefore Equation 5.2 becomes:

$$N^A_{QCD} = \frac{\left[N^B - c_B(N^A - N^A_{QCD})\right]\left[N^C - c_C(N^A - N^A_{QCD})\right]}{N^D - c_D(N^A - N^A_{QCD})}$$

To make it more symmetric, N^A_{QCD} can be substituted with $N^A - c_A(N^A - N^A_{QCD})$ where clearly c_A is equal to 1 for construction. The previous equation thus becomes:

$$N^A - c_A(N^A - N^A_{QCD}) = \frac{\left[N^B - c_B(N^A - N^A_{QCD})\right]\left[N^C - c_C(N^A - N^A_{QCD})\right]}{N^D - c_D(N^A - N^A_{QCD})} \tag{5.5}$$

Equation 5.5 is a second order equation in $(N^A - N^A_{QCD})$. Calling $x = N^A - N^A_{QCD}$:

$$(c_A c_D - c_B c_C)x^2 + (N^B c_C + N^C c_B - N^A c_D - N^D c_A)x + (N^A N^D - N^B N^C) = 0$$

Just one of the solutions can be accepted, with the requirements that it is positive and smaller than N^A. Finally, the result of the QCD background extraction method is $N^A_{QCD} = N^A - x$.

The estimated QCD background in region A is 47.8 ± 4.7 events and non-QCD events in region A is 249.2 ± 20.8. The observed EW and signal yield has therefore a purity of 84% in the signal region.

The statistical error on N^A_{QCD} includes both the uncertainty on the calculation of the c_i coefficients, due to the limited Monte Carlo statistics, and the uncertainty on the amount of data in the four control regions. The statistical error on N^A_{QCD} has been therefore evaluated using a toy Monte Carlo in which the populations of the four regions were varied within an uncertainty equal to $\sqrt{N_i}$ and the values of the number of expected events of signal and EW background within their statical uncertainty reported in Table 5.7. The c_i coefficients were then recalculated and the N^A_{QCD} extracted.

5.6.2 Method validation

One of the positive features of the 2D side-bins method is that it allows to use the side-bins to estimate the shape of kinematic variables for the background process. This shape comparison is not used for signal extraction and therefore can be used to validate the quality of the background estimation.

In the following, distributions will be shown in different regions:

Combined region AB Data is taken from signal region A and control region B, as well as Monte Carlo signal and EW background. The shape of QCD background is extracted

from data in control regions C and D, from which Monte Carlo signal and EW background in regions C and D were subtracted. The QCD distribution is then normalised to the numbers of QCD events extracted in regions A and B, i.e. to $\mathrm{N}^{\mathrm{A}}_{\mathrm{QCD}} + \mathrm{N}^{\mathrm{B}} - \mathrm{c}_{\mathrm{B}}(\mathrm{N}^{\mathrm{A}} - \mathrm{N}^{\mathrm{A}}_{\mathrm{QCD}})$. Monte Carlo signal, EW background and extracted QCD background are summed.

Combined region AC Data is taken from signal region A and control region C, as well as Monte Carlo signal and EW background. The shape of QCD background is extracted from data in control regions B and D, from which Monte Carlo signal and EW background in regions B and D were subtracted. The QCD distribution is then normalised to the numbers of QCD events extracted in regions A and C, i.e. to $\mathrm{N}^{\mathrm{A}}_{\mathrm{QCD}} + \mathrm{N}^{\mathrm{C}} - \mathrm{c}_{\mathrm{C}}(\mathrm{N}^{\mathrm{A}} - \mathrm{N}^{\mathrm{A}}_{\mathrm{QCD}})$. Monte Carlo signal, EW background and extracted QCD background are summed.

Signal region A, with normalisation in control region B Data is taken just from signal region A, as well as Monte Carlo signal and EW background. The shape of QCD background is extracted from data in control region B, from which Monte Carlo signal and EW background in regions B were subtracted. The QCD distribution is then normalised to the numbers of QCD events extracted in regions A, i.e. to $\frac{\mathrm{N}^{\mathrm{C}} - \mathrm{c}_{\mathrm{C}}(\mathrm{N}^{\mathrm{A}} - \mathrm{N}^{\mathrm{A}}_{\mathrm{QCD}})}{\mathrm{N}^{\mathrm{D}} - \mathrm{c}_{\mathrm{D}}(\mathrm{N}^{\mathrm{A}} - \mathrm{N}^{\mathrm{A}}_{\mathrm{QCD}})}$. Monte Carlo signal, EW background and extracted QCD background are summed.

Signal region A, with normalisation in control region C The same as the previous, where the QCD background shape is extracted from region C and again normalised to $\frac{\mathrm{N}^{\mathrm{B}} - \mathrm{c}_{\mathrm{B}}(\mathrm{N}^{\mathrm{A}} - \mathrm{N}^{\mathrm{A}}_{\mathrm{QCD}})}{\mathrm{N}^{\mathrm{D}} - \mathrm{c}_{\mathrm{D}}(\mathrm{N}^{\mathrm{A}} - \mathrm{N}^{\mathrm{A}}_{\mathrm{QCD}})}$.

The first two projections allow to show the quality of the approximation by showing the background shapes from one side-bin to the other one enriched in signal (Figure 5.8 and 5.9). When concentrating on the signal region A instead a choice must be done about which of the directly adjacent side-bins should be used for shape information and for normalisation.

For distributions concerning $E_{\mathrm{T}}^{\mathrm{miss}}$ quantities, QCD is usually extracted from control region C, to have events with similar $S_{E_{\mathrm{T}}^{\mathrm{miss}}}$ distribution, while for distributions concerning τ_{h} identification and kinematic quantities, QCD is usually extracted from control region B, to have τ_{h} with the same level of identification.

A first results of the QCD background estimation can be seen in Figure 5.8 for the $S_{E_{\mathrm{T}}^{\mathrm{miss}}}$ distribution. The data distribution corresponds to the combined region AB. The QCD background shape is extracted from regions CD and the normalisation is as just explained. A good agreement is observed, with an excess of data that is compatible with the simulated distribution of $W \to \tau_{\mathrm{h}}\nu_\tau$ signal events.

The variables used in the τ_{h}-ID were also studied. Figure 5.9 shows the distributions for $f_{\mathrm{trk,l}}$, R_{track} and R_{EM}, which have been described in detail in Chapter 2. τ_{h}-ID variables distributions clearly show that the observed events have the typical characteristics of hadronic taus.

For completeness, other variables usually used for τ_{h} identification are shown in Figure 5.10

Figure 5.11 shows the distribution of the number of tracks of the τ_{h} candidate. Data distribution in signal region A is shown, as well as the distribution of QCD events obtained from control region C with the additional expectation from signal and EW background.

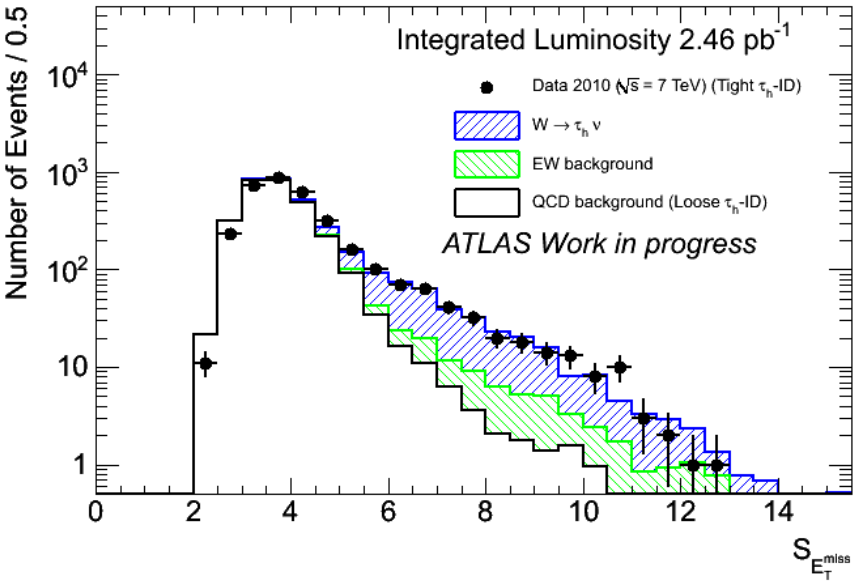

Figure 5.8: $S_{E_{\mathrm{T}}^{\mathrm{miss}}}$ distribution for the combined region AB (tight τ_{h}-ID region). QCD background is evaluated from the combined control region CD (loose τ_{h}-ID region). Monte Carlo signal and EW background in region AB are also shown.

This distribution shows strong evidence of hadronic τ decays. In fact, hadronically decaying taus result in one or three charged particles (i.e. one or three charged tracks) and the track multiplicity spectrum shows this behaviour. Moreover, the probability of decaying in one charged particle is higher than the one in three particles: this is also observed. Signal events with two or four tracks are due to track misreconstruction.

Kinematic observables for the τ_{h} candidates are shown in Figure 5.12.

Other distributions are useful to check if the observed events not only come from τ_{h}, but if they are compatible with τ_{h} coming from W decays. Figure 5.13 shows the $\Delta\phi(\tau_{\mathrm{h}}, E_{\mathrm{T}}^{\mathrm{miss}})$ and m_{T}[1] distributions for data in region AB, with the QCD extracted from control regions CD and normalised as explained before. Figure 5.14 shows instead the same distributions for the signal region A only. The QCD shape is taken from control region C.

In both figures the expected characteristic signature of $W \to \tau_{\mathrm{h}}\nu_\tau$ decays can be observed. $E_{\mathrm{T}}^{\mathrm{miss}}$ and the τ_{h} are most likely to lie in opposite direction in the transverse plane. The lower limit at 0.5 is connected with the requirement for the event to have the minimum of $\Delta\phi(\mathrm{jet}, E_{\mathrm{T}}^{\mathrm{miss}}) > 0.5$ rad. The transverse mass distribution reaches its maximum between 50 and 80 GeV.

Figure 5.15 shows the distribution of the electric charge of the τ_{h} candidate. Data distribution in signal region A is shown, as well as the distribution of QCD events obtained from control region C with the additional expectation from signal and EW background.

The electric charge distribution of the τ_{h} candidate also shows the expected behaviour for taus coming from W decay. In fact, in contrast to proton-antiproton collisions, the cross sections for W^+ and W^- production measured with proton-proton collisions are asymmetric due to the absence of valence anti-quarks in the proton. An excess of events with positive electric charge is expected. This asymmetry was already observed in other

[1] The transverse mass in a $W \to \tau_{\mathrm{h}}\nu_\tau$ decay is defined as $m_{\mathrm{T}} = \sqrt{2 \cdot E_{\mathrm{T}}^{\tau_{\mathrm{h}}} \cdot E_{\mathrm{T}}^{\mathrm{miss}} \cdot (1 - \cos\Delta\phi\,(\tau_{\mathrm{h}}, E_{\mathrm{T}}^{\mathrm{miss}}))}$.

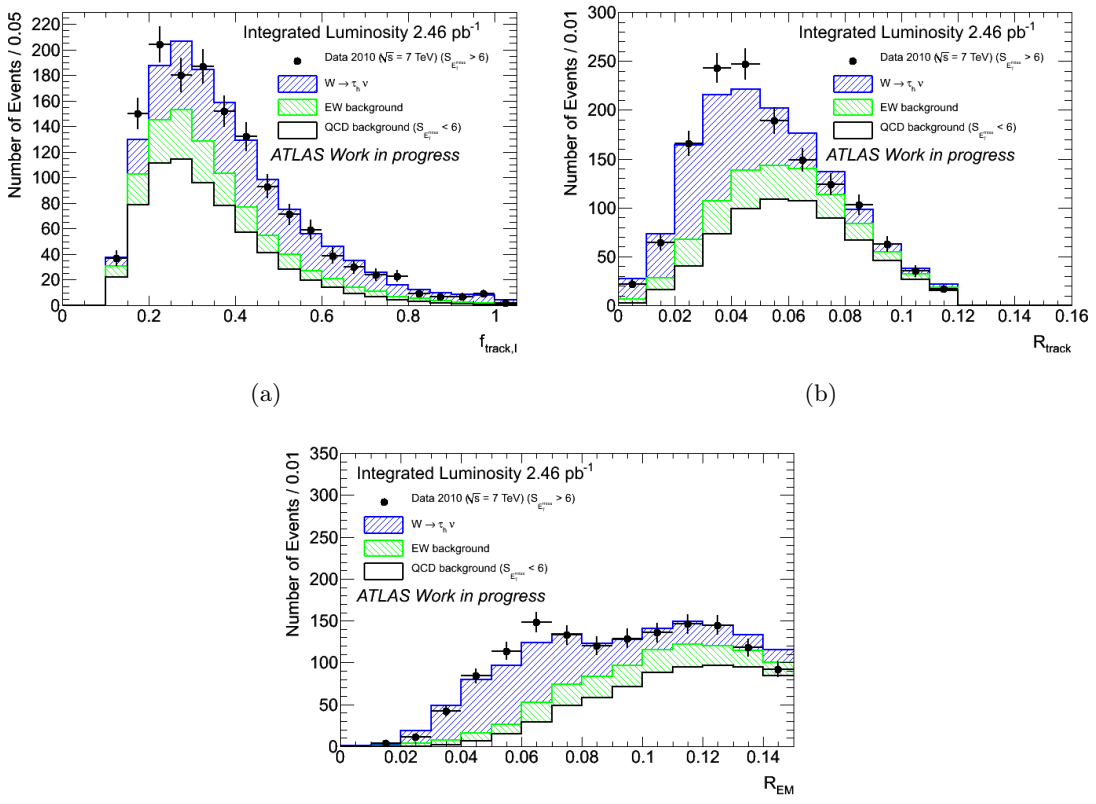

(a) (b)

(c)

Figure 5.9: Distribution of the τ_{h}-ID variables for the regions with $S_{E_{\mathrm{T}}^{\mathrm{miss}}} > 6$ and $S_{E_{\mathrm{T}}^{\mathrm{miss}}} < 6$ (regions AC and BD) combined with the expected signal and EW background contributions from simulation.

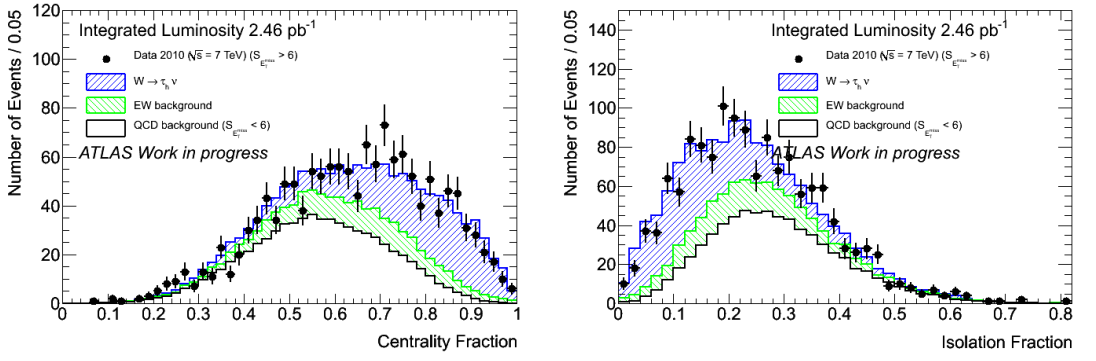

(a) (b)

Figure 5.10: Distribution of the τ_{h}-ID related variables for the regions with $S_{E_{\mathrm{T}}^{\mathrm{miss}}} > 6$ and $S_{E_{\mathrm{T}}^{\mathrm{miss}}} < 6$ (regions AC and BD) combined with the expected signal and EW background contributions from simulation.

analysis of W decays with the ATLAS Experiment [102, 19].

Some additional $E_{\mathrm{T}}^{\mathrm{miss}}$ related distributions are shown in Figure 5.16.

The agreement between data in the signal region and the control regions, based on

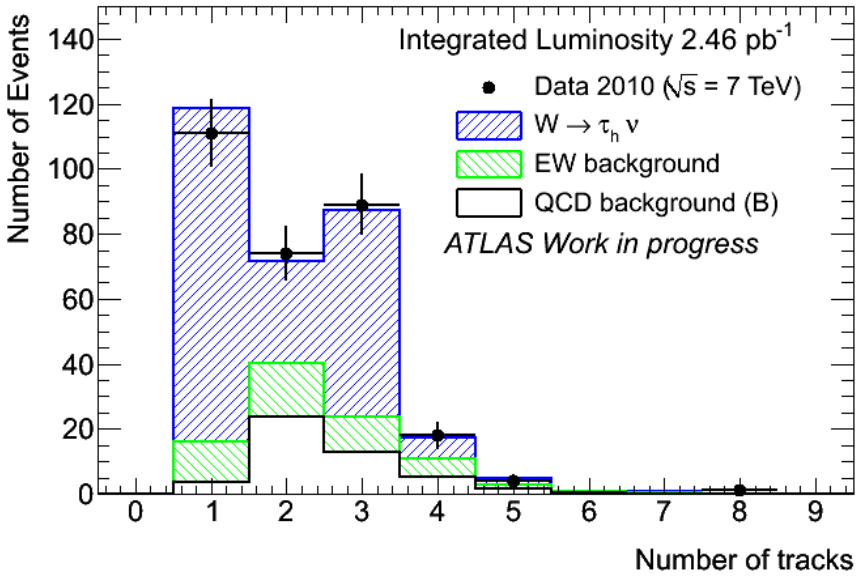

Figure 5.11: Distribution of the number of tracks of the τ_{h} candidates in signal region A. Data is shown as well as Monte Carlo signal and EW background. QCD background shape has been extracted from control region C and normalised as described in the text.

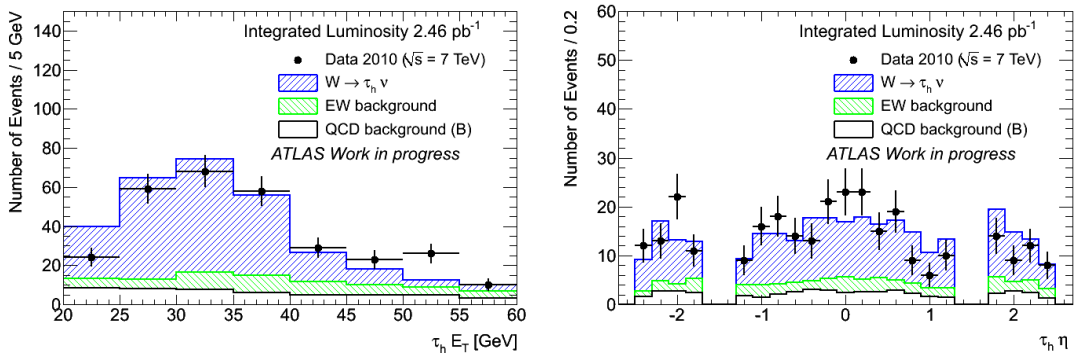

(a) (b)

Figure 5.12: Distribution of (a) the p_{T} spectrum and (b) η of the τ_{h} candidates. Data is shown as well as Monte Carlo signal and EW background. QCD background shape has been estimated in control region B and normalised as described in the text.

the estimated values from the data-driven method, combined with the signal and EW expectation from Monte Carlo strongly support that the excess of data seen is due to the decay $W \to \tau_{\mathrm{h}}\nu_\tau$ and therefore the observation of hadronically decaying τ leptons from $W \to \tau_{\mathrm{h}}\nu_\tau$ decays in ATLAS.

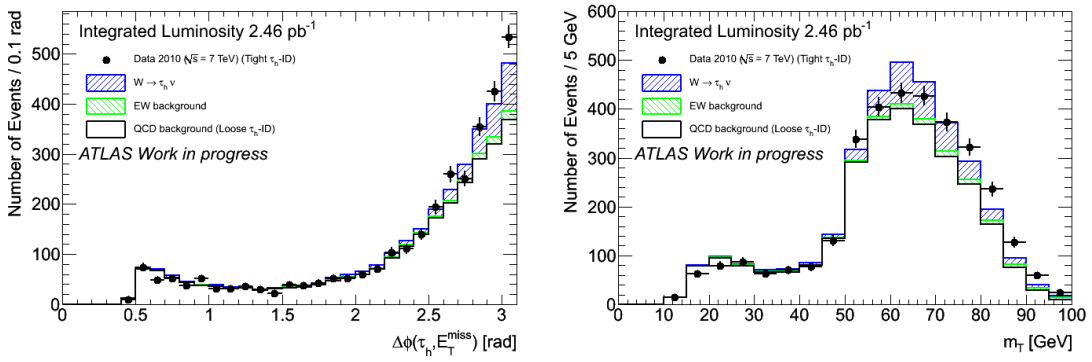

(a) (b)

Figure 5.13: Distributions of (a) $\Delta\phi(\tau_{\mathrm{h}}, E_{\mathrm{T}}^{\mathrm{miss}})$ and (b) transverse mass m_{T} for data in region AB, combined with Monte Carlo signal and EW background. The QCD background distribution is extracted from control regions CD and normalized as described in the text.

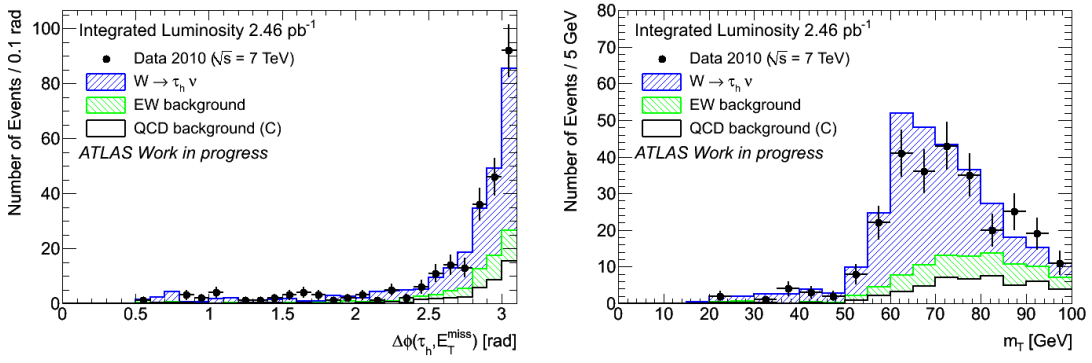

(a) (b)

Figure 5.14: Distributions of (a) $\Delta\phi(\tau_{\mathrm{h}}, E_{\mathrm{T}}^{\mathrm{miss}})$ and (b) of transverse mass m_{T} for data in the signal region A, combined with Monte Carlo signal and EW background. The QCD background shape is extracted from control region C. The QCD background distributions are normalised as described in the text.

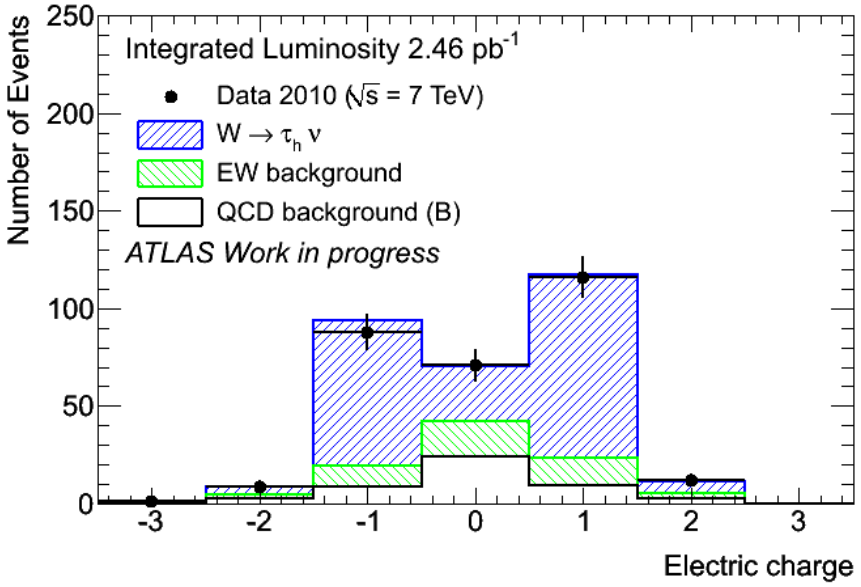

Figure 5.15: Distribution of the electric charge of the τ_{h} candidates in signal region A. Data is shown as well as Monte Carlo signal and EW background. QCD background shape has been extracted from control region C and then normalised to $\mathrm{N}^{\mathrm{A}}_{\mathrm{QCD}}$.

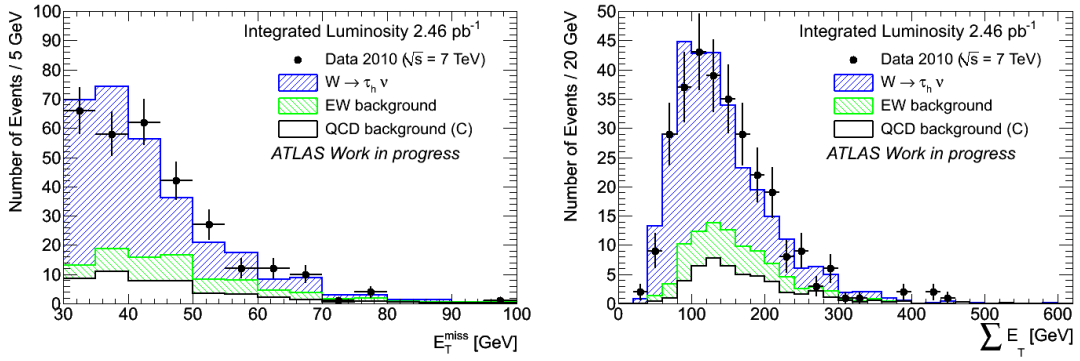

(a) (b)

Figure 5.16: Distributions of (a) the missing transverse energy and of (b) $\sum E_{\mathrm{T}}$, in signal region A. Data is shown as well as Monte Carlo signal and EW background. QCD background shape has been extracted from region C and then normalised to $\mathrm{N}^{\mathrm{A}}_{\mathrm{QCD}}$.

5.6.3 Verification of the assumptions from the data-driven method

As a test of the validity of the data-driven method, the assumption that the $S_{E_{\mathrm{T}}^{\mathrm{miss}}}$ and τ_{h}-ID variables are not correlated is verified in this section. This study, however, could not be performed using QCD Monte Carlo simulation due to the small size of the event samples combined with the large rejection factors of the event selection criteria, even after loosening some of the criteria, e.g. replacing the tight τ_{h}-ID criterion by the medium τ_{h}-ID. Therefore, the tests needed to be done on data, using a background enriched control sample obtained by selecting τ_{h} candidates with more than three tracks ($\mathrm{N_{track}} > 3$)[2].

Shape of $S_{E_{\mathrm{T}}^{\mathrm{miss}}}$ distribution

For the successful prediction of the number of QCD background events in the signal region with the data-driven method it has to be verified first that the $S_{E_{\mathrm{T}}^{\mathrm{miss}}}$ distribution for the QCD background in the combined regions AB and CD is the same, i.e. that the $S_{E_{\mathrm{T}}^{\mathrm{miss}}}$ distribution is independent of the τ_{h}-ID selection. This has been done with a data control sample of τ_{h} candidates with more than three tracks: Figure 5.17(a) compares the $S_{E_{\mathrm{T}}^{\mathrm{miss}}}$ distribution for events that pass the loose τ_{h}-ID but fail the tight τ_{h}-ID with events that pass the tight τ_{h}-ID, with the additional requirement that the selected τ_{h} candidates have $\mathrm{N_{track}} > 3$. Both distributions agree within the statistical uncertainties. To check if these distributions also represent events with selected τ_{h} candidates with any number of tracks, Figure 5.17(b) compares $S_{E_{\mathrm{T}}^{\mathrm{miss}}}$ for τ_{h} candidates that pass the loose but fail the tight τ_{h} ID. A similar level of agreement is observed.

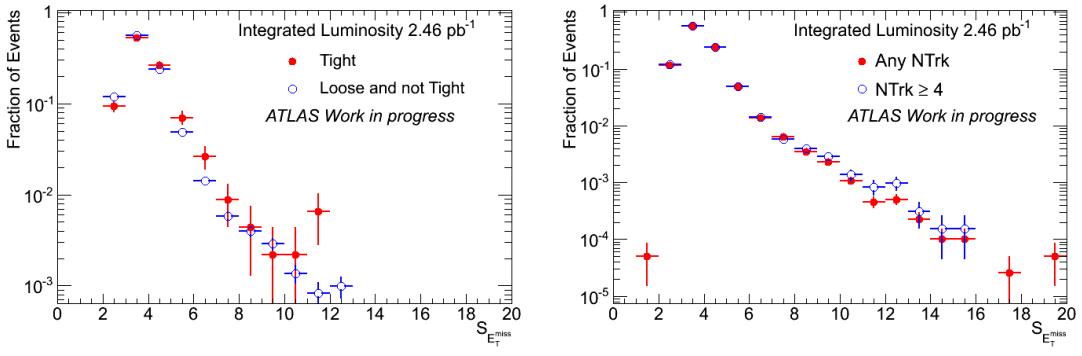

(a) (b)

Figure 5.17: $S_{E_{\mathrm{T}}^{\mathrm{miss}}}$ distributions. (a) Distribution for a data control sample of τ_{h} candidates with $\mathrm{N_{track}} > 3$, for τ_{h} candidates that pass the loose τ_{h}-ID but fail the tight τ_{h}-ID and for τ_{h} candidates that pass the tight τ_{h}-ID. (b) Distribution for selected τ_{h} candidates that pass the loose τ_{h}-ID for $\mathrm{N_{track}} > 3$ and for any number of tracks.

[2]Reconstructed τ_{h} candidates with large track multiplicities are dominated by misidentified jets.

5.6.4 Additional tests for the data-driven method

In order to confirm that the data-driven method yields consistent results and can be used to estimate the number of QCD background, several cross checks are performed. The method is applied to different subsamples of the selected events and the results are compared with the expectations.

Applying the data-driven method to a control sample

In order to verify if the data-driven method correctly predicts the number of QCD background events in the signal region, the method is applied to a control sample: a QCD background enriched sample produced by selecting τ_{h} candidates with more than three tracks. The number of events in each region are listed in Table 5.8.

	A	B	C	D
Data	23	435	404	12771
$W \to \tau_{\mathrm{h}}\nu_\tau$	9.4±1.3	4.7±0.9	51.8±3.0	43.4±2.7
EW	7.4±0.7	2.9±0.4	80.2±2.4	41.4±1.6
c_i		0.45±0.20	7.87±0.23	5.06±0.19

Table 5.8: Number of observed events in the four regions for the data-driven estimation of QCD background, considering a control sample obtained by selecting τ_{h} candidates with more than three tracks. Monte Carlo estimates of the number of $W \to \tau_{\mathrm{h}}\nu_\tau$ signal and EW background events and the correction coefficients c_i are also shown.

As can be observed in Table 5.8, the data samples with selected τ_{h} candidates with $N_{\mathrm{track}} > 3$ are quite small and, according to Monte Carlo simulations, still contain a significant contribution of signal and EW background events. Nonetheless, the estimated number of QCD background events of 10.3±2.2 in signal region A is in agreement with the observed number of data events which remain when the signal and EW background expectations are subtracted. This indicates the consistency of the data-driven method.

Study of τ_{h} candidates in different p_{T} ranges

A different approach to confirm the validity of the data-driven method for a QCD background estimation is to consider τ_{h} candidates in different p_{T} regions separately. The regions have been chosen to probe different efficiency/rejection point for τ_{h}-ID:

- τ_{h} candidates with a transverse momentum between 20 GeV $< p_{\mathrm{T}} <$ 30 GeV;
- τ_{h} candidates with a transverse momentum between 30 GeV $< p_{\mathrm{T}} <$ 60 GeV.

The number of events for the first sample (20 GeV $< p_{\mathrm{T}} <$ 30 GeV) in data and the signal and EW Monte Carlo samples in the four different regions are listed in Table 5.9.

	A	B	C	D
Data	83	1043	255	13625
$W \to \tau_{\mathrm{h}}\nu_\tau$	78.7±3.7	70.6±3.5	112.5±4.4	134.1±4.8
EW	9.8±0.7	9.7±0.6	45.7±1.6	44.1±1.6
c_i		0.91±0.06	1.79±0.06	2.01±0.06

Table 5.9: Number of observed events in the four regions for the data-driven estimation of QCD background for a data sample with τ_{h} candidates with transverse momentum in the range 20 GeV $< p_{\mathrm{T}} <$ 30 GeV. Monte Carlo estimates of the number of $W \to \tau_{\mathrm{h}}\nu_\tau$ signal and EW background events and the correction coefficients c_i are also shown.

The number of expected QCD-background events, based on the numbers in Table 5.9, is 8.9 ± 2.1. Figure 5.18 shows the distributions of kinematic and τ_{h}-ID variables for these τ_{h} candidates.

The number of events in the four regions, for τ_{h} candidates of the second sample within 30 GeV $< p_{\mathrm{T}} <$ 60 GeV, are given in Table 5.10.

	A	B	C	D
Data	214	2017	870	24831
$W \to \tau_{\mathrm{h}}\nu_\tau$	128.4±4.7	128.7±4.7	183.4±5.6	176.6±5.5
EW	37.1±1.4	23.4±1.0	150.4±3.1	83.0±2.2
c_i		0.92±0.04	2.02±0.04	1.57±0.04

Table 5.10: Number of observed events in the four regions for the data-driven estimation of QCD background for a data sample with τ_{h} candidates with transverse momentum in the range 30 GeV $< p_{\mathrm{T}} <$ 60 GeV. Monte Carlo estimates of the number of $W \to \tau_{\mathrm{h}}\nu_\tau$ signal and EW background events and the correction coefficients c_i are also shown.

The resulting number of expected QCD background events in signal region A is 39.1 ± 4.4. The distribution of kinematic and τ_{h}-ID variables for these τ_{h} candidates are shown in Figure 5.19.

The resulting number of QCD background events are consistent with the estimation for the whole sample of 47.8 ± 4.7 events, which again confirms the validity of the data-driven method for an estimation of QCD background events. The excess of data events in the high p_{T} region with respect to the low p_{T} region is compatible with statistical fluctuations.

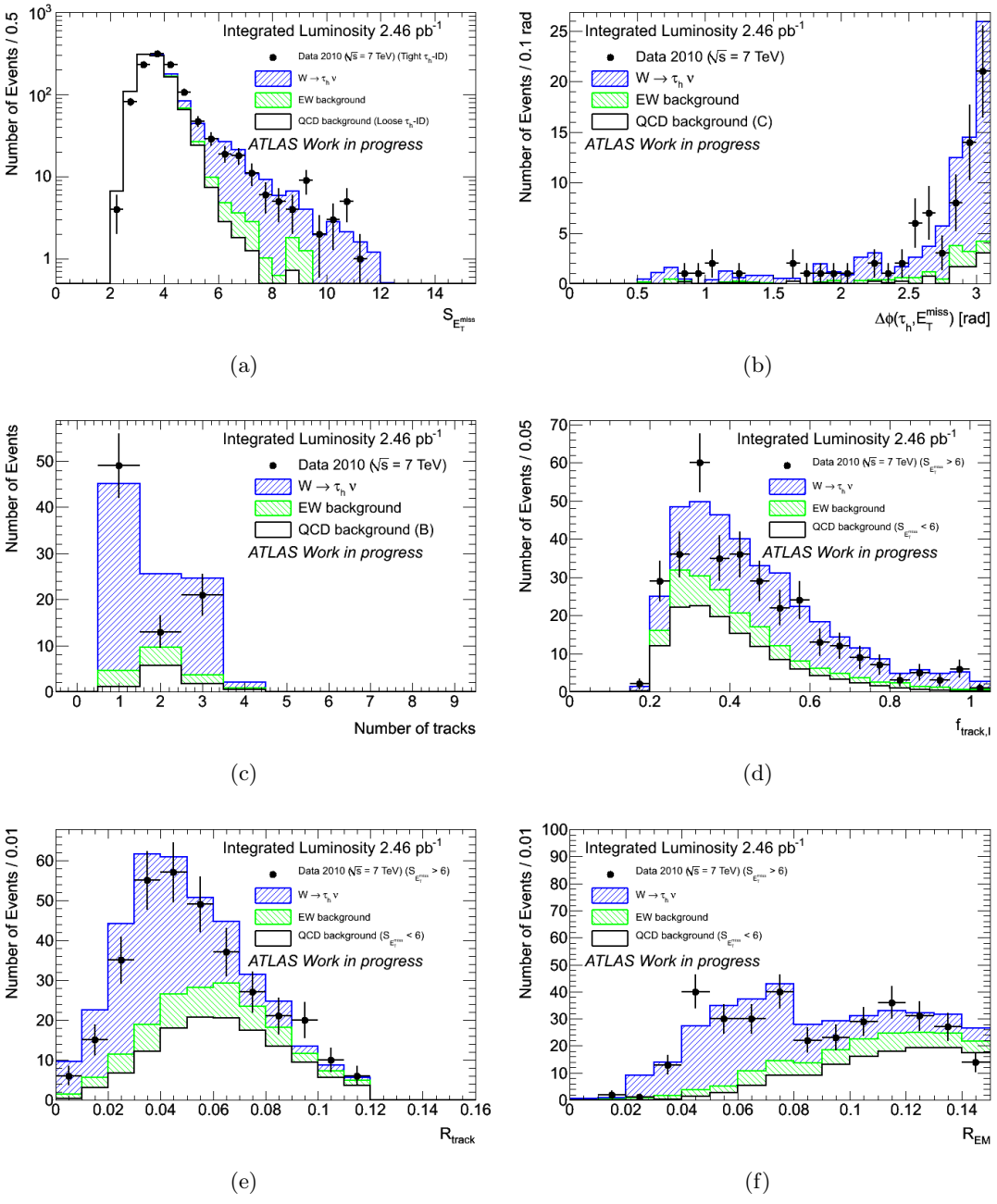

Figure 5.18: Comparison of data and different control regions with the additional expected contribution of signal and EW backgrounds for τ_{h} candidates within a transverse momentum range of 20 GeV $< p_{\mathrm{T}} <$ 30 GeV. (a) $S_{E_{\mathrm{T}}^{\mathrm{miss}}}$ distribution for tight τ_{h} candidates (region AB) and loose candidates failing the tight τ_{h}-ID (region CD). (b) $\Delta\phi(\tau_{\mathrm{h}}, E_{\mathrm{T}}^{\mathrm{miss}})$ distribution for events in the signal region A and for loose candidates failing the tight τ_{h}-ID (region C). (c) Track multiplicity distribution for τ_{h} candidates. (d) - (f) Distribution of the τ_{h}-ID variables for events with $S_{E_{\mathrm{T}}^{\mathrm{miss}}}$ >6 (region AC) and $S_{E_{\mathrm{T}}^{\mathrm{miss}}}$ <6 (region BD).

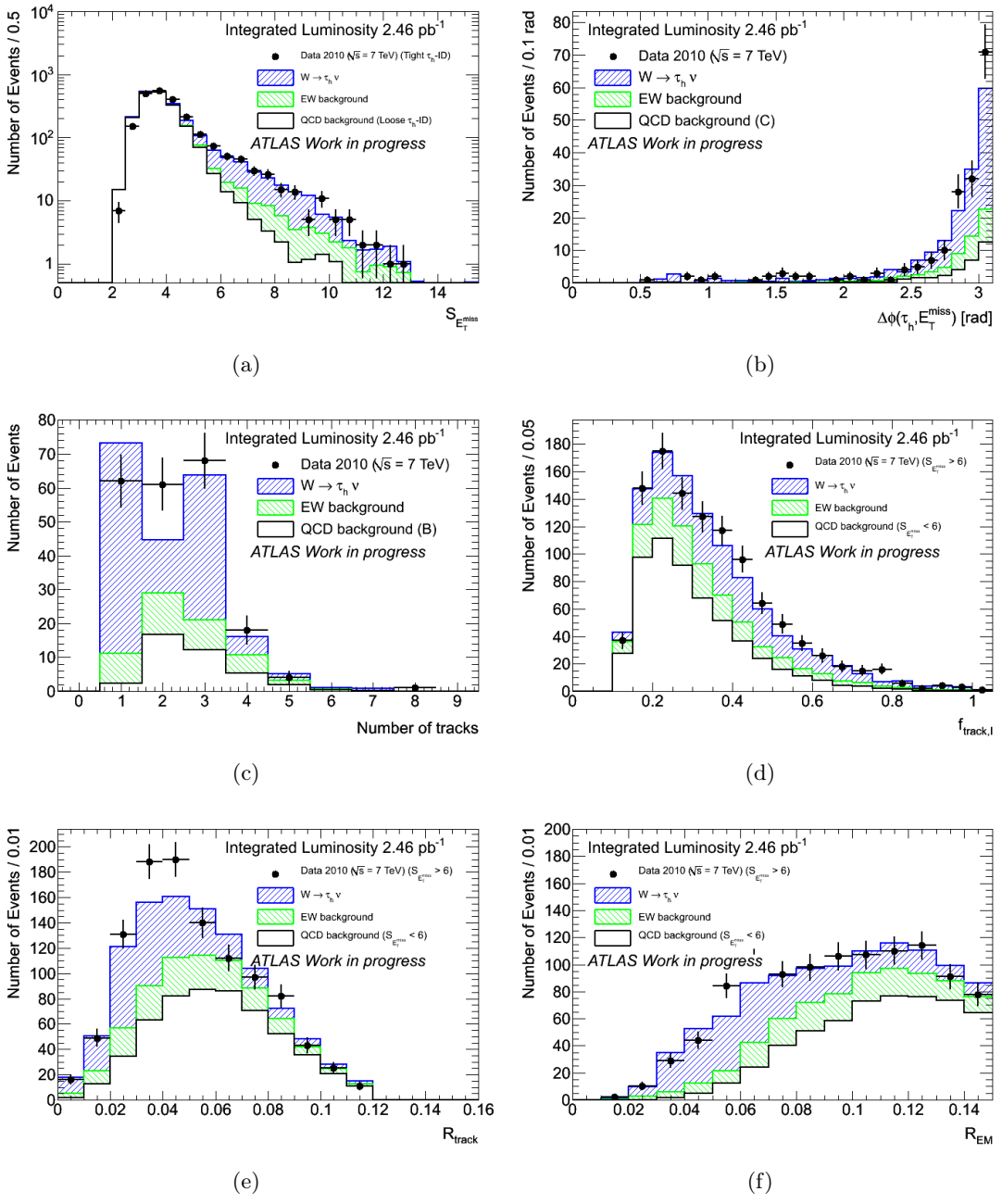

Figure 5.19: Comparison of data and different control regions with the additional expected contribution of signal and EW backgrounds for τ_{h} candidates within a transverse momentum range of 30 GeV $< p_{\mathrm{T}} <$ 60 GeV. (a) $S_{E_{\mathrm{T}}^{\mathrm{miss}}}$ distribution for tight τ_{h} candidates (region AB) and loose candidates failing the tight τ_{h}-ID (region CD). (b) $\Delta\phi(\tau_{\mathrm{h}}, E_{\mathrm{T}}^{\mathrm{miss}})$ distribution for events in the signal region A and for loose candidates failing the tight τ_{h}-ID (region C). (c) Track multiplicity distribution for τ_{h} candidates. (d) - (f) Distribution of the τ_{h}-ID variables for events with $S_{E_{\mathrm{T}}^{\mathrm{miss}}}$ >6 (region AC) and $S_{E_{\mathrm{T}}^{\mathrm{miss}}}$ <6 (region BD).

Separation of 1-prong and multi-prongs τ_{h} candidates

For a further confirmation of the validity of the data-driven method to extract the QCD background, the selected events have been divided into subsamples according to their number of tracks, and the performance of the method has been studied separately. The following subsamples have been defined:

- τ_{h} candidates with exactly one track ("1-prong").
- τ_{h} candidates with more than one track ("multi-prong").

For the 1-prong candidates, the number of data events in the four defined regions as well as the Monte Carlo expectations for signal and EW backgrounds are listed in Table 5.11.

	A	B	C	D
Data	111	327	157	1556
$W \to \tau_{\mathrm{h}}\nu_\tau$	102.5±4.2	92.5±4.0	104.1±4.2	130.4±4.7
EW	12.4±0.8	12.4±0.6	15.7±0.9	13.0±0.7
c_i		0.91±0.05	1.04±0.05	1.25±0.05

Table 5.11: Number of observed events in the four regions for the data-driven estimation of QCD background for a data sample with 1-prong τ_{h} candidates. Monte Carlo estimates of the number of $W \to \tau_{\mathrm{h}}\nu_\tau$ signal and EW background events and the correction coefficients c_i are also shown.

The number of expected QCD background events obtained from the method is 8.1 ± 3.8. The distribution of kinematic and τ_{h}-ID variables for 1-prong τ_{h} candidates is shown in Figure 5.20.

For the multi-prong candidates, the number of data events in the four defined regions as well as the Monte Carlo expectations for signal and EW backgrounds are listed in Table 5.12.

	A	B	C	D
Data	186	2733	968	36900
$W \to \tau_{\mathrm{h}}\nu_\tau$	104.6±4.2	106.8±4.3	191.8±5.7	180.3±5.6
EW	34.4±1.4	20.7±1.0	180.4±3.4	114.1±2.6
c_i		0.92±0.05	2.68±0.05	2.12±0.05

Table 5.12: Number of observed events in the four regions for the data-driven estimation of QCD background for a data sample with multi-prong τ_{h} candidates. Monte Carlo estimates of the number of $W \to \tau_{\mathrm{h}}\nu_\tau$ signal and EW background events and the correction coefficients c_i are also shown.

Based on the numbers in Table 5.12 the expected QCD background in the signal region A is 41.3 ± 4.8.

For this sample of 3-prong candidates, the distribution of several important variables is shown in Figure 5.21.

Also in the case of 3-prong candidates an excellent agreement of all distributions in data and compared to the QCD control sample and the additional Monte Carlo expectation for signal and EW background can be observed.

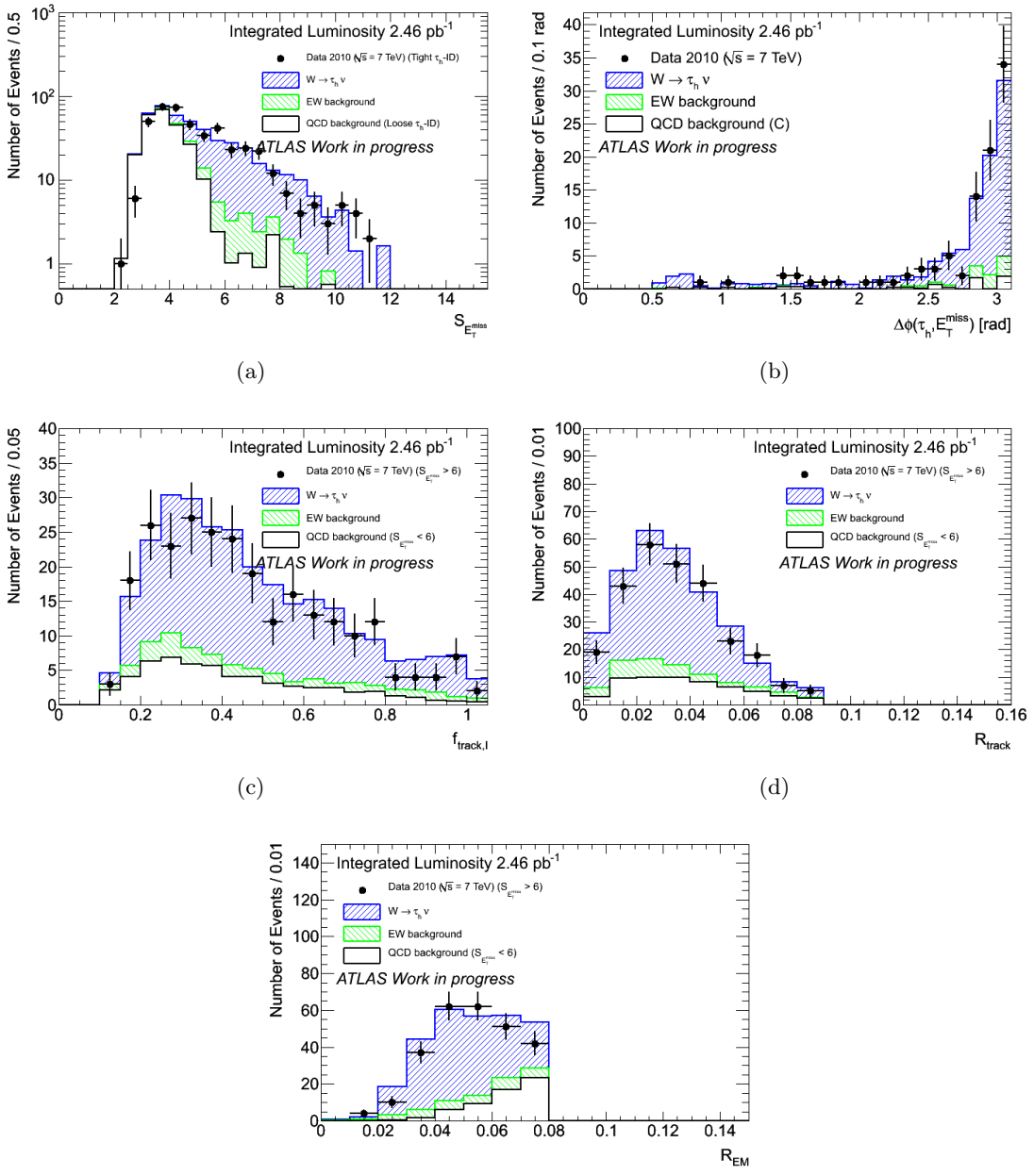

(a) (b) (c) (d) (e)

Figure 5.20: Comparison of data and different control regions with the additional expected contribution of signal and EW backgrounds for 1-prong τ_{h} candidates. (a) $S_{E_{\mathrm{T}}^{\mathrm{miss}}}$ distribution for tight τ_{h} candidates (region AB) and loose candidates failing the tight τ_{h}-ID (region CD). (b) $\Delta\phi(\tau_{\mathrm{h}}, E_{\mathrm{T}}^{\mathrm{miss}})$ distribution for events in the signal region A and for loose candidates failing the tight τ_{h}-ID (region C). (c) - (e) Distribution of the τ_{h}-ID variables for events with $S_{E_{\mathrm{T}}^{\mathrm{miss}}}$ >6 (region AC) and $S_{E_{\mathrm{T}}^{\mathrm{miss}}}$ <6 (region BD).

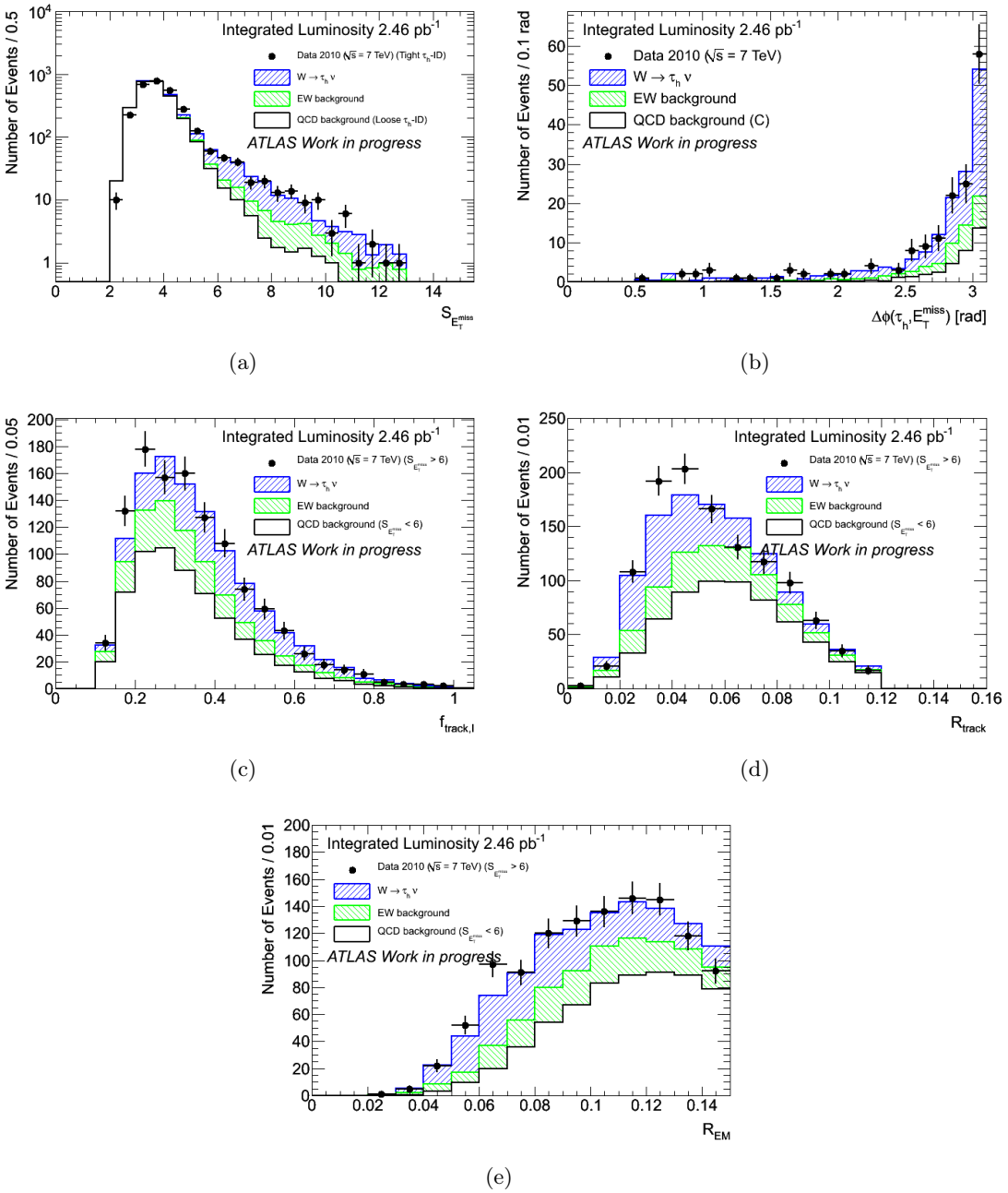

Figure 5.21: Comparison of data and different control regions with the additional expected contribution of signal and EW backgrounds for multi-prong τ_{h} candidates. (a) $S_{E_{\mathrm{T}}^{\mathrm{miss}}}$ distribution for tight τ_{h} candidates (region AB) and loose candidates failing the tight τ_{h}-ID (region CD). (b) $\Delta\phi(\tau_{\mathrm{h}}, E_{\mathrm{T}}^{\mathrm{miss}})$ distribution for events in the signal region A and for loose candidates failing the tight τ_{h}-ID (region C). (c) - (e) Distribution of the τ_{h}-ID variables for events with $S_{E_{\mathrm{T}}^{\mathrm{miss}}}$ >6 (region AC) and $S_{E_{\mathrm{T}}^{\mathrm{miss}}}$ <6 (region BD).

In addition, the extracted numbers for the QCD background in the signal region A, obtained separately for the subsamples of 1-prong and 3-prongs τ_{h} candidates are consistent with the total number of QCD background estimated with this method for the whole data sample of 47.8 ± 4.7 events, which again corroborates the reliability of this method.

Redefining the signal and control regions

Another test consists in redefining the signal and control regions in the following way:

- Region A: events with $S_{E_{\rm T}^{\rm miss}} > 4$ and $\tau_{\rm h}$ candidates satisfying the tight $\tau_{\rm h}$-ID;
- Region B: events with $S_{E_{\rm T}^{\rm miss}} < 4$ and $\tau_{\rm h}$ candidates satisfying the tight $\tau_{\rm h}$-ID;
- Region C: events with $S_{E_{\rm T}^{\rm miss}} > 4$ and $\tau_{\rm h}$ candidates satisfying the loose $\tau_{\rm h}$-ID but failing the tight $\tau_{\rm h}$-ID;
- Region D: events with $S_{E_{\rm T}^{\rm miss}} < 4$ and $\tau_{\rm h}$ candidates satisfying the loose $\tau_{\rm h}$-ID but failing the tight $\tau_{\rm h}$-ID;

In this way the four regions are all dominated by the QCD background. The results of this test are used to estimate the systematic effect connected with the correlation between $S_{E_{\rm T}^{\rm miss}}$ and the $\tau_{\rm h}$ identification (Section 5.7.6).

The number of events in the new regions are shown in Table 5.13.

	A	B	C	D
Data	1510	1847	12641	26940
$W \to \tau_{\rm h}\nu_\tau$	385.7±8.1	20.8±1.9	565.2±9.7	41.4±2.7
EW	76.2±2.0	3.7±0.4	306.0±4.3	17.2±1.0
c_i		0.05±0.34	1.89±0.02	0.13±0.14

Table 5.13: Number of observed events in the four regions for the data-driven estimation of QCD background, where the four regions have been redefined as described in the text. Monte Carlo estimates of the number of $W \to \tau_{\rm h}\nu_\tau$ signal and EW background events and the correction coefficients c_i are also shown.

Based on the numbers in Table 5.13 the expected QCD background in the signal region A is 755 ± 23.

Study of τ_{h} medium candidates

As a final consistency test for the data-driven method, the number of QCD background is also estimated for a looser τ_{h}-ID selection, replacing the tight by the medium τ_{h} ID requirement. The number of data events in the four defined regions as well as the Monte Carlo expectations for signal and EW backgrounds are listed in Table 5.14. The number of estimated QCD background in region A is 240.4±25.4.

	A	B	C	D
Data	786	16474	654	26383
$W \to \tau_{\mathrm{h}}\nu_\tau$	376.5±8.0	392.8±8.2	128.4±4.7	120.0±4.5
EW	132.1±2.8	91.1±2.2	113.5±2.7	69.0±2.0
c_i		0.95±0.02	0.48±0.04	0.37±0.05

Table 5.14: Number of observed events in the four regions for the data-driven estimation of QCD background for a data sample with medium τ_{h} candidates. Monte Carlo estimates of the number of $W \to \tau_{\mathrm{h}}\nu_\tau$ signal and EW background events and the correction coefficients c_i are also shown.

Also for these events several characteristic variables are shown. Figure 5.22 shows the $S_{E_{\mathrm{T}}^{\mathrm{miss}}}$ distribution for data in the signal region A and the QCD control region combined with the expected signal and EW contributions, from Monte Carlo simulation.

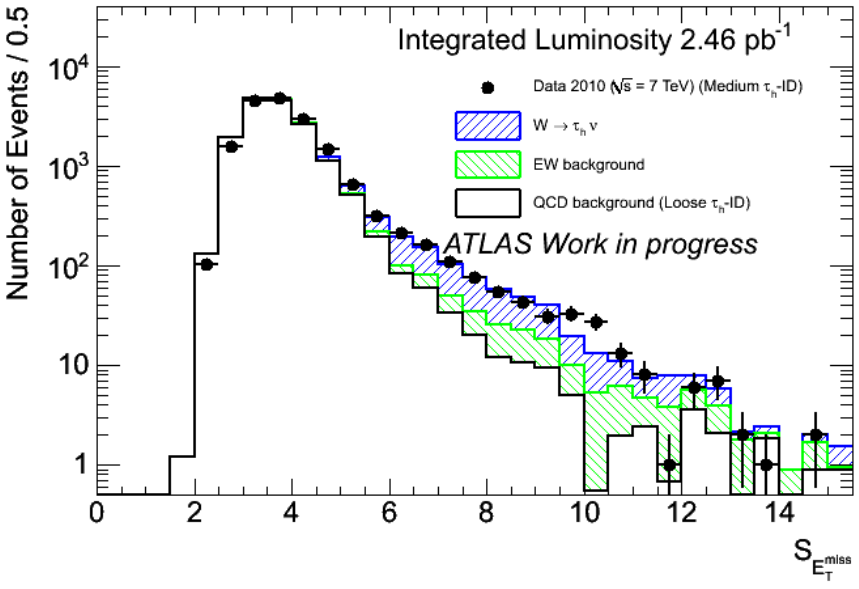

Figure 5.22: $S_{E_{\mathrm{T}}^{\mathrm{miss}}}$ distribution for the combined region AB (medium τ_{h}-ID region). QCD background is evaluated from the combined control region CD (loose τ_{h}-ID region). Monte Carlo signal and EW background in region AB are also shown.

Figures 5.23, 5.24 and 5.25 show the distributions of the number of track, kinematic and τ_{h}-ID variables for the medium τ_{h} candidates.

The results show again a good agreement among the distributions, indicating a very good reliability of the data-driven method.

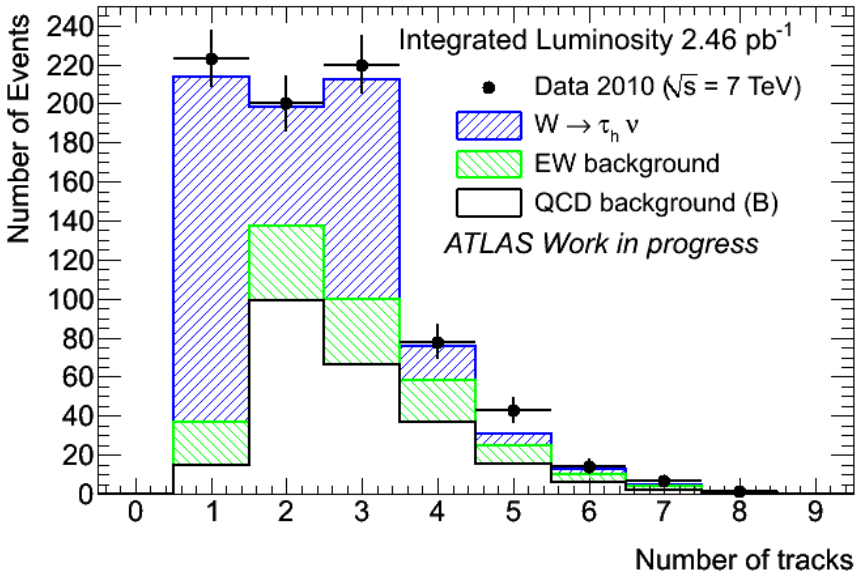

Figure 5.23: Distribution of the number of tracks of the τ_h candidates in signal region A. Data is shown as well as Monte Carlo signal and EW background. QCD background shape has been extracted from control region C and then normalised to N^A_{QCD}.

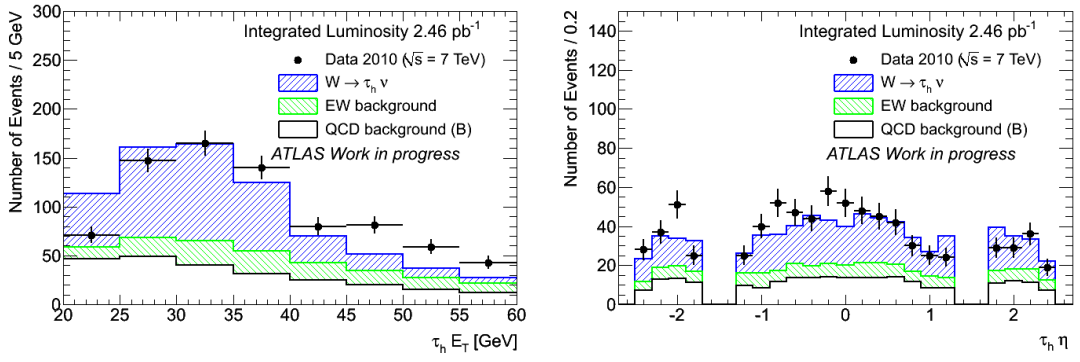

(a) (b)

Figure 5.24: Distribution of (a) the p_T spectrum and (b) η of the τ_h candidates. Data is shown as well as Monte Carlo signal and EW background. QCD background has been estimated in control region B.

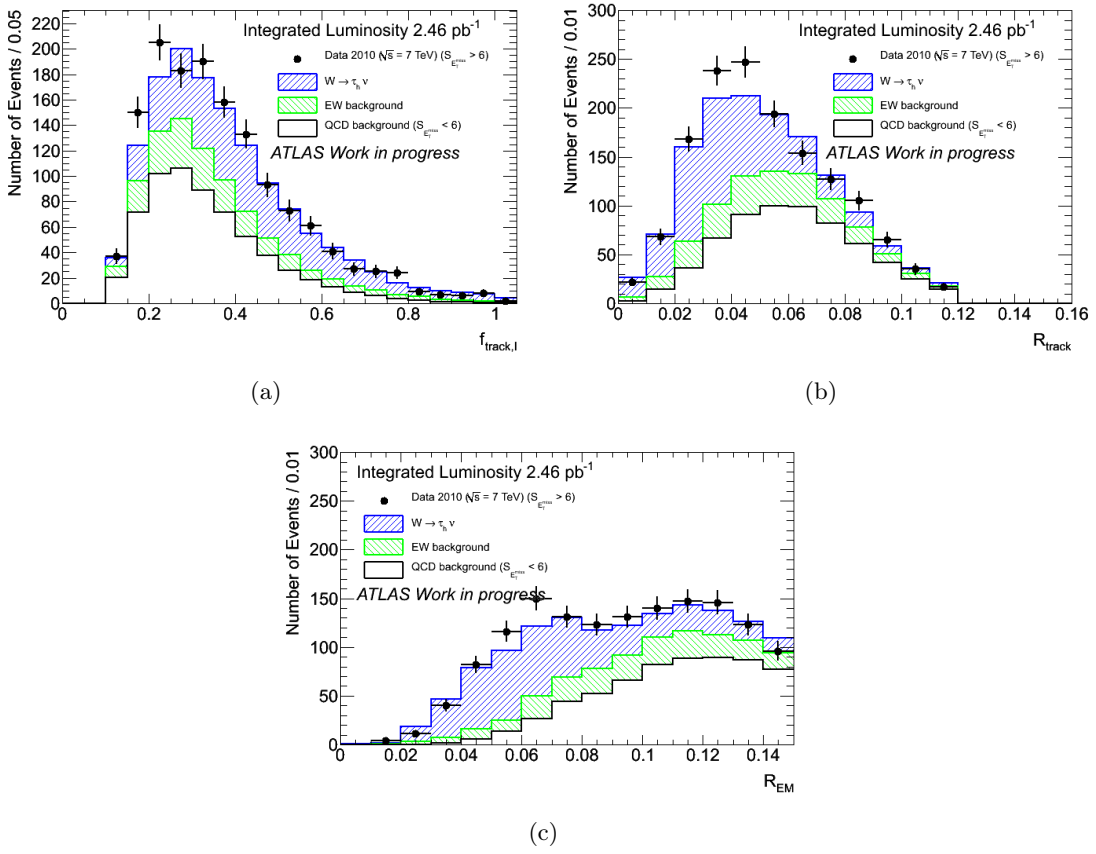

Figure 5.25: Distribution of the τ_{h}-ID variables for the regions with $S_{E_{\mathrm{T}}^{\mathrm{miss}}}$ >6 and $S_{E_{\mathrm{T}}^{\mathrm{miss}}}$ <6 (regions AC and BD) combined with the expected signal and EW background contributions from simulation.

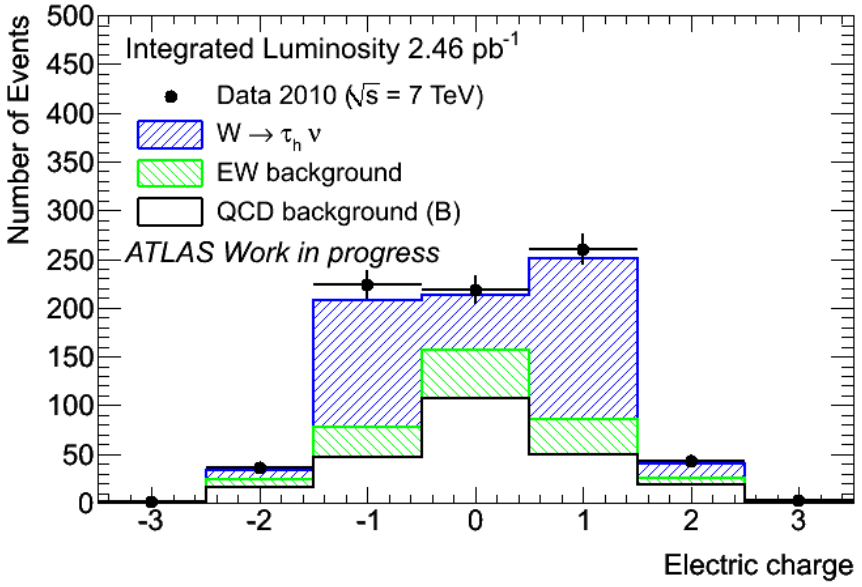

Figure 5.26: Distribution of the electric charge of the τ_{h} candidates in signal region A. Data is shown as well as Monte Carlo signal and EW background. QCD background shape has been extracted from control region B and then normalised to $\mathrm{N}^{\mathrm{A}}_{\mathrm{QCD}}$.

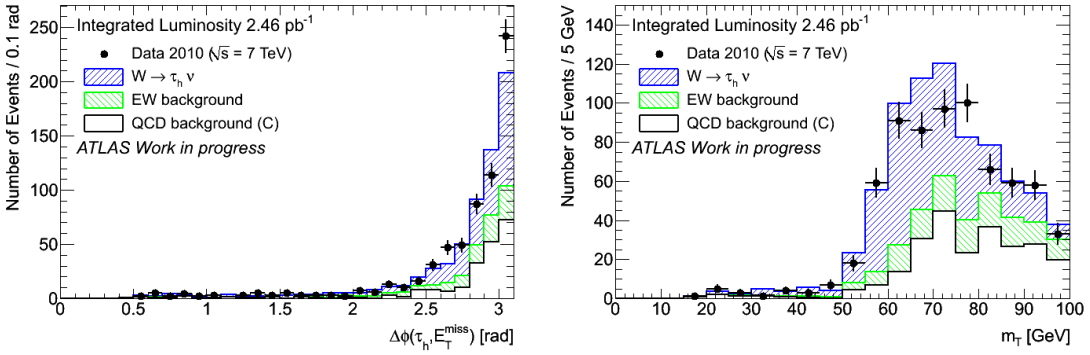

(a) (b)

Figure 5.27: Distributions of (a) $\Delta\phi(\tau_{\mathrm{h}}, E_{\mathrm{T}}^{\mathrm{miss}})$ and (b) of transverse mass m_{T} for data in the signal region A, combined with Monte Carlo signal and EW background. The QCD background shape is extracted from control region C. The QCD background distributions are normalised to the expected number of events in the signal region ($\mathrm{N}^{\mathrm{A}}_{\mathrm{QCD}}$).

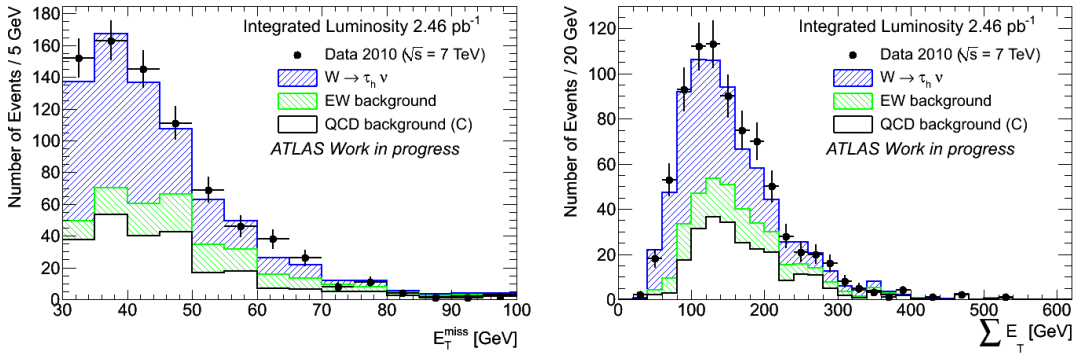

(a) (b)

Figure 5.28: Distributiona of (a) $E_{\mathrm{T}}^{\mathrm{miss}}$ and of (b) $\sum E_{\mathrm{T}}$, in signal region A. Data is shown as well as Monte Carlo signal and EW background. QCD background shape has been extracted from control region C and then normalised to $\mathrm{N}_{\mathrm{QCD}}^{\mathrm{A}}$.

5.7 Evaluation of systematic uncertainties

To claim for the observation of $W \to \tau_{\mathrm{h}}\nu_\tau$ decays it is important to assess the systematic uncertainties affecting the number of events expected, both for signal and for backgrounds. The systematic uncertainties on the backgrounds are needed to define the signal significance, while the systematic uncertainties connected with the number of expected signal events allows to understand if the observed number of events is compatible with Monte Carlo estimations.

In this section the various sources of systematic effects are presented, both for the number of Monte Carlo signal and EW background expected events, and for the number of QCD background events extracted from data. Table 5.15 summarizes the resulting systematic uncertainties.

	signal	EW background	QCD background
Central values [events]	207.2	46.9	47.8
Statistical error [events]	±6.0	±1.6	±4.7
Systematic uncertainties			
Theoretical cross section	± 5%	±5%	–
Luminosity	± 11%	±11%	–
Energy scale	±21%	±14%	–
Electron veto	–	±5%	–
Muon veto	–	±16%	–
Monte Carlo tuning	±16%	±15%	–
Data driven QCD estimation	–	–	±29%
Total systematic uncertainty [events]	±60.2	±13.7	±13.9

Table 5.15: Summary of the systematic uncertainties for simulated signal and EW backgrounds and for the data-driven estimation of the QCD background. The single systematic uncertainties are quoted as relative values, while the resulting total uncertainties are quoted as absolute values.

5.7.1 Cross section and luminosity

The expected number of signal and EW background events is computed from Monte Carlo samples and scaled according to their NNLO cross sections and the integrated luminosity of the data sample.

The systematic uncertainties connected with the cross section has been evaluated already in the context of the W cross section measurement (in the electron and muon channels) in ATLAS and it has been estimated to be 5% [103]. This uncertainty was obtained using the MSTW 08 NNLO PDF error eigenvectors at the 90% C.L. limit, variations of α_S in the range 0.1145 – 0.1176, and variations of the renormalisation and factorisation scales by factors of two around the nominal scales $\mu_R = \mu_F = m_{W/Z}$.

For the systematic uncertainty connected with luminosity calculation, the absolute luminosity calibration obtained from van der Meer beam scans at $\sqrt{s} = 7$ TeV have a systematic uncertainty of 11% which is dominated by the uncertainty in the bunch intensities [55].

5.7.2 Energy scale

The signal acceptance depends on the energy scale of the topological clusters used in the computation of $E_{\rm T}^{\rm miss}$ and $S_{E_{\rm T}^{\rm miss}}$. At the current level of detector calibration in the region $|\eta| < 3.2$, the uncertainty on the energy scale is better than 7% for energetic clusters. In the forward region $|\eta|$ >3.2, it is estimated to be 10%. In addition, the yield of signal and EW background events is sensitive to the resolution of $E_{\rm T}^{\rm miss}$.

To evaluate the energy scale uncertainties, the checks have been performed following the same procedures as in [104]: topocluster energies have been scaled within their uncertainties. The $E_{\rm T}^{\rm miss}$ and $\sum E_{\rm T}$ have been recomputed accordingly. In the test on the energy scale for $|\eta| < 3.2$, also the tau energy has been rescaled, using the rescaled topocluster. The description of tests is given below. Test results are summarized in Table 5.16 for signal and the main EW background contributions. As systematic uncertainty the maximum deviations for each of the four tests are summed in quadrature. Since the upper and lower variation are very similar, it is preferred to quote symmetric uncertainties on the acceptances for signal and EW background of ±21% and ±14%, respectively.

Topological cluster energy scale

The transverse energy originating in W and Z events is mainly deposited in the central region of the calorimeter ($|\eta| < 3.2$). The uncerainty on the cluster energy scale is derived from E/p studies on single hadrons [105, 106] as the difference between data and Monte Carlo simulation. It is at most 20% for $p_{\rm T}$ of 500 MeV and within 5% at high $p_{\rm T}$. Clusters in this angular region have been scaled according to a factor $1 + a\left(1 + \frac{N-1}{p_{\rm T}}\right)$ where a indicates the jet energy scale deviation at high momentum and N is fixed to give a 20% scale factor at 500 MeV. Different values of a have been used to cover conservatively the above uncertainties. The $\tau_{\rm h}$ $E_{\rm T}$ has also been scaled according to the $E_{\rm T}$ variation of the topological clusters associated to the reconstructed $\tau_{\rm h}$ candidate.

The variations (summarised in Table 5.16) are larger than the 3% systematic mismatch between the reconstructed and the true visible energy of the tau, as shown in Figure 5.29. The mismatch has been evaluated also on Monte Carlo signal sample with different tuning of the underlying event (DW sample) and was found to be compatible with the mismatch found in MC09 samples.

The effect of the variation of the energy scale for $|\eta| < 3.2$ on $E_{\rm T}^{\rm miss}$, $S_{E_{\rm T}^{\rm miss}}$ and the selected tau energy are shown in Figure 5.30 for the signal, and in Figures 5.31 and 5.32 for the $W \to \tau_\ell\nu_\tau$ and $Z \to \tau\tau$ samples. The $E_{\rm T}^{\rm miss}$ distribution is shown for events just before and just after the requirement on $E_{\rm T}^{\rm miss}$, as well as the distribution of $S_{E_{\rm T}^{\rm miss}}$. The distribution of the selected tau energy is shown for events just before and after the cut on the tau energy.

In the forward region ($|\eta| > 3.2$) the energy scale uncertainty is estimated from data to be $a = \pm 10\%$ [106] and therefore FCal clusters have been scaled by that amount.

$E_{\rm T}^{\rm miss}$ resolution

The resolution on $E_{\rm T}^{\rm miss}$ is measured to be $0.49\sqrt{\sum E_{\rm T}}$ in minimum bias events (see Chapter 3), but it is slightly degraded when requiring the presence of high-$p_{\rm T}$ jets [74]. The sensitivity to the $E_{\rm T}^{\rm miss}$ resolution has been checked adding a gaussian smearing on the x and y components of $E_{\rm T}^{\rm miss}$, in order to reproduce in the simulation a $E_{\rm T}^{\rm miss}$ resolution of $\alpha\sqrt{\sum E_{\rm T}}$, with a range of values for α which covers the uncertainty due to te presence of high-$p_{\rm T}$ jets.

	$W \to \tau_{\mathrm{h}}\nu_\tau$	$W \to e\nu_e$	$W \to \mu\nu_\mu$	$W \to \tau_\ell\nu_\tau$	$Z \to \tau\tau$	Total EW background
Expected events	207.2	16.3	14.4	8.2	7.6	46.9
Systematics uncertainties						
relative	+22%	+12%	+7%	+12%	+29%	+13%
	-20%	-14%	-5%	-12%	-34%	-14%
events	+45.6	+2.0	+1.0	+1.0	+2.2	+6.2
	-41.4	-2.3	-0.7	-1.0	-2.6	-6.6
Energy scale $\lvert\eta\rvert < 3.2$						
a $N-1$						
0.07 0.93	+14%	+7%	-6%	+5%	+20%	
0.06 1.17	+12%	+6%	-6%	+7%	+16%	
0.05 1.50	+9%	+5%	-5%	+9%	+13%	
-0.05 1.50	-9%	+1%	+4%	-5%	-4%	
-0.06 1.17	-13%	0%	+2%	-5%	-7%	
-0.07 0.93	-17%	-1%	-2%	-5%	-11%	
Energy scale $\lvert\eta\rvert > 3.2$						
a						
0.10	-1%	-1%	-3%	-8%	-2%	
-0.10	+3%	+4%	+1%	0%	+4%	
$E_{\mathrm{T}}^{\mathrm{miss}}$ resolution						
α [GeV $^{1/2}$]						
0.50	+1%	-1%	0%	+2%	+8%	
0.55	+5%	+2%	-1%	+8%	+9%	
0.60	+7%	+6%	-1%	+6%	+16%	
0.65	+11%	+8%	0%	+6%	+25%	
Excluding FCAL inner ring	+8%	+9%	+3%	+2%	+10%	

Table 5.16: Relative variation of acceptances for the systematics tests on the topological cluster energy scale, for signal and EW backgrounds

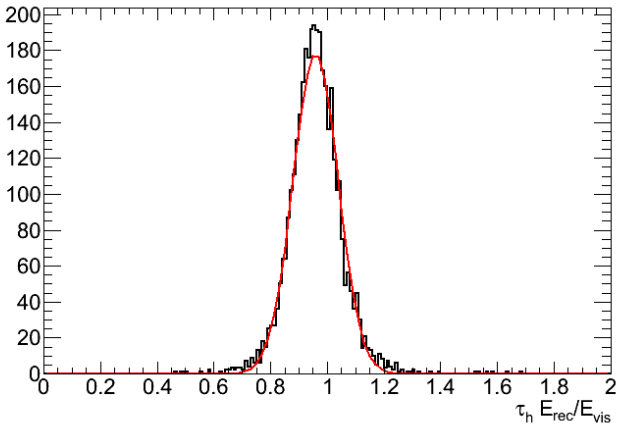

(a)

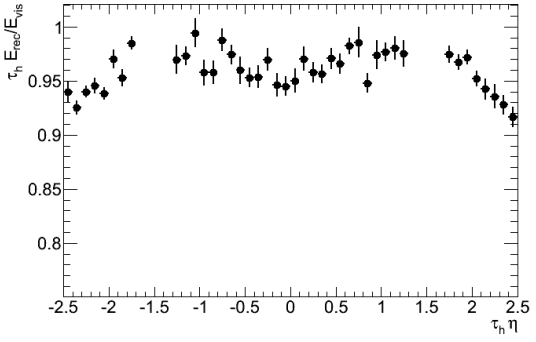

(b)

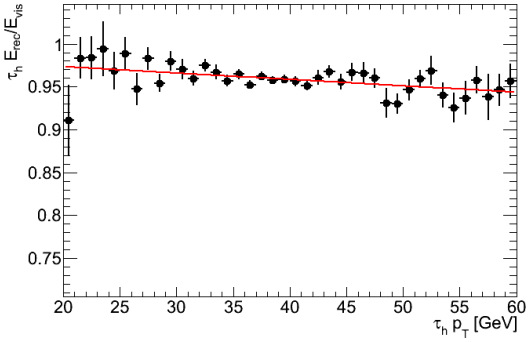

(c)

Figure 5.29: (a) Mismatch between the reconstructed and the true visible energy of the tau candidate. The distribution has been fitted with a gaussian distribution, whose mean is 0.97 and sigma is 0.08. (b) Mismatch as a function of η and (c) of the τ_{h} p_{T} . The mismatch dependence on p_{T} is 0.98-0.0003p_{T} .

Energy reconsctruction in FCAL inner ring

The energy reconstruction in the FCal inner ring cells, $|\eta| > 4.5$, is poorly reproduced in Monte Carlo. The impact of excluding this region when computing $E_{\mathrm{T}}^{\mathrm{miss}}$ and $\sum E_{\mathrm{T}}$ is mainly a reduction of $\sum E_{\mathrm{T}}$ and therefore an increase in the acceptance for the $S_{E_{\mathrm{T}}^{\mathrm{miss}}}$ selection.

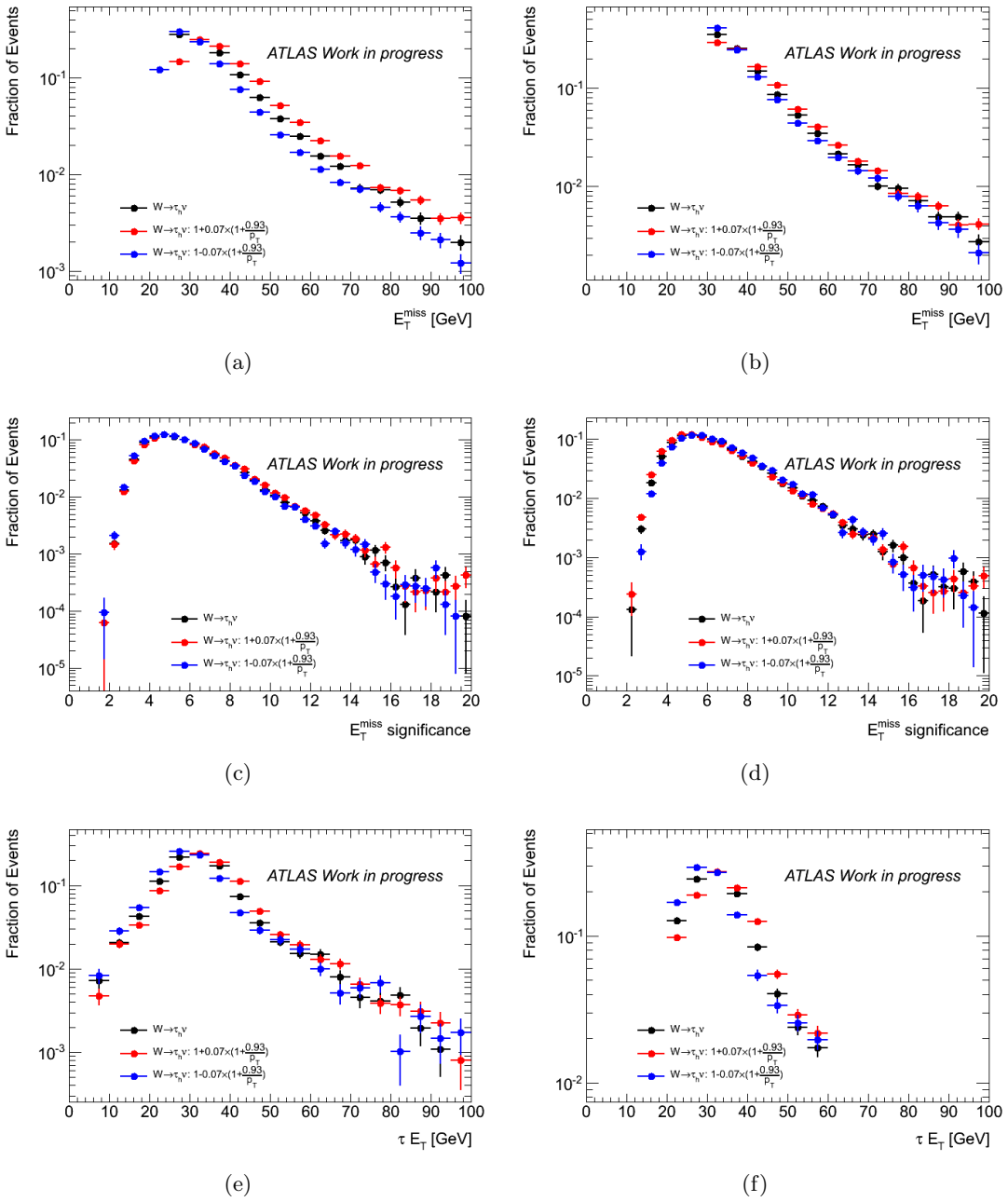

Figure 5.30: $E_{\mathrm{T}}^{\mathrm{miss}}$, $S_{E_{\mathrm{T}}^{\mathrm{miss}}}$ and selected tau energy distribution for signal events, when varying the topological cluster energy scale. The $E_{\mathrm{T}}^{\mathrm{miss}}$ distribution is shown for events just before (left) and just after (right) the requirement on $E_{\mathrm{T}}^{\mathrm{miss}}$, as well as the distribution of $S_{E_{\mathrm{T}}^{\mathrm{miss}}}$. The distribution of the selected tau energy is shown for events just before (left) and after (right) the cut on the tau energy.

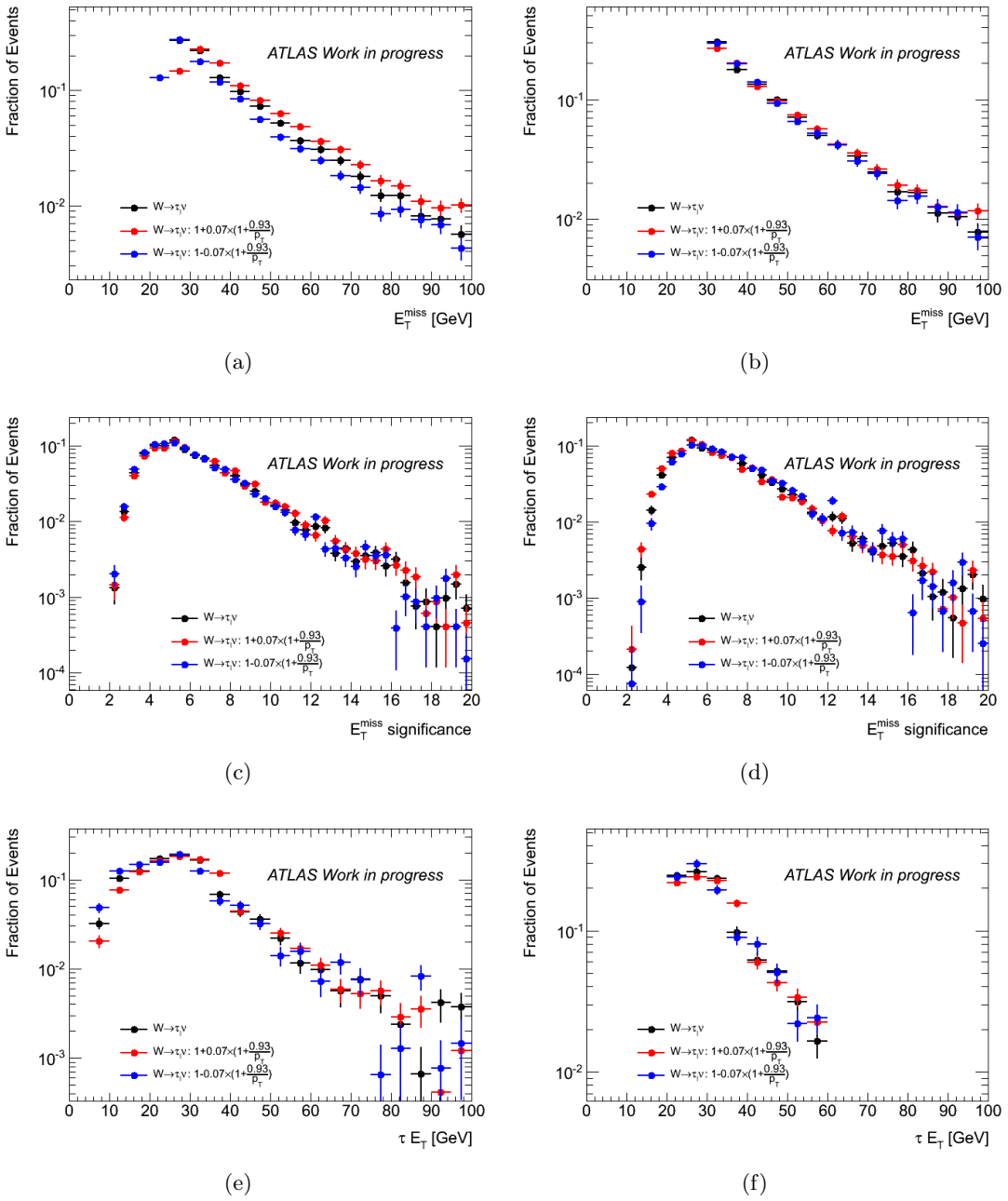

Figure 5.31: $E_{\mathrm{T}}^{\mathrm{miss}}$, $S_{E_{\mathrm{T}}^{\mathrm{miss}}}$ and selected tau energy distribution for $W \to \tau_\ell\nu_\tau$ events, when varying the topological cluster energy scale. The $E_{\mathrm{T}}^{\mathrm{miss}}$ distribution is shown for events just before (left) and just after (right) the requirement on $E_{\mathrm{T}}^{\mathrm{miss}}$, as well as the distribution of $S_{E_{\mathrm{T}}^{\mathrm{miss}}}$. The distribution of the selected tau energy is shown for events just before (left) and after (right) the cut on the tau energy.

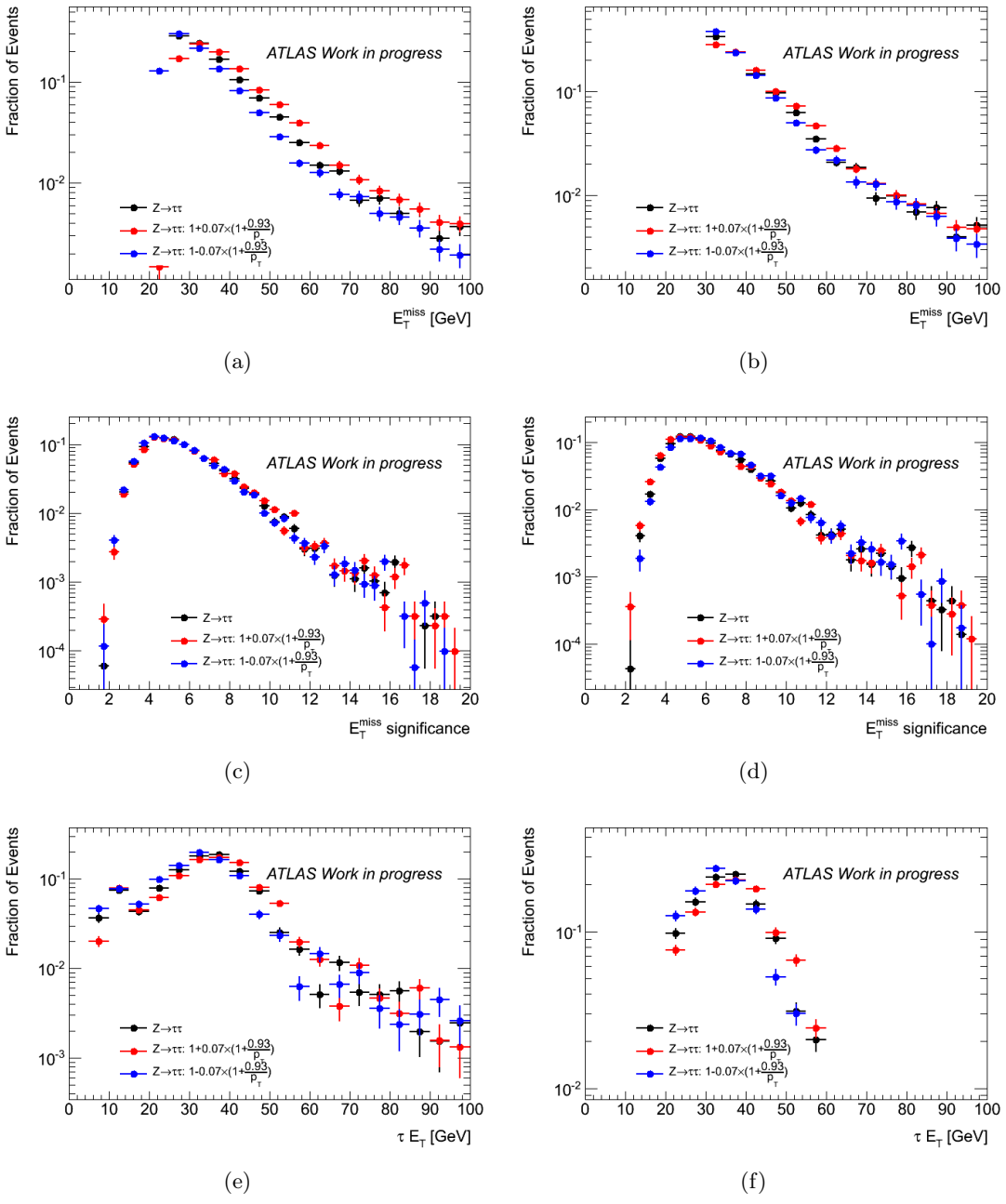

Figure 5.32: $E_{\mathrm{T}}^{\mathrm{miss}}$, $S_{E_{\mathrm{T}}^{\mathrm{miss}}}$ and selected tau energy distribution for $Z \to \tau\tau$ events, when varying the topological cluster energy scale. The $E_{\mathrm{T}}^{\mathrm{miss}}$ distribution is shown for events just before (left) and just after (right) the requirement on $E_{\mathrm{T}}^{\mathrm{miss}}$, as well as the distribution of $S_{E_{\mathrm{T}}^{\mathrm{miss}}}$. The distribution of the selected tau energy is shown for events just before (left) and after (right) the cut on the tau energy.

5.7.3 Electron Veto

Since the variables used for the τ_{h}-ID do not discriminate between τ hadronic decays and electrons, providing a reliable estimate of the efficiency of the electron veto algorithm described in Section 2.4 is important for the expected signal estimation. Its fake rate, that is the probability that a real electron is not rejected by the algorithm, instead affects directly the background estimation. It is therefore of paramount importance to verify and, if needed, to correct the Monte Carlo evaluation with data-driven techniques.

The Monte Carlo efficiency was estimated selecting an independent sample of τ_{h} candidates. The potential systematic uncertainty on the number of hadronic τ decays passing the electron veto flag has been computed based on a sample of jets misidentified as tight τ_{h} candidates in the following way. The efficiency of the electron veto has been defined as a fraction of τ_{h} candidates passing the tight τ_{h}-ID requirements described in Section 2.3 and electron veto (using the tight veto) with respect to all tau candidates passing the τ_{h}-ID tight selection. The selected τ_{h} candidates were also required to be identified as neither loose electrons nor combined muons. This efficiency has been measured in data and in simulations, yielding (87.7±0.8) % and (87.6±1.0) % respectively. Given the good agreement between these numbers, no systematic uncertainty is assigned for the effect of the electron veto on the QCD background.

The uncertainty on the effect of the electron veto in rejecting high momentum electrons has been accessed using a "tag-and-probe" method on a sample of $Z \to ee$ events. One electron is selected as the tag object and a the second one is selected as a probe object when it has been misidentified as a τ_{h} candidate. In this method, the electron to τ fake rate is defined as the ratio of the number of events where the probe passes τ_{h} identification and the electron veto and the number of events passing the τ_{h} identification. The tag electron is required to be selected by the tight electron identification with $E_{\mathrm{T}} > 20$ GeV lying centrally in the detector and outside the gap in the calorimeter systems ($|\eta| < 1.37$ or $1.52 < |\eta| < 2.47$). As a probe candidate a tight τ_{h} candidate seeded by both reconstruction algorithms is selected, with the same E_{T} and pseudorapidity requirements as the tag electron and with a distance $\Delta\mathrm{R} > 0.4$ from it. In addition, an opposite sign of the electric charge of tag electron and probe τ_{h} candidate is required. This selection provides a pure sample of $Z \to ee$ events. Only pairs which have an invariant mass within the range 80 to 100 GeV are considered for the estimation of the fake rate.

The measured fake rate in data is $(0.06 \pm 0.02)\%$, which has to be compared to the Monte Carlo estimation of $(0.07 \pm 0.04)\%$. Due to the limited number of events in data a method to estimate the remaining background of QCD and other EW processes could not yet be applied.

The ratio of the fake rate between data and simulation is therefore 0.85 ± 0.57. This difference of 15% between data and simulation is used as a systematic uncertainty on the $W \to e\nu_e$ background rate and results in an overall systematic uncertainty of 5% on the EW background.

5.7.4 Muon veto

The background coming from $W \to \mu\nu_\mu$ and $Z \to \mu\mu$ processes is suppressed by rejecting events if there is a combined muon reconstructed by the STACO [107] algorithm with $p_{\mathrm{T}} > 5$ GeV. The efficiency of this suppression cannot be cross checked with the same tag and probe method as for the electron veto because in most cases (∼83%) the τ_{h}-candidate is a QCD jet from the underlying event and not a muon from the W and Z decay (as it can be seen in Figure 5.2(b)).

In this case, the rate of backgrond events passing the muon veto is proportional to the muon reconstruction inefficiency. This has been assessed with the standard tag-and-probe techniques on the $Z \to \mu\mu$ samples for the measurement of the W cross section. From a recent review of the results from different groups [108], the Monte Carlo estimation of the muon reconstruction efficiency for STACO is ∼92%. Comparison with data shows a dependence of the efficiency from the running conditions and for the period corresponding to the data sample used in this analysis it is 88%.

Taking the difference between data and Monte Carlo estimation as the systematic error, the muon reconstruction inefficiency is evaluated to be (8 ± 4) %. This 50% uncertainty on the reconstruction inefficiency translates in a systematic error of 7.3 events over the combined $W \to \mu\nu_\mu$ and $Z \to \mu\mu$ background of 14.7 events and in an overall systematic uncertainty on the EW background of 16%.

5.7.5 Underlying event modelling

Concerning the description of the underlying event, there is a discussion going on in the physics community about which is the Monte Carlo tuning that better describes data. It has been recently shown that the DW tune [70] of Pythia, which uses virtuality-ordered showers and was derived to describe the CDF II underlying event and Drell-Yan data, models the forward activity of the underlying event better than the MC09 tune [68], which is the default for Pythia. On the other hand this tuning turned out to be not very good in the description of charge multiplicity.

As it has been shown in Chapter 2, the variables used to identify $\tau_{\rm h}$ are better described by the DW tune of the underlying event. This fact suggests to use Monte Carlo with DW tune for the analysis. But, as Monte Carlo sample with this tune and simulated pile-up events are not available at the moment, the only viable solution is to give systematic uncertainty on the underlying event modelling.

The systematic uncertainty was evaluated by comparing signal and EW background samples simulated without pile-up and with the two different description of the underlying event: MC09 and DW.

In Tables 5.17, 5.18 it is shown the cut-flow for different signal Monte Carlo samples: the first column refers to the default Pythia tune, the second column refers to the DW tune and the last column is the cut-flow for simulated events with MC09 tune and pile-up. From these tables it can be seen that the main difference between MC09 and DW concerns the cut on $S_{E_{\rm T}^{\rm miss}}$, which is strictly connected with the underlying event. The effect on trigger is about 1.7% and the one on tau identification is approximately 1%. The systematic is evaluated to be 16%.

Figure 5.33 shows the distributions of $E_{\rm T}^{\rm miss}$ and $S_{E_{\rm T}^{\rm miss}}$ related quantities for Monte Carlo signal, comparing simulations with MC09 and DW tunings. The plots on the left refer to events passing the event selection (Section 5.4) up to the cut on $E_{\rm T}^{\rm miss}$ (included). The plots on the right show the same distributions for events passing the full events selection but the cut on $S_{E_{\rm T}^{\rm miss}}$. From the plots on $\sum E_{\rm T}$ it can be seen how the Monte Carlo with the DW tune has a higher $\sum E_{\rm T}$, as the underlying event contribution is larger.

Concerning the EW background, the samples with DW tune were available only for $Z \to \tau\tau$ and $W \to \tau_\ell\nu_\tau$ channels. The effect on the $W \to e\nu_e$ channel is expected to be of similar size, since it has a sensitivity on $\sum E_{\rm T}$ comparable to the $\tau_{\rm h}$ channels, as can be seen from the results of the forward energy test shown in Table 5.16. The $W \to \mu\nu_\mu$ channel should be instead be much less sensitive. So the effect of the tuning has been conservatively evaluated only on τ channels and the highest of the two systematics (15%

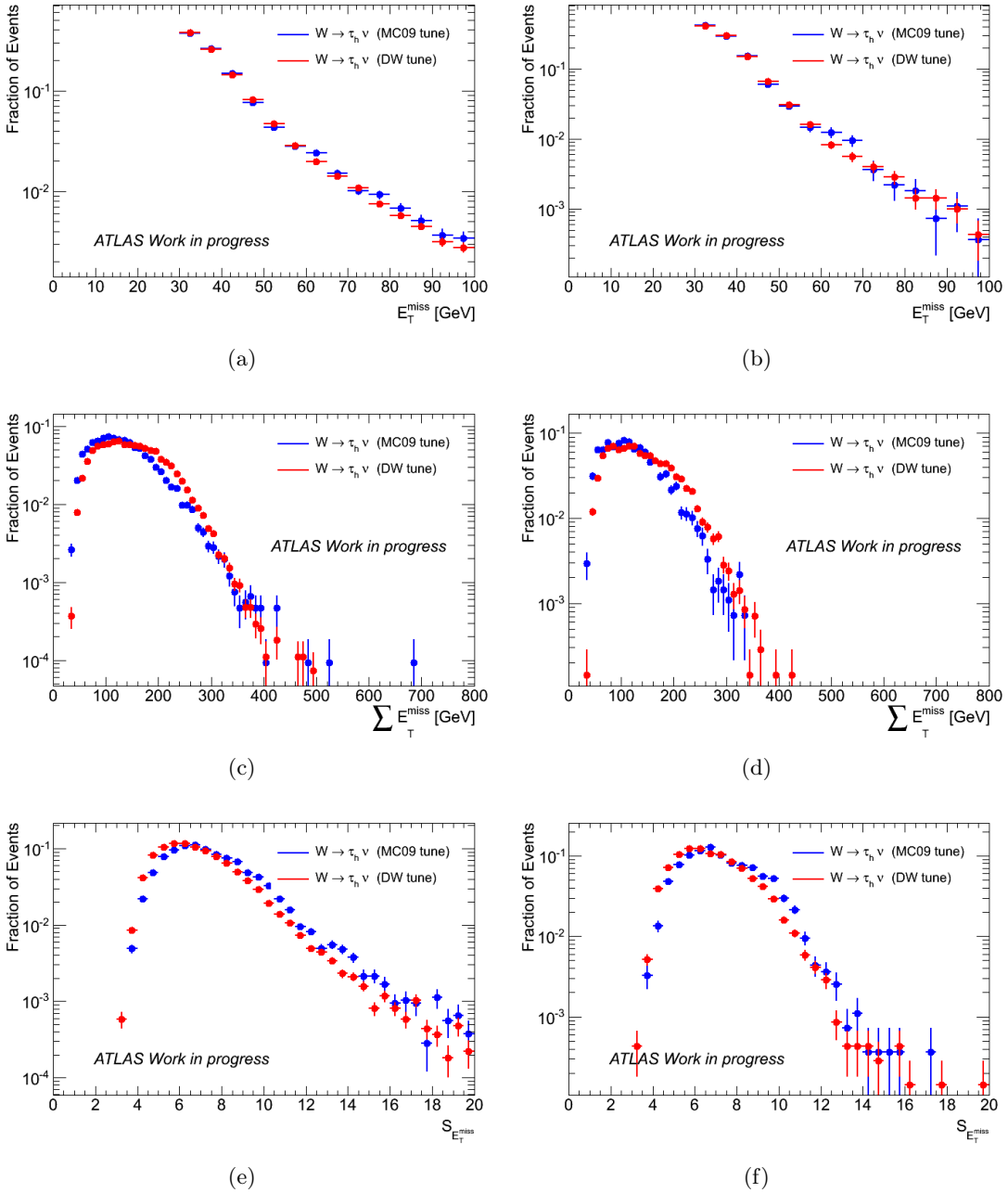

Figure 5.33: $E_{\mathrm{T}}^{\mathrm{miss}}$, $S_{E_{\mathrm{T}}^{\mathrm{miss}}}$ and $\sum E_{\mathrm{T}}$ distributions for signal events, for Monte Carlo with MC09 and DW tunings. The plots on the left refer to events passing the cut on $E_{\mathrm{T}}^{\mathrm{miss}}$ and the plots on the right show events just before the cut on $S_{E_{\mathrm{T}}^{\mathrm{miss}}}$.

for $Z \to \tau\tau$ and 11% for $W \to \tau_\ell\nu_\tau$) has been considered for all the EW backgrounds. In Tables 5.21, 5.22 and 5.19, 5.20, the cut-flows for Monte Carlo $Z \to \tau\tau$ and $W \to \tau_\ell\nu_\tau$ are reported.

	$W \to \tau_{\mathrm{h}}\nu_\tau$ MC09	$W \to \tau_{\mathrm{h}}\nu_\tau$ DW	$W \to \tau_{\mathrm{h}}\nu_\tau$ MC09+PileUp
Events	16664.7	16664.7	16664.7
Skimming	5606.5±24.8	5512.2±15.2	6033.5±25.8
Trigger	3294.9±20.9	3186.6±12.7	3473.6±21.8
Collision cleaning	3285.7±20.9	3184.4±12.7	3445.1±21.8
Jet cleaning	3254.5±20.8	3150.2±12.6	3390.6±21.6
Jet in gap veto	2642.4±19.2	2547.5±11.6	2717.2±19.9
$min(\Delta\Phi(jet, E_{\mathrm{T}}^{\mathrm{miss}})) > 0.5$	2533.2±18.8	2438.0±11.4	2577.6±19.4
$E_{\mathrm{T}}^{\mathrm{miss}} > 30$ GeV	1768.8±16.2	1705.0±9.8	1857.3±16.9
τ_{h} identification	637.6±10.1	608.2±6.0	582.0±9.9
$20 < p_{\mathrm{T}}(\tau_{\mathrm{h}}) < 60$ GeV	555.9±9.4	536.1±5.7	512.7±9.3
τ_{h} in gap veto	550.2±9.4	530.0±5.7	507.4±9.2
τ_{h}-ID electron veto	481.2±8.8	462.0±5.3	436.9±8.6
Electron veto	455.9±8.6	439.5±5.2	408.3±8.3
Muon veto	454.0±8.5	437.7±5.2	406.5±8.3
$S_{E_{\mathrm{T}}^{\mathrm{miss}}} > 6$	343.1±7.4	286.9±4.2	207.2±6.0

Table 5.17: Number of events passing the selection criteria for Monte Carlo signal with MC09 and DW tunes without pile up and with pile up.

	$W \to \tau_{\mathrm{h}}\nu_\tau$ MC09	$W \to \tau_{\mathrm{h}}\nu_\tau$ DW	$W \to \tau_{\mathrm{h}}\nu_\tau$ MC09+PileUp
Events	1	1	1
Skimming	0.336	0.331	0.362
Trigger	0.588	0.578	0.576
Collision cleaning	0.997	0.999	0.992
Jet cleaning	0.991	0.989	0.984
Jet in gap veto	0.812	0.809	0.801
$min(\Delta\Phi(jet, E_{\mathrm{T}}^{\mathrm{miss}})) > 0.5$	0.959	0.957	0.949
$E_{\mathrm{T}}^{\mathrm{miss}} > 30$ GeV	0.698	0.699	0.721
τ_{h} identification	0.360	0.357	0.313
$20 < p_{\mathrm{T}}(\tau_{\mathrm{h}}) < 60$ GeV	0.872	0.881	0.881
τ_{h} in gap veto	0.990	0.989	0.990
τ_{h}-ID electron veto	0.875	0.872	0.861
Electron veto	0.948	0.951	0.935
Muon veto	0.996	0.996	0.996
$S_{E_{\mathrm{T}}^{\mathrm{miss}}} > 6$	0.756	0.656	0.510

Table 5.18: Relative efficiency of the cuts for Monte Carlo signal with MC09 and DW tunes without pile up and with pile up. The efficiency refers to events passing the previous cut.

	$W \to \tau_\ell \nu_\tau$ MC09	$W \to \tau_\ell \nu_\tau$ DW	$W \to \tau_\ell \nu_\tau$ MC09+PileUp
Events	9056.4	9056.4	9056.4
Skimming	1917.7±11.6	1744.2±9.2	2055.7±16.4
Trigger	1139.6±9.5	970.1±7.2	1111.9±12.8
Collision cleaning	1138.0±9.4	969.6±7.2	1105.2±12.8
Jet cleaning	1128.3±9.4	958.7±7.2	1083.5±12.7
Jet in gap veto	911.5±8.6	776.0±6.6	874.8±11.5
$min(\Delta\Phi(jet, E_{\mathrm{T}}^{\mathrm{miss}})) > 0.5$	869.9±8.4	740.8±6.4	826.5±11.2
$E_{\mathrm{T}}^{\mathrm{miss}} > 30$ GeV	623.1±7.2	536.3±5.5	608.2±9.8
τ_h identification	288.6±5.0	234.4±3.7	251.8±6.4
$20 < p_{\mathrm{T}}(\tau_h) < 60$ GeV	193.4±4.1	163.4±3.1	174.1±5.4
τ_h in gap veto	192.1±4.1	162.8±3.1	172.6±5.3
τ_h-ID electron veto	31.2±1.7	23.8±1.2	27.2±2.1
Electron veto	22.4±1.4	18.7±1.1	21.2±1.9
Muon veto	12.1±1.0	11.6±0.8	11.2±1.4
$S_{E_{\mathrm{T}}^{\mathrm{miss}}} > 6$	10.5±1.0	9.4±0.8	8.2±1.2

Table 5.19: Number of events passing the selection criteria for Monte Carlo $W \to \tau_\ell \nu_\tau$ with MC09 and DW tunes without pile up and with pile up.

	$W \to \tau_\ell \nu_\tau$ MC09	$W \to \tau_\ell \nu_\tau$ DW	$W \to \tau_\ell \nu_\tau$ MC09+PileUp
Events	1	1	1
Skimming	0.212	0.193	0.227
Trigger	0.594	0.556	0.541
Collision cleaning	0.999	1.000	0.994
Jet cleaning	0.991	0.989	0.980
Jet in gap veto	0.808	0.809	0.807
$min(\Delta\Phi(jet, E_{\mathrm{T}}^{\mathrm{miss}})) > 0.5$	0.954	0.955	0.945
$E_{\mathrm{T}}^{\mathrm{miss}} > 30$ GeV	0.716	0.724	0.736
τ_h identification	0.463	0.437	0.414
$20 < p_{\mathrm{T}}(\tau_h) < 60$ GeV	0.670	0.697	0.691
τ_h in gap veto	0.993	0.996	0.992
τ_h-ID electron veto	0.162	0.146	0.158
Electron veto	0.718	0.789	0.777
Muon veto	0.540	0.619	0.532
$S_{E_{\mathrm{T}}^{\mathrm{miss}}} > 6$	0.867	0.807	0.730

Table 5.20: Relative efficiency of the cuts for Monte Carlo $W \to \tau_\ell \nu_\tau$ with MC09 and DW tunes without pile up and with pile up. The efficiency refers to events passing the previous cut.

	$Z \to \tau\tau$ MC09	$Z \to \tau\tau$ DW	$Z \to \tau\tau$ MC09+PileUp
Events	2434.4	2434.4	2434.4
Skimming	504.3±2.2	501.8±1.4	570.1±3.3
Trigger	267.2±1.7	264.4±1.1	299.8±2.5
Collision cleaning	267.0±1.7	264.4±1.1	297.2±2.5
Jet cleaning	264.2±1.7	260.8±1.1	291.7±2.5
Jet in gap veto	205.3±1.5	202.7±1.0	221.4±2.2
$min(\Delta\Phi(jet, E_{\mathrm{T}}^{\mathrm{miss}})) > 0.5$	167.7±1.4	164.9±0.9	179.1±2.0
$E_{\mathrm{T}}^{\mathrm{miss}} > 30$ GeV	117.3±1.2	115.1±0.7	128.1±1.7
τ_{h} identification	54.4±0.8	52.8±0.5	53.3±1.1
$20 < p_{\mathrm{T}}(\tau_{\mathrm{h}}) < 60$ GeV	43.3±0.7	42.7±0.5	42.6±1.0
τ_{h} in gap veto	42.8±0.7	42.3±0.5	42.0±1.0
τ_{h}-ID electron veto	32.2±0.6	31.6±0.4	30.6±0.9
Electron veto	28.2±0.6	27.3±0.4	26.1±0.8
Muon veto	19.6±0.5	19.2±0.3	18.3±0.7
$S_{E_{\mathrm{T}}^{\mathrm{miss}}} > 6$	13.2±0.4	11.3±0.2	7.6±0.4

Table 5.21: Number of events passing the selection criteria for Monte Carlo $Z \to \tau\tau$ with MC09 and DW tunes tunes without pile up and with pile up.

	$Z \to \tau\tau$ MC09	$Z \to \tau\tau$ DW	$Z \to \tau\tau$ MC09+PileUp
Events	1	1	1
Skimming	0.207	0.206	0.234
Trigger	0.530	0.527	0.526
Collision cleaning	0.999	1.000	0.992
Jet cleaning	0.990	0.987	0.982
Jet in gap veto	0.777	0.777	0.759
$min(\Delta\Phi(jet, E_{\mathrm{T}}^{\mathrm{miss}})) > 0.5$	0.817	0.813	0.809
$E_{\mathrm{T}}^{\mathrm{miss}} > 30$ GeV	0.699	0.698	0.716
τ_{h} identification	0.464	0.459	0.416
$20 < p_{\mathrm{T}}(\tau_{\mathrm{h}}) < 60$ GeV	0.795	0.809	0.798
τ_{h} in gap veto	0.990	0.991	0.986
τ_{h}-ID electron veto	0.751	0.746	0.730
Electron veto	0.876	0.865	0.852
Muon veto	0.697	0.704	0.703
$S_{E_{\mathrm{T}}^{\mathrm{miss}}} > 6$	0.673	0.588	0.412

Table 5.22: Relative efficiency of the cuts for Monte Carlo $Z \to \tau\tau$ with MC09 and DW tunes without pile up and with pile up. The efficiency refers to events passing the previous cut.

5.7.6 ABCD method

The following sources of systematic uncertainty have been considered for the estimation of QCD background from data described in Section 5.6:

Correction for signal and EW background As it has been explained, one assumption of the QCD extraction method is that there is no signal contamination in the control regions. But it has been shown that this contamination is not negligible, as well as the contamination from EW backgrounds. Therefore corrections extracted from Monte Carlo have been applied. A systematic effect connected with these corrections is evaluated by varying the fraction of EW background events within the combined statistical and systematic uncertainties of the Monte Carlo prediction presented in Table5.15. This systematic uncertainty is ±6%.

$S_{E_{\mathrm{T}}^{\mathrm{miss}}}$ **and** τ_{h}**-ID correlation** The other assumption of the method used for the estimation of QCD background is that these two variables used to select data samples are not correlated. As can be seen in Figures 5.17(a) and 5.8, the $S_{E_{\mathrm{T}}^{\mathrm{miss}}}$ distribution for region AB is slightly shifted towards higher $S_{E_{\mathrm{T}}^{\mathrm{miss}}}$ values compared to region CD. This may be an effect of a non-negligible correlation between $S_{E_{\mathrm{T}}^{\mathrm{miss}}}$ and the τ_{h}-ID, as the tau identification has a dependence on the τ_{h} p_{T} (as shown in Chapter 2). The observed shift can cause a systematic effect when computing the number of QCD expected events in region A. As a check, the regions A and C have been enlarged by changing the value used in the $S_{E_{\mathrm{T}}^{\mathrm{miss}}}$ requirement from 6 to 4 (Section 5.6.3), in order to obtain QCD-background-dominated samples in all four regions. The observed value of N^{A}, after subtraction of EW and signal contributions based on Monte Carlo, has been compared with the estimate from Equation 5.2. The same check is performed for the medium τ_{h}-ID. The largest disagreement is observed for the first cross-check and amounts to 28% (while the second is about 20%). Since moving the lower edge of regions A and C down to $S_{E_{\mathrm{T}}^{\mathrm{miss}}} > 4$ integrates the whole region where there is the maximum disagreement in the $S_{E_{\mathrm{T}}^{\mathrm{miss}}}$ distribution, this systematic uncertainty covers the correlation in a conservative approach.

Other cross-checks Many other cross checks have been presented in Section 5.6.3, to show the good reliability of the QCD extraction method. In $W \to \tau_{\mathrm{h}}\nu_\tau$ events, $E_{\mathrm{T}}^{\mathrm{miss}}$, and therefore also $S_{E_{\mathrm{T}}^{\mathrm{miss}}}$, is correlated with the p_{T} of the τ_{h} candidate. The fact that the τ_{h} identification efficiency is not uniform as a function of p_{T} can lead to a potential systematic uncertainty. In order to verify this, the analysis has been repeated for two different p_{T} ranges: 20–30 GeV and 30–60 GeV (Section 5.6.3). The stability of the background estimation is also checked separately for τ_{h} candidates with 1 or more tracks. All variations on the expected number of QCD background events in the signal region are statistically compatible with the estimation on the full sample.

The total systematic uncertainty associated with the QCD background estimation is determined to be 29%, as the sum in quadrature of the 6% from the corrections due to the signal leakage and the 28% from the $S_{E_{\mathrm{T}}^{\mathrm{miss}}}$– τ_{h}-ID correlation. Since this systematic uncertainty is computed comparing samples with different τ_{h} identification efficiencies (as the comparison is performed between regions with tight and loose τ_{h}-ID), it also includes the uncertainties due to the τ_{h} identification algorithm.

5.7.7 Trigger

At this early stage of operation of the ATLAS experiment, a suitable event sample with τ_{h} candidates and $E_{\mathrm{T}}^{\mathrm{miss}}$ selected by a trigger that is independent from the one used in this analysis is not yet available. The trigger selection has therefore been evaluated based on Monte Carlo simulations for events passing events selection described in Section 5.4.

Given that the tauNoCut_hasTrk6_EFxe15_noMu requirements on $E_{\mathrm{T}}^{\mathrm{miss}}$ and τ_{h} p_{T} are much softer than those applied in the event selection, expected systematic uncertainty is low. The trigger is fully efficient for events with $E_{\mathrm{T}}^{\mathrm{miss}}$ above 30 GeV and for τ_{h} with p_{T} in the range 20–60 GeV (see Figures 4.7(a) and 4.7(b)). The systematic uncertainty is below 0.1% which corresponds to the statistical uncertainty of the efficiency calculated on the signal Monte Carlo. The systematic is therefore negligible.

Furthermore, the chosen trigger, tauNoCut_hasTrk6_EFxe15_noMu , was running in various periods using different track reconstruction algorithms at L2 (namely SiTrack and IDScan [82]). This results in an efficiency variation of 0.4% across the whole sample which is estimated from the Monte Carlo signal sample. This source of systematic error is negligible compared to the other sources and therefore is not considered in the analysis.

5.7.8 Pile-up

As already mentioned in Section 5.5, the LHC running conditions changed very much during the data taking period from which the data analysed in this thesis come from. Very soon the number of pile-up events in data has become not negligible. To take into account this fact, Monte Carlo with simulated pile-up have been used. As Monte Carlo samples were simulated with $< n_{\mathrm{pile-up\ vtx}} >= 2$, the events in simulations have been rescaled to match the same reconstructed vertex multiplicity in data.

This rescaling is affected by the uncertainty on the rescaling factors. A systematic effect has therefore been studied.

Different approaches are tried. The event weights are varied within their statistical uncertainties: the systematic uncertainty is found to be 0.1% for Monte Carlo signal events, as well as for EW backgrounds.

A further check was performed by estimating the weights assuming a Poissonian distribution for data and Monte Carlo. To verify the sensitivity to the exact tuning, the means of the distributions were also changed by 5%, which is a much higher value than the statistical uncertainty, which varies from 1% to 2% depending on the sample. This check brought to even smaller systematic uncertainties.

Therefore, the systematic uncertainty coming from the rescaling connected with pile-up is not considered, as found to be negligible.

5.8 Conclusions

In this thesis, it has been described the observation of hadronic decaying taus in $W \to \tau_{\mathrm{h}}\nu_\tau$ events in 7 TeV collision data collected by the ATLAS Experiment.

Using a data sample corresponding to an integrated luminosity of 2.46 ± 0.27 pb^{-1}, with the selection described in Section 5.4, 297 events were selected in data. The QCD background has been extracted directly from data, by means of a 2D side-bins method, and has been evaluated to be $47.8 \pm 4.7(\mathrm{stat.}) \pm 13.9(\mathrm{syst.})$ events. This corrsponds to a number of non QCD events of 249.2 ± 20.8 events. From Monte Carlo, the expected $W \to \tau_{\mathrm{h}}\nu_\tau$ signal amounts to $207.2 \pm 6.0(\mathrm{stat.}) \pm 60.2(\mathrm{syst.})$ and the total background coming from leptonic W and Z boson decays (EW background) is $46.9 \pm 1.6(\mathrm{stat.}) \pm 13.7(\mathrm{syst.})$ events.

A detailed study of the systematics affecting the observation has been done. The main systematics are connected with the description of quantities related to the measurement of missing energy, to the energy scale uncertainty and the description of the underlying event.

From what has been obtained, an evaluation of the cross section can be done, even though clearly affected by huge systematic uncertainties. The value obtained is $10.21 \pm 1.05(\mathrm{stat.}) \pm 1.44(\mathrm{lumi.}) \pm 2.86(\mathrm{syst.})$ nb.

For a $W \to \tau_{\mathrm{h}}\nu_\tau$ cross section measurement, different improvements of the analysis are needed. The full data sample of 45 pb^{-1} collected in the year 2010 will be used and this will implicate that a different trigger from the one used in the analysis presented here must be chosen. But the key point for a good measurement is the reduction of the systematic uncertainties. As the main uncertainties are connected with $E_{\mathrm{T}}^{\mathrm{miss}}$ and $S_{E_{\mathrm{T}}^{\mathrm{miss}}}$, it is necessary to rethink this selection. Exploiting more data, the $E_{\mathrm{T}}^{\mathrm{miss}}$ cut can be tightened, not having to rely any more on the selection based on $S_{E_{\mathrm{T}}^{\mathrm{miss}}}$. Furthermore, a new τ_{h} identification, based on multivariate techniques, will give the opportunity to discriminate better hadronic tau jets from QCD background jets.

Concerning the uncertainty on the jet energy scale, with the new reprocessed data and with the the determination of the tau energy scale, we can think that this uncertainty can be lowered to a reasonable amount.

Moreover, the uncertainty on the collected luminosity is expected to be reduced by a revised analysis of the luminosity measurement.

Bibliography

[1] ATLAS Collaboration, *The ATLAS Experiment at the CERN Large Hadron Collider*, JINST **3** (2008) S08003.

[2] L. Evans and P. Bryant, *LHC Machine*, JINST **3** (2008) S08001.

[3] S. Montesano, L. Dell'Asta, and T. Lari, *Calibration of the charge sharing algorithm for the ATLAS Pixel Detector using cosmic ray data*, ATL-INDET-INT-2010-011, CERN, Geneva, Jun, 2010.

[4] L. Dell'Asta, H. Gray, and S. Strandberg, *Measuring the Charge Scale of the Pixel Detector with Cosmic Ray Data*, ATL-INDET-INT-2010-003, CERN, Geneva, Feb, 2010.

[5] S. Aoun, L. Dell'Asta, F. Djama, H. Gray, and S. Strandberg, *Properties of the Pixel Cluster Charge in Cosmic Ray Data and Simulation*, ATL-INDET-INT-2010-004, CERN, Geneva, Feb, 2010.

[6] ATLAS Collaboration, *The ATLAS Inner Detector commissioning and calibration*, accepted by Eur. Phys. J. C (2010) 1–35. `http://arxiv.org/abs/1004.5293`

[7] M. L. Perl *et al.*, *Evidence for Anomalous Lepton Production in $e^+ - e^-$ Annihilation*, Phys. Rev. Lett. **35** (1975) 1489 – 1492.

[8] M. L. Perl *et al.*, *Properties of anomalous $e\mu$ events produced in e^+e^- annihilation*, Phys. Lett. B **63** (1976) 4, 466 – 470.

[9] K. Nakamura *et al.* (Particle Data Group), *Review of particle physicss*, J. Phys. G **37** (2010) 075021.

[10] A. Andreazza, *Measurement of the tau lifetime with the DELPHI detector*, Nucl. Phys. B - Proc. Suppl. **144** (2005) 97 – 104, TAU 2004.

[11] A. Djouadi, J. Kalinowski, and M. Spira, *HDECAY: a program for Higgs boson decays in the Standard Model and its supersymmetric extension*, Comput. Phys. Commun. **108** (1998) 1, 56 – 74.

[12] ALEPH Collaboration and DELPHI Collaboration and L3 Collaboration and OPAL Collaboration and LEP Higgs Working Group, *Search for Charged Higgs bosons: Preliminary Combined Results Using LEP data Collected at Energies up to 209 GeV*. `http://arxiv.org/abs/hep-ex/0107031v1`

[13] CDF Collaboration, *Search for the charged Higgs boson in the decays of top quark pairs in the $e\tau$ and $\mu\tau$ channels at $\sqrt{s}$ = 1.8 TeV*, Phys. Rev. D **62** (2000) 1.

[14] D0 Collaboration, *Direct Search for Charged Higgs Bosons in Decays of Top Quarks*, Phys. Rev. Lett. **88** (2002) 15.

[15] ATLAS Collaboration, *Introduction on Higgs Boson Searches*, ch. in *Expected performance of the ATLAS experiment: detector, trigger and physics*, pp. 1198–1211, CERN-OPEN-2008-020, CERN, Geneva, 2008.

[16] UA1 Collaboration, *Studies of intermediate vector boson production and decay in UA1 at the CERN proton-antiproton collider*, Zeitschrift für Physik C Particles and Fields **44** (1989) 15–61.

[17] J. M. Campbell, J. W. Huston, and W. J. Stirling, *Hard interactions of quarks and gluons: a primer for LHC physics*, Reports on Progress in Physics **70** (2007) 1, 89.

[18] ATLAS Collaboration, *Measurement of the $Z \to \ell\ell$ production cross section in proton-proton collisions at $\sqrt{s}$ = 7 TeV with the ATLAS detector*, ATLAS-CONF-2010-076, CERN, Geneva, Jul, 2010.

[19] ATLAS Collaboration, *Measurement of the $W \to \ell\nu$ and $Z/\gamma^* \to \ell\ell$ production cross sections in proton-proton collisions at $\sqrt{s}$ = 7 TeV with the ATLAS detector*, submitted to JHEP, CERN-PH-EP-2010-037 (2010) .

[20] CDF Collaboration, *Measurement of the Lepton Charge Asymmetry in W-Boson Decays Produced in $p\bar{p}$ Collisions*, Phys. Rev. Lett. **81** (1998) 26, 5754 – 5759.

[21] CDF Collaboration, *Measurement of the forward-backward charge asymmetry from $W \to e\nu$ production in $p\bar{p}$ collisions at $\sqrt{s}$ = 1.96 TeV*, Phys. Rev. D **71** (2005) 5.

[22] D0 Collaboration, *Measurement of the Electron Charge Asymmetry in $p\bar{p} \to W + X$ Events at $\sqrt{s}$ = 1.96 TeV*, Phys. Rev. Lett. **101** (2008) 21.

[23] D0 Collaboration, *Measurement of the muon charge asymmetry from W boson decays*, Phys. Rev. D **77** (2008) 1.

[24] A. D. Martin, W. J. Stirling, R. S. Thorne, and G. Watt, *Parton distributions for the LHC*, Eur. Phys. J. C **63** (2009) 2, 97.

[25] J. Pumplin, D. R. Stump, J. Huston, H.-L. Lai, P. Nadolsky, and W.-K. Tung, *New Generation of Parton Distributions with Uncertainties from Global QCD Analysis*, JHEP **2002** (2002) 07, 012.

[26] CDF Collaboration, *Measurement of $\sigma(\mathrm{p\bar{p}} \to Z)Br(Z \to \tau\tau)$ in $\mathrm{p\bar{p}}$ collisions at $\sqrt{s}$ = 1.96 TeV*, Phys. Rev. D **75** (2007) 9.

[27] D0 Collaboration, *Measurement of $\sigma(\mathrm{p\bar{p}} \to Z + X)Br(Z \to \tau^+\tau^-)$ at $\sqrt{s}$ = 1.96 TeV*, Phys. Lett. B **670** (2009) 4-5, 292 – 299.

[28] M. Bachtis, *First results from $Z \to \tau^+\tau^-$ at CMS*, Talk at TAU2010.

[29] CDF Collaboration, *Measurement of the ratio $B(W \to \tau\nu)/B(W \to e\nu)$ in $p\bar{p}$ collisions at $\sqrt{s}$ =1.8 TeV*, Phys. Rev. Lett. **68** (1992) 23, 3398 – 3402.

[30] D0 Collaboration, *Measurement of the $W \to \tau\nu$ Production Cross Section in $p\bar{p}$ Collisions at $\sqrt{s} = 1.8TeV$*, Phys. Rev. Lett. **84** (2000) 25, 5710 – 5715.

[31] UA1 Collaboration, *Studies of intermediate vector boson production and decay in UA1 at the CERN proton-antiproton collider*, Zeitschrift für Physik C Particles and Fields **44** (1989) 15–61.

[32] UA2 Collaboration, *A search for charged Higgs from top quark decay at the CERN pp collider*, Phys. Lett. B **280** (1992) 1-2, 137 – 145.

[33] A. N. Safonov, *Physics with Taus at CDF*, Nucl. Phys. B - Proc. Suppl. **144** (2005) 323 – 332, TAU 2004.

[34] CMS Collaboration, *The CMS experiment at the CERN LHC*, JINST **3** (2008) S08004.

[35] LHCb Collaboration, *The LHCb Detector at the LHC*, JINST **3** (2008) S08005.

[36] ALICE Collaboration, *The ALICE experiment at the CERN LHC*, JINST **3** (2008) S08002.

[37] ATLAS Collaboration, *Expected performance of the ATLAS experiment: detector, trigger and physics.* CERN-OPEN-2008-020, CERN, Geneva, 2009.

[38] ALEPH Collaboration, DELPHI Collaboration, L3 Collaboration, OPAL Collaboration and The LEP Working Group for Higgs Boson Searches, *Search for the Standard Model Higgs boson at LEP*, Phys. Lett. B **565** (2003) 61–75.

[39] CDF Collaboration, *Combination of Tevatron Searches for the Standard Model Higgs Boson in the W^+W^- Decay Mode*, Phys. Rev. Lett. **104** (2010) 061802.

[40] ATLAS Collaboration, *Supersymmetry Searches*, ch. in *Expected performance of the ATLAS experiment: detector, trigger and physics*, pp. 1514–1524, CERN-OPEN-2008-020, CERN, Geneva, 2008.

[41] ATLAS Collaboration, *Observation of a centrality-dependent dijet asymmetry in lead-lead collisions at $\sqrt{s_{NN}}$ = 2.76 TeV with the ATLAS detector at the LHC*, accepted by Phys. Rev. Lett. (2010) .
`http://arxiv4.library.cornell.edu/abs/1011.6182`

[42] A. Aad *et al.*, *ATLAS pixel detector electronics and sensors*, JINST **3** (2008).

[43] I. Peric *et al.*, *The FEI3 readout chip for the ATLAS pixel detector*, Nucl. Instrum. Meth. A **565** (Sep, 2006) 178 – 187.

[44] A. Abdesselam *et al.*, *The barrel modules of the ATLAS semiconductor tracker*, Nucl. Instrum. Meth. A **568** (2006) 2, 642 – 671.

[45] A. Abdesselam *et al.*, *The ATLAS semiconductor tracker end-cap module*, Nucl. Instrum. Meth. A **575** (2007) 3, 353 – 389.

[46] A. Ahmad *et al.*, *The silicon microstrip sensors of the ATLAS semiconductor tracker*, Nucl. Instrum. Meth. A **578** (2007) 1, 98 – 118.

[47] F. Campabadal *et al.*, *Design and performance of the ABCD3TA ASIC for readout of silicon strip detectors in the ATLAS semiconductor tracker*, Nucl. Instrum. Meth. A **552** (2005) 292 – 328.

[48] The ATLAS TRT collaboration, *The ATLAS TRT Barrel Detector*, JINST **3** (2008) P02014.

[49] The ATLAS TRT collaboration, *The ATLAS TRT end-cap detectors*, JINST **3** (2008) P10003.

[50] The ATLAS TRT collaboration, *The ATLAS TRT electronics*, JINST **3** (2008) P06007.

[51] D. Attree *et al.*, *The evaporative cooling system for the ATLAS inner detector*, JINST **3** (2008) P07003.

[52] ATLAS Collaboration, *Readiness of the ATLAS Liquid Argon Calorimeter for LHC Collisions*, accepted by Eur. Phys. J. C (2009). `http://arxiv.org/abs/0912.2642`

[53] ATLAS Collaboration, *Readiness of the ATLAS Tile Calorimeter for LHC collisions*, accepted by Eur. Phys. J. C (2010). `http://arxiv.org/abs/1007.5423`

[54] ATLAS Collaboration, *Commissioning of the ATLAS Muon Spectrometer with Cosmic Rays*, accepted by Eur. Phys. J. C (2010). `http://arxiv.org/abs/1006.4384`

[55] ATLAS Collaboration, *Luminosity Determination Using the ATLAS Detector*, ATLAS-CONF-2010-060, CERN, Geneva, Jul, 2010.

[56] A. Sbrizzi, *A Cherenkov Detector for Monitoring ATLAS Luminosity*, ATL-LUM-PROC-2010-004, CERN, Geneva, Sep, 2010.

[57] P. Ruzicka, *Forward physics at the ATLAS experiment*, ATL-LUM-PROC-2010-001, CERN, Geneva, Jan, 2010.

[58] *ATLAS computing: Technical Design Report*, Technical Design Report ATLAS, CERN, Geneva, 2005.

[59] *ROOT*, http://root.cern.ch/.

[60] R. Jones and D. Barberis, *The ATLAS computing model*, J. Phys.: Conf. Ser. **119** (2008) 072020.

[61] M. Cacciari, G. P. Salam, and G. Soyez, *The anti-k_t jet clustering algorithm*, JHEP **2008** (2008) 04, 063.

[62] W. Lampl *et al.*, *Calorimeter Clustering Algorithms: Description and Performance*, ATL-LARG-PUB-2008-002, CERN, Geneva, Apr, 2008.

[63] ATLAS Collaboration, *Properties of Jets and Inputs to Jet Reconstruction and Calibration with the ATLAS Detector Using Proton-Proton Collisions at $\sqrt{s} = 7$ TeV*, ATLAS-CONF-2010-053, CERN, Geneva, Jul, 2010.

[64] Y. Freund and R. E. Schapire, *Experiments with a New Boosting Algorithm*, in *ICML*, pp. 148–156, 1996.

[65] L. Breiman, J. Friedman, C. Stone, and R. Olshen, *Classification and Regression Trees*. Chapman & Hall, 1984.

[66] ATLAS Collaboration, *Tau Reconstruction and Identification Performance in ATLAS*, ATLAS-CONF-2010-086, CERN, Geneva, Oct, 2010.

[67] ATLAS Collaboration, *Reconstruction of hadronic tau candidates in QCD events at ATLAS with 7 TeV proton-proton collisions*, ATLAS-CONF-2010-059, CERN, Geneva, Jul, 2010.

[68] ATLAS Collaboration, *ATLAS Monte Carlo tunes for MC09*, ATL-PHYS-PUB-2010-002, CERN, Geneva, Mar, 2010.

[69] ATLAS Collaboration, *Track-based underlying event measurements in pp collisions at $\sqrt{s}$ = 900 GeV and 7 TeV with the ATLAS Detector at the LHC*, ATLAS-CONF-2010-029, CERN, Geneva, Jul, 2010.

[70] R. Field, *Min-Bias and the Underlying Event at the Tevatron and the LHC*, A talk presented at the FERMILAB MC Tuning Workshop, FERMILAB (Oct, 2002).

[71] Z. Czyczula and M. Dam, *Electron Suppression in Hadronic One-prong Tau Decays*, ATL-COM-PHYS-2006-017, CERN, Geneva, Feb, 2006.

[72] ATLAS Collaboration, *Reconstruction and Identification of Hadronic tau Decays*, ch. in *Expected performance of the ATLAS experiment: detector, trigger and physics*, pp. 229–259, CERN-OPEN-2008-020, CERN, Geneva, 2008.

[73] ATLAS Collaboration, *Commissioning of the ATLAS Tau-Lepton Reconstruction Using 900 GeV Minimum-Bias Data*, ATLAS-CONF-2010-012, CERN, Geneva, Jul, 2010.

[74] ATLAS Collaboration, *Performance of the Missing Transverse Energy Reconstruction and Calibration in Proton-Proton Collisions at a Center-of-Mass Energy of 7 TeV with the ATLAS Detector*, ATLAS-CONF-2010-057, CERN, Geneva, Jul, 2010.

[75] ATLAS Collaboration, *Data-Quality Requirements and Event Cleaning for Jets and Missing Transverse Energy Reconstruction with the ATLAS Detector in Proton-Proton Collisions at a Center-of-Mass Energy of $\sqrt{s}$ = 7 TeV*, ATLAS-CONF-2010-038, CERN, Geneva, Jul, 2010.

[76] ATLAS Collaboration, *Performance of the missing transverse energy reconstruction in minimum bias events at $\sqrt{s}$ of 900 GeV and 2.36 TeV with the ATLAS detector*, ATLAS-CONF-2010-008, CERN, Geneva, Jun, 2010.

[77] ATLAS Collaboration, *Performance of the missing transverse energy reconstruction in proton-proton collisions at center-of-mass energy of $\sqrt{s} = 7$ TeV with the ATLAS detector*, ATLAS-CONF-2010-039, CERN, Geneva, Jul, 2010.

[78] ATLAS Collaboration, *The Trigger for Early Running*, ch. in *Expected performance of the ATLAS experiment: detector, trigger and physics*, pp. 550–564, CERN-OPEN-2008-020, CERN, Geneva, 2008.

[79] ATLAS Collaboration, *Tau Trigger: Performance and Menus for Early Running*, ch. in *Expected performance of the ATLAS experiment: detector, trigger and physics*, pp. 592–618, CERN-OPEN-2008-020, CERN, Geneva, 2008.

[80] M.P. Casado *et al.*, *The ATLAS tau trigger*, Nucl. Phys. B - Proc. Suppl. **189** (2009) 291 – 298, TAU 2008.

[81] J. Garvey *et al.*, *Use of an FPGA to identify electromagnetic clusters and isolated hadrons in the ATLAS level-1 calorimeter trigger*, Nucl. Instrum. Meth. A **512** (2003) 3, 506 – 516.

[82] ATLAS Collaboration, *HLT Track Reconstruction Performance*, ch. in *Expected performance of the ATLAS experiment: detector, trigger and physics*, pp. 565–583, CERN-OPEN-2008-020, CERN, Geneva, 2008.

[83] ATLAS Collaboration, *Performance of the ATLAS tau trigger in p-p collisions at* $\sqrt{s}$*=900 GeV*, ATLAS-CONF-2010-021, CERN, Geneva, Jul, 2010.

[84] ATLAS Collaboration, *Performance of the ATLAS tau trigger in p-p collisions at* $\sqrt{s}$*=7 TeV*, ATLAS-CONF-2010-090, CERN, Geneva, Aug, 2010.

[85] ATLAS Collaboration, *Overview and Performance Studies of Jet Identification in the Trigger System*, ch. in *Expected performance of the ATLAS experiment: detector, trigger and physics*, pp. 697–722, CERN-OPEN-2008-020, CERN, Geneva, 2008.

[86] P. H. Beauchemin, *Performance of the ATLAS missing* E_T *trigger with first* $\sqrt{s}$ *= 7 TeV data*, ATL-DAQ-PROC-2010-024, CERN, Geneva, Aug, 2010.

[87] ATLAS Collaboration, *The ATLAS missing Et trigger performance with initial LHC runs at sqrt(s) = 900 GeV*, ATLAS-CONF-2010-026, CERN, Geneva, Jul, 2010.

[88] C. Anastasiou, L. Dixon, K. Melnikov, and F. Petriello, *High-precision QCD at hadron colliders: Electroweak gauge boson rapidity distributions at next-to-next-to leading order*, Phys. Rev. D **69** (2004) 094008.

[89] W. L. van Neerven and E. B. Zijlstra, *The* $O(\alpha_s^2)$ *corrected Drell-Yan K-factor in the DIS and MS schemes*, Nucl. Phys. B **382** (1992) 1, 11 – 62.

[90] R. Hamberg, W. L. van Neerven, and T. Matsuura, *A complete calculation of the order* α_s^2 *correction to the Drell-Yan K-factor*, Nucl. Phys. B **359** (1991) 2-3, 343 – 405.

[91] Y. Coadou, P. Malecki, and E. Richter-Was, *Prospects for physics measurements with the* $W \to \tau_{\mathrm{h}}\nu_\tau$ *process for 100* pb^{-1} *with the ATLAS detector*, ATL-PHYS-INT-2009-011, CERN, Geneva, Aug, 2008.

[92] G. Nunes Hanninger, L. Dell'Asta, A. Andreazza, D. Casadei, Y. Coadou, J. C. Dingfelder, O. Igonkina, J. Kroseberg, P. Malecki, M. Neubauer, E. Richter-Was, and A. Sfyrla, *Prospects for Studying* $W \to \tau_{\mathrm{h}}\nu_\tau$ *Decays with ATLAS Data Corresponding to an Integrated Luminosity of 100* pb^{-1}, ATL-PHYS-INT-2010-073, CERN, Geneva, Aug, 2010.

[93] T. Sjöstrand, S. Mrenna, and P. Skands, *PYTHIA 6.4 physics and manual*, JHEP **2006** (2006) 05, 026.

[94] S. Agostinelli *et al.*, *G4–a simulation toolkit*, Nucl. Instrum. Meth. A **506** (2003) 3, 250 – 303.

[95] ATLAS Collaboration, *The ATLAS Simulation Infrastructure*, accepted by Eur. Phys. J. C (2010). `http://arxiv.org/abs/1005.4568`

[96] S. Frixione, P. Nason, and B. Webber, *Matching NLO QCD and parton showers in heavy flavour production*, JHEP **2003** (2003) 08, 007.

[97] ATLAS Collaboration, *Observation of inclusive electrons in the ATLAS experiment at* $\sqrt{s}$ *=7 TeV*, ATLAS-CONF-2010-073, CERN, Geneva, Jul, 2010.

[98] ATLAS Collaboration, *Muon Performance in Minimum Bias pp Collision Data at* $\sqrt{s}$ *=7 TeV with ATLAS*, ATLAS-CONF-2010-036, CERN, Geneva, Jul, 2010.

[99] ATLAS Collaboration, *Performance of primary vertex reconstruction in proton-proton collisions at* $\sqrt{s}$ *=7 TeV in the ATLAS experiment*, ATLAS-CONF-2010-069, CERN, Geneva, Jul, 2010.

[100] ATLAS Collaboration, *Evidence for prompt photon production in pp collisions at* $\sqrt{s}$ *= 7 TeV with the ATLAS detector*, ATLAS-CONF-2010-077, CERN, Geneva, Jul, 2010.

[101] ATLAS Collaboration, *Observation of* $W \to \tau\nu$ *Decays with the ATLAS Experiment*, ATLAS-CONF-2010-097, CERN, Geneva, Nov, 2010.

[102] ATLAS Collaboration, *Measurement of the* $W \to \ell\nu$ *production cross-section and observation of* $Z \to \ell\ell$ *production in proton-proton collisions at* $\sqrt{s}$ *= 7 TeV with the ATLAS detector*, ATLAS-CONF-2010-051, CERN, Geneva, Jul, 2010.

[103] M. Schott, D. Froidevaux, and M. Boonekamp, *Supporting Document: Total inclusive W and Z boson cross-section measurements, cross-section ratios and combinations in the electron and muon decay channels at 7TeV based on* $300nb^{-1}$, ATL-COM-PHYS-2010-703, CERN, Geneva, Sep, 2009.

[104] A. Ahmed *et al.*, *Supporting Document: Measurement of the W cross section and asymmetry in the electron and muon decay channels at* $\sqrt{s}$*=7 TeV*, ATL-PHYS-INT-2010-116, CERN, Geneva, Sep, 2010.

[105] ATLAS Collaboration, *Jet energy scale and its systematic uncertainty for jets produced in proton-proton collisions at* $\sqrt{s}$ *= 7 TeV and measured with the ATLAS detector*, ATLAS-CONF-2010-056, CERN, Geneva, Jul, 2010.

[106] ATLAS Collaboration, *In-situ pseudo-rapidity inter-calibration to evaluate jet energy scale uncertainty and calorimeter performance in the forward region*, ATLAS-CONF-2010-055, CERN, Geneva, Jul, 2010.

[107] ATLAS Collaboration, *Muon Reconstruction and Identification: Studies with Simulated Monte Carlo Samples*, ch. in *Expected performance of the ATLAS experiment: detector, trigger and physics*, pp. 162–184, CERN-OPEN-2008-020, CERN, Geneva, 2008.

[108] *ATLAS* $Z \to \mu\mu$ *performance workshop*, CERN, 8 September 2010.